Investigation of focused Very High Energy Electrons (VHEEs) as a new radiotherapy method

by

Karolina Zofia Kokurewicz

A thesis presented for the degree of
Doctor of Philosophy in Physics

Physics Department, University of Strathclyde, Glasgow

Supervisors:
Prof. Dino Jaroszynski
Dr. Enrico Brunetti

February 11, 2020

Abstract

Currently, external beam radiotherapy is faced with the challenge of delivering doses which exceed standard clinical fractions to target radioresistant tumours. However, any dose escalation in the tumour is limited by radiation tolerance of healthy tissues, including skin, which is among the most sensitive tissue. An improved efficiency can be accomplished at the cost of irreversible damage to these tissues. A similar problem is found when high doses are delivered to deep-seated tumours while trying to avoid intolerable doses in surrounding tissue.

This thesis investigates a new treatment modality that uses a single Very High Energy Electron (VHEE, $50 - 250$ MeV) beams focused by a magnetic lens to create a high dose region in a small volume, which is referred to here as a *volumetric element*. This can be scanned over the radioresistant regions of a tumour at typical depths of deep-seated cancers. Monte Carlo simulations were performed to model irradiation of a tissue-equivalent phantom with focused VHEE beams. These are confirmed by an experimental investigation of this treatment method that was undertaken at the CLEAR user facility at CERN. The results show a significant enhancement of the target dose and a simultaneous reduction of the dose to surrounding healthy tissue.

The experimental part of this study required a new dosimetry protocol to be established for VHEEs. The energy dependence and dose response of radiochromic films up to 50 MeV were studied using the electron research accelerator at the Physikalisch-Technische Bundesanstalt (PTB) in Braunschweig and the clinical accelerator at the National Physical Laboratory (NPL) in London. The response of radiochromic films in the VHEE range was cross-calibrated against alanine based secondary standard.

Acknowledgements

Completion of this doctoral dissertation was possible with the support of several people, including my friends, colleges, funding agencies and various institutions who contributed in many ways to the success of this study. I would like to express my sincere gratitude to all of them.

At the forefront, I would like to express deep gratitude to my academic supervisors. Prof. Jaroszynski for giving me this opportunity to be part of his research group. I would like to express my thanks for his guidance, which helped me through this challenging task of conducting a PhD project and gaining the identity of an independent researcher. Moreover, I would like to thank Prof. Jaroszynski for encouraging me to think beyond the possible, follow ideas that drive innovation, and create the scientific values based on the fruitful networks and collaborations and for his crucial remarks that shaped my final dissertation.

I am especially indebted to Dr. Brunetti for his patient guidance, enthusiastic encouragement and insightful critiques, which helped in completion of this dissertation. I appreciate all discussions that we had, the help with the simulations and experiments and his precious time for sharing his expertise.

Furthermore, I would like to thank to Dr. Gregor Welsh for being a great advisor during the first three years. Thank you for reacting to my worries and concerns, and for patience to instil confidence in both myself and my work.

I would like to thank to Dr. Anna Subiel for her great advice in data analysis, for performing the measurements with the clinical accelerator at the National Physical Laboratory and scientific contribution to the manuscripts and papers.

Dr. Antoni Ruciński, who has been supportive of my career goals, who convinced me during our many discussions that I should pursue a doctoral degree.

Dr. Ralf-Peter Kapsch who provided me with access to the laboratory at the German Metrology Institute in Braunschweig for dosimetry measurements using Gafchromic® films.

My sincere thanks also goes to Dr. Andreas Schüller, who arranged the experimental setup at PTB and help solve technical problems, the accelerator group, Mr Christoph Makowski, Mr Markus Meier and Mr Markus Schrader, as well as Mr. Thomas Hackel for preparing and analysing the alanine samples.

Dr. Roberto Corsini who provided me with access to the laboratory at the CLEAR user facility at CERN where I conducted the cross-calibration of Gafchromic® films and alanine for VHEEs and focused VHEE experiments.

I would like to express my special appreciation and thanks to Dr. Wilfrid Farabolini who spent an extensive time in the accelerator bunker to make the experiment on focused VHEEs possible. His devotion and compassion in work is exemplary. I would also like to thank the CLEAR research group at CERN, which comprises of Dr. Alessandro Curcio, Dr. Davide Gamba, Dr. Luca Garolfi, Mr Antonio Gilardi, Dr. Kyrre Ness Sjøbæk and Mr Eugenio Senes, for their help during measurements.

I would also like to thank Mr Lars Fredrik Fjæra for providing me with the FLUKA input file for simulations used in this thesis, as well as helping me with modifications when necessary.

I thank Mr Thomas McGrory for technical support.

I wanted to take this opportunity to thank also my office mates, Giorgio Battaglia, Dr. Lewis Reid and George Holt for the friendly atmosphere and interesting chats during everyday lunch as well as help with correcting my English. I would also like to thank my group colleges and the members of the Strathclyde Student Community for Optics, Physics and Engineering for the great moments we shared in Glasgow on many occasions.

I would also like to thank Jonathan for his love and support. Thank you for being with me during the most difficult moments and for our small escapes to the beautiful

Chapter 0.   Acknowledgements

Scottish landscape.

Last but not the least, I wish to thank my mother for her support and encouragement throughout my life and for her understanding.

Role of the author

The idea of focused Very High Energy Electrons (VHEEs) for radiotherapy was conceived by Prof. Dino Jaroszynski. The Monte Carlo simulations were performed by the author in consultation with Dr. Enrico Brunetti. The experimental part of this doctoral project was performed in collaboration with three research institutes, the Physikalisch-Technische Bundesanstalt (PTB) in Braunschweig thanks to the head of the working group Dr. Ralf-Peter Kapsch and Dr. Andreas Schüller, the CERN Linear Electron Accelerator for Research (CLEAR) user facility in Geneva thanks to the leader of the research group Dr. Roberto Corsini and Dr. Wilfrid Farabolini, and the National Physical Laboratory (NPL) in London thanks to Dr. Anna Subiel. The experiment at PTB, the calibration of Gafchromic® films for electron energies < 50 MeV, the analysis and interpretation of the results were conducted by the author with the help of Dr. Enrico Brunetti and Dr. Andreas Schüller who arranged, built and tested the experimental setup in compliance with the PTB dosimetry standards and who performed reference dosimetry with the Advanced Markus Chamber, and the research accelerator team; Mr Christoph Makowski, Mr Markus Meier and Mr Markus Schrader. The experiment at CERN, the calibration of alanine and Gafchromic® films for electron energies 50 – 200 MeV as well as the focused VHEE experiment was proposed by the author and conducted with the help of Dr. Enrico Brunetti and the CLEAR research group. The experimental equipment for both experiments was designed by the author and constructed by Mr Thomas McGrory. The setup and the test beamline at the CLEAR facility was built by Dr. Wilfrid Farabolini, Dr. Kyrre Ness Sjøbæk and Mr Antonio Gilardi. The design of the collimator for the calibration irradiation was carried out

using Monte Carlo calculations by Dr. Kyrre Ness Sjøbæk. The optimisation of the electron beam was performed by Dr. Wilfrid Farabolini, Dr. Alessandro Curcio, Dr. Davide Gamba, Dr. Luca Garolfi, Mr Antonio Gilardi and Dr. Kyrre Ness Sjøbæk. The MAD-X (Methodical Accelerator Design) simulations of the beam optics were carried out by Mr Eugenio Senes. Mr. Thomas Hackel prepared and analysed the alanine samples. Dr. Anna Subiel performed the calibration of Gafchromic® films using the clinical accelerator at NPL. The author performed the data analysis and interpretation of the results. The input file to calculate 2D LET using FLUKA MC code was shared by Mr Lars Fredrik Fjæra. Prof. Dino Jaroszynski provided overall supervision.

List of publications

1. K Kokurewicz, E Brunetti, G H Welsh, S M Wiggins, M Boyd, A Sorensen, A J Chalmers, G Schettino, A Subiel, C DesRosiers, and D A Jaroszynski. Focused very high-energy electron beams as a novel radiotherapy modality for producing high-dose volumetric elements. *Scientific Reports*, 9(1):1-10, 2019.

2. K Kokurewicz, G H Welsh, E Brunetti, S M Wiggins, M Boyd, A Sorensen, A Chalmers, G Schettino, A Subiel, C DesRosiers, and D A Jaroszynski. Laser-plasma generated very high energy electrons (VHEEs) in radiotherapy. *Proceeding of International Society for Optics and Photonics*, 10239:102390C, 2017.

3. K Kokurewicz, E Brunetti, A Curcio, D Gamba, L Garolfi, A Gilardi, E Senes, K N Sjøbæk, W Farabolini, R Corsini, and D A Jaroszynski. Focused very high energy electron (VHEE) beams as a precise radiotherapy tool, *Nature Communications* (submitted).

4. K Kokurewicz, A Schüller, E Brunetti, A. Subiel, R. Kranzer, T Hackel, M. Meier, R-P Kapsch, and D A Jaroszynski. Dosimetry for new radiation therapy approaches using high energy electron accelerators. *Special issue of the Biophysics Collaboration Frontiers in Physics, Dosimetry for new radiation therapy approaches with high energy electron accelerators* (accepted).

During the course of this PhD the author has contributed to the following publications:

1. E Brunetti, K Kokurewicz, S Cipiccia, A Maitrallain, M Shahzad, R Spesyvtsev, D A Jaroszynski. A simple method of producing a focused X-ray beam. *Proceeding of International Society for Optics and Photonics*, 11036:110360S, 2019.

2. A Kornaszewski, R Spesyvtsev, M Shahzad, E Brunetti, P W Wachulak, T Fok, Ł Węgrzyński, G Battaglia, B Ersfeld, J Feehan, L Ivan Inigo Gamiz, K Kokurewicz, W Li, A Maitrallain, A Noble, L Reid, M Tooley, G Vieux, S Wiggins, S Yoffe, H Fiedorowicz, and D A Jaroszynski. Plasma density shaping for attosecond electron bunch generation. *Proceeding of International Society for Optics and Photonics*, 11036:110360R, 2019.

3. D A Jaroszynski, M P Amnania, C Aniculaesei, G Battaglia, E Brunetti, S Chen, S Cipiccia, B Ersfeld, D R Gil, D W Grant, P Grant, M S Hur, L I Inigo Gamiz, T Kang, K Kokurewicz, A Kornaszewski, W Li, A Maitrallain, G G Manahan, A Noble, L R Reid, M Shahzad, R Spesyvtsev, A Subiel, M P Tooley, G Vieux, S M Wiggins, G H Welsh, S R Yoffe, and X Yang. Compact radiation sources based on laser-driven plasma waves. *Proceeding of International Society for Optics and Photonics*, 11042:110420Y, 2019.

Contents

Contents

Contents

Contents

Chapter 1

Introduction

The work presented in this dissertation involves a feasibility study on the application of Very High Energy Electrons (VHEEs) in cancer treatment. This chapter presents the cancer statistics and the historical background of radiotherapy. In the following sections the mechanisms of cell and tissue response to radiation are discussed and a brief introduction to the currently available radiotherapy modalities and techniques is given. The chapter also reviews past and ongoing progress in the field of VHEE therapy and proposes a new treatment method based on strongly focused VHEEs. The novelty of the method is that it utilises the properties of VHEEs to target precisely deep-seated and radioresistant tumours, which has hitherto never been employed in clinical practice. The motivation of this doctoral project and thesis outline are given in the last section of this chapter.

1.1   Cancer statistics

Cancer is the uncontrolled growth and spreading of genetically damaged cells, which are triggered by a range of factors, generally categorised as biological (age, gender, inherited genetic defects and skin type), environmental (natural, UV and cosmic radiation), occupational (chemicals, radioactive materials and asbestos) and lifestyle-related factors (diet, physical condition). It is a global disease and the leading cause of death in economically developed countries according to the Global Cancer Observatory (Fig-

ure 1.1). The estimated population living with cancer in the UK in 2015 is 2.5 million. Prolonged life expectancy is foreseen to increase this number to 4 million by 2030 [1]. The common methods of curing cancer are surgery, chemotherapy and radiotherapy. Radiotherapy, often administrated in combination with surgery and chemotherapy, accounts for 40% of all cancer cures. However, access to radiotherapy in large parts of the world is still very limited due to its high cost, which tends to increase with technology advancement. The future delivery of high-quality radiotherapy services relies on innovative radiotherapy techniques. Cost-effective and efficient solutions are necessary to enable broad access.
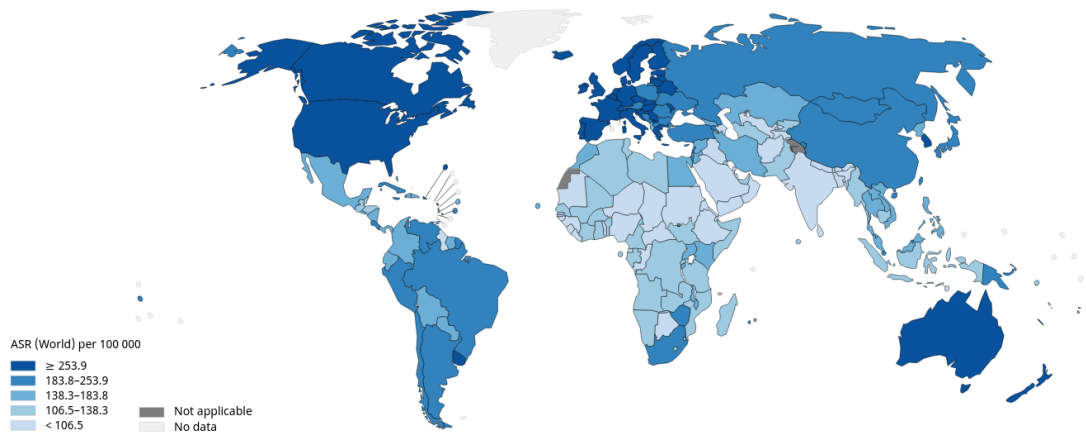
Figure 1.1: Worldwide estimates of age-standardised incident rates (ASR) of all common types of cancers in 2018 [2].

1.2   Brief history of radiotherapy

The origins of radiotherapy can be traced back as far as 1896, barely a year after the discovery of X-rays by Wilhelm Conrad Röntgen [3], when a 55-year old woman suffering from recurrent inoperable breast cancer was exposed to X-rays by the Chicago chemist and homeopathic physician Emil Grubbé [4]. Similar attempts are documented worldwide. In the same year in Lyon, Victor Despeignes started pioneering treatment of patients with stomach cancers [5], and a year later the Viennese doctor Leopold Freund used X-rays to cure a skin tumour in a five-year old girl [6]. The initial successful treatment outcomes triggered mass-market investments into manufacture of the

first clinical versions of X-ray machines, even though safe application of radiation was not fully investigated until 1928 when the International Commission on Radiological Protection (ICRP) was established to address radiation safety issues [7].

A plethora of discoveries in radiation physics occurred during the last decade of the XIX century. In 1896, while Henri Becquerel studied fluorescent minerals he observed that uranyl sulfate emits a penetrating radiation similar to X-rays [8]. In 1898 Maria Skłodowska-Curie and her husband Pierre Curie measured radiation from pitchblende, an ore from which uranium is extracted, and named the spontaneous emission as *radio-activity*. They also extracted radium, an element that is million times more radioactive than uranium [9, 10]. Becquerel and Curie collaborated on reporting the physiologic effects of radium rays in 1901 [11]. Potential application of radium was at first considered by Henri Danlos and Paul Bloch from Paris, who applied the sealed radium source in the treatment of a patient suffering from the autoimmune skin disease lupus erythematous [12]. In the early 1920s, lead containers were designed to insert needles and tubes of radium into the patient over distances of few centimetres [13, 14]. This technique became known as *tele-radium therapy* [15], and was widely used in the United States, France and Belgium.

The following century witnessed revolutionary advances in radiotherapy, such as the introduction of cobalt treatment systems, that produced high-energy γ-rays, electron linear accelerators (also known as electron linacs) [16], and discovery of diagnostic and therapeutic radioactive isotopes, such as ^{99m}Tc, ^{14}C, ^{18}F, ^{15}O and ^{131}I, which are still commonly used. The earliest application of electrons was reported in 1940, mainly for skin cancers due to their weak penetration in tissue. A few years later the physicist Robert R. Wilson published a work titled *Radiological Use of Fast Protons* [17], which began the era of particle beam therapy. The first clinical use of a proton beam was reported in 1954 [18] at the Lawrence Berkeley National Laboratory (LBNL). The second dedicated proton therapy (PT) centre was built in 1957 in Sweden. Since then many other particles, mainly neutrons, helium, neon, and carbon ions, and some exotic species, such as pions and antipions were investigated for cancer treatment. Research on the application of fast neutrons started in 1965 at the Hammersmith Hospital in

London, and in 1971 Dr. Mary Catterall performed the first clinical trials. The LBNL group involved in the proton therapy project embarked on helium therapy in 1957 and neon therapy in 1975 [19]. Several thousands patients have been treated with pions since the 1970s at the pion therapy centres: Paul Scherrer Institute (PSI), TRIUMF and Los Alamos Meson Physics Facility (LMAPF). However, poor clinical outcomes [20, 21] eventually led institutions to abandon this therapy. In 2015, the number of PT facilities was 56 and 12 for carbon ion therapy (CIT), including 6 for CIT alone and 6 for both CIT and PT [22]. In addition, several new CIT facilities are currently under construction in Japan (2), China (1) and Korea (1), and 4 PT centres are being commissioned in the United Kingdom.

1.3   Cell and tissue response to radiation

The biological effects of radiation are the consequences of a long series of physical and chemical processes [23]. Table 1.1 shows the temporal scales of processes occurring after exposure to radiation. Tumour formation (carcinogenesis) is a stochastic radiation-induced effect, which usually occurs after many years. Over the course of time, cells mutate, proliferate and create a tumour. Non-stochastic effects, such as cataracts, skin erythema and radiation sickness are short-term consequences of cell damage or death. Understand the formation of confined ionisation clusters is important for determining the temporal and spatial distributions of radiation in tissue [24, 25]. If ionisation events take place in close proximity to each other their collective effect causes irreversible damage to the genetic material of cell, DNA (deoxyribonucleic acid), and can lead to cell apoptosis or necrosis.

Table 1.1: Timescale of physical, chemical and biological processes induced by radiation.

Time	Event
$10^{-20} - 10^{-8}$ s	ionisation (tissue atoms gaining or losing electrons),
	excitation (tissue atoms gaining a discrete amount of energy)
$10^{-18} - 10^{-9}$ s	damage cause by unstable atoms (free radical)
10^{-3} – hours	chemical and enzymatic repair
hours – weeks	cell death, animal death
years	carcinogenesis

Cells are killed or partially damaged by a radiation through ionisation. Three types of damage to the DNA are possible: single strand break (SSB), double strand break (DSB), or nucleotide base damage [26]. A combination of SSB or DSB (Figure 1.2), with associated base lesions or apurinic/apyrimidinic (AP) sites forming as a consequence of the removal of damaged or inappropriate bases, create clustered damage sites [27]. The complexity of clusters increases with increasing ionisation density of the radiation [28]. However, non-DSB clusters can also form a DSB lesion, which adds to the complexity of DSBs and significantly affects their repair [29].
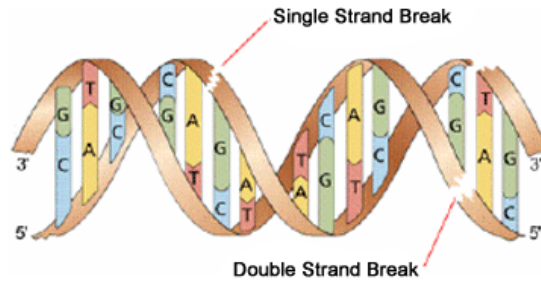
Figure 1.2: DNA double and single strand breaks [30].

The number of DSBs is related to delivered dose (absorbed energy). The relation between radiation dose and cell survival is described by the linear-quadratic (LQ) model [31], expressed as follows:

$$SF = \exp[-(\alpha D + \beta D^2)], \tag{1.1}$$

The parameters α and β are the linear and quadratic components, respectively. This model is the representation of survival fraction after a single acute dose (typically 2 Gy). For multiple fractions the model includes additional variables as follows:

$$SF = \exp[-\alpha D - \frac{\beta D^2}{f} + \lambda(T - T_k)], \tag{1.2}$$

where D is the dose delivered in a number of fractions f. λ is a constant related to cell proliferation (repopulation) after irradiation, which is expressed as $\ln(2)/T_p$, where T_p is the tumour potential doubling time (repair half time). The parameter T is the

treatment time and T_k is the starting time of accelerated proliferation, which is the time at which repopulation begins.

The LQ model has been applied to the survival fraction data of mammalian cells (HeLa cell line) irradiated with X-rays, which was initially published by Puck and Marcus [32] (Figure 1.3). The dose-response relationship was later studied for electron radiation, however the literature data is limited and focus mainly on electrons in keV range which have higher radiobiogical effect than γ-rays [33]. It has been observed that the number of cells that survived exposure to radiation decreases inversely with the delivered dose. The shape of the survival fraction curve saturates at the point where any increase in dose causes injuries to accumulate faster than the repair actions (misrepair). Although the discovery of this phenomenon has had a significant impact on modern radiotherapy and radioprotection methods, the mathematical description of the LQ model lacks information on the processes that govern cell repair activities or DNA mutations occurring long after exposure to radiation.
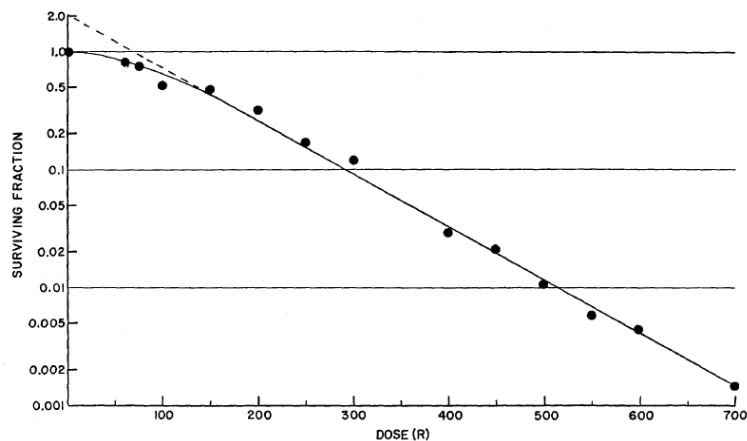
Figure 1.3: Survival fraction of HeLa cells as a function of X-ray dose, from [32].

A schematic response of healthy and tumour tissue to increasing dose is shown in Figure 1.4. The sinusoid-shaped curves represent the normal (healthy) tissue complication probability (NTCP) and tumour control probability (TCP). The NTCP model has been developed to estimate complications that result from partial irradiation of healthy tissue lying adjacent to the tumour, whereas TCP is a measure of probabil-

ity of cancerous cell kill after treatment. The ultimate goal of radiotherapy is to find a treatment that will ensure a high TCP with an acceptable NTCP. Therefore, both models are used to optimise clinical outcomes based on the information on the tolerance doses for various tissue that are established through cytogenetic studies [34]. In the most optimal dose range, where TCP > 0.5 and NTCP < 0.5, the probability of tumour control without complications (shaded area in Figure 1.4) reaches maximum. This region is often referred to as a therapeutic window. All recent efforts towards high efficiency radiotherapy are focused on methods and protocols that can stimulate a radiobiological effect within this range.
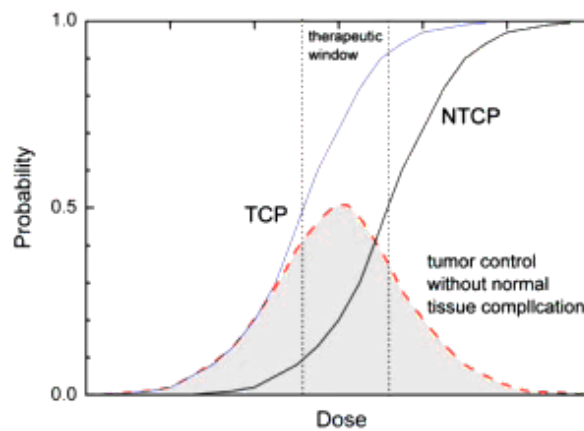
Figure 1.4: Dose-dependence of TCP and NTCP models [35, 36].

1.4 Selected radiotherapy treatment modalities

Radiotherapy uses different types of radiation, referred to as radiotherapy modalities, to kill cancer. The depth-dose (absorbed energy) distribution along the propagation axis of radiation in tissue-equivalent material, such as water, reveals different mechanisms of energy deposition and unique properties of each of the types. The commonly radiotherapy modalities are photons and particulate radiation, such as low energy electrons and protons. Figure 1.5 shows a simulation of normalised depth-dose distribution close to the beam propagation axis for the aforementioned modalities in a $30 \times 30 \times 30$ cm^3 water phantom. Water is used to reproduce radiation absorption and scattering in soft tissue and muscles. The attenuation of the photon beam is governed by the Beer-

Lambert law [37], which explains the exponential decrease of the beam intensity with the distance from the phantom entrance (curve **a**). In contrast, clinical electron beams (4 – 25 MeV) deposit their maximum doses near the entrance (curve **b**). The peak is followed by a sharp dose fall-off and a long tail that is produced by bremsstrahlung radiation. Protons, on the other hand, deposit their maximum dose at the end of their range, in the so called Bragg peak [38] (curve **c**). Carbon ions, not shown in Figure 1.5, have similar energy-range characteristics to protons, but the ratio of Bragg peak dose to the dose in the entrance region is larger than for protons and the Bragg peak is sharper. In particle beam therapy a uniform dose in the target, spread-out-Bragg peak (SOBP, curve **d**), is created by superposing multiple beams of different energies.
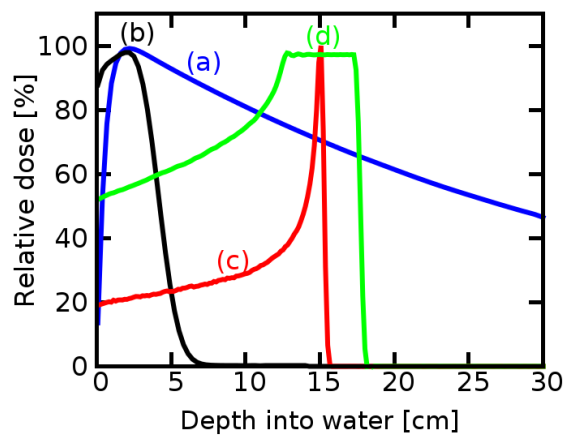
Figure 1.5: Percentage depth-central axis dose profiles for different types of radiation in radiotherapy. (a) photons, (b) low energy electrons, (c) protons, (d) SOBP.

1.5 Selected radiotherapy treatment techniques

The main aim of radiotherapy is to kill cancer cells, while simultaneously protecting healthy tissue from the detrimental effects of radiation. Early methods of delivering X-ray and radium treatment developed into two main branches: teletherapy, the administration of radiation from external sources, and brachytherapy, the insertion of radiation-emitting sources directly into the tumour or adjacent areas. Externally applied high energy X-rays are produced, either directly from ^{60}Co sources, or by conversion of electron beams from linear accelerators (linacs) into bremstrahlung radiation.

The first models of ^{60}Co units were limited to selected applications due to their low photon energies (average 1.25 MeV) and associated scattering [39, 40]. Nowadays, their main application is in the GammaKnife®, which is a treatment machine that employs a large number of ^{60}Co sources mounted behind a collimator helmet that directs the X-ray beams onto a single point within the tumour [41].

Modern radiotherapy techniques, based on 3D conformal radiation therapy (3D-CRT), employ computed tomography (CT) images to determine the location of the tumour and its geometry prior to treatment [42]. Based on the information from CT scans, several different angles are set by the positions of the movable linac's arm (gantry), which delivers multiple beams, each tailored to the size and shape of the tumour projection by multileaf collimator (MLC) [43]. An additional function of MLCs is modulation of the beam intensity for individual treatment angles, which is achieved by employing a composition of various shaped segments within each treatment beam in order to perform intensity modulated radiotherapy (IMRT) [44, 45]. An advanced form of IMRT, volumetric modulated arc therapy (VMAT), allows continuous radiation delivery while a gantry rotates around the patient [46].

An alternative radiation delivery system is CyberKnife® [47], which replaces the gantry with a robotic arm that delivers non-isocentric beams through the full 6 degrees of freedom of movement. In this case, a linac produces X-rays with energies up to 6 MV that are combined with an image tracking system. This allows both the arm position and orientation to be modified to compensate for patient movement, which enables the accuracies of < 1 mm to be obtained.

A conventional radiotherapy is typically delivered in multiple fractions over a course of 6 weeks to allow healthy tissue to recover after irradiation. However, the excellent spatial accuracy of dose delivery of GammaKnife® and CyberKnife®, allows 2-3 times dose escalation to the tumour with fewer treatments than standard radiotherapy. The increased doses result in high local control rates of up to 90% and more, without causing severe toxicities. These techniques are known as Stereotactic Ablative Radiotherapy (SART) [48] and are typically used to treat small tumours that were detected at early stage.

Proton and carbon ion beams are produced by circular accelerators: cyclotrons or synchrotrons. Cyclotrons have a frequency modulated accelerating voltage that increases the radius of particle trajectories until they reach a maximum and the particles leave the accelerating structure. Synchrotrons, on the other hand, have a constant orbit radius imposed by bending magnets and the particles are released when they reach the final energy of the accelerator. Particle beams are delivered to the patient by a gantry equipped with magnets and a scanning nozzle that guides the beam to the patient. The particle energy is modulated through passive absorbers or active scanning [49]. A passive delivery system usually consists of range-modulator wheels, which spread the beam in depth, beam foils, which spread the beam laterally, collimators to create beam conformity and compensators for shaping the beam distally (Figure 1.6a). In scanning delivery systems the shape of the target is painted by a narrow (pencil) mono-energetic beam at fixed depth and the beam energy is gradually decreased in order to scan a tumour in 3D, as shown in Figure 1.6b.
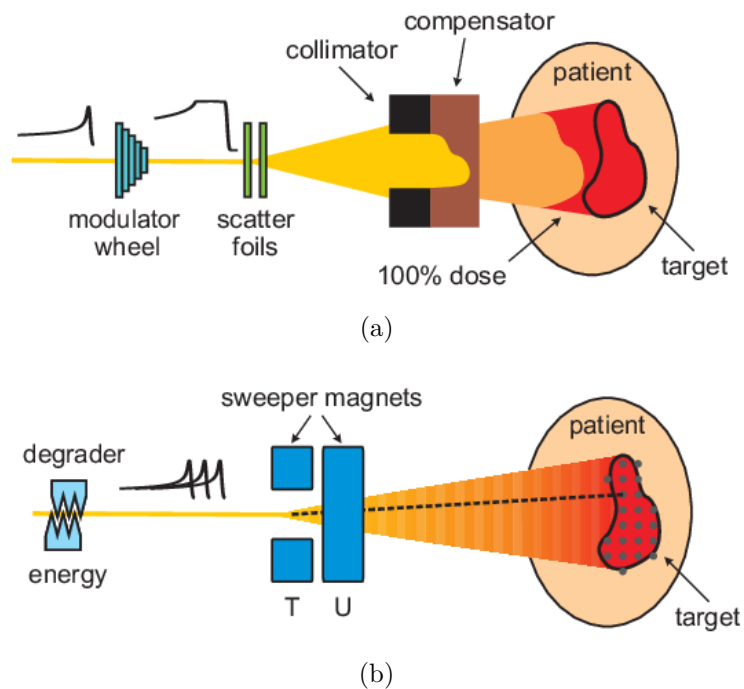

(a)

(b)

Figure 1.6: Proton therapy delivery, (a) passive and (b) active scanning [50].

The future accelerator technology for radiotherapy is focused on compacted multi-

modal machines that will produce all types of therapeutic beams in one treatment room. The laser-plasma accelerator, where an ultra-short ultra-intense laser plasma interactions establish huge electric field gradients that can accelerate almost all kinds of particle beams [51] is considered for future implementation of novel radiotherapy methods.

1.6 The need for more effective radiotherapy methods

Conventional radiotherapy methods, discussed in the previous sections, aim to deliver a uniformly distributed dose throughout the tumour volume. However, in some cases the central parts of a tumour are permanently isolated from blood vessels, which supply cancer cells with oxygen, and become radioresistant. This phenomenon, known as hypoxia, was studied by Gray and co-workers in 1953 [52]. Hypoxia results from uncontrolled tumour growth, which is more aggressive and susceptible to increased metastasis. Standard doses are often insufficient, and in many cases result in tumour recurrence. Therefore, a prognosis for hypoxic tumours that are treated with existing radiotherapy methods is poorer compared with most conventionally developed tumours.

Achieving a uniform cell kill throughout the volume of tumours with heterogeneous radiosensitivity is essential for enhancing tumour control of hypoxic cancers. Conventional radiotherapy becomes lengthy and complex when doses exceeding standard fractions are delivered to hypoxic parts of the tumour. Moreover, dose escalation in the tumour is limited by toxicity of surrounding healthy tissues. Therefore, improved efficiency is accomplished at the cost of irreversible damage to those tissue and impaired quality of life. FLASH radiotherapy [53] is a promising treatment modality, which relies on delivery of ultra-high dose rates, which are orders of magnitude higher than currently used in conventional radiotherapy. Figure 1.7 shows the post-irradiation toxicity in normal tissue (pulmonary lesions) expose to dose rates of 1.8 Gy/min and 3600 Gy/min. The extremely short duration of delivery of radiation leads to a reduction in normal tissue toxicity which increases with time but significantly slower than for prolonged irradiation.

Selective and time-effective escalation of dose in hypoxic tumours, so-called hypoxia dose painting strategies [54], are currently an active topic of research. Tissue-specific manifestation of normal tissue toxicity is an additional issue that must be addressed. Some organs, such as lungs have two types of normal tissue toxicity following irradiation: early inflammatory damage (radiation pneumonitis), occurring within hours to a few days after radiotherapy exposure, and later complications of chronic scarring (radiation fibrosis), occurring months to years after the treatment. The level of manifestation of the side effects depends on the delivered dose and irradiated volume [55].
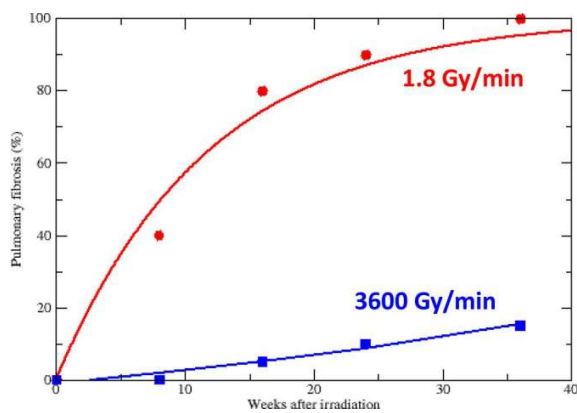
Figure 1.7: Development of pulmonary lesions in mice after thoracic irradiation at conventional (circles) or ultra-high dose rate (squares) [53, 56].

The aforementioned effects, in addition to the increased radio-resistance due to adaptive responses of cells, require specific approaches. The objective of this doctoral thesis is to investigate the possibility of using strongly focused electron beams as a cost effective and precise alternative to currently available hypoxia-dose painting strategies and to address tissue-specific manifestation of normal tissue toxicity by reducing dose delivered to healthy tissue. This focused beam modality is discussed in detail in the following sections.

1.7   Very high energy electron therapy

The concept of very high energy electron (VHEE) therapy was first proposed in 2000 by Colleen DesRosiers [57, 58]. This theoretical study and further work [59, 60], showed that VHEEs (50 – 250 MeV) have several advantages over clinical photon (6 – 22 MeV) beams:

- increased depth of penetration (>20 cm for 150 MeV),

- reduced scattering in air and tissue,

- absence of electric disequilibrium at interfaces with varying densities, improved uniformity of dose in the target surrounded by highly variable densities as in head-and-neck and lung cancers,

- shorter irradiation time since a smaller number of electrons is required to deliver the same dose, compared with photons.

After the introduction of this new concept, studies were conducted on treatment planning, dosimetry and treatment machine for VHEE therapy, as summarised in the next two sections.

1.7.1   Treatment planning

As the future VHEE accelerators most likely will incorporate laser-plasma technology, the treatment planning studies were carried out using typical experimental parameters of VHEE beams produced by laser-plasma accelerators. In 2008 the PENELOPE code which was used previously by DesRosiers *et al.* [57] to study VHEE interactions in tissue-equivalent materials was extended to simulate particle transport in computed tomography (CT) voxel geometry [61, 62]. A treatment planning study conducted with this new code for prostate and lung cancers showed that VHEEs provide more uniform coverage of the tumour volume than clinical photons [59]. Furthermore, the ratio of integral dose to the target, compared with the ratio of integral dose to healthy tissue and sensitive organs, was found to be higher for VHEE than for photon beams.

A preliminary treatment planning optimisation of VHEE therapy was performed using a two-dimensional model of a prostate cancer by varying variables, such as the beam energy, number of energy bins, number of beams and beam orientations [63]. The overall quality of plans based on 250 MeV electrons was between intensity-modulated X-ray therapy and intensity-modulated proton therapy [64]. Fuchs *et al.* [65] used an in-house developed treatment planning system for a clinical prostate case, to validate VHEEs against clinical photons. The very high energy electron therapy (VHEET) provided better target coverage and sparing of the surrounding volume than photons. The PENELOPE code was further used for the dosimetric evaluation of spatially fractionated GRID therapy with VHEEs [66]. The spatial fractionation of the dose in the healthy tissue was clearly observed, while a more homogeneous dose distribution in the tumour was achieved.

Treatment planning based on scanning of $100 - 120$ MeV VHEE pencil beams was performed for five clinical cases of head-and-neck, lung and prostate cancers [67, 68, 69]. A $10 - 42\%$ reduction of the mean dose to the brainstem, optic chiasm, and both orbits for head and neck cancer was obtained for VHEEs compared with VMAT (Figures 1.8a and 1.8b). In all cases VHEEs delivered higher normal (healthy) tissue dose sparing than corresponding VMAT plans. For small and shallow targets, the VHEE plans provided similar outcome to VMAT plans, in addition to more homogeneous dose distribution within the target volume.

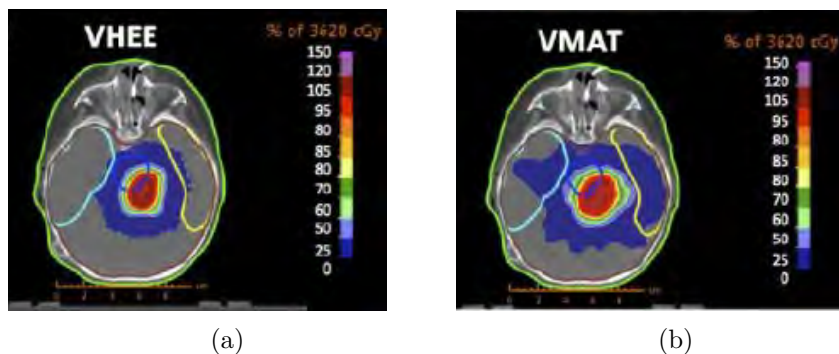(a)   (b)

Figure 1.8: Paediatric case dose distribution in the head cancer, (a) $100 - 120$ MeV VHEE plan and (b) 6 MV VMAT plan [67].

In 2017 Schüler *et al.* [70] performed treatment plans using intensity and energy

modulated VHEE pencil beams. They reported that the proposed treatment technique reduced the number of beams required to deliver sufficient target dose, and hence the integral dose. The overall quality of VHEE treatment plans was between VMAT and proton pencil beam scanning (PPBS) for four cancer cases.

1.7.2   Dosimetry

The first experimental measurements of dose deposition by VHEE beams were conducted in 2010 by Lundh *et al.* using a polystyrene phantom [71]. Following this, detailed dosimetry of VHEEs were performed by Subiel *et al.* [72] who studied calibration of radiochromic films in VHEE fields. The dose response to a 165 MeV conventional linac and a 135 MeV laser-plasma accelerator were found to be in excellent agreement with results from a clinical 20 MeV electron accelerator, indicating the possibility of easy and cost effective adaptation of existing methods and protocols to VHEEs. In another study performed by Bazalova *et al.* [73] with $50 - 70$ MeV electron beams, the measurements of the dose distribution using radiochromic films and predictions from Monte Carlo simulations were in agreement within 5%.

However, the dosimetry of VHEE beams was found challenging using ionisation chambers, the gold standard dosimeters in radiotherapy, due to a unique characteristic of femtosecond to picosecond duration VHEE bunches. The study of temporal and spectral evolution of ultrashort VHEE beams in a water phantom shows that ionisation chambers are not suitable for dosimetry of ultrashort pulsed VHEE beams due to strong recombination effect in the sensitive volume of the dosimeter [74]. The experimental investigation of dose deposition by VHEEs in inhomogeneous media was performed using air and bone equivalent cavities embedded in water with 197 MeV electron beam. VHEEs were found to be less susceptible to tissue inhomogeneities than photons, which potentially can lower the uncertainties associated with delivered dose [75].

1.7.3   VHEE accelerators

Studies focused on the design of a VHEE accelerator fall into three areas; acceleration mechanisms, transport and delivery systems. Steward *et al.* [76] studied beam scanning

system, a delivery method of VHEE beams first suggested in 2004 [77]. Collimated electron beams were found preferable over a divergent beams. A simple scanning system which incorporates a coil magnet, as shown in Figure 1.9, was discussed.
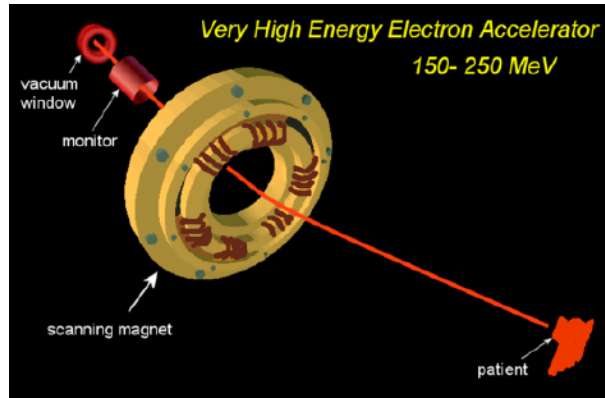

Figure 1.9: VHEE scanning system proposed by Steward *et al.* [76].

The University of Stanford started a new project on a novel ultra-fast radiation therapy technology, referred to as pluridirectional high-energy agile scanning electron radiotherapy (PHASER), which is capable of delivering high doses to the tumour using VHEE beams on sub-second timescales [78, 79]. The machine utilises multiple VHEE sources arranged around the patient in a compact gantry as shown in Figure 1.10 which allows instantaneous irradiation. It is estimated that the treatment time can be reduced to less than one second, effectively freezing physiological motions which are a major source of uncertainties during extended treatment times. In 2015 the prototype of a clinical laser-plasma accelerator robotic system for VHEET was proposed by Nakajima *et al.* [80].

1.7.4 Focused electron beams as a new radiotherapy technique

Electrons are attractive for radiotherapy due to their potentially cost-effective production and delivery, but they are highly susceptible to lateral scattering at low energies. Over the past 70 years there has been effort to reduce the off-axis dose resulting from scattering, which can cause long-term radiation side effects in healthy tissue. One idea is to use an external magnetic field to suppress the effect of strong scattering.
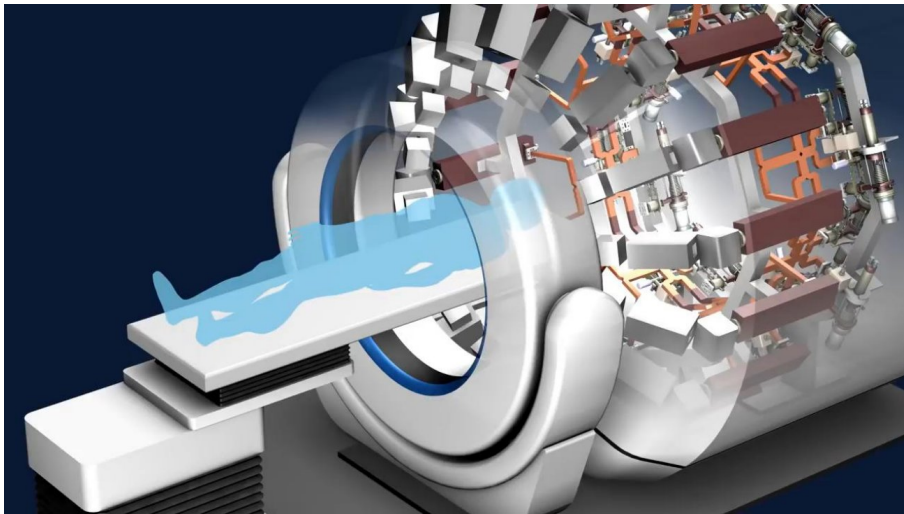
Figure 1.10: Prototype of PHASER [81].

Two general approaches using longitudinal and transverse magnetic fields were reported. Calculations of electron trajectories in the presence of a longitudinal magnetic field were performed by Bostick [82], who demonstrated the formation of an 'enhanced Bragg peak' using a simplified physical model based on electron-induced ionisation and scattering. Figure 1.11 shows the results of Monte Carlo modelling that implements Landau straggling, multiple scattering and a space dependent magnetic field [83]. The 'Bragg peak' like effect is clearly visible for 70 MeV electron beams contained by a 6 T magnetic field. Monte Carlo calculations including full electron and photon transport, as well as interaction of electrons with a magnetic field, were performed by Weinhous *et al.* [84], reproducing Bostick's results.

Experiments on dose distribution enhancement for both longitudinal and transverse magnetic fields were performed using homogeneous [85, 86, 87] and inhomogeneous phantoms [87]. For example, Whitemire *et al.* [88] observed that uniform transverse-magnetic fields applied to $10 - 45$ MeV electron beams modify the electron dose distribution in tissue and lung-equivalent phantoms. These results showed that the surface dose was reduced by 40% compared to conventional clinical beams for the same clinical case, whereas the integral dose was decreased by around 50% for tumour depths of $10 - 14$ cm. In the study of Litzenberg *et al.* [89] strong transverse and longitudinal confine-
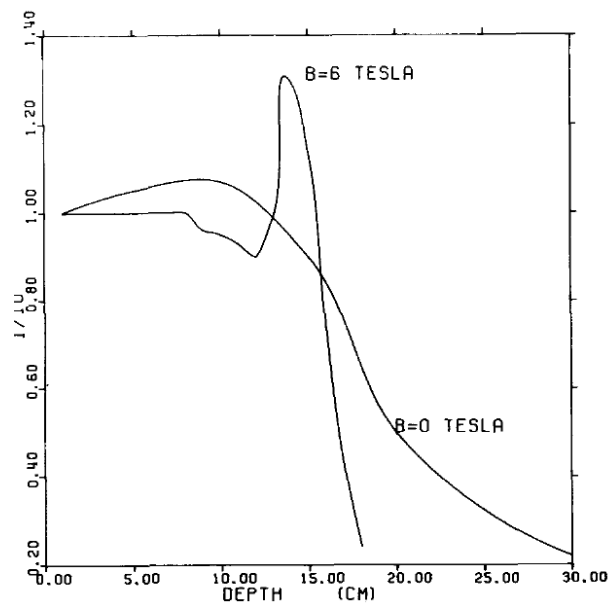
Figure 1.11: Simulations of central axis relative depth-dose distribution in the presence and absence of a 6 T magnetic field [83].

ment of the electron beam was obtained in the presence of a longitudinal non-uniform field. The beam profile acquired on photographic films showed dose enhancement in the presence of a strong magnetic field (Figure 1.12b), in contrast to a collimated beam (Figure 1.12a).

Monte Carlo simulations conducted by Bielajew [90] for a 20 MeV electron beam and a $3 - 20$ T uniform longitudinal magnetic fields inside the phantom proved that for broad beams the enhancement of the depth-dose profile maximum is not a Bragg peak, but is due to electron fluence enhancement at depth caused by the magnetic field. Further simulations for a 15 MeV electron beam and a 3 T transverse magnetic field showed surface dose reduction by a factor of 2 when compared with field-free irradiation [91]. Following these, a simple stereotactic treatment planning study with a skull-tissue phantom was performed by Chen *et al.* [92]. In this study six 35 MeV electron beams were focused by a longitudinal solenoid magnetic field of 6 T. The peak dose profile (Figure 1.13) shows that a high dose can be concentrated in a few cm^3 volume, as a result of superposition of the beams. Chen also noted that few studies have been conducted on the effect of strong magnetic fields on cell damage [93].
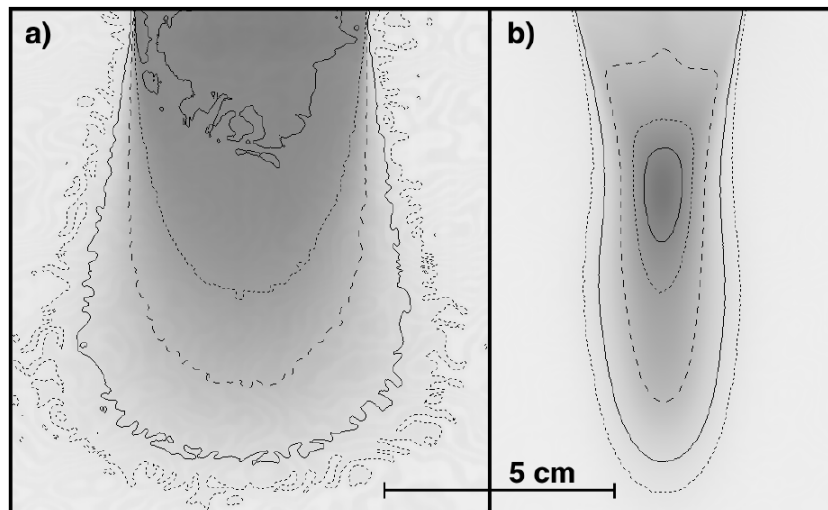
Figure 1.12: XV film (Kodak Ready Pack) after exposure to a 20 MeV electron beam when (a) no magnetic field is present, and (b) the beam passes through a 3 T solenoid (b) [89].

The first design of a treatment machine for focused electron beam therapy was proposed by Weinhous *et al.* [84] who performed simulations to optimise a superconducting magnet system that could be incorporated into a mobile treatment table for use with a standard radiation therapy accelerator. The magnet with a field strength of $1-4$ T was tested by simulating 20 and 30 MeV electron beams. The peak to entrance dose ratio was around four times higher than for beams without the magnetic field.

In addition to this extensive research on magnetic confinement of electrons in tissue, a few studies have been conducted on the use of magnetic fields outside the phantom. In 1960 Sempert [94] reported the development of magnetic focusing electron lenses to improve the dose distribution of 35 MeV electrons at depth of 10 to 20 cm. Earl *et al.* performed simulations showing up to 70% dose enhancement at depth of $5-30$ cm for 18 -50 MeV electron beams focused by a uniform longitudinal magnetic field [95]. Glinec *et al.* performed simulations demonstrating improved dose distribution using a weak focusing system (quadrupole triplet) designed for 170 MeV electron beams produced by a laser-plasma accelerator [96]. Studies of focused beams have also been conducted for photons [89, 90, 97, 98, 99, 100] and proton beams [101].
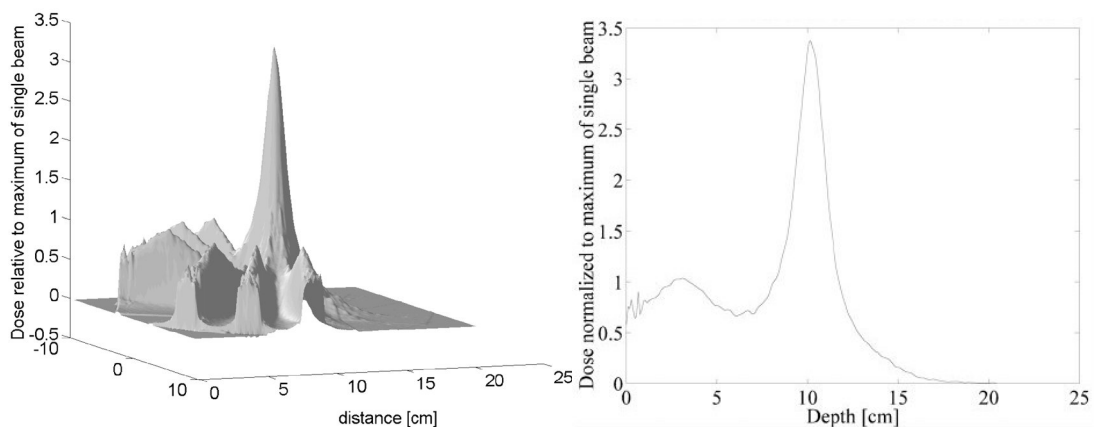
Figure 1.13: 3D dose distribution (left) and 2D central axis depth-dose distribution (right) of an electron beam with energy of 35 MeV focused by a 6 T solenoid magnetic field [92].

1.7.5 The concept of focused VHEEs

The main challenge for using VHEEs in radiotherapy of deep seated tumours is their nearly uniform depth-dose distribution. Consequently, high dose (around 70% of the target dose) is delivered to the skin, which has low radiation tolerance. Photons also deposit a high entrance dose, but can be delivered in multiple beams from varying angles, overlapping at the tumour site. The dose within the tumour is enhanced while in other parts of the body it is spread out over a large volume. This solution allows to create sufficient contrast between doses that are delivered to healthy and cancerous tissue.

In this thesis, a new treatment modality using a single VHEE beam and a magnetic lens, to create a high dose volume, referred here as a *volumetric element*, deep in tissue is proposed. This method could potentially achieve similar effect to multiple beams but would limit the amount of tissue exposed to radiation. A schematic diagram of traditional conformal radiotherapy administrated by photon beams is shown in Figures 1.14b, and a single VHEE beam focused into a patient's head shown in Figure 1.14a. For a converging VHEE beam the dose, which is proportional to the electron flux, is concentrated into a small volume at the beam waist. The exit and entrance doses are spread over a larger area, lowering the exposure and thus reducing

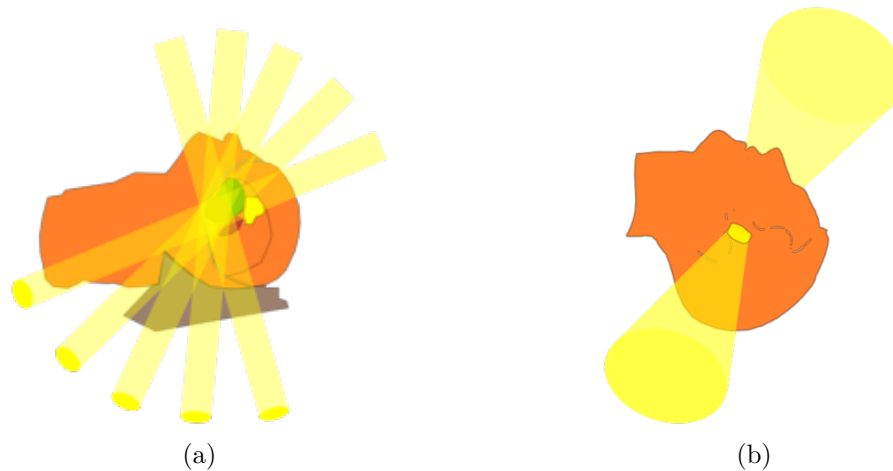the biological insult to the skin and surface areas.

<table>
(a)   (b)
</table>

Figure 1.14: Irradiation techniques, (a) multiple beams IMRT and (b) focused beam irradiation of a perfectly round target.

1.8   Thesis objective and outline

This doctoral project investigates the development of a new radiotherapy method for deep-seated and hypoxic tumours with strongly focused VHEEs. The aim of this study is to validate the hypothesis that strongly focused VHEE beams can significantly enhance the dose gradient between the surface and the tumour depth, and thus can reduce the exposure of healthy tissue to radiation. In order to validate the concept of focused VHEEs experimentally, a new dosimetry protocol was established.

The thesis is organised as follows. Chapter 2 provides a brief overview of accelerator technology as well as beam diagnostics. Chapter 3 includes the basis of the physical processes governing electron and photon interactions and introduces Monte Carlo simulations for dosimetry studies. Chapter 4 includes methods and details on the simulations performed with focused MeV and GeV electron beams using different beam geometries. Chapter 5 is dedicated to the experimental results of the dosimetry of VHEEs that was performed in collaboration with the national metrology institute in Germany and the National Physical Laboratory in the United Kingdom. Chapter 6 discusses the experimental results obtained during the dosimetry campaign at the CLEAR facility

at the European Organisation for Nuclear Research (CERN) in Switzerland. Chapter 7 presents the experimental results of a focused VHEE experiment performed at CLEAR. In Chapter 8 the outcomes of the research and future plans are discussed, together with suggestions of possible directions for the next research step.

Chapter 2

Very high energy electron accelerators

This chapter provides a brief summary of the working principles of radio-frequency (RF) accelerators and laser-plasma electron accelerators. The experimental part of this doctoral project was performed in collaboration with three research institutes, the Physikalisch-Technische Bundesanstalt (PTB) in Braunschweig, European Organisation for Nuclear Research (CERN) in Geneva and National Physical Laboratory (NPL) in London. The first stage of this project, the calibration of Gafchromic films® for electron beam energies up to 50 MeV, was performed at the PTB research linear accelerator [102], which is briefly described in subsection 2.1.1. The calibration of Gafchromic® films and alanine dosimeters, and the focused VHEE experiment, were carried out using very high energy range electron beams (50 – 200 MeV) produced at the CERN Linear Electron Accelerator for Research (CLEAR) facility which accommodates the updated CLIC Test Facility (CTF3) beamline and probe beam injector CALIFES designed to demonstrate key concepts of the Compact Linear Collider [103]. This accelerator is described in subsection 2.1.2. The calibration using extremely high doses was performed with low energy electron beams produced by the Elekta Synergy® clinical accelerator at NPL [104], which is described in subsection 2.1.3. Section 2.4 briefly reviews the beamline optics and diagnostics that are commonly used in particle accelerator

facilities.

2.1   RF accelerators

Electron accelerators producing energies greater than 20 MeV usually use high-power radio-frequency (RF) structures to generate electromagnetic fields suitable for particle acceleration [105]. Higher accelerating gradients can be achieved by increasing the RF frequency. However, RF breakdown in cavities sets a limit to the maximum electromagnetic field strength achievable for stable operation [106]. Therefore, accelerator design is often a trade-off between accelerating gradient and machine size. Currently available accelerator technologies operate in 5 different band modes, which are listed in Table 2.1.

Table 2.1: Radar bands for RF accelerators.

Frequency Range	Microwave bands
216 – 450 MHz	P–Band
1 – 2 GHz	L–Band
2 – 4 GHz	S–Band
4 – 8 GHz	C–Band
8 – 12 GHz	X–Band

Most medical accelerators use frequencies in the S-band range. X-band linacs operate at frequencies that are three times higher and employ accelerator cells with cross-sectional area approximately 10 times smaller, which permits a reduction of any shielding mass along the linac by at least the same factor. The higher gradient of X-band linacs also results in shorter accelerating cavities and thus a more compact machine. Figure 2.1 shows an X-band RF cavity designed for the Compact Linear Collider (CLIC) at CERN, which has a target accelerating gradient of 100 MV/m. This technology is the result of years of intense research and development at the Stanford Linear Accelerator Center (SLAC) in the USA, the High Energy Accelerator Research Organisation (KEK) in Japan, and at CERN. X-band accelerator technology is used in industrial and clinical applications. Examples of clinical machines that employ X-band technology are Mobetron, intraoperative radiotherapy mobile accelerator, GammaKnife® and
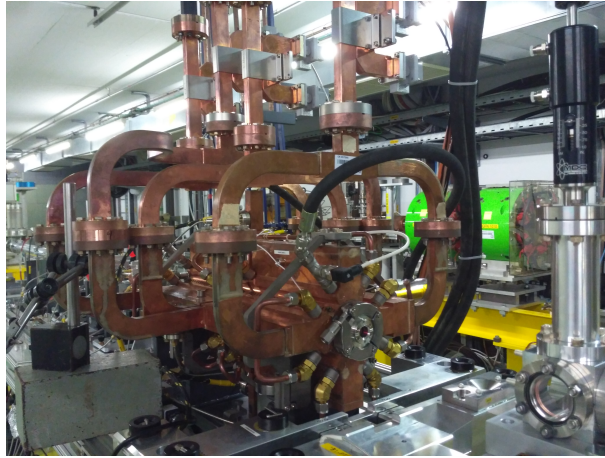
CyberKnife® [107].

Figure 2.1: An X-band structure at the CLEAR facility at CERN.

2.1.1 Research Electron Accelerator beamline at PTB

The research accelerator at PTB produces an electron beam with an energy up to a maximum of 50 MeV. The accelerator has been custom-built by ACCEL/RI Research Instruments GmbH Bergisch-Glodbach, installed and commissioned at the Metrological Electron Accelerator Facility (MEAF) in 2008 [108, 102]. Figure 2.2 shows a schematic drawing of the PTB research beamline including beam diagnostic units for measuring the properties of the electron beam, such as spatial profile, energy spectrum and current. Beam diagnostics are described in detail in section 2.4.

Table 2.2: Parameters of the electron beam in the PTB research accelerator.

Parameter	
Energy range	$0.5 - 50$ MeV
Energy spread (FWHM)	< 0.1 MeV
Repetition rate	$1 - 100$ Hz
Macropulse bunch length	$2.5 - 3$ μs
Macropulse bunch charge	< 100 nC
Pulse current*	< 200 mA
Electron beam power	1 kW
Maximum dose rates	4 Gy/min
Number of micro-bunches in train	7500
Micro-bunch spacing	3 GHz

average current during the beam macropulse

The accelerator consists of two sections, the low energy measurement area, which enables irradiation with electron energies in the range of $0.5 - 10$ MeV (F) and the high energy measurement area, which covers an electron energy range from 6 MeV to 50 MeV (D – H). Selected electron beam parameters at the end of the high-energy section are listed in Table 2.2. The accelerator produces macropulses with a maximum pulse duration of 2.5 μs. The micro-pulse duration and energy spread of the beam can be optimised using an electromagnetic chicane placed between the two accelerator sections. The inter-pulse charge fluctuation is typically about 3%.

2.1.2   CALIFES accelerator at the CLEAR facility

The linear research accelerator at the CLEAR facility is hosted by the CLEX experimental area at CERN and consists of the 25 m long CALIFES injector followed by a 16 m long beamline. The layout of the accelerator is depicted in Figure 2.3.

The RF-gun produces microsecond duration macropulses trains of bunches that are sent to three 4.5 m-long accelerating structures powered by two 3 GHz klystrons delivering 45 MW pulses with duration of 5.5 μs at a maximum repetition rate of 5 Hz (with possible extension to 25 Hz). The first accelerating structure can be used to tune the micropulse bunch length from 300 μm to 1.2 mm rms. through velocity bunching.

A sample of the output voltage for both klystrons supplying the CALIFES line
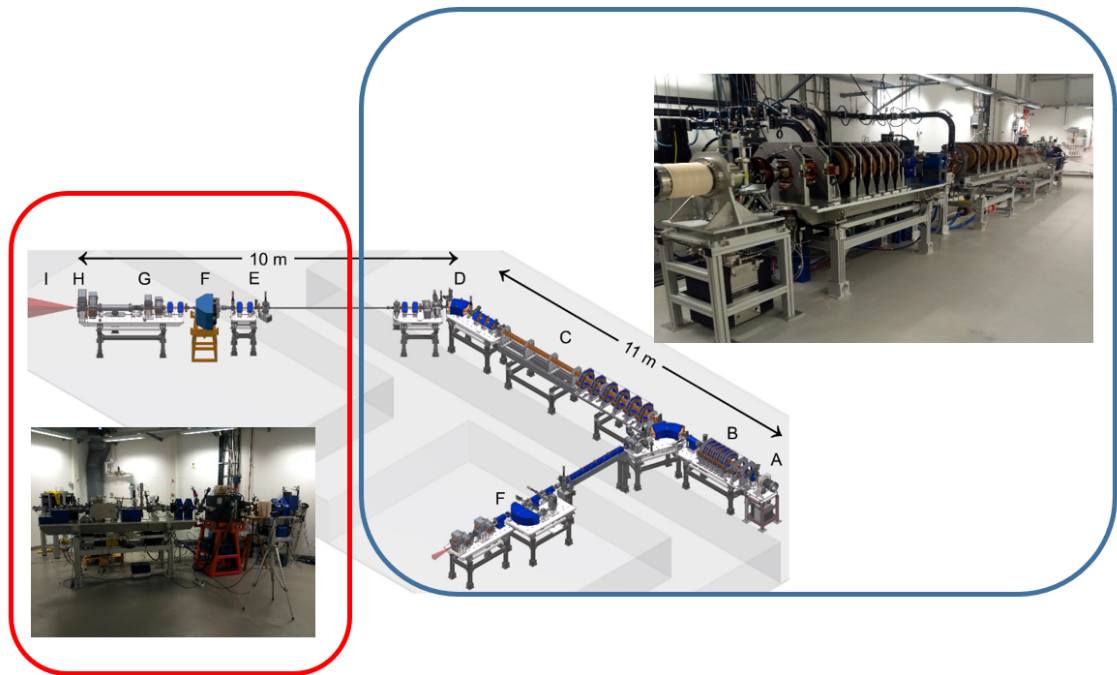
Figure 2.2: Schematic of the PTB custom-designed electron linac, A: electron gun. B: low-energy section (0.5 MeV to 10 MeV), C: high-energy section (6 MeV to 50 MeV), D: dipole magnet for energy separation and beam dump, E: collimator. F: magnetic spectrometer, G: beam intensity monitor (current transformer), H: Faraday cup or metal target for bremsstrahlung generation, I: photon/electron beam. Grey areas: walls of the radiation protection bunker. Length of acceleration path A – D is about 11 m. Length of high-energy beamline D – H is about 10 m [109].

during warm-up time is shown in Figure 2.4. The blue curve shows a klystron in full power operation. The gun, buncher and first accelerating structure are immersed in a tunable solenoid field for focusing and space charge compensation. Three electromagnetic quadrupoles and an electron spectrometer are placed after the injector, forming the irradiation test bench VESPER [111], which is used to perform studies on VHEE beams for medical application and single event upset effects on electronics designed to be used in space missions. The parameters of the beam at the end of the CALIFES injector are listed in Table 2.3.
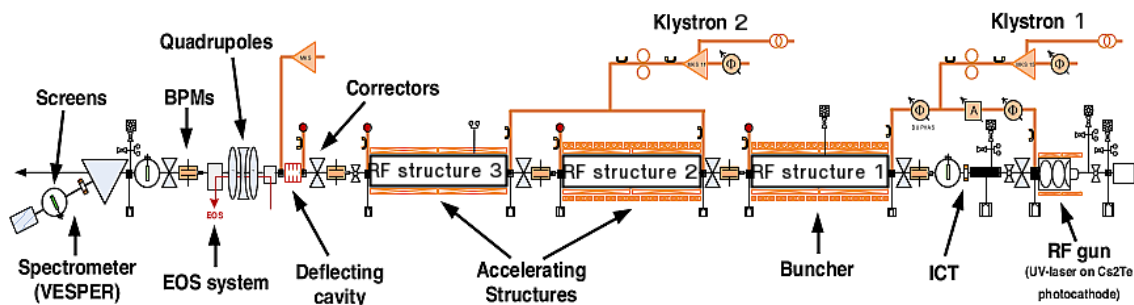
Figure 2.3: The layout of the CALIFES injector, beamline and test bench VESPER (the beam travels from right to left) [110].

Table 2.3: Electron beam parameters at the end of the CLEAR linac.

Parameter	
Energy range	$60 - 220$ MeV
Energy spread (FWHM)	< 1 MeV
Repetition rate	$0.8 - 5$ Hz
Micropulse bunch length	$0.2 - 10$ ps
Micropulse bunch charge	$1 - 400$ pC
Normalised emittance	$3 - 30$ μm
Number of micro-bunches in train	$1 - 150$
Micro-bunch spacing	1.5 GHz

2.1.3   Clinical accelerator at NPL

NPL hosts a commercial clinical accelerator. A typical medical linac consists of the injection system, RF power sources (magnetrons or klystrons), travelling wave accelerating structures, beam transport and collimation, and monitoring systems. A thermonic cathode electron gun provides a continuous source of electrons with a duration equal to the duration of the applied voltage signal. The linac arm contains a microwave RF cavity with typical frequency of 2856 MHz (S-band). The length of the travelling wave accelerating structure depends on the final electron energy required, and varies from $\sim$30 cm for 4 MeV to $\sim$150 cm for 25 MeV. Typical clinical linacs are dual-modal. The electron beam can be converted to X-rays in a tungsten target placed in the accelerator head at the end of a gantry structure. The accelerator gantry arm performs isocentric rotation around a treatment coach and is equipped with a primary field collimator (jaws), which shapes the rectangular treatment field, and multileaf collimator (MLC),
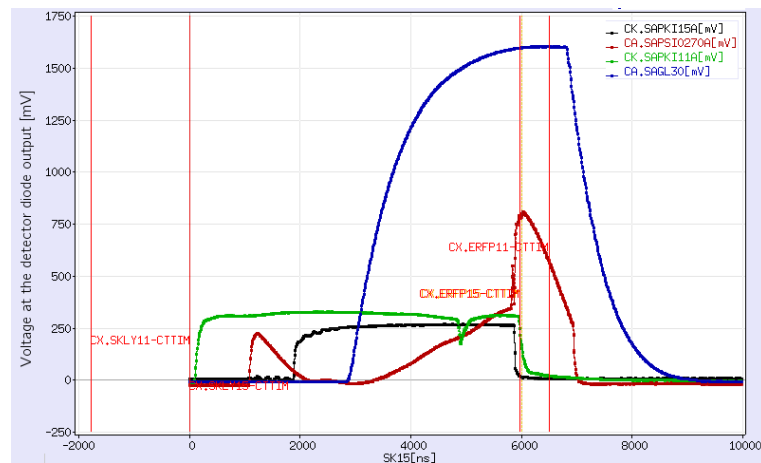
28

Figure 2.4: A sample trace showing the output voltage versus time measured at the output of the CALIFES klystrons at the input of the resonant cavities during warm-up. CK.SAPKI15A is the voltage delivered by the klystron 1 at the first RF structure input, CK.SAPKI11A is the voltage delivered by the klystron 2 at the second RF structure input, CA.SAPSI0270A is the voltage delivered by the klystron 2 at the third RF structure input, and CA.SAGL30 is the voltage of the gun-loop antenna which represents the accelerating field in the gun.

which creates complex field shapes corresponding to the target contours.

Clinical accelerators are significantly smaller than the previously discussed research accelerators, due to their lower energy. The Elekta Synergy® linac at the National Physical Laboratory, where the dosimetry measurements were performed, was commissioned in November 2008. It is the first linear accelerator with integrated kilovoltage X-ray volume imaging (cone beam) CT for high resolution 3D imaging. The MLCi2 multi-leaf collimator (80 leaves) uses a tracking system to reduce transmission between the leaves. The linac is capable of generating 7 photon and 10 electron beams with nominal energies 4 – 25 MeV and 4 – 22 MeV, respectively. The layout of the accelerator is shown in Figure 2.5.
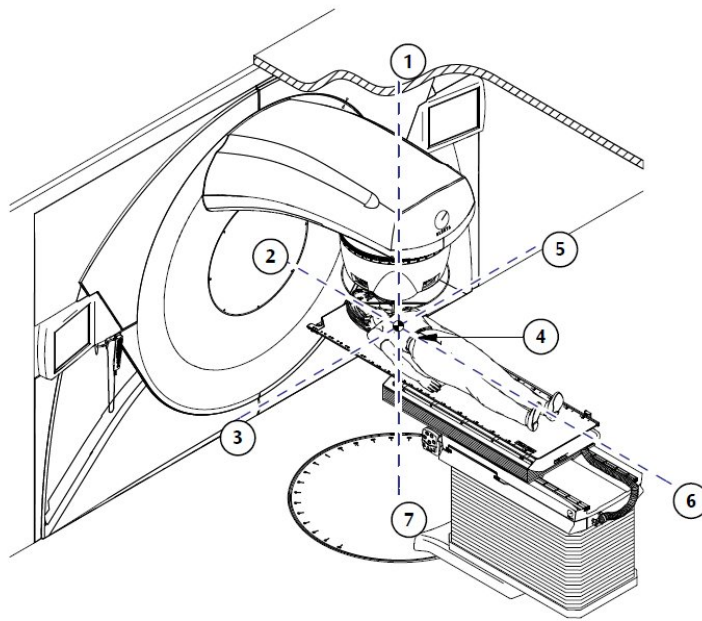
Figure 2.5: Layout of the Elekta Synergy® Platform, adapted from [104], (1) treatment room ceiling, (2) digital accelerator gun, (3) digital accelerator, (4) machine isocenter, (5) digital accelerator B-side, (6) digital accelerator target, (7) treatment room floor.

2.2   Laser-plasma accelerators

In 1979, Tajima and Dawson proposed a new type of particle accelerator based on laser-driven plasma waves that was capable of producing accelerating gradients two to three orders of magnitude higher than in conventional RF cavities [112]. In laser-plasma accelerators (LPAs) an intense laser pulse is focused onto a gas or plasma target. For a plasma density below the critical density, n_c [cm^{-3}] $= 1.1 \times 10^{21}/\lambda_0^2$ [μm] for a laser wavelength λ_0, the light pressure of the laser (ponderomotive force) creates charge density oscillations (plasma wake) analogous to waves in the wake of a ship. In the strongly nonlinear regime the wake structure becomes evacuated, forming an ion-filled cavity (bubble) trailing behind the laser pulse, as shown in Figure 2.6. Background plasma electrons can be trapped in the bubble and accelerated to extremely high energies, ranging from 10s MeV to several GeV, over several millimetres to centimetres. This regime is accessed when the laser normalised vector potential

$a_0 = 8.5 \times 10^{-10} \lambda_0 [\mu m] \sqrt{I_0 [\text{W/cm}^2]} > 1$, with I_0 the laser intensity.

The experimental realisation of LPAs was simultaneously reported in 2004 by three research groups in the Nature edition *Dream Beams* [113, 114, 115], which included an Imperial Collage team led by the ALPHA-X team at the University of Strathclyde. Quasi-monoenergetic electron beams with energies between 80 and 170 MeV were generated in mm-scale length using high-power lasers. Two years later, a 1 GeV electron beam was produced by channelling a 40 TW peak-power laser pulse in a 3.3-cm-long gas-filled capillary discharge waveguide [116]. Subsequently, 4.2 GeV electron beams were produced using a 300 TW laser and a 9 cm long plasma waveguide [117], and electrons with an energy up to 7.8 GeV were produced by guiding a 0.85 PW laser in a 20 cm long plasma [118]. Beam-driven plasma acceleration was also demonstrated at SLAC by doubling the energy of a 42 GeV electron beam after propagation through an 85 cm long plasma [119]. The accelerating gradient was 52 GV/m, approximately 3,000 times the gradient of the SLAC linac.
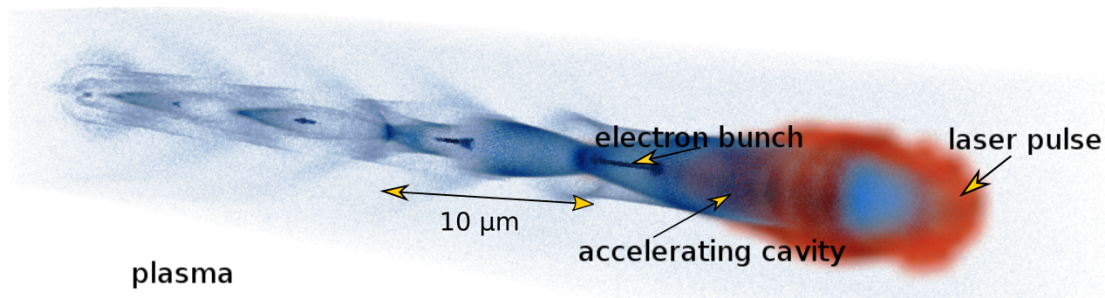

Figure 2.6: Simulation of laser wakefield acceleration using the 3D particle-in-cell OSIRIS code [120]. Plasma density distribution modeled with an 800 nm, 20 fs laser pulse with normalised vector potential $a_0 = 3$ waist $w_0 = 10$ μm, interacting with plasma with density of 1.7×10^{19} cm^{-3}. Electron bunches are trapped in plasma cavities (bubbles) created behind the laser pulse. Figure provided by Dr. Enrico Brunetti.

The compact size, accelerating gradient and extremely short bunch length are the main advantageous features of LPAs over the conventional accelerators. Typical electron beam parameters for conventional and LP accelerators are listed in Table 2.4.

Table 2.4: Electron beam parameters of the LWFA and conventional high-energy linear and circular accelerators.

Parameter	LWFA accelerator	Conventional linear and circular accelerators
Electron energy	84 GeV	13 TeV
Accelerating gradient	10-100 GV/m	10-50 MV/m (limited by RF breakdowns)
Bunch length	0.3 μm ($\sim$1 fs)	2-50 μm (6.7-167 fs)
Bunch charge	5-10 pC	20-250 pC
Peak current	1 kA	1kA
Repetition rate	10 Hz	5-1000 Hz (linear accelerators)
		10-500 MHz (circular accelerators)

2.3   Scottish Centre for the Application of Plasma-based Accelerators (SCAPA)

The Scottish Centre for the Application of Plasma-based Accelerators (SCAPA) was funded by the University of Strathclyde and the Scottish Universities Physics Alliance (SUPA). The laboratory is located at the University of Strathclyde and comprises three shielded experimental bunkers, as shown schematically in Figure 2.7, which contains 7 beamlines driven by a 40 TW (three lines) and 350 TW (four lines) titanium sapphire laser system, with parameters listed in Table 2.5. The 350 TW laser, designed and manufactured by the Thales Group [121], fits in a 120 m^2 clean-room. After commissioning in 2017 the laser was announced as the world's highest average-power laser of its kind. LPAs are multi-modal machines, which opens the door to multidisciplinary experiments and a wide range of applications, all in one laboratory. The following types of radiation will be produced in the SCAPA laboratory:

- monoenergetic electron beams of energy 100 MeV – 4 GeV,

- proton and light ion beams of energy up to 100 MeV,

- neutron beams,

- coherent radiation in the UV to hard X-ray,

- transversely coherent betatron (plasma wiggler) radiation in the X-ray to gamma-ray (1 keV to MeV) range, and

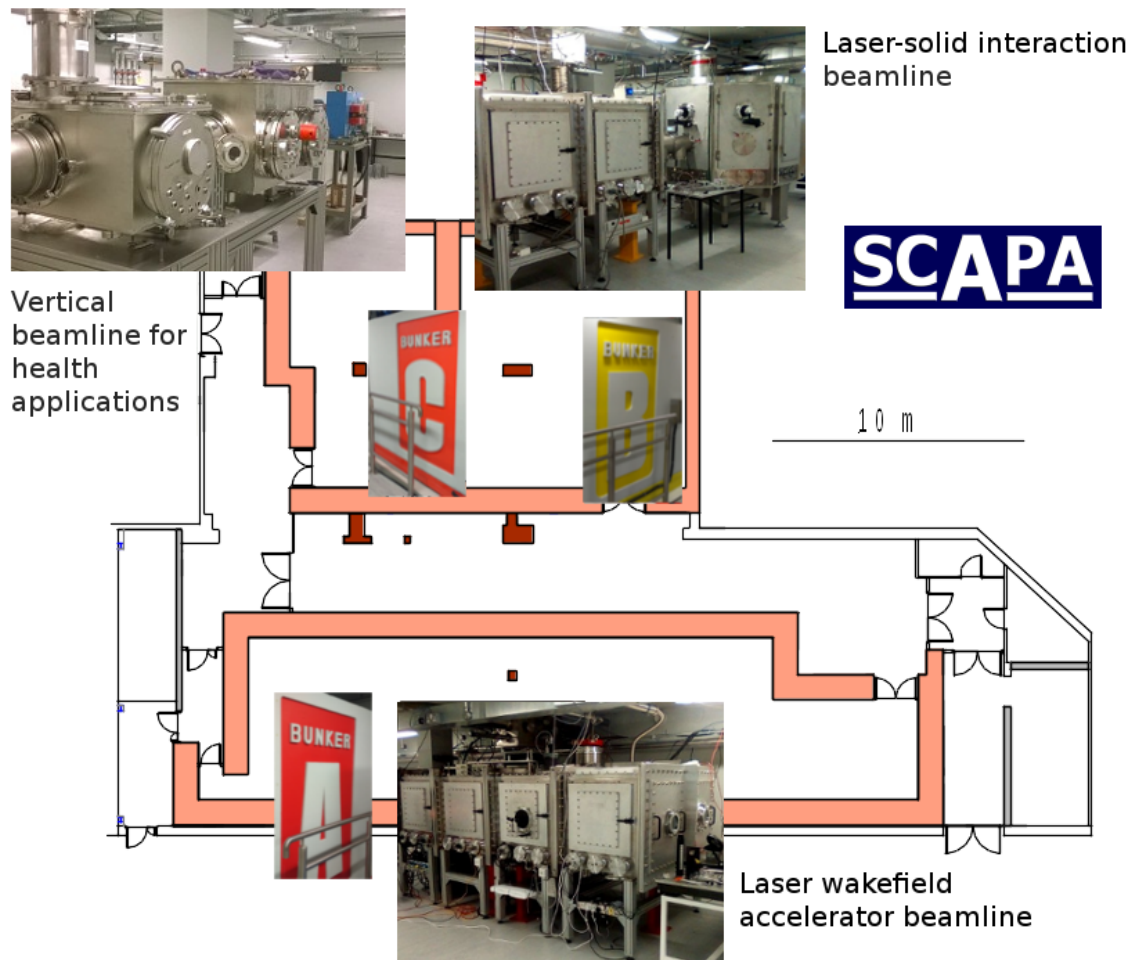- high brightness THz and infra-red radiation.

Figure 2.7: Space management plan of SCAPA.

These radiation sources can be exploited for radiobiology experiments, phase-contrast X-ray imaging, spatio-temporal probing of ultrafast processes, as well as radioisotope production. Medical applications received particular attention from the founders of SCAPA. A beamline at SCAPA will provide a vertical electron beam, as opposed to the LPA community standard of a horizontal accelerator. This layout is dedicated to pioneering radiotherapy cell studies using VHEEs in a traditional patient style layout.

Key components of a LPA discussed are based on the ALPHA-X (Advanced Laser-Plasma High-energy Accelerators towards X-rays) beamline, which is driven by a 40 TW,

Table 2.5: Parameters of the laser systems in SCAPA laboratory.

Parameter	350 TW laser	40 TW laser
Wavelength [nm]	800	800
Energy [J]	8.75	1.4
FWHM duration [fs]	25	35
Peak power [TW]	350	40
Repetition rate [Hz]	5	10

35 fs laser, with a central wavelength of 800 nm, repetition rate of up to 10 Hz and on-target energy > 0.9 J. The laser beam from the compressor is focused by a spherical mirror into a supersonic helium gas jet, forming a plasma channel approximately 2 mm long to accelerating electrons to relativistic energies. Removable Lanex screens can be used to measure the transverse profile of the electron beam. Three custom-designed miniature permanent magnet quadrupoles [122] can be inserted a few centimetres after the plasma to partly re-collimate the electron beam.
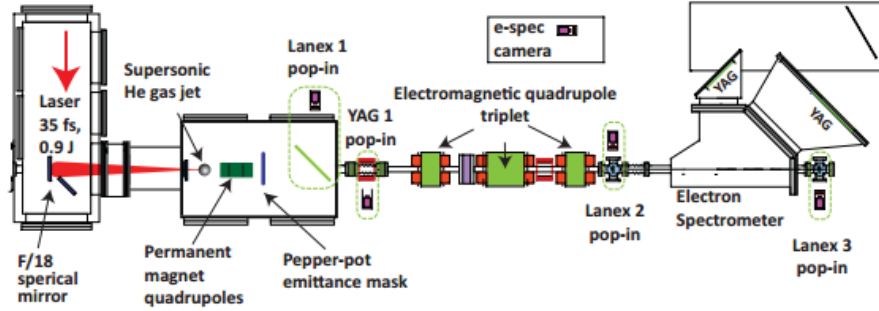
Figure 2.8: ALPHA-X beamline.

Three electromagnetic quadrupoles can be used to collimate or focus the beam. The energy spectrum is measured by a magnetic dipole spectrometer. The detailed layout of the accelerator is shown in Figure 2.8. The electron beams produced by the ALPHA-X beamline can reach energies of 300 MeV with energy spread of $1 - 10\%$, emittance of 1π mm mrad, divergence of $1 - 3$ mrad, bunch length of $1 - 5$ fs and charge of $1 - 10$ pC [123]. An example of an electron beam spectrum obtained on the ALPHA-X beamline is presented in Figure 2.9.
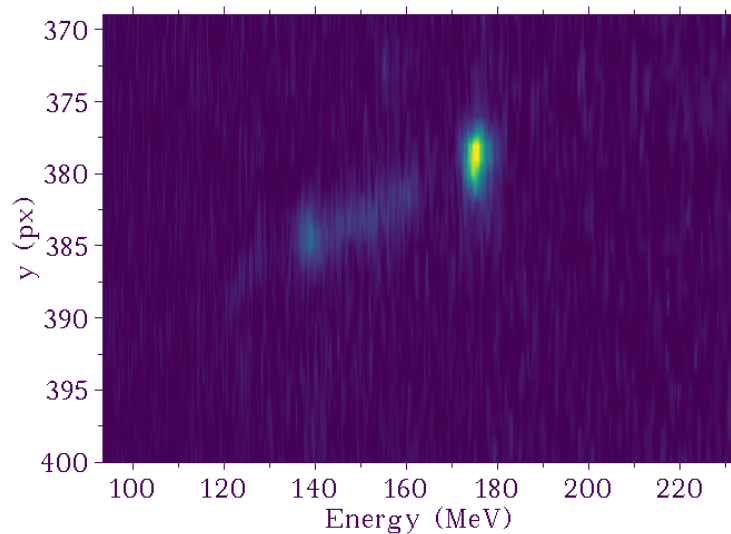
Figure 2.9: Electron energy spectrum for a single shot measured at the ALPHA-X lab at the University of Strathclyde. The intensity scale is expressed in arbitrary units.

2.4 Electron beam diagnostics

Electron beam diagnostic systems are used to ensure high beam quality, delivery of desired beam characteristics and reproducibility of the beam parameters. Accurate measurements can be used to predict experimental outcomes, for instance, beam charge and energy which are essential in order to estimate the absorbed dose.

2.4.1 Energy measurement

The most direct and well-established method of measuring electron beam energy is magnetic spectrometry [124]. In the research accelerators at PTB magnetic spectrometers are installed in both sections of the accelerator, whereas at the CLEAR facility the energy spectrum is measured at the end of the CALIFES injector. The general design of a magnetic spectrometer is discussed based on the spectrometers used at PTB. Figure 2.10 shows the device layout, which consists of two water-cooled electromagnets (dipoles) separated by a vacuum gap where electrons move on a semicircular trajectory with reference radius of 170 mm. This trajectory mainly depends on the magnetic field and kinetic energy of the electrons, but also on the entrance position and angle.

Assuming a constant magnetic field and neglecting fringe fields, the electron kinetic energy can be calculated using the equation:

$$E_{kin} = \sqrt{B^2 \cdot r^2 \cdot c^2 \cdot e^2 + (m_0 \cdot c^2)^2} - m_0 \cdot c^2, \qquad (2.1)$$

where B is the magnetic flux density, r is the radius of the electron trajectory, c is the speed of light, m_0 is the electron rest mass and e is the electron charge. A more accurate reconstruction of the electron trajectory inside the spectrometer can be obtained with knowledge of the magnetic field map. At the exit of the spectrometer a movable wire scans the electron beam cross-section horizontally. Two beam position monitor (BMP) units are mounted on the front and back side of the spectrometer, as shown in Figure 2.10a (BPM in and out), to measure the electron charge. This is used to normalise the signal from the wire in order to avoid temporal instabilities and spurious signals resulting from beam drift during the acquisition of the wire signal.
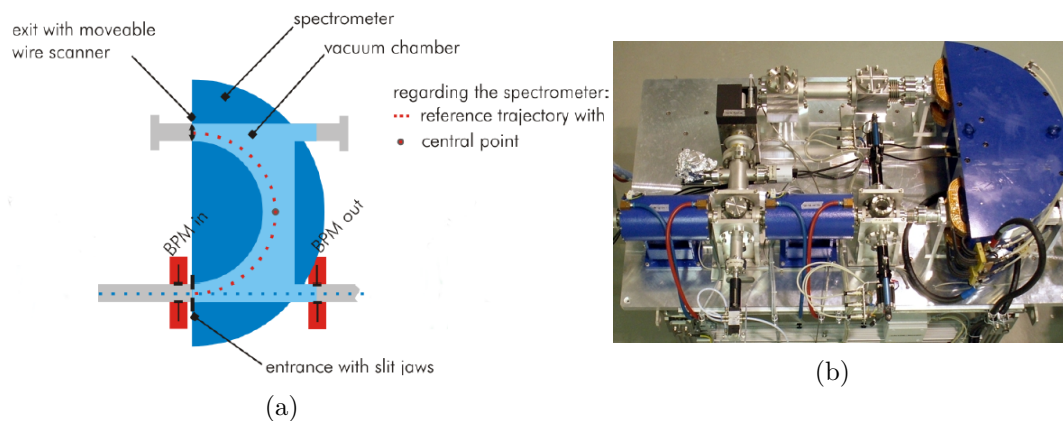

Figure 2.10: Magnetic spectrometer, (a) schematic of the spectrometer at PTB, (b) photography of the spectrometer at CLEAR [125, 126].

2.4.2 Charge measurement

The electron beam charge is directly associated with the absorbed dose. At both the PTB and CLEAR accelerators the beam charge is measured with an integrating current transformer (ICT) [127, 128] (in-flange version: ICT-CF4.5/34.9-070-50:1-UHV, SN 1650, and in-air version: ICT-055-070-5.0-UHV, SN 3550) manufactured by Bergoz

Instrumentation [129]. In the experiment at PTB the ICT has been cross-calibrated against a Faraday cup ("H" in Figure 2.2), which is an alternative but destructive method of measuring electron charge.

Figure 2.11: Faraday cup [130].

The cup opening (Figure 2.11) is set to allow electrons to enter and induce a current in the metal housing, which is collected in an electrometer circuit and translated into electron charge. The advantage of using a Faraday cup is its robustness (sensitivity is constant in time and mass independent, with collection efficiency > 99%) and the possibility of absolute charge measurement.

The ICT, on the other hand, is non-destructive, the beam travels through a coil with embedded *Q-loop* wire and stays intact. Real-time charge measurements can be performed with picocoulomb resolution. The basic principle of operation is the combination of two transformers; a current transformer for loading the full bunch charge instantly into capacitors and a readout transformer for transferring charge to the output. Two cores are annealed to lower their coercive field and further minimise core loss. The output voltage is proportional to the beam pulse charge. The in-flange version depicted in Figure 2.12a can be mounted between two flanges as a vacuum component in the beamline and has been used at on PTB research accelerator ("G" in Figure 2.2) and next to the electron gun at the CLEAR accelerator, whereas the in-air version (Figure 2.12b) was mounted after the spectrometer at the end of the VESPER test bench. An example of charge measurements per shot at CLEAR is shown in Figure 2.13.
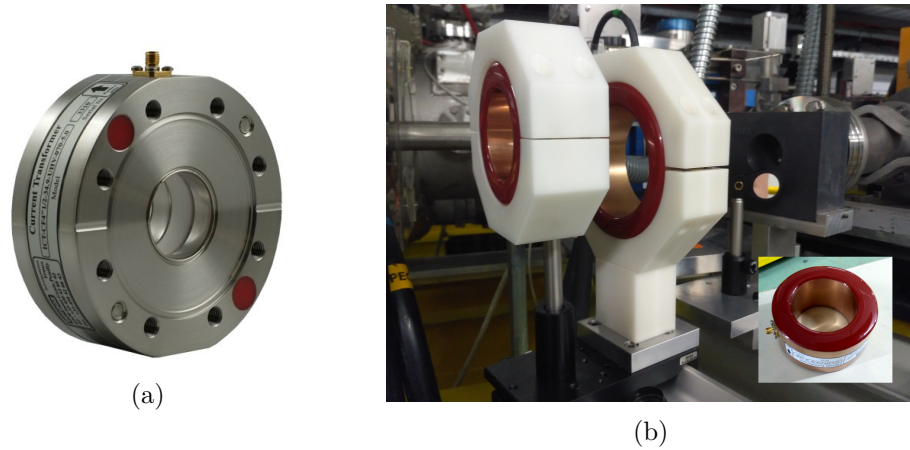
(a)

(b)

Figure 2.12: Integrating current transformer, (a) in-flange (adapted from [129]) and (b) in-air.

Figure 2.13: Charge and RF power measurement performed at the CALIFES electron gun and VESPER test bench.

2.4.3   Beam profile measurement

The charge density distribution of electron beams can be measured using fluorescent screens. A commonly used screen material for high energy electron beams is cerium activated yttrium aluminium garnet (YAG, $Y_3Al_2O_{12}$). Optical transition radiation screens (OTR) are also frequently used. They are typically made of a silicon substrate with a thin metal coating, e.g. aluminium (to enhance the transition radiation).

Figure 2.14: Monochrome CCD camera with filter wheel.

A lens system guides the light from the screen to a CCD camera (Figure 2.14). The number of photons generated after a single electron strikes the YAG screen is 35×10^3 ph/e$^-$/MeV [131], which is emitted isotropically. The number of photons generated when a single electron crosses a metal foil in OTR systems is $N_{ph} = \dfrac{\alpha}{\pi}(2 \ln \gamma - 1) \ln \dfrac{\nu_2}{\nu_1}$, where α is the fine structure constant, γ is the beam relativistic factor, and ν_1 and ν_2 is the photon frequency region [131]. In this case, emission is concentrated in a narrow cone of size approximately $1/\gamma$. Therefore, for high charge beams OTR screens are preferable over YAG screens, where the performance deteriorates due saturation effects.
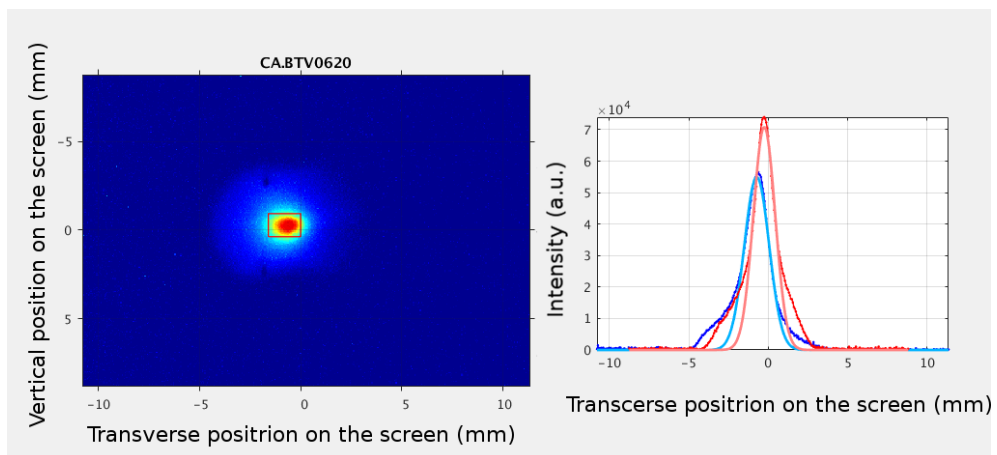
Figure 2.15: Image and histograms of the transverse beam profile on a YAG screen obtained at the CLEAR facility.

2.4.4 Emittance measurement

Emittance is a measure of the volume (or area) occupied by a particle beam in phase space, as discussed in the next section. Knowledge of the emittance is important in designing beam transport systems and for minimising beam losses along the line. In the CLEAR experiments, emittance measurements were performed to determine the initial beam parameters required for the tuning of the focusing system described in the next section.
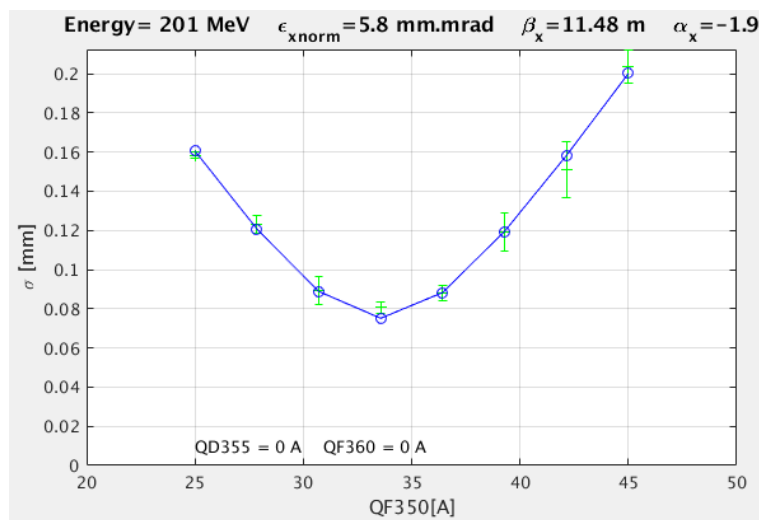

Figure 2.16: Beam size σ (rms) as a function of the current applied to an electromagnetic quadrupole magnet. This measurement was performed at the CLEAR facility.

There are several methods of performing emittance measurements: slit, pepper pot [132], methods based on Schottky signal analysis [133, 134] and direct methods based on measurements of the beam divergence and transverse profiles [135]. During the experiment at the CLEAR facility the emittance was measured using the quadrupole scan technique. In this method the beam size is measured on OTR or YAG screens as a function of the magnetic field strength of a quadrupole magnet. The emittance value is reconstructed by modelling the electron beam propagation through the magnetic field. A sample emittance measurement after the CALIFES injector is shown in Figure 2.16.

2.5 Beam optics

Beam optics in high energy accelerators consist of dipole, quadrupole and sextupole magnets. The former are used to deflect electrons, for example to steer the beam or perform energy measurements, as described in subsection 2.4.1. Dipole magnets are also used for fine orbit corrections and in chicanes for bunch compression, energy spread reduction or other functions. Quadrupole and sextupole magnets are used to focus and transport particle beams over a long distance. In quadrupoles the magnetic field increases linearly from the centre of the magnet (where $B = 0$) radially outward, while in sextupoles it exhibits quadratic growth. Quadrupole magnets were used for the purpose of this doctoral project to focus electron beam at the end of the CALIFES beamline. Therefore, operating principles of a single quadrupole magnet and a lattice of quadrupole magnets are discussed in detail in the following sections.

2.5.1 Twiss parameters

The beam emittance can be described in a modified phase-space with axes of position and angle (x, x') (trace-space), where $x' = p_x/p_z$ for a beam propagating along the z axis with longitudinal momentum $p_z \gg p_{x,y}$, with $p_{x,y}$ the transverse momenta. If the transverse motion along the x and y coordinates is uncoupled, particles are distributed within an ellipse described by the equation [136]:

$$\gamma_x x^2 + 2\alpha_x x x' + \beta_x x'^2 = \epsilon_x, \tag{2.2}$$

where α_x, β_x and $\gamma_x = (1 + \alpha_x^2)/\beta_x$ are the Twiss parameters, also called betatron or Courant-Snyder functions [137]. The emittance is $\epsilon_x = A/\pi$, with A the area of the ellipse contoured at the standard deviation σ of the particle position. The electron beam parameters can be derived from the Twiss parameters. The rms beam size σ_x is $\sqrt{\beta_x \epsilon_x}$, the rms divergence is $\sqrt{\gamma_x \epsilon_x}$ and the parameter α_x defines the level of correlation between x and x'. If $\alpha_x > 0$ the beam is converging, whereas for $\alpha < 0$ it is diverging. When $\alpha = 0$ the beam has minimum or maximum size.

The emittance can also be defined in terms of the statistical properties of a beam

of n particles as:

$$\epsilon_x = \sqrt{\langle x^2 \rangle \langle x'^2 \rangle - \langle xx' \rangle^2}$$ (2.3)

with

$$\langle x^2 \rangle = \frac{\sum x^2}{n} - \left(\frac{\sum x}{n} \right)^2,$$ (2.4)

$$\langle x'^2 \rangle = \frac{\sum x'^2}{n} - \left(\frac{\sum x'}{n} \right)^2,$$ (2.5)

$$\langle xx' \rangle = \frac{\sum xx'}{n} - \frac{\sum x \sum x'}{n^2}.$$ (2.6)

It is useful to introduce an emittance definition that remains invariant when the beam is accelerated under ideal condition. This is the normalised emittance $\epsilon_n = \beta\gamma\epsilon$, with β and γ the relativistic parameters.

2.5.2 FODO lattice

A particle beam can be focused to a symmetrical spot by using a combination of quadrupoles. The setup of alternated focusing (**F**) and defocusing (**D**) in the same plane quadrupoles of equal strength separated by a drift space (**O**) is called the FODO lattice. For a FODO lattice, the maximum/minimum of the β function is located at the centre of the focusing quadrupole.

The evolution of the particle position x and angle x' in a beamline can be calculated using a matrix formalism, so that $\mathbf{u}(s_1) = \mathbf{M}\,\mathbf{u}(s_0)$ with $\mathbf{u} = (x, x')$ and $\mathbf{M}$ a matrix representing a beamline element such as a drift or magnetic element. The matrices for focusing (M_{QF}) and defocusing (M_{QD}) quadrupole magnets are:

$$M_{QF} = \begin{bmatrix} \cos\left(\sqrt{K}\,l_{ef}\right) & \frac{1}{\sqrt{K}}\sin\left(\sqrt{K}\,l_{ef}\right) \\ -\sqrt{K}\sin\left(\sqrt{K}\,l_{ef}\right) & \cos\left(\sqrt{K}\,l_{ef}\right) \end{bmatrix},$$ (2.7)

$$M_{QD} = \begin{bmatrix} \cosh\left(\sqrt{|K|}\,l_{ef}\right) & \frac{1}{\sqrt{|K|}}\sinh\left(\sqrt{|K|}\,l_{ef}\right) \\ \sqrt{|K|}\sinh\left(\sqrt{K}\,l_{ef}\right) & \cosh\left(\sqrt{|K|}\,l_{ef}\right) \end{bmatrix},$$ (2.8)

with K and l_{ef} the quadrupole strength and effective length [138]. In the thin lens approximation:

$$M_{QF} = \begin{bmatrix} 1 & 0 \\ -\dfrac{1}{f} & 1 \end{bmatrix} \qquad M_{QD} = \begin{bmatrix} 1 & 0 \\ \dfrac{1}{f} & 1 \end{bmatrix}, \tag{2.9}$$

where the focal length is:

$$\frac{1}{f} = K l_{ef} \left(\frac{qc}{E} \right). \tag{2.10}$$

The total transformation matrix for a FODO lattice is:

$$M_{FODO} = M_{QF} \cdot M_{drift} \cdot M_{QD} \cdot M_{drift} \cdot M_{QF}, \tag{2.11}$$

where the drift space matrix M_{drift} is:

$$M_{drift} = \begin{bmatrix} 1 & L \\ 0 & 1 \end{bmatrix}, \tag{2.12}$$

with L the distance between quadrupoles. The solution of equation 2.11 gives the end-up matrix as a combination of L and f:

$$M_{FODO} = \begin{bmatrix} 1 - \dfrac{L^2}{2f^2} & 2L\left(1 + \dfrac{L}{2f}\right) \\ \dfrac{-L}{2f^2}\left(1 - \dfrac{L}{2f}\right) & 1 - \dfrac{L^2}{2f^2} \end{bmatrix}. \tag{2.13}$$

2.6   Beam focusing system at CLEAR

The experiment at the CLEAR facility employed two triplets of quadrupole magnets to transport and focus the electron beam onto the water phantom. The first triplet was placed before the VESPER test bench, at the end of the CALIFES injector (Figure 2.3). It consisted of quadrupoles (QFD0350, QDD0355, QFD0360), as shown in Figure 2.17. A second triplet with quadrupoles (QFD0510, QDD0515, QFD0520) was placed before

the water phantom.
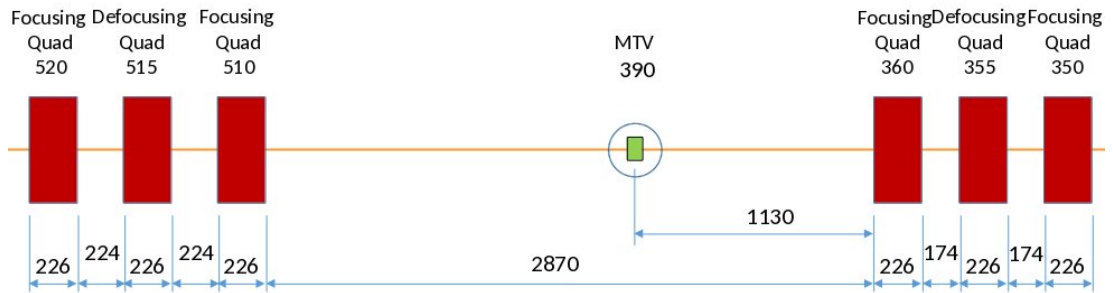
Figure 2.17: Beam optics used during the experiment at the CLEAR facility. The green square named "MTV" is a profile monitor. The beam travels from right to left and distances are in mm.

All quadrupole magnets are Q*D-type electromagnetic quadrupoles (EMQs) model QPMA-26 produced by Scanditronix. They have a nominal gradient of 11.2 T/m, inscribed radius of 29 mm and yoke length of 200 mm (Figure 2.18). The integrated gradient homogeneity for currents of 100 and 200 A is shown in Figure 2.19, which is heavily affected by a large uncompensated dodecapole component. The integrated strength increases linearly with the applied current (Figure 2.20) and is about 2% stronger than the value specified by the manufacturer (Table 2.6). Figure 2.21 shows the longitudinal variation of the field strength.
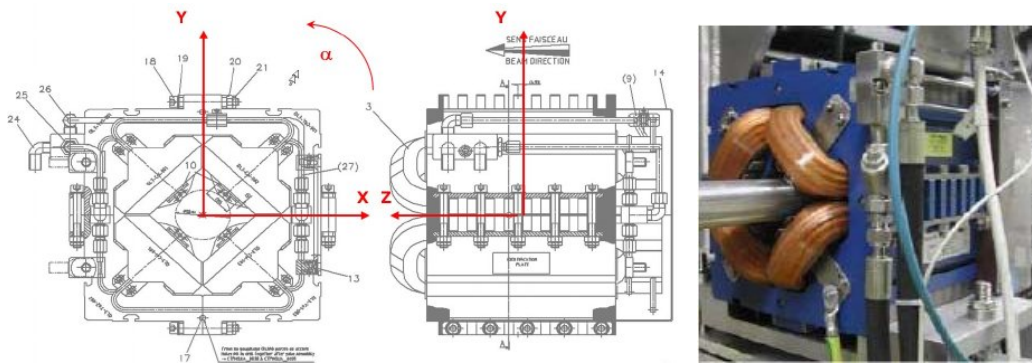
Figure 2.18: Schematic design and picture of a QPMA-26 Scanditronix quadrupole. The x and y axis are in the horizontal and vertical direction, respectively.
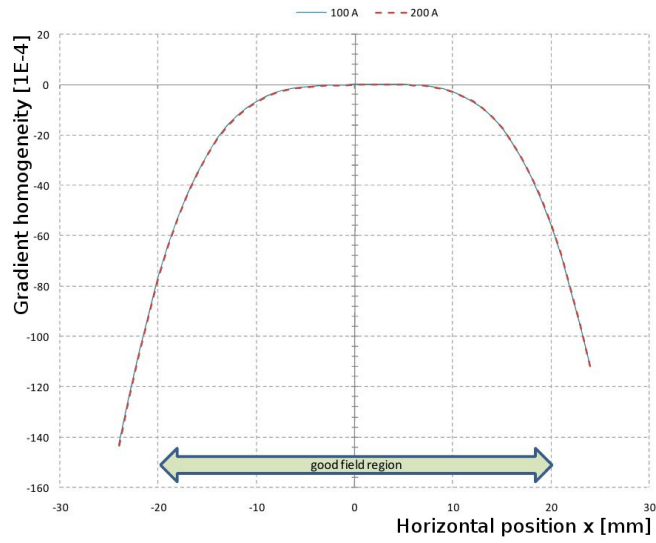
Figure 2.19: Integrated gradient uniformity of a QPMA-26 Scanditronix quadrupole.

Table 2.6: QPMA-26 Scanditronix quadrupole magnet specifications.

Parameter	
Nominal gradient [T/m]	11.2
Inscribed radius [mm]	29
Integrated gradient [T/m/m]	2.53
Nominal current [A]	200
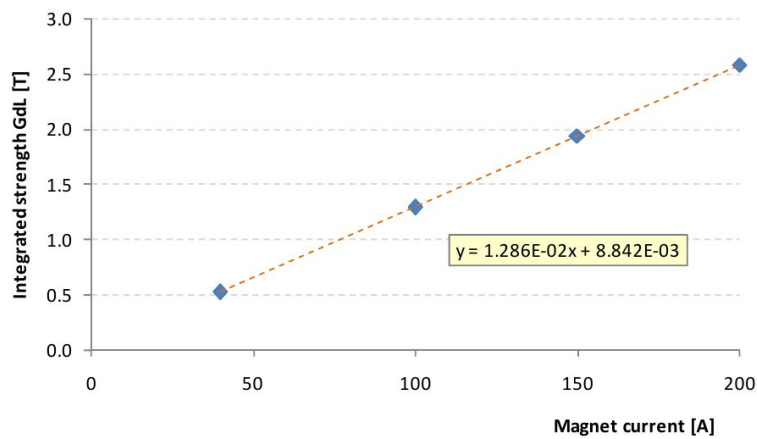
Figure 2.20: Integrated strength as a function of the applied current for a QPMA-26 Scanditronix quadrupole.
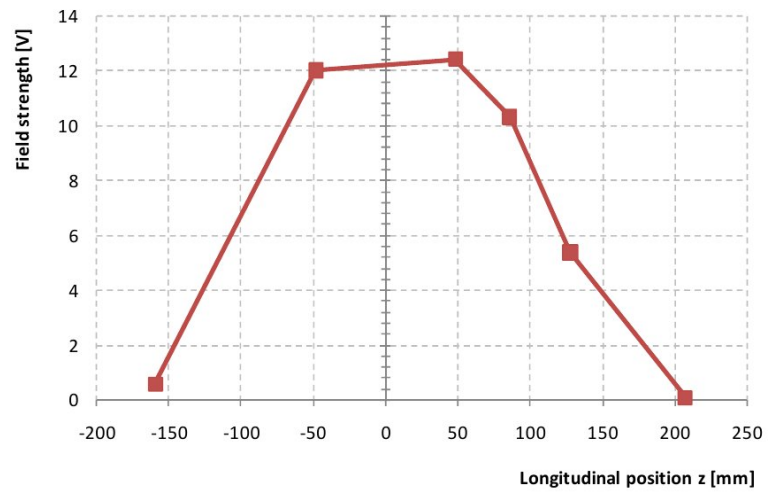
Figure 2.21: Longitudinal field variation of a QPMA-26 Scanditronix quadrupole.

Chapter 3

Interaction of electrons with matter

Modelling the propagation of charged particles in matter requires detailed knowledge of the types of interaction, probability of each interaction, and possible end products for all particles participating in the interaction chain. This chapter describes the fundamental electromagnetic and nuclear processes governing the interaction of electrons with matter and explains how relevant physical models are implemented in Monte Carlo codes used in this work to plan experiments and simulate experimental outcome.

3.1 Mechanisms of electron energy loss

Charged particles deposit their energy in a medium mainly through interaction with the orbital electrons and the nuclei of atoms forming the material [139]. The interaction probability depends on the particle energy, target density and thickness. Interactions with orbital electrons result in ionisation, electronic, vibrational and rotational excitation. To excite an atom, orbital electrons absorb energy from the charged particle and occupy higher quantum energy levels for a short time. Ultimately, the atom returns to the ground state while emitting photons with an energy corresponding to the energy difference between the atomic levels. In the case of ionisation, the charged particle liberates the orbiting electron from the binding Coulomb force. The released electron

can cause further ionisation and lead to the production of δ-rays. Rotational excitation occurs when a charged particle collides with a molecule. Angular momentum of molecules is quantised and corresponds to different rotational energy states. When the charged particle interacts with the molecule it gives a torque to it. The molecule reacts to this change by performing transitions between quantised rotational states.

Interaction of charged particles with the nuclear Coulomb field results in the production of bremsstrahlung radiation, that can dominate the energy loss for light particles such as electrons and positrons. Emission of Cherenkov radiation is also possible when the charged particle velocity is higher than the phase velocity of light in the medium, as discussed in subsection 3.1.5. Heavy particles such as protons and photons can also trigger nuclear reactions, but are very rare for electrons.

3.1.1 Stopping power

The mean energy loss per unit path length of a charged particle in a medium is called the linear stopping power. It depends on the properties of the particle and the medium through which the particle travels. The stopping powers for various materials are given in the ICRU Report 49 [140]. The total stopping power is determined by a combination of radiative and collisional components. The collisional energy loss results from Coulomb interaction of the charged particle with the orbital electrons in the medium, as discussed in subsection 3.1.3. The radiative energy loss for electrons occurs as bremsstrahlung radiation, described in subsection 3.1.4. At high energies the stopping power of light particles is dominated by radiative loss, as shown in Figure 3.1 for electrons in water.

3.1.2 Continuous Slowing Down Approximation

Collision and radiative losses typically result in the transfer of a very small amount of energy. The propagation of a charged particle in a medium can therefore by treated as a continuous energy loss. This is the formalism of the continuous slowing down approximation (CSDA) [142].
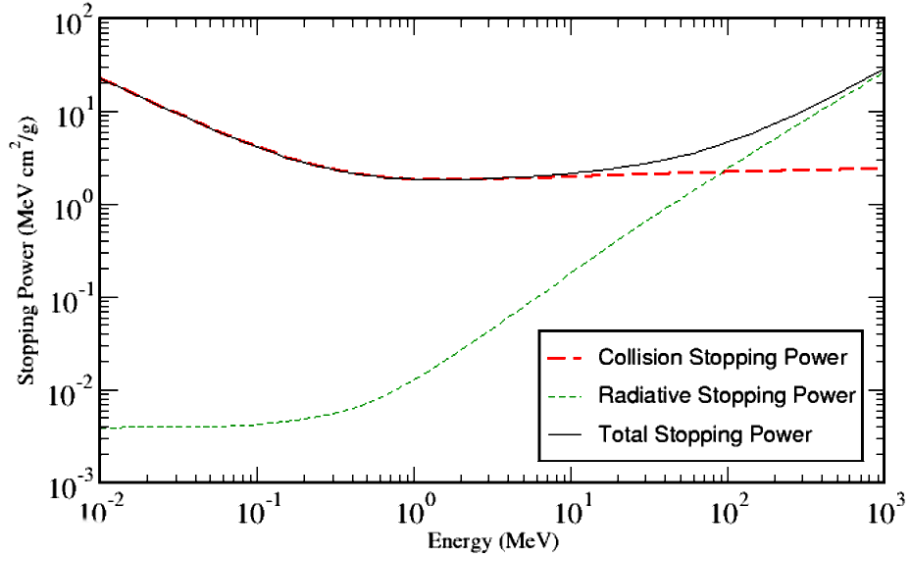
Figure 3.1: The collision and radiative stopping powers of electrons in water as a function of the electron kinetic energy, from [141].

The CSDA is calculated by integrating the inverse of the linear stopping power (dE/dx) of the particle from zero to the initial kinetic energy E_0:

$$R_{CSDA} = \int_0^{E_0} \frac{1}{|dE/dx|} dE. \tag{3.1}$$

Figure 3.2 shows the values of the CDSA range of electrons in liquid water as tabulated from [143, 140].

3.1.3 Collision stopping power

The interaction of both light and heavy charged particles with orbital electrons can be described using the Bethe theory [144, 145]. The collision stopping power for electrons is:

$$-\left\langle \frac{dE}{dx} \right\rangle = \rho K \frac{Z}{A} \frac{1}{\beta^2} \left[\ln \left(\frac{T}{I} \right)^2 + \ln \left(1 + \frac{\tau}{2} \right) + F(\tau) - \delta \right], \tag{3.2}$$
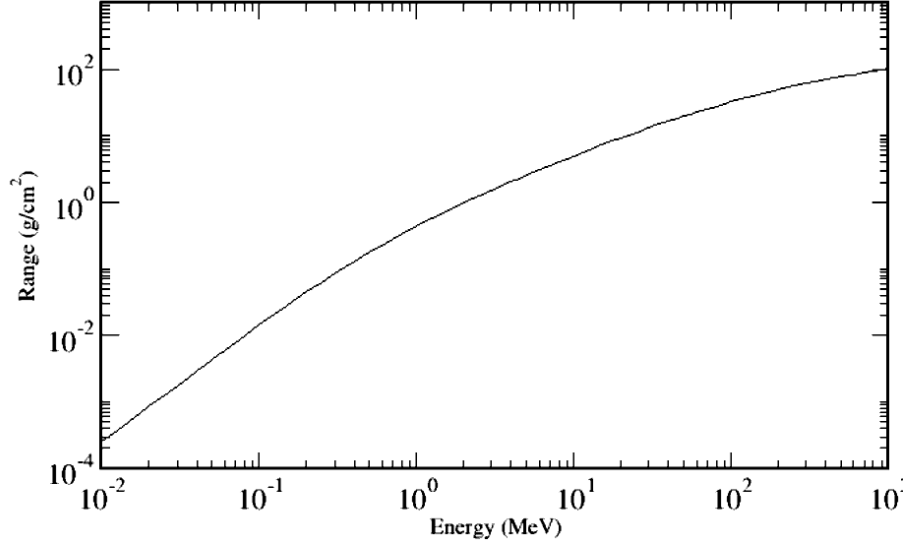
Figure 3.2: Continuous slowing down approximation (CSDA) range as a function of energy for electrons in liquid water resulting from reference tabulations [143, 140].

where ρ, Z, and A are the density, atomic number and atomic mass of the material, $\beta = v/c$, with v the electron velocity and c the speed of light, and

$$K = 4\pi N_A r_e^2 m_e c^2 \approx 0.307 \text{ MeV mol}^{-1} \text{ cm}^2, \tag{3.3}$$

with N_A Avogadro's number, m_e the electron mass and r_e the classical electron radius. I is the mean excitation energy of the medium, $T = (\gamma - 1)m_e c^2$ is the electron kinetic energy, with γ the relativistic factor, and

$$F(\tau) = \left(1 - \beta^2\right)\left[1 + \frac{\tau^2}{8} - (2\tau + 1)\ln 2\right], \tag{3.4}$$

with $\tau = T/(m_e c^2)$. Furthermore, δ is a density correction, which accounts for a reduction of the stopping power due to polarisation of the atoms in the material, an effect that is stronger for dense media and ultra-relativistic particles. The stopping power for positrons is also given by equation 3.2, but with

$$F(\tau) = 2\ln 2 - \frac{\beta^2}{12}\left[23 + \frac{14}{\tau + 2} + \frac{10}{(\tau + 2)^2} + \frac{4}{(\tau + 2)^3}\right]. \tag{3.5}$$

The energy loss increases at low velocities for both light and heavy charged particles, resulting in the formation of the Bragg peak [146], which is clearly manifested, for example, in the depth-dose profiles of proton or carbon ion beams. For electrons, however, the Bragg peak is not clearly observed for multiple electrons because of the large scattering angle, which causes electrons to follow irregular trajectories and deposit their final energies at different locations. Figure 3.3 presents the depth-dose distribution in water of a 30 MeV electron beam calculated using different models. The curve labelled *STRAIGHT AHEAD* does not include multiple scattering and bremsstrahlung production, resulting in the formation of an electron Bragg peak. The kinetic energy of electrons forming the Bragg peak is less than about 1 keV [147].
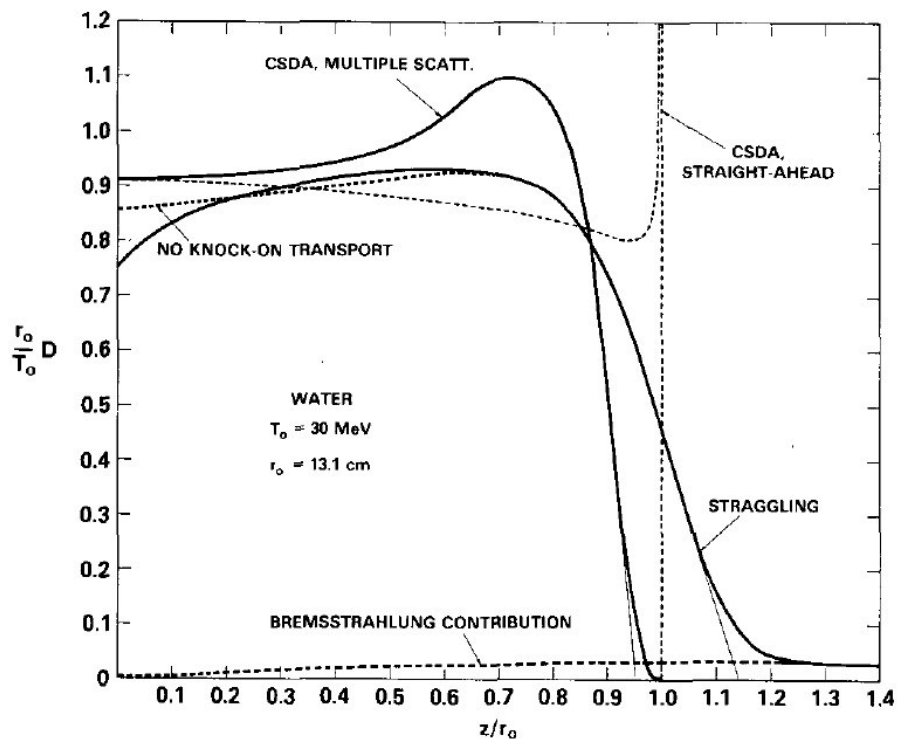
Figure 3.3: The effect of various approximations on the electron depth-dose curve for a broad, 30 MeV electron beam in water illustrating the physics of electron interactions, from [148]. The dose is expressed as the ratio of the mean range r_0 to the electron energy T_0, and the depth z is expressed as fraction of r_0.

3.1.4 Bremsstrahlung production

Electrons produce bremsstrahlung radiation as a result of deceleration in the Coulomb field of the nucleus. The bremsstrahlung cross-section is proportional to the square of the atomic number of the material [149, 150]. The energy loss (radiative stopping power) due to bremsstrahlung after propagation through a unit thickness of matter containing n_{at} atoms is:

$$-\frac{dE}{dx} = n_{at} \int_0^{k_{max}} k \frac{d\sigma}{dk} dk, \tag{3.6}$$

where k is the energy of the radiated photons and σ the bremsstrahlung cross-section. In general, $d\sigma/dk$ can only be calculated numerically, but for electrons with energy $E \gg m_e c^2/(\alpha Z^{1/3})$, with α the fine structure constant, the integral can be performed analytically obtaining

$$-\frac{dE}{dx} = \frac{E}{X_0}, \tag{3.7}$$

which has solution:

$$E(x) = E(0) \exp\left(-\frac{x}{X_0}\right), \tag{3.8}$$

where

$$\frac{1}{X_0} = 4\alpha r_e^2 n_{at} \left\{ Z^2[L_{rad} - f(Z)] + Z L'_{rad} \right\} \tag{3.9}$$

is the radiation length, the distance traversed by the electron until its energy is $1/e$ of its initial value. The symbol r_e is the classical electron radius, L_{rad} and L'_{rad} are tabulated values for different materials and $f(Z)$ is a Coulomb correction factor.

3.1.5 Cherenkov radiation

Cherenkov radiation is emitted when a charged particle travels in a medium with velocity larger than the phase velocity of light at wavelength λ. The emission is due to an asymmetric polarisation of the medium in front and at the rear of the moving particle,

giving rise to a varying electric dipole momentum [151]. Radiation is emitted at an angle θ, such that $\cos\theta = 1/\beta n$, where n is the refractive index of the material and $\beta = v/c$, with v the particle velocity and c the speed of light. For propagation in water $(n = 1.33, v \approx c)$ $\theta = 43°$. The number of photons N emitted per unit path length and unit wavelength is:

$$\frac{d^2N}{d\lambda dx} = \frac{2\pi z^2 \alpha}{\lambda^2}\left(1 - \frac{1}{\beta^2 n^2(\lambda)}\right),\tag{3.10}$$

with α the fine structure constant and ze the particle charge. For many materials the radiation intensity is proportional to the frequency and Cherenkov radiation in the visible spectral region appears blue.

3.2 Mechanism of energy transport by secondary products of electron interactions

3.2.1 Photon energy transport and absorption

Electrons interacting with matter produce a large number of bremsstrahlung photons. As photons have no mass and no charge, their mechanism of interaction differs in nature from that of electrons. Photons can interact with orbital electrons of the atoms constituting the material, resulting in the photoelectric effect, Rayleigh scattering and Compton scattering [152]. They can also interact with the nuclei, resulting in pair production and nuclear processes. These mechanisms are described in detail in the following sections.

The propagation of photons in a material can be described by the linear attenuation coefficient μ, which depends on the photon energy and on the atomic number Z of the material. It corresponds to the attenuation per unit thickness of material:

$$\mu = \ln(I_0/I_x)/x,\tag{3.11}$$

where I_x is the photon beam intensity at depth x and I_0 is the original intensity. A related quantity is the mass attenuation coefficient, defined as $\mu_m = \mu/\rho$, with

ρ the medium density. The attenuation coefficient is the sum of contributions from photoelectric effect (τ), Rayleigh scattering (σ_r), Compton absorption (σ_a), Compton scattering (σ_s) and pair production (κ). The importance of each contribution depends on the photon energy, as shown in Figure 3.4 for water.
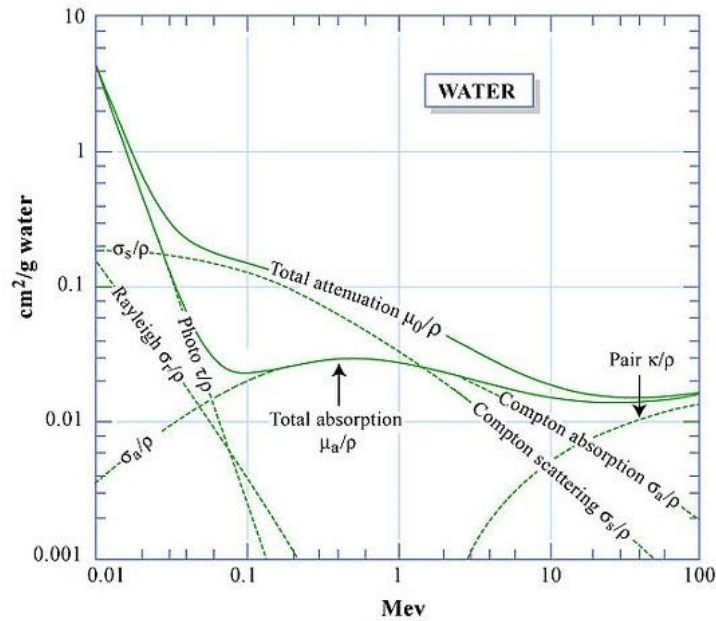

Figure 3.4: The total attenuation coefficient in water as a function of photon energy, showing the contribution from different photon interaction mechanisms, from [153].

The photoelectric effect is dominant for low energy photons ($\approx$ 20 keV) and occurs frequently in bones that are rich in elements with high atomic number, such as calcium. At higher photon energies (>80 keV) photons are attenuated mainly through Compton scattering in both water (representing soft tissue) and bones.

3.2.2   Photoelectric effect

Photoelectric effect is the interaction of a photon with an orbital electron of an atom [154]. The photon loses its entire energy in a single collision and the electron acquires sufficient energy to be ejected from the atom. The kinetic energy of the electron is:

$$K_{max} = h(\nu - \nu_0), \tag{3.12}$$

where h is Planck's constant, ν the photon frequency and ν_0 a threshold frequency that depends on the material. The vacancy created by the expelled electron can be filled by another electron from the upper shell, with the emission of a characteristic photon or Auger electron [155].

3.2.3 Compton scattering

A photon can interact with a free or outer-shell orbital electron of an atom through Compton scattering, losing part of its energy. After interaction, the photon is scattered at an angle θ and part of its energy is transferred to the recoiling electron. If the initial photon energy is $E_0 = h\nu$, the scattered photon has energy [156]

$$E_1 = \frac{h\nu}{1 + \alpha(1 - \cos\theta)} = \frac{m_e c^2}{1 + (1/\alpha - \cos\theta)}, \tag{3.13}$$

where $\alpha = h\nu/m_e c^2$, with h Planck's constant and m_e the electron mass. When $\theta = 0°$ the photon energy does not change as a result of the scattering and the electron is scattered at $90°$. This low-energy limit of Compton scattering is commonly refereed to as Thomson scattering. The cross-section for Compton scattering is independent of the atomic number of the absorbing material and is directly proportional to the electron density.

3.2.4 Positron electron pair production

In the pair production process a high energy photon (gamma-ray) interacts with a nucleus to form an electron-positron pair. The positron-electron pair process is described mathematically by the Bethe-Heitler formula [157]. Energy conservation requires the photon energy to be at least twice the electron rest energy and momentum conservation requires interaction with an additional Columb field from a nucleus or orbital electron. In the laboratory frame, where the nucleus is assumed at rest, the threshold energy for

pair production is:

$$E_{th}^{lab} = \frac{2m_ec^2(m_ec^2 + Mc^2)}{Mc^2}, \qquad (3.14)$$

where m_ec^2 is the electron rest energy (511 keV) and Mc^2 is the rest energy of a nucleus or orbital electron. In the case of a nucleus, $M \gg m_e$ and

$$E_{th}^{lab} \approx \frac{2m_ec^2}{Mc^2}(Mc^2) = 2m_ec^2 = 1.022 \text{ MeV.} \qquad (3.15)$$

In the case of an orbital electron, $M = m_e$ and

$$E_{th}^{lab} = \frac{2m_ec^2}{m_ec^2}(m_ec^2 + m_ec^2) = 4m_ec^2 = 2.044 \text{ MeV.} \qquad (3.16)$$

This second case is also known as triplet production, since it results in the emission of one positron and two electrons. The cross-section for pair production increases approximately with the square of the atomic number Z, whereas the cross-section for triplet production increases linearly with Z.

3.2.5 Photo-disintegration

Electron matter interaction results in the production of bremsstrahlung photons that can interact with the nuclei. If the photon energy is equal to or greater than the binding energy of a nucleon, the nucleus undergoes photo-disintegration. The energy threshold varies from around 6 MeV, for heavy nuclei, to around 12 MeV, for most light nuclei [158]. For moderate energies ($\lesssim$ 10 MeV) the most probable processes are (γ, p) and (γ, n). At higher energies reactions such as (γ, np) and (γ, αn) can also occur. For photon energies up to about 25 MeV the cross-section for photonuclear reaction is governed by the giant dipole resonance, which has a peak at about 23 MeV for light nuclei ($A \lesssim 40$) and at about 12 MeV for heavy nuclei ($A \gtrsim 40$). Above 25 MeV the photoneutron cross-section is smaller and can be described by a quasi-deuteron model [158], obtaining

$$\sigma_{qd} = \sigma_d D(A - Z)Z/A, \qquad (3.17)$$

where (A-Z)Z is the number of quasi-deuteron pairs, D is the quasi-deuteron constant correlated with the interaction distance of the photon and σ_d is a photodeuteron cross-section.

3.2.6 Muon pair production

The muon pair production process is analogous to electron positron pair production. Only photons with energies greater than 211 MeV ($2m_\mu c^2$) can trigger the production of muon pairs. The cross-section is about 5 orders of magnitude lower than for electron-positron production, because of the larger mass [159].

3.3 Monte Carlo methods

Monte Carlo (MC) methods are powerful and versatile tools that allow to predict experimental results and simulate systems where experimental data are not directly available. Common research areas of Monte Carlo applications are radiation protection, treatment planning, dosimetry, accelerator-driven systems, detector design, cosmic rays detection and neutrino physics. In Monte Carlo methods the possible scenarios (events) of a particle behaviour satisfy a probability density function (PDF) [160]. The sampling from the input probability distribution is random, meaning that deterministic values in equations are replaced by probabilistic values. The system response is averaged over all events. The estimation of statistical uncertainties follows the central limit theorem (the more trials of sampling, the more realistic outcome and therefore smaller statistical error). The system is the transport of particles through a defined geometry and an event is a single interaction with matter. The residual effect of the calculations is the particle track. The most common Monte Carlo techniques for radiotherapy studies are FLUKA (FLUktuierende KAskade), EGSnrc (Electron-Gamma-Shower), MCNP (Monte Carlo N-Particle Transport), GEANT4 (GEometry ANd Tracking) and PENELOPE (Penetration and Energy Loss of Positron and Electrons). For the purpose of this doctoral project the experimental predictions and the design of the experimental setups were carried out with FLUKA MC code described in detail in the following

section.

3.3.1 FLUKA

The FLUKA code [161, 162, 163] is a general purpose Monte Carlo code that was originally developed at CERN in the 1960s to simulate interactions and transport of hadrons, heavy ions, and electromagnetic particles. It has been invented as a result of a collaborative effort of CERN and the Italian Institute for Nuclear Physics (INFN). The user support interface and routines, are implemented using FORTRAN programming language. FLUKA provides features to manage the entire simulation process including geometry generation and material assignment. Complex objects are built in through Boolean operations on basic geometrical shapes [164, 165]. FLUKA provides different configurations of the physics models that are suitable for specific problems such as shielding, hadron therapy or transmutation. The fundamental electromagnetic phenomena in FLUKA, continuous energy losses, energy loss straggling, delta-ray production and multiple Coulomb scattering, are briefly discussed in the following sections. The electron interaction cross-sections are calculated based on the tabulated values (EEDL97 database [166]) and electron bremsstrahlung cross-section (EPDL97 database [167]). Powerful biasing techniques allow to reduce the calculation time. FLUKA allows to set the production threshold of secondary electrons (δ-rays), step-length, and the contribution of distant collisions to energy loss fluctuations. The development and maintenance of FLUKA are performed in the framework of an INFN-CERN agreement.

3.3.2 Sampling

FLUKA is equipped with a 64-bit random number generator [168], which distributes particles according to a defined probability density function. Each particle colliding with matter produce secondary particles. The distance from the origin of the projectile to the event is defined as a single step. History is a collection of steps performed by the first parent (the source particle) and all progeny particles. Probability distributions are redefined at each step in time and space based on the tabulated cross-sections for the specific materials in compounds. Additional complexity results from the multi-energy

mixed radiation beams and complex material composition.

3.3.3 Variance estimation

The statistical error decreases inversely with the square-root of the number of histories. The variance in FLUKA is calculated batch by batch. Instead of running a simulation of N histories, B simulations of N/B histories are performed. Each of the B simulations is made independent by applying unique random number seeds. At the completion of each simulation, the averaged score for each batch is calculated as:

$$x_b = \frac{\sum_{i=1}^{N/B} x_{b,i}}{N/B}.$$ (3.18)

The final score is obtained by averaging over all batches and the standard deviation is:

$$\sigma = \sqrt{\frac{1}{B-1}\left[\frac{\sum_{i=1}^{B} x_i^2}{B} - \left(\frac{\sum_{i=1}^{B} x_i}{B}\right)^2\right]}.$$ (3.19)

3.3.4 Range straggling and Coulomb multiple scattering

As discussed in subsection 3.1.2, the interaction of a charged particle with matter can be described in terms of a continuous energy loss (CSDA). This approximation, however, neglects the statistical fluctuations (energy straggling) affecting the energy losses. Due to the small mass, the range straggling for electrons is enhanced in comparison with heavy particles. The fluctuations of energy loss by ionisation of a charged particle in a thin layer of matter can be described by the Landau [169] and Vavilov [170] distributions. These models, however, have several limitations and are difficult to implement in Monte Carlo codes [171]. Instead, FLUKA provides a correct and complete treatment of the stochastic nature of the energy loss in the interactions with atoms based on Molière formalism [172, 173] of multiple Coulomb scattering. A single scattering model is also included for cases where Molière theory does not apply, such as in very thin layers.

3.3.5 δ-ray production

An arbitrary threshold for the explicit production of secondary electrons (δ-rays), can be defined in FLUKA for arbitrary step-lengths, and for the contribution of distant collisions to energy loss fluctuations, while assuring the exact match of the average restricted stopping power (energy deposited in the vicinity of the particle track). The lowest threshold for production of secondary electrons in FLUKA is 1 keV.

Chapter 4

Focused MeV and GeV electrons

In this chapter a study is undertaken using the FLUKA Monte Carlo code to validate the concept of focused VHEEs explained in chapter 1. An extreme case where electron energy is significantly higher than in the VHEE regime is also investigated to study the effect of beam focusing while scattering in water is almost completely eliminated. Different beam geometries are studied using a perfect magnetic lens. This model does not incorporate beam artefacts caused by system imperfections that could introduce asymmetry and further undesirable effects in dose distribution. The design of a focusing system for VHEEs is discussed in chapter 7, which describes an experiment performed during the campaign at CERN. The physics models suitable for VHEEs are established using FLUKA MC package. An estimation of on-axis, off-axis, surface and exit doses, and the contributions of secondary particles, such as positrons, neutrons and muons, in a water phantom are presented and discussed. The post-irradiation activity induced in a phantom containing bone and muscle materials, and linear energy transfer are investigated. This study does not aim to achieve clinical accuracy, as this would require advance treatment planning studies using patient data. Nevertheless, the results build solid foundations for future dosimetry, radiation safety and treatment planning studies of focused VHEEs.

4.1 Methods

4.1.1 Beam characteristics and model geometry

The results presented in this chapter are produced using the FLUKA Monte Carlo code, version 2011.2c.6. Simulations are performed with 10^7 histories. Monoenergetic ($\delta E = 0$) electron beams with energies of 200 MeV and 2 GeV, with a $\sigma = 10$ cm, Gaussian transverse profile are considered. 200 MeV electrons are within the established energy range of VHEE beams [57], while 2 GeV electrons are referred to as ultra-high electron energy (UHEE). The latter are used to investigate the extreme case where the electron energy is significantly higher than in the VHEE regime, and electrons penetrate deeply with reduced scattering [174].
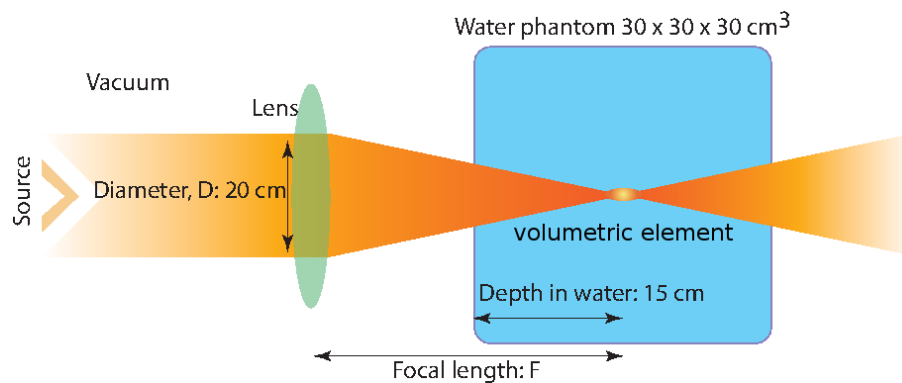
Figure 4.1: Focused electron beam geometry. Different focusing configurations are studied by varying the position and focal length of the lens, while keeping the focus position (in vacuum) fixed at a depth of 15 cm.

Figure 4.1 illustrates the modelled geometry, which comprises a beam of initial diameter D focused to a point at the centre of a $30 \times 30 \times 30$ cm^3 water phantom (soft tissue equivalent material). The beam is focused by an ideal magnetic lens with a focal length F. The dosimetry protocols of the American Association of Physicists in Medicine (AAPM) (TG-51, [175]) and the International Atomic Energy Agency (IAEA) (TRS-398, [176]) recommend that liquid water is used as a phantom material for reference dosimetry due to high phantom material reproducibility. Water is routinely used in dosimetry calculations and measurements because it is a natural, easily available

and almost cost-less body surrogate. It emulates, with sufficient approximation, the radiation absorption and scattering properties of soft tissue and muscles, while the calculations of interaction cross-sections are simpler than for bio-compounds.

The ratio F/D (*f-number*) is a quantitative representation of focusing strength. Low *f-numbers* correspond to the smallest beam size at focus, whereas ∞ corresponds to a collimated beam. Nine electron beams are simulated with *f-numbers* in the range of $f/1.2 - f/11.5$. The term *strongly focused beam* refers to an electron beam with a *f-number* less than $f/3.8$. The electron beam size (FWHM) at the phantom entrance is inversely proportional to the *f-number* and varies between 2.5 cm (for ∞) and 15.9 cm (for $f/1.2$) for the simulated beams. The diameter D is fixed in all simulations.

Beam geometry for different *f-numbers* is modelled by altering distance between the source and the focus, defined initially at the centre of the phantom, from 24.1 cm to 229 cm, which corresponds to a focal length of the strongest ($f/1.2$) and weakest ($f/11.5$) focusing, respectively. Scattering in air is of concern for electrons within the clinical energy range, but as energy increases the effect becomes less adverse and eventually almost negligible in the VHEE range [177]. The beam size increases by less than 1% at the entrance of the phantom compared with the simulations in vacuum for all *f-numbers*. The study aims to investigate the focused beam propagation in water including effects caused by physical properties of water and electron interaction physics, therefore to avoid additional external effects and to achieve the optimal simulation time the beams were propagated in vacuum before entering the water phantom. The model also does not consider imperfections of the magnetic lens. The magnetic lens is assumed to focus the beam perfectly at a defined point in space. In a real magnetic lens with quasi-uniform magnetic field, which is produced by quadrupole magnets, electrons which move near the central axis are focused further than the outer electrons, moving on the edge of the beam. This, so called beam aberration, if incorporated in the model, would be stronger for smaller *f-numbers*.

The FLUKA user routine source.f is modified to model particle trajectories. The coordinates of projectiles at the source are sampled from a normal distribution using FLUKA random number generator. The beam propagates along the z axis. The

electron momentum coordinates in the Cartesian system are calculated according to the equations:

$$\cos \phi_x = \frac{x - x_0}{\sqrt{(x - x_0)^2 + (y - y_0)^2 + (z - z_0)^2}}, \tag{4.1}$$

$$\cos \phi_y = \frac{y - y_0}{\sqrt{(x - x_0)^2 + (y - y_0)^2 + (z - z_0)^2}}, \tag{4.2}$$

$$\cos \phi_z = \sqrt{1 - \cos(\phi_x)^2 - \cos(\phi_y)^2}, \tag{4.3}$$

where x_0, y_0, z_0 are the source coordinates and x, y, z are the focus coordinates and ϕ_x, ϕ_y and ϕ_z are the angles between particle momentum direction and the beam propagation axis. Details of the physics settings, beam parameters, as well as different detector configurations for estimation of the physical quantities, such as dose and fluence, are given below.

4.1.2 Physics settings

Simulations are performed using the PRECISIOn physics setting, which provides interaction models for all electromagnetic and nuclear processes that are relevant to the transport of VHEEs, including gamma interactions with nuclei. More on the interactions included in the chosen physics model can be found in the FLUKA manual [178]. Here, a detailed description of the FLUKA input settings that are used to simulate focused VHEEs, is provided.

Neutron production occurs for photon energies above a few MeV. The energy range of bremsstrahlung photons produced by 200 MeV and 2 GeV electron beams in water extends from 0 MeV up to electron nominal energy. Therefore, photonuclear reactions are activated by the card PHOTONUC (with SDUM left blank) at three energy regions that have large cross-sections for specific photo-nuclear processes, as explained in chapter 3. These are nuclear resonance fluorescence, triggered by photons with energies $E\gamma < 2$ MeV, giant dipole resonance (GDR), most likely caused by photons with energies $5 < E\gamma < 30$ MeV, and quasi-deuteron effect of interaction of photons with energies $30 < E\gamma < 140$ MeV. In addition to this, for 2 GeV electrons, these processes are acti-

vated in the high energy range (above 0.7 GeV). The cross-sections for photo-nuclear processes in the VHEE regime is, however, much smaller than those for electromagnetic processes. Moreover, the calculations of photo-neutron production or photoactivation is in general extremely time-consuming in an analogue mode. An artificial reduction of the photo-nuclear mean free path, which is compensated by suitable adjustment of statistical weights, so called biasing, is commonly used in many radioprotection problems to reduce the calculation (CPU) time and achieve sufficient statistics if photo-nuclear events occur rarely. In the simulations of VHEE beams, survival probability of a single photon, that is produced via hadronic interactions, is set to 0.002 and 0.02 for secondary photons for 200 MeV and 2 GeV, respectively. This number is usually determined as a ratio of tabulated values of the photo nuclear (γ, n) cross-section ([179, 141]) to the total photon interaction cross-section. It is recommended that this value is carefully estimated to prevent abrupt termination of simulations while neutron transport and interaction are switched on. It should be noted that the increased survival probability ultimately increases the variance.

The energy transfer to electrons lower than the threshold is estimated according to CSDA, which is discussed in chapter 3. The threshold for transport and production of δ-particles and photons (ECUT, PCUT) is set to 10 keV in water (the default threshold for PRECISION settings is 100 keV). However, it is recommended to set photon thresholds slightly lower as photons penetrate tissue deeper than electrons. Production of photons, secondary electrons (based on the Moliére theory [172]) and positrons (based on the Bhabha theory [180]) via interactions with atomic electrons is simulated explicitly above this threshold.

The percentage depth-dose distribution for various radiation modalities were performed with different physics settings. The photon beam is collimated with the energy spectrum emulating the output of a 6 MV Elekta Synergy$^{®}$ linac at NPL. Simulations for protons are performed with the HADRONTHERAPY setting, which includes the EVAPORAT and COALESCEnce models and full heavy particle transport.

4.1.3   Scoring settings

The dose distribution in water for focused VHEEs is simulated using a $30 \times 30 \times 30$ cm^3 USRBIN mesh, with a resolution of 1.5 mm, which is defined within the phantom covering uniformly the whole volume. Different USRBIN cards are used to score the total dose (SDUM: Dose) and electron flux (SDUM: Electrons). The integral surface and exit doses are calculated in a 0.15 cm thick slice of the phantom at the entrance and exit. The peak surface and exit doses are simulated within a $0.15 \times 30 \times 0.15$ cm^3 detector volume at the entrance and exit of the phantom. The on-axis depth-dose profiles are calculated in a longitudinal $0.3 \times 0.3 \times 30$ cm^3 volume centred on the propagation axis. The off-axis dose corresponds to the integrated dose deposited in the rest of the phantom, outside of this central slice. A smaller ($4 \times 4 \times 4$ cm^3) high resolution (0.2 mm in the transverse and 0.1 mm in the longitudinal direction) mesh is used for the samples of the magnified 2D transverse profile plots at the beam waist.

4.1.4   Data processing and visualisation

Post processing (merging) of the output data files is performed with FLUKA routines specific for each detector type. All plots are performed in Gnuplot (version 4.6.0 and 5.0.3) except for the on-axis depth-dose curves in Figure 4.3 and 2D dose distribution in Figure 4.5, which is generated using Matlab (release 2017a).

4.1.5   Calculation time

A simulation for a 200 MeV electron beam, using 100,000 primaries and the full physics for neutrons, takes about 35 min (average of 10 runs) on a workstation with an Intel Xeon CPU E5-2640 v3 @ 2.60GHz. The execution time increases approximately linearly with the number of primaries. FLUKA does not support multiprocessing, as implemented for example in Geant4, but different cycles can be run in parallel.

4.2 Results

4.2.1 Depth-dose distribution

Figure 4.2 shows the central axis PDD of focused VHEEs for $f/1.2$ juxtaposed with single beam profiles for currently available radiotherapy modalities discussed in chapter 1. Two-dimensional data that are necessary to evaluate dose distributions in regions lying off the central beam axis, particularly those directly imparted by radiation, are presented later in this chapter. For direct comparison, doses are normalised to the dose at the depth of a deep-seated tumour, which is chosen to be 15 cm.
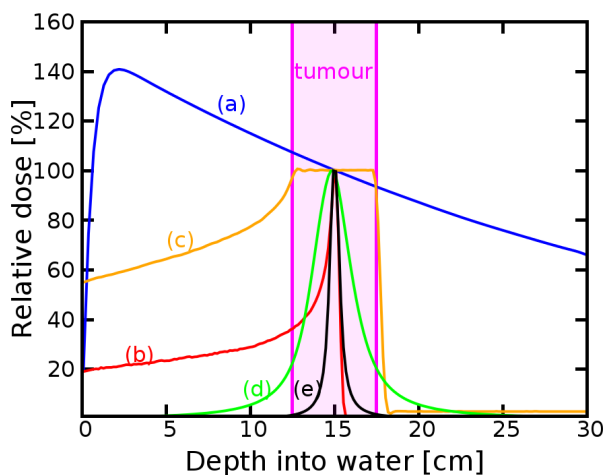
Figure 4.2: Percentage, on-axis, depth-dose curves of different types of radiation in a water phantom. 6 MV photons (a), Bragg peak of 147 MeV protons (b), spread-out Bragg peak (c), 200 MeV electrons (d), 2 GeV electrons (e), both beams focused at 15 cm. For comparison, each curve is normalised to the dose at the reference depth (15 cm). Curves (a – c) correspond to a Gaussian beam with FWHM diameter of 15.9 cm, matching the size of the focused beams (curves d, e) at the phantom entrance.

Simulations are performed over 5 cycles, except for the photon beam, for which the number of cycles is increased to 15 to minimise the stochastic error arising from the random seed generator of the code. The statistical uncertainties of depth-dose curves for different modalities and focused beams are less than 2%. The modelled beams have a Gaussian transverse distribution. The full-width-at-half-maximum (FWHM) of the photon and proton beams at the phantom entrance is set to 15.9 cm, which matches

the size of a $f/1.2$ focused electron beam at the phantom entrance and provides a quasi-uniform dose distribution in the scoring volume.

Preliminary modelling data indicate that focused 200 MeV and 2 GeV beams achieve highly localised dose deposition at the target depth, as shown by curves **d** and **e**, respectively. Moreover, the surface and exit doses are significantly lower than for photons and protons. For clinical photon energies the dose at the target (15 cm) constitutes around 70% of the maximum dose which is localised near the surface. For protons the target is aligned with the Bragg peak receiving the maximum dose of which 20% is delivered to the surface area. For SOBP the surface dose increases up to almost 60% of the dose at the target due to a cumulation of doses from superimposed Bragg peaks.

The initial focus position is defined at 15 cm from the front surface of the phantom filled with vacuum. In water a small shift is observed for a 200 MeV beam due to scattering, while for 2 GeV, the peak is well localised at the simulated depth, and is sharper. Figure 4.3 shows the effect of scattering on the peak depth for all chosen *f-numbers*. The profile for 2 GeV and $f/11.5$ is slightly deformed at the top, due to the dimension of the scoring volume (part of dose at the peak is scored outside of that volume). The focus is shifted towards the phantom entrance by approximately 0.4 – 4.5 cm for 200 MeV, and 0.1 – 0.3 cm for 2 GeV (Table 4.1). The shift increases with each *f-number* for 200 MeV, whereas it is fixed at 0.29 cm for *f-numbers* $f/1.2 – f/2.3$ for 2 GeV. The displacement of the dose peak is more pronounced for lower electron energies.

Table 4.1: Shift of the peak (D_{max}) positions from the reference depth (15 cm) for 200 MeV and 2 GeV electron beams focused with $f/11.5 - f/1.2$.

f-no.	200 MeV (cm)	2 GeV (cm)
1.2	0.42	0.29
1.4	0.45	0.29
1.6	0.49	0.29
1.9	0.55	0.29
2.3	0.64	0.29
2.8	0.80	0.28
3.8	1.13	0.27
5.7	1.94	0.25
11.5	4.50	0.15
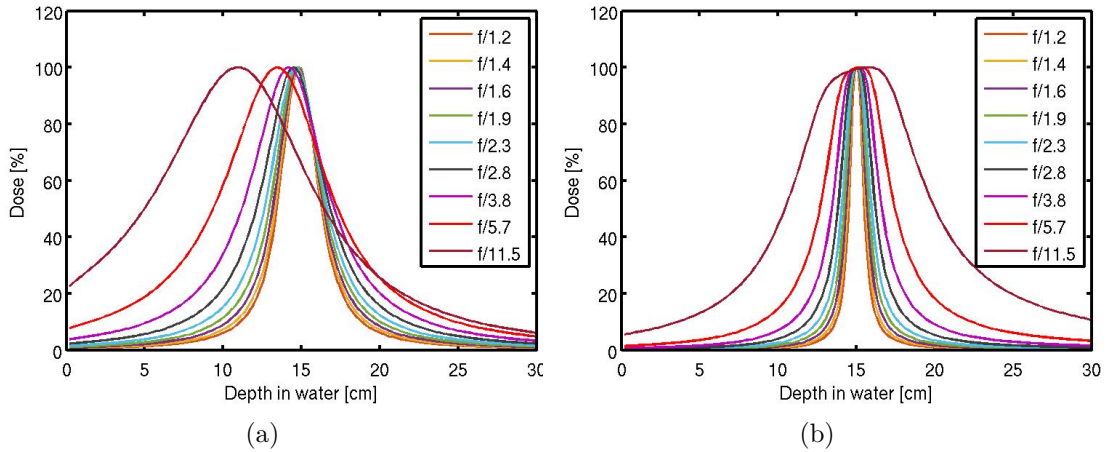
Figure 4.3: Percentage on-axis depth-dose curves for 200 MeV (a) and 2 GeV (b) beams focused with f/1.2-f/11.5.

The magnetic lens strength (or position) can be adjusted to scan the tumour at depth with the focus of the beam, and in conjunction with a dipole magnet, to scan cross-sectional area of the tumour at each depth, in an analogous way to proton scanning systems, as shown in Figure 4.4. An overlap of multiple focused VHEE beams at the tumour site creates a flat profile with sharp symmetrical ramps. The entrance and exit doses are almost negligible compared with the dose at the plateau. This, however is not the case for proton beams, for which the surface dose in the spread-out-Bragg peak profile can be as much as 60% of the target dose. Different algorithms for delivering scanned beams can be exploited to find the most appropriate distribution.

Figure 4.5 shows 2D depth-dose distributions for 200 MeV and 2 GeV electron beams focused at depth of 15 cm with *f-numbers* $f/1.2 - f/11.5$ and a reference collimated beam indicated denoted by f/∞ (a,b), and at 5, 10 and 15 cm for $f/1.2$ (c, d) which produces the most tightly focused beam. Different focus depths are obtained by displacing the phantom further downstream from the source, effectively moving the focus closer to the entrance.

In contrast to collimated beams, focused beams concentrate dose into a small, well-defined *volumetric element*. However, each *f-number* creates different scattering conditions along the beam propagation direction. These depend on the beam intensity,

(a)

(b)

(c)

(d)
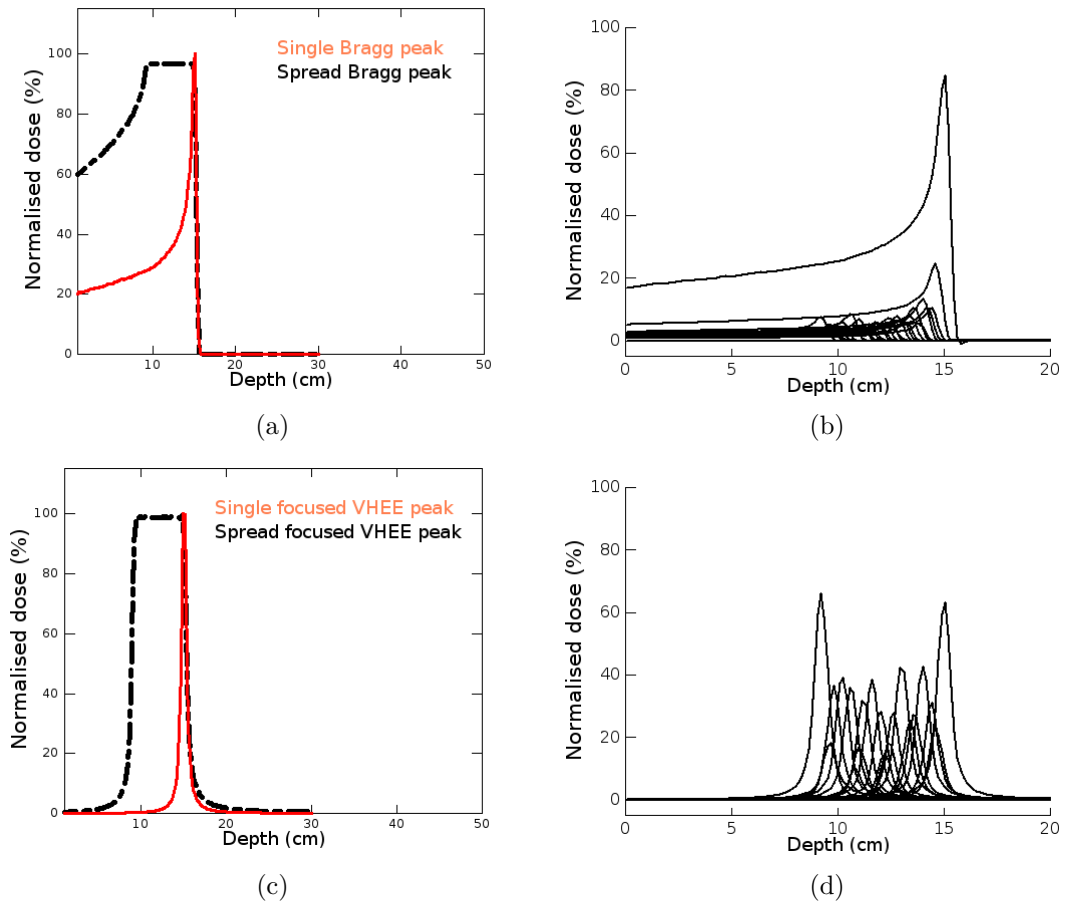
Figure 4.4: Simple modelling of central axis depth-dose profiles for scanned beams performed with EXTREMA (version 4.4.5). Single proton Bragg peak (a) and spread-out-Bragg peak (b). Single peak of focused VHEE ($f/1.2$, c) and an overlap of multiple profiles with varied depths and peak doses (d). The central axis depth-dose profiles of a single beam are simulated in FLUKA.

energy, and area of overlap between the beam and the target material. The target material, here water, has a defocussing effect on the electron beam, which causes a small increase of the transverse size of the *volumetric element*, mostly for lower energies (200 MeV) and large field sizes (small *f-numbers*). The peak dose increases with *f-number* indicating that for weakly focused beams electrons lose less energy outside of the *volumetric element*. This energy, however, in contrast to strongly focused beams is cumulated around the central beam axis. The peak dose also changes when the focus depth is altered while the *f-number* is fixed. The 2D dose distributions for $f/1.2$ focused

70

at 5, 10 and 15 cm are investigated for 200 MeV (Figure 4.5c) and 2 GeV (Figure 4.5d) beams. The peak dose decreases significantly with depth for the 200 MeV beam. The 2 GeV beam is more penetrating and results in an increase of peak dose with depth over the phantom length. The shape and size of the *volumetric element* is independent of the propagation distance from the surface to the defined focus depth in water.
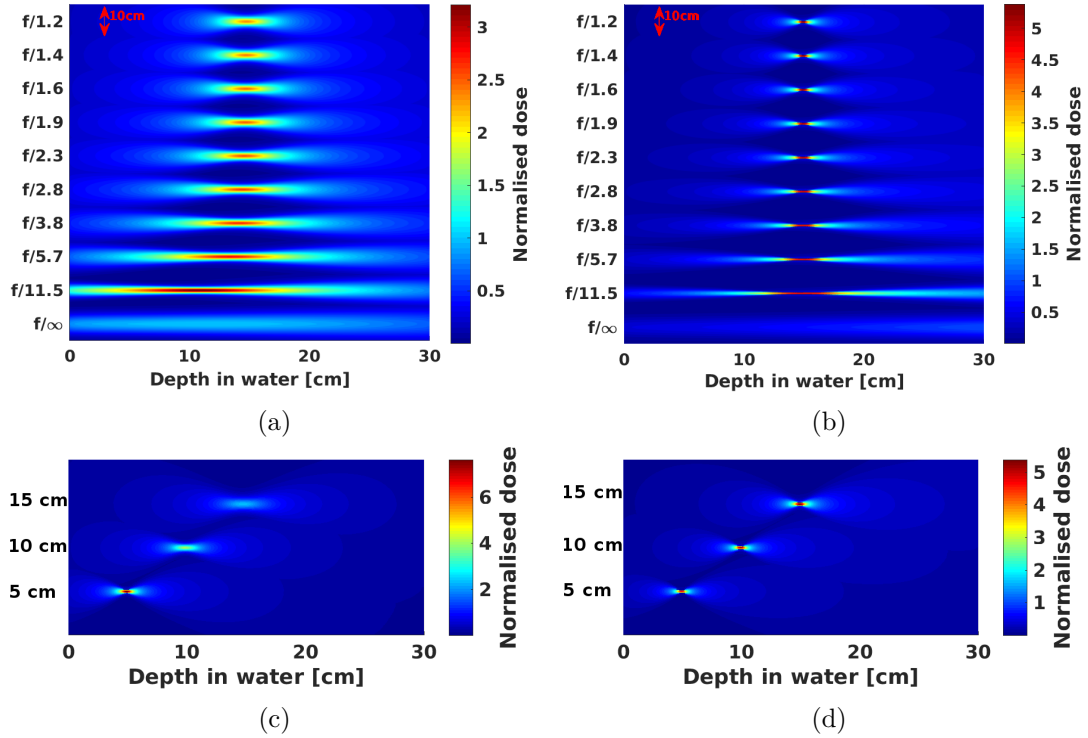
Figure 4.5: 2D depth-dose deposition map in the water phantom. (a) 200 MeV and (b) 2 GeV electron beams focused 15 cm from the entrance of the water phantom for $f/11.5 - f/1.2$ and collimated geometry (f/∞); (c) 200 MeV and (d) 2 GeV electron beams focused at 5, 10 and 15 cm from the entrance of the water phantom for $f/1.2$. The dose is normalised to the maximum dose of a collimated beam.

Figure 4.6 shows the FWHM of electron flux and dose transverse profiles as a function of depth for 200 MeV and 2 GeV beams focused with $f/1.2$ and $f/11/5$. The beam diameter decreases gradually as electrons approach the target depth for all *f-numbers*. However, the change is more dynamic for $f/1.2$. The electron flux transverse profiles agree perfectly with the dose transverse profiles across the phantom, except for a small difference observed for 200 MeV and $f/11.5$, and also for 2 GeV and $f/1.2$ at

71

the exit of the phantom. The peak dose is aligned with a depth of maximum electron flux density for both electron energies, and therefore the dose enhancement at 15 cm is a result of an increased electron flux density.
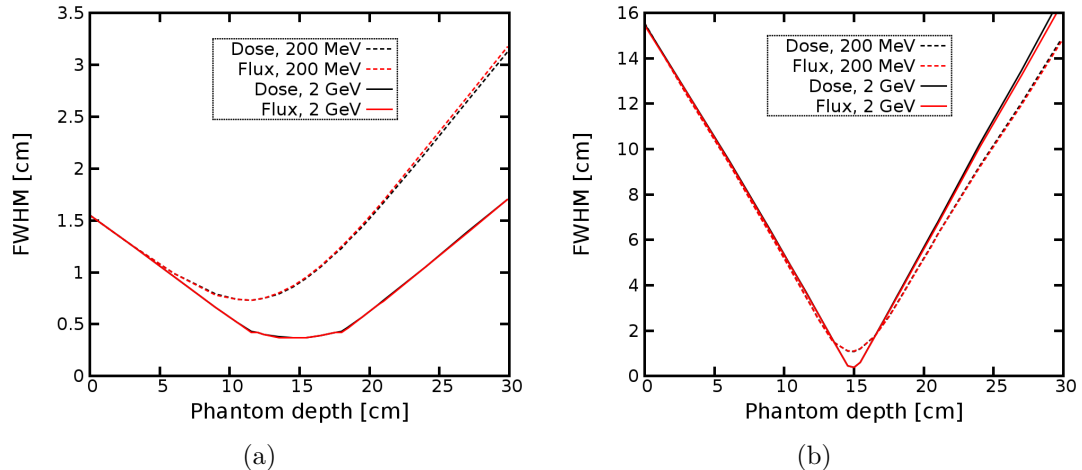
Figure 4.6: Depth-dose and electron flux FWHM for 200 MeV and 2 GeV beams focused with $f/11.5$ (a) and $f/1.2$ (b).

Table 4.2: FWHM of the volumetric elements for 200 MeV and 2 GeV electron beams focused at 15 cm from the entrance of the water phantom for $f/11.5 - f/1.2$.

f-no.	200 MeV		2 GeV	
	$\mathbf{FWHM}_z$ (cm)	$\mathbf{FWHM}_x$ (cm)	$\mathbf{FWHM}_z$ (cm)	$\mathbf{FWHM}_x$ (cm)
1.2	1.26	0.97	0.33	0.32
1.4	1.37	0.93	0.35	0.31
1.6	1.50	0.89	0.41	0.29
1.9	1.67	0.86	0.48	0.28
2.3	1.91	0.82	0.58	0.27
2.8	2.27	0.79	0.73	0.26
3.8	2.84	0.77	0.98	0.26
5.7	3.82	0.72	1.47	0.25
11.5	5.57	0.61	2.97	0.25

The shape of the *volumetric element* is studied for 200 MeV and 2 GeV beams and all *f-numbers* by performing simulations using a high-resolution scoring mesh in the dose peak region. Magnified lateral dose profiles (shown in Figure 4.7 and Figure 4.8 for $f/1.2$) are symmetrical with respect to the propagation axis, for both electron energies

and all *f-numbers*. For a better visualisation of the change in the *volumetric element* shape, the black reference contour connects points that received equal dose (50% of the maximum dose).

(a)

(b)

(c)

(d)

(e)

(f)

(g)

(h)

(i)
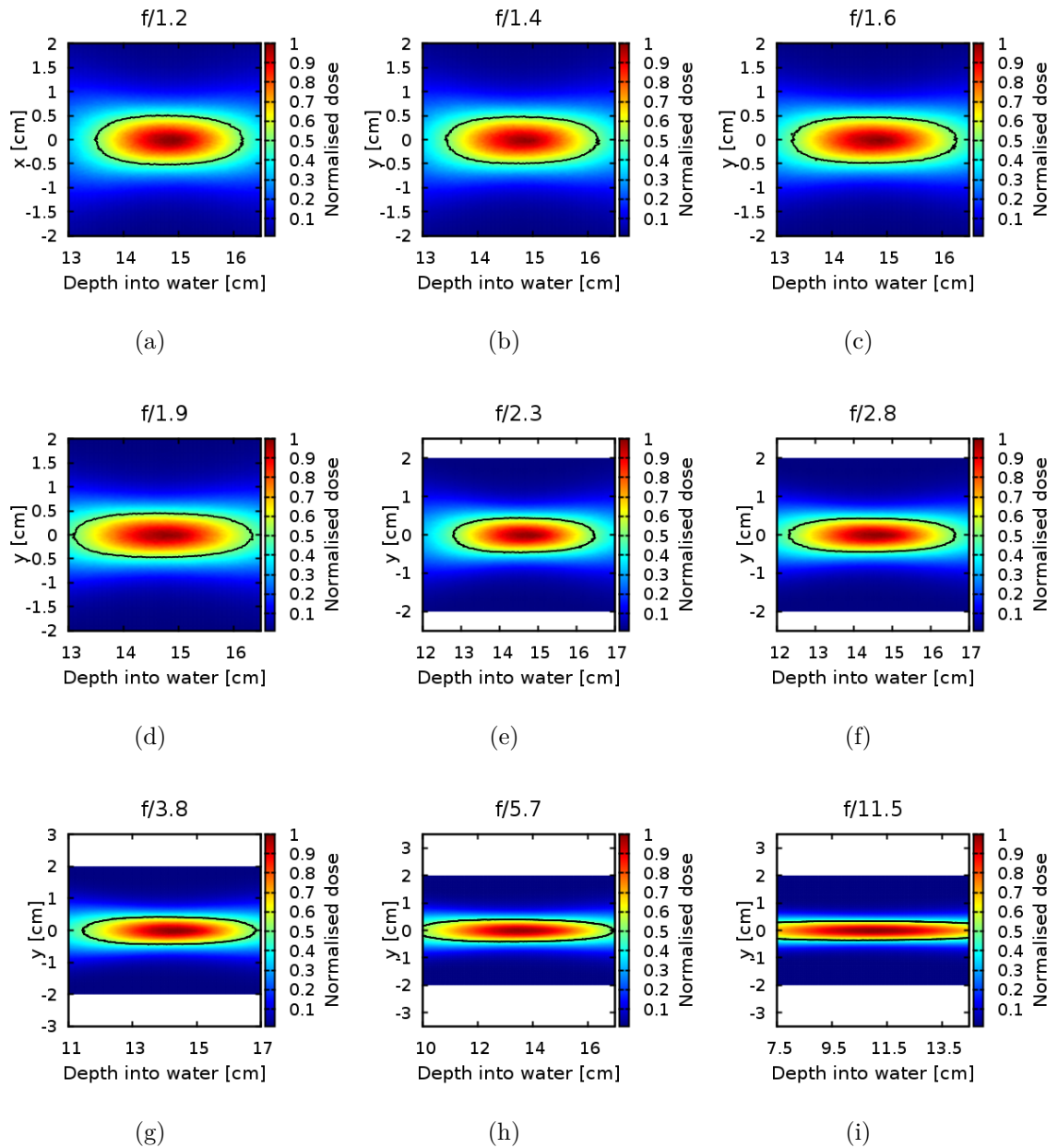
Figure 4.7: Samples of magnified dose profiles at the focus for 200 MeV focused at a depth of 15 cm for $f/1.2 - f/11.5$ (a-i). The contour (black line) shows the iso-dose at half-maximum.
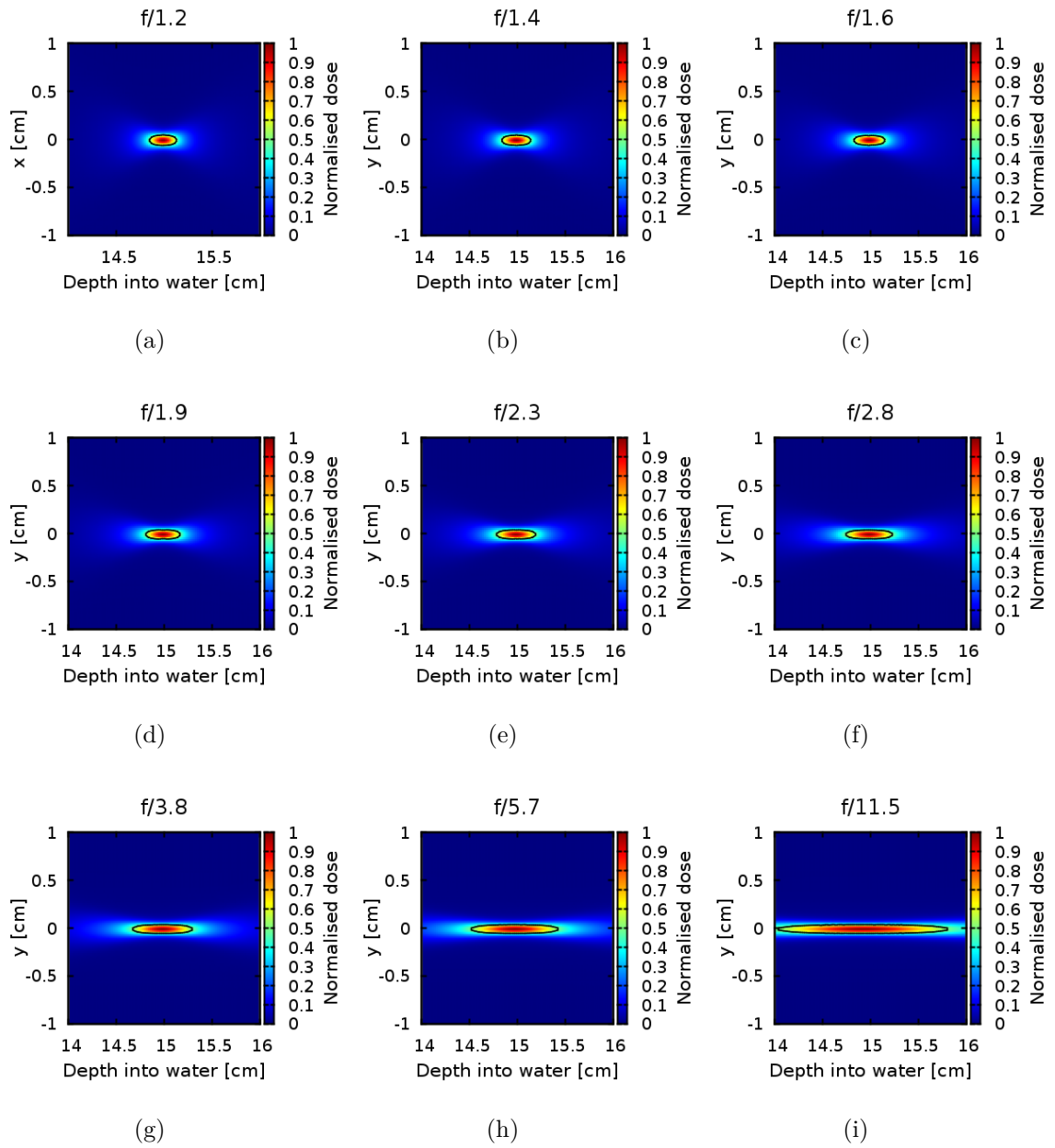
Figure 4.8: Samples of magnified dose profiles at the focus for 2 GeV focused at a depth of 15 cm for $f/1.2 - f/11.5$ (a-i). The contour (black line) shows the iso-dose at half-maximum.

The shape of the *volumetric element* evolves from almost perfectly round ($f/1.2$) to an ellipsoidal ($f/11.5$) shape. The transverse and longitudinal sizes were calculated by fitting Gaussian and Cauchy-Lorentz functions, respectively. The longitudinal positions of the dose peak, FWHM in longitudinal (FWHM_z) and transverse (FWHM_x) directions are summarised in Table 4.2. $\text{FWHM}_x/\text{FWHM}_z$ ratios for the selected *f-numbers* were in the range $0.1 - 0.8$ for 200 MeV and 0.08-1 for 2 GeV, respectively, where values close to 1 indicate near-spherical shape. The FWHM_z increases more rapidly than FWHM_x for both electron energies. Because of reduced scattering, 2 GeV beams produced the smallest and most symmetrical shapes, with radii down to 0.3 cm. For 200 MeV, the transverse size was $0.6 - 1.0$ cm for the chosen *f-numbers*. The area of 95% isodose (clinically acceptable dose heterogeneity [181]) corresponds to 4% of the area of 50% isodose for 200 MeV energy, and 9% for 2 GeV, which indicates that the dose gradient is sharper for GeV, providing better protection of adjacent tissue. The beam energy and the *f-number* can both be adjusted to optimally match the 95% isodose area to the tumour shape.

Total doses (D_{tot}) integrated over the phantom volume and normalised to a 2 Gy peak dose (D_{max}), modelling a typical radiotherapy fraction, are presented in Table 4.3. For all focused beams the total dose increases with the beam size at the phantom entrance, however for f/∞ which has the beam size around 6 times smaller than that for $f/1.2$ the total dose is the highest. The change of the total dose with *f-number* is more prominent for lower electron energies. It decreases by $77.8 - 84.9\%$ for 200 MeV and $97.2 - 97.5\%$ for 2 GeV.

Tables 4.4 and 4.5 summarise the maximum and integrated surface ($\text{D}_{surf,max}$, $\text{D}_{surf,int}$) and exit ($\text{D}_{exit,max}$, $\text{D}_{exit,int}$) doses normalised to a 2 Gy peak dose (D_{max}) for all *f-numbers* and collimated beam. For strongly focused beams ($f/1.2 - f/2.8$) with 200 MeV and 2 GeV energy $\text{D}_{surf,max}$ is reduced by $40 - 211$ and $250 - 1800$ times, compared to f/∞, respectively. For both electron beams $\text{D}_{exit,max}$ decreases from 20 to 54 for 200 MeV and from 230 to 1100 for 2 GeV compared to f/∞. Entrance and exit doses obtained for 2 GeV energies are smaller than for 200 MeV for all *f-numbers* because the 2 Gy target dose can be delivered by a lower charge electron beam.

Table 4.3: Total doses for 200 MeV and 2 GeV electron beams focused at 15 cm (in vacuum) from the entrance of the water phantom for $f/11.5 - f/1.2$. The doses are normalised to a single fraction of 2 Gy delivered in the peak (D_{max}).

f-no.	200 MeV	2 GeV
	$\mathbf{D}_{tot}$	$\mathbf{D}_{tot}$
	(Gy)	(Gy)
1.2	108.55	9.53
1.4	99.78	9.18
1.6	92.07	8.89
1.9	85.02	8.65
2.3	79.18	8.47
2.8	73.68	8.34
3.8	68.59	8.25
5.7	61.35	8.18
11.5	44.46	8.15
∞	488.24	340.37

Table 4.4: Surface doses, integral ($D_{surf,int}$) and maximum ($D_{surf,max}$), for 200 MeV and 2 GeV electron beams focused at 15 cm (in vacuum) from the entrance of the water phantom for $f/11.5 - f/1.2$. The doses are normalised to a single fraction of 2 Gy delivered in the peak (D_{max}).

f-no.	200 MeV		2 GeV	
	$\mathbf{D}_{surf,max}$	$\mathbf{D}_{surf,int}$	$\mathbf{D}_{surf,max}$	$\mathbf{D}_{surf,int}$
	(Gy)	(Gy)	(Gy)	(Gy)
1.2	0.01	0.38	0.00	0.02
1.4	0.01	0.36	0.00	0.02
1.6	0.01	0.34	0.00	0.02
1.9	0.02	0.31	0.00	0.02
2.3	0.03	0.29	0.00	0.02
2.8	0.04	0.27	0.00	0.02
3.8	0.07	0.25	0.01	0.02
5.7	0.14	0.22	0.01	0.02
11.5	0.40	0.16	0.05	0.02
∞	1.67	1.80	0.85	0.91

Figure 4.9 shows cross-sectional dose integrated over a $30 \times 30 \times 0.15$ cm^3 slice at the surface, exit and 15 cm depth for $f/1.2$ and $f/11.5$ and normalised to 2 Gy target dose for 200 MeV and 2 GeV energies. Surface and exit dose in the slice had similar profile and value for 200 MeV and $f/1.2$, whereas for 2 GeV the surface dose is 7 times

Table 4.5: Exit doses, integral ($D_{exit,int}$) and maximum ($D_{exit,max}$), for 200 MeV and 2 GeV electron beams focused at 15 cm from the entrance of the water phantom for $f/11.5 - f/1.2$. The doses are normalised to a single fraction of 2 Gy delivered in the peak (D_{max}).

f-no.	200 MeV		2 GeV	
	$\mathbf{D}_{exit,max}$ (Gy)	$\mathbf{D}_{exit,int}$ (Gy)	$\mathbf{D}_{exit,max}$ (Gy)	$\mathbf{D}_{exit,int}$ (Gy)
1.2	0.02	0.49	0.00	0.07
1.4	0.01	0.47	0.00	0.07
1.6	0.02	0.45	0.00	0.07
1.9	0.03	0.43	0.00	0.07
2.3	0.03	0.40	0.01	0.07
2.8	0.38	8.34	0.01	0.06
3.8	0.06	0.35	0.02	0.06
5.7	0.09	0.32	0.03	0.06
11.5	0.11	0.23	0.11	0.06
∞	0.86	2.53	1.98	2.62

lower than the exit dose. For $f/11.5$ and 200 MeV the peak dose at the surface slice is almost as high as the peak dose, whereas for $f/1.2$ it is more than 10 times lower. The peak dose in the slice at 15 cm for 2 GeV is two orders of magnitude higher than at the surface and more than one order of magnitude higher than at the exit.
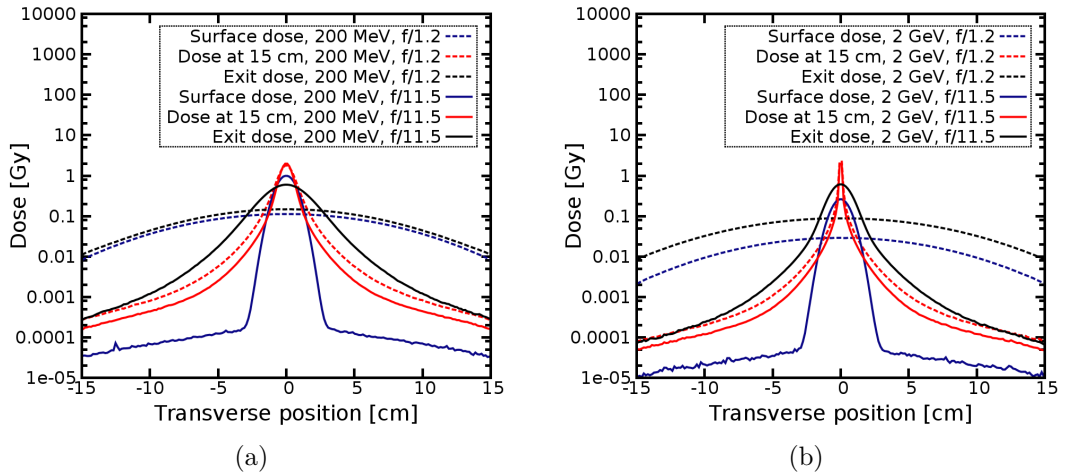
Figure 4.9: Lateral dose profiles at the surface, 15 cm depth and exit of the phantom normalised to 2 Gy target dose for 200 MeV (a) and 2 GeV (c) focused with $f/1.2$ and $f/11.5$.

4.2.2   Contribution of secondary radiation

The interaction of electrons with water through ionisation, Compton scattering and pair production, which are discussed in chapter 3, results in the production of secondary particles with different radiobiological effectiveness. Electrons slowing down in the Coulomb field of atomic nuclei produce bremsstrahlung photons, which has the highest yield of all the secondary radiation. These secondary photons can then produce additional particles, depending on their energy. Above 1.02 MeV, photons can interact with the Coulomb field of the nuclei and create electron-positron pairs, while at a few MeV they also trigger nuclear reactions, which results in the production of neutrons. The energy threshold for photo-nuclear reactions is about $10 - 19$ MeV for low-Z materials (up to $Z = 20$, such as H, C, N and O) and $4 - 6$ MeV for high-Z materials (above $Z = 20$, such as Ca). Photons with energies above 211 MeV can produce muon pairs, a process similar to electron-positron pair-production, but with a cross-section about 5 orders of magnitude smaller, because of the larger mass of muons. The mechanism of dose deposition by VHEEs studied includes the contribution of all secondary particles.

The energy spectra of electrons, photons, positrons and neutrons are obtained using USRBDX cards, which calculate the fluence double differential in energy, based on the number of particles crossing the boundary between the medium and the defined detector area. The FLUKA physics settings for electrons, photons and positrons are explained in the context of GeV beams, where additional cards are necessary, which is described later in this section. The $0.01 \times 30 \times 30$ cm^3 rectangular plain detectors were placed orthogonal to the propagation axis at depths of 0, 3.5, 9.5, 15, 20.5, 26.5 and 30 cm from the entrance of the water phantom. The fluence is calculated as the sum of particle tracks within a given detector volume, assigned to the USRBIN card, divided by this volume. The USRBDX cards are set to score only outgoing particles, providing a linear binning in energy and solid angle, with 444 energy bins and one angular bin.
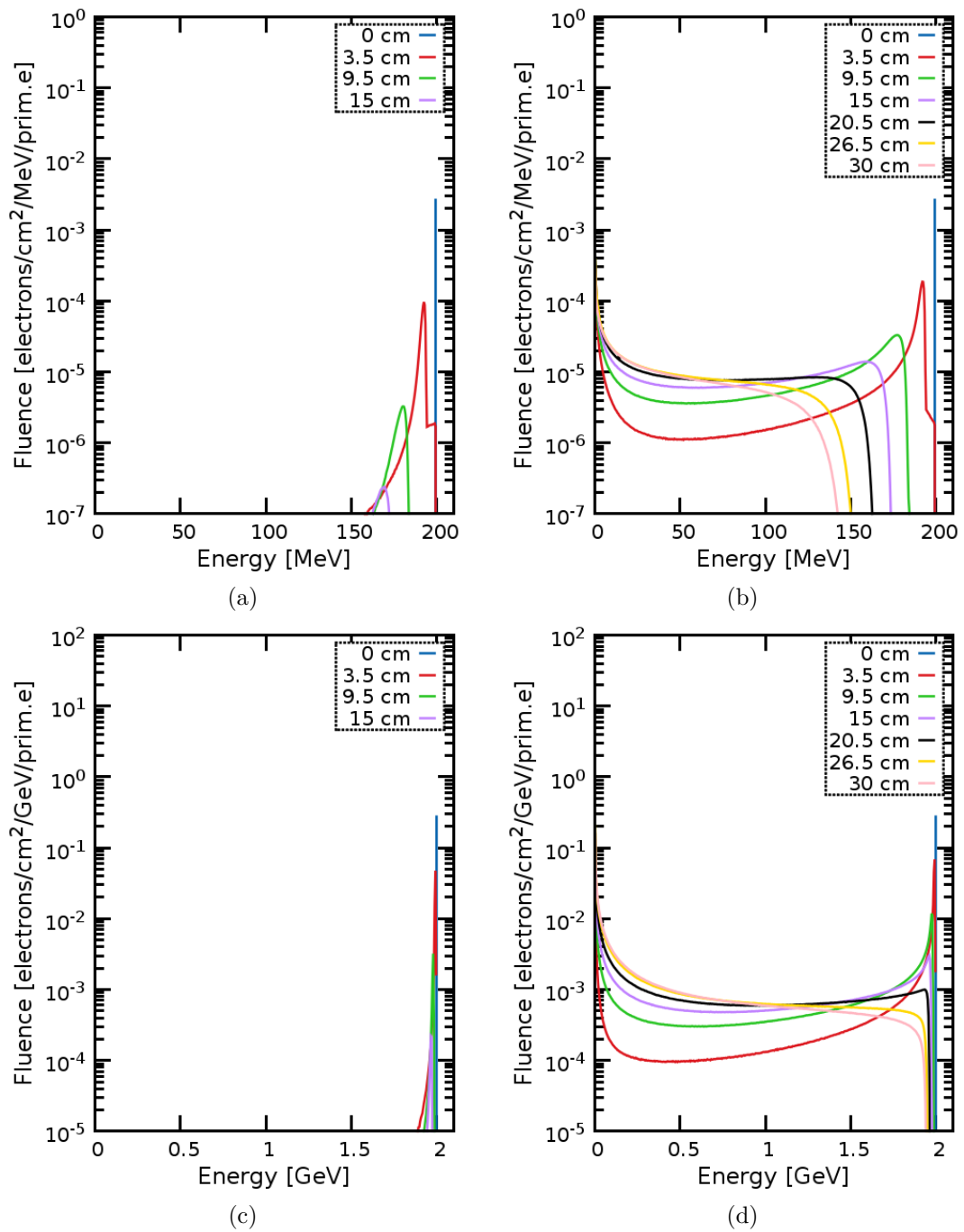
Figure 4.10: Energy spectra of electrons at selected depths in the phantom and generated by an electron beam focused at 15 cm with $f/1.2$. Fluence of primary beam particles for 200 MeV (a) and 2 GeV (c) initial electron energies. Fluence of primary beam particles and secondary electrons for 200 MeV (b) and 2 GeV (d) initial electron energies.
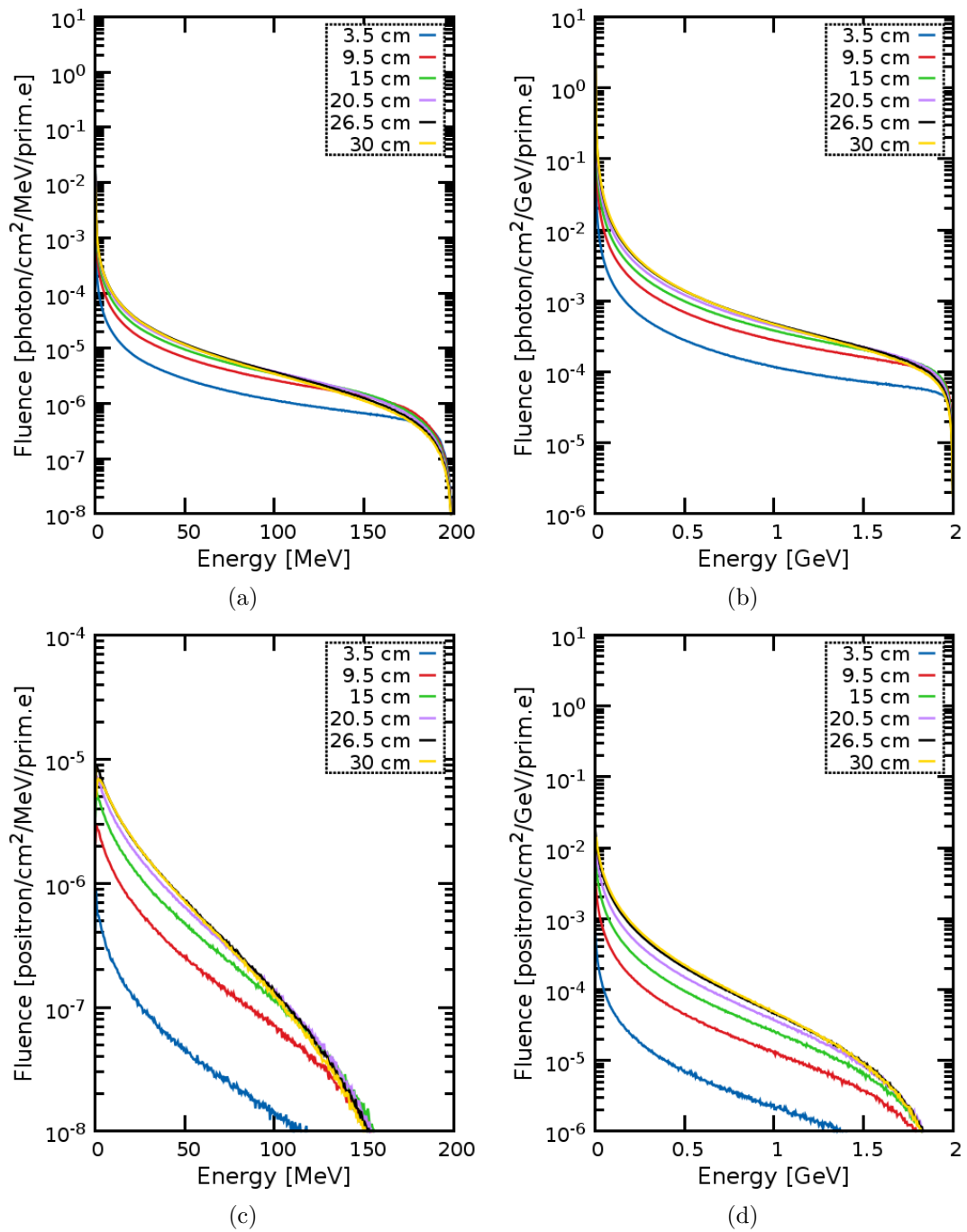
Figure 4.11: Energy spectra of photons and positrons at selected depths in the phantom and generated by an electron beam focused at 15 cm with $f/1.2$. Photon fluence for 200 MeV (a) and 2 GeV (b) initial electron energies. Positron fluence for 200 MeV (c) and 2 GeV (d) initial electron energies.

Figure 4.10 shows the energy spectra of all electrons (primary and secondary), and separately for beam particles. The beam propagates in vacuum before entering water, therefore the energy spectrum at the entrance of the phantom (0 cm) corresponds to the energy distribution at the defined monoenergetic source. At each depth the spectrum becomes wider as a result of electron multiple collisions with the water molecules, and subsequent emission of bremsstrahlung. The spectrum shifts towards low energies and the number of electrons becomes nearly constant in each energy bin for depths 9.5 – 20.5 cm except for energies of few MeV where the yield of secondary electrons reaches a maximum.

Figure 4.11 shows spectra of photons and positrons produced by 200 MeV and 2 GeV electron beams at various depths in the water phantom for $f/1.2$. The photon fluence decreases monotonically with the energy, forming a broad spectrum that extends to the maximum electron energy (bremsstrahlung endpoint) at each depth. The fraction of photons for the detectors are similar for both electron energies. However, the total yield for 2 GeV is two orders of magnitude higher at each depth.
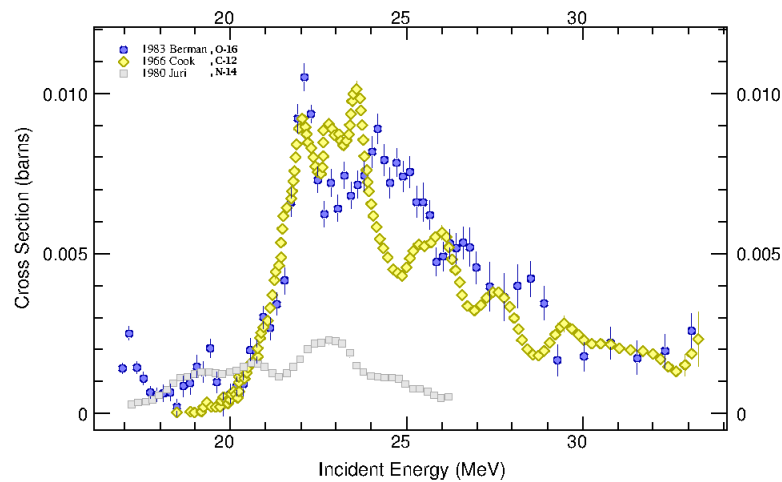
Figure 4.12: Photon cross-section for (γ, n) and (γ, 2n) reactions with tissue components ^{12}C, ^{16}O, and ^{14}N [182].

Figures 4.11c and 4.11d show the positron fluence for 200 MeV and 2 GeV for $f/1.2$. Beyond 3.5 cm the maximum energy of produced positrons is around 150 MeV for 200

MeV, and 1.75 GeV for 2 GeV. The number of positrons at depths larger than 15 cm is constant for both electron energies and becomes nearly linear as a function of energy. The yield of positrons is around two orders of magnitude lower than for photons, and the highest number of positrons is found in the low-energy range. These low-energy positrons can collide with electrons and annihilate, leading to the emission of Auger electrons, characteristic X-rays and γ-ray photons.
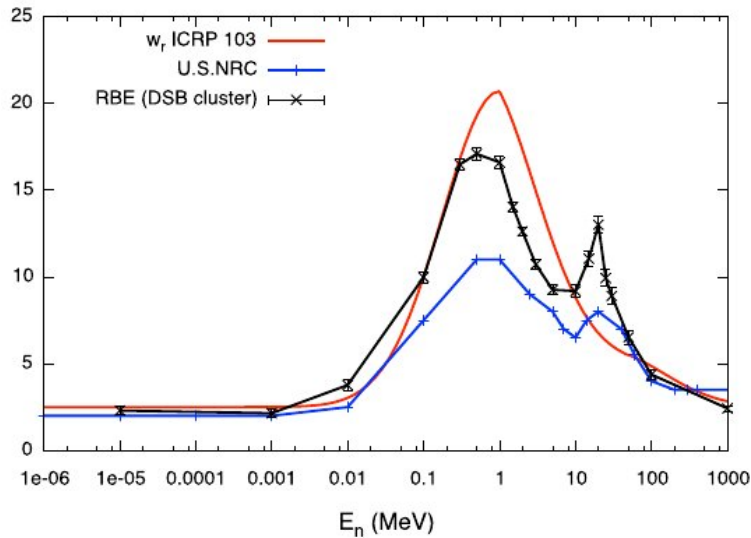
Figure 4.13: RBE as a function of neutron energy obtained using PARTRAC DNA double-strand break cluster induction model (black line) [183], ICRP 103 (red line) [184] and U.S. NRC (blue line) [185] standards for weighting factors.

The energy determines the type of interaction between photons and matter. Of particular interest are photo-nuclear reactions, which can produce neutrons. Figure 4.14 summarises the number of photons in the energy ranges of 10 keV – 20 MeV, 20 – 30 MeV and > 30 MeV and neutrons with energies < 0.4 eV and 0.1 – 10 MeV, both as a function of depth in water. Calculations are performed for electron beam energies of 200 MeV and 2 GeV, with a statistical uncertainty below 4%. In the energy range 20 – 30 MeV photons have high cross-section for neutron production for the most common chemical elements in tissue such as ^{16}O, ^{12}C (Figure 4.12). Two energy groups defined in Figure 4.14b represents neutrons with the lowest and highest RBE (Figure 4.13). In FLUKA, energy group structures includes 42 photon (10^{-6} – 10^{-5} GeV) and 260

neutron groups (2×10^{-14} – 0.02 GeV) with a maximum energy of the low-energy cross-section neutrons. The groups are defined by the scattering transfer probabilities. For each chosen depth, one USRBDX card is used to calculate the yield of photons. However, due to much larger number of neutron groups, the linear binning is set with USRBDX in two steps, for the two energy ranges, < 20 MeV (44 energy bins) and > 20 MeV (400 energy bins). The additional PHOTONUCLEAR card is activated to include electro-nuclear interactions at all electron energies. Physical processes characteristic for neutron production, such as coalescence and evaporation, are activated in the FLUKA input file by relevant PHYSICS cards. The LOW-NEUTRON card is included to activate a multi-group algorithm for low energy neutrons for which the transport mechanism is assumed to be continuous. The energy thresholds for specific energy groups are defined in the FLUKA manual [178].
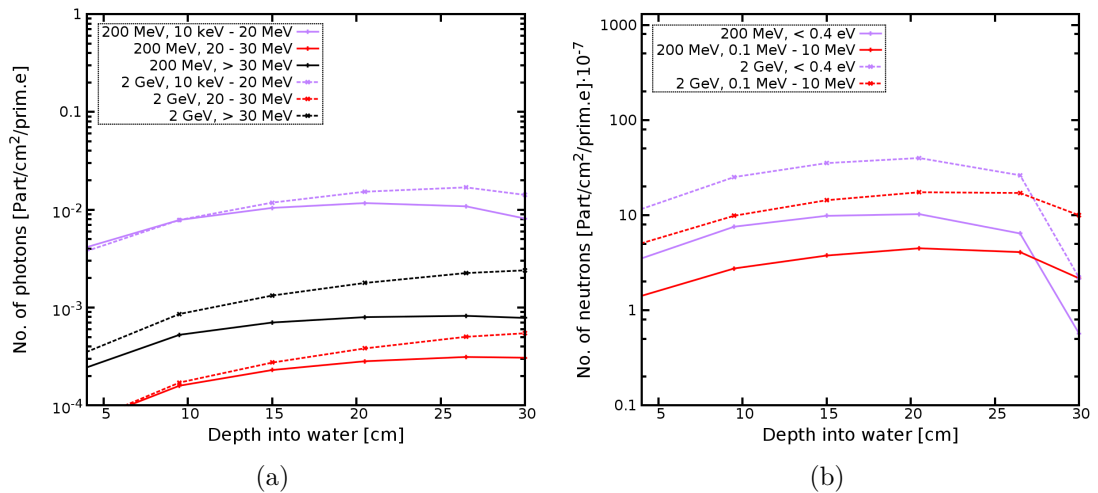
Figure 4.14: Photon and neutron yield integrated on the surface of the thin slice of the phantom and normalised to its area. Number of photons (a) and neutrons (b) as a function of depth for 200 MeV and 2 GeV electron beams focused at 15 cm from the entrance of the water phantom for $f/1.2$.

Figure 4.14a shows the photon flux at different depths in water. The highest number of photons is found in the low energy range, below 20 MeV, where the main mechanisms of interaction with low-Z materials are ionisation, Compton scattering and pair-production. Photons in the 20 – 30 MeV range, on the other hand, have a high cross-section for (γ, n) and (γ, 2n) reactions with tissue components such as ^{12}C, ^{16}O, and

^{16}N as shown in Figure 4.12. However, because of the small photon flux in this energy range, only a few neutrons are produced.

Photons and neutrons are indirectly ionising forms of radiation. They undergo multiple nuclear reactions and become a source of mixed field of directly ionising charged species. Neutrons are the most radiobiologicaly interesting particles. Their nuclear reaction cross-sections strongly depend on energy, and therefore, energy lost by neutrons through collisions can results in the production of different secondary particles across the target. The neutron yield at different depths in water is shown in Figure 4.14b for two energy ranges. The yield of neutrons with energy lower than 0.4 eV, referred as epithermal neutrons, is $\sim 20 \cdot 10^{-6}$ neutrons/cm^2/prim.e for 200 MeV and $75 \cdot 10^{-6}$ neutrons/cm^2/prim.e for 2 GeV. In this energy range neutrons have limited biological effect. Above 0.4 eV, approximately 10^{-6} neutrons/cm^2/prim.e are obtained for 200 MeV for $f/1.2$ at a depth of $15 - 20$ cm. The corresponding neutron yield for a 2 GeV beam is an order of magnitude higher. Table 4.6 includes a summary of neutron flux integrated over the cross-sectional area of the water phantom at different depths. The highest concentration of neutrons is at depth slightly shifted towards the exit w.r.t. the position of the *volumetric element* for both electron energies. Almost 50 % are localised at depth of $15 - 20$ cm for 200 MeV and $20 - 25$ cm for 2 GeV. From around the middle of this depth range, towards the exit of the phantom, the number of neutrons decreases, more rapid for 200 MeV than 2 GeV. Figure 4.15 shows the peak of neutron spectra at 9.5, 15 and 20.5 cm depths of the highest neutron yield. Although the spectra cover wide range of energies, a few eV is not enough for neutrons to travel far. At the entrance and exit, the number of neutrons is found to be negligible. At a depth of $9.5 - 20.5$ cm, the number of neutrons in each energy bin is nearly constant with depth for both electron energies.

The production of muon pairs by high-energy photons is investigated for a 2 GeV beam (200 MeV is below the threshold for muon production). The transport of all light and heavy ions is activated by the IONTRANS card. The DELTARAY card is included in order to set the kinetic energy for δ-ray production to 100 keV. The default step size of muons is changed to 0.02 (2% of the initial kinetic energy), using the FLUKAFIX card.

The energy transport cut-off of muons and anti-muons is set to 10 keV using the card PART-THRes. The additional PHOTONUClear card with the option MUMUPAIR sets interaction length biasing factor to 10^{-4} for better statistics of muon pair production by photons. The PAIRBREM card with the option MUPHOTONs controls the mechanism of muon interaction by setting the kinetic energy threshold for bremsstrahlung and pair production to 10 keV. Simulations show that the number of muons produced for 2 GeV electron beam energy is two orders of magnitude lower than the number of neutrons.
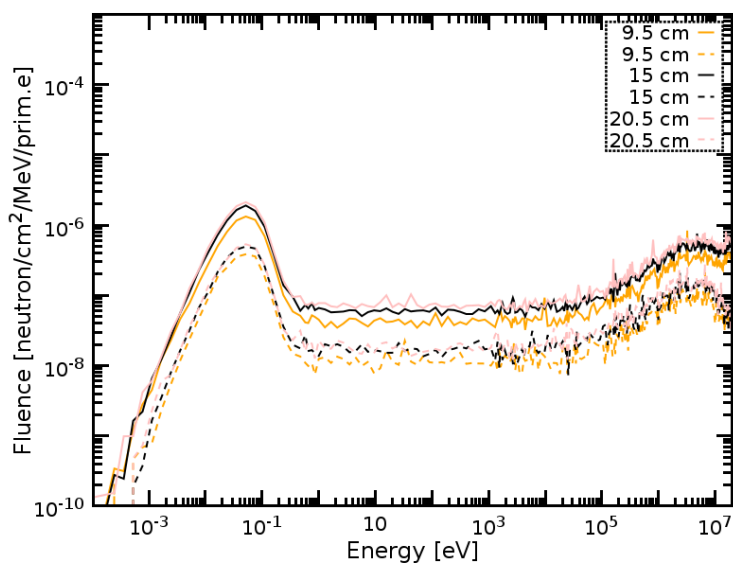
Figure 4.15: Energy spectra of neutrons at selected depths in the phantom generated by 200 MeV (dash line) and 2 GeV (solid line) electron beams focused at 15 cm with f/1.2.

Photons

In contrast to charge particles, photons deposit dose indirectly through interactions of induced secondary radiation [186]. The photon dose, using FLUKA, is obtained through implementation of custom user routines, contrarily to the other types of secondary particles, for which the dose is simply scored with a USRBIN detector filtered by an AUXSCORE card activated with the defined particle species. The FLUKA user routines, stupre.f and comscw.f are used to include contribution of all secondary particles produced by photons. The particles whose parents are photons are selected in the

Table 4.6: Neutron yield integrated over the cross-sectional area of the water phantom at different depths for 200 MeV and 2 GeV electron beams focused at $f/1.2$.

Depth (cm)	200 MeV		2 GeV	
	Neutrons yield $\times\ 10^{-7}$ (n/cm^2/prim.e.)	Error (%)	Neutrons yield $\times\ 10^{-7}$ (n/cm^2/prim.e.)	Error (%)
0.0	0.0	0.0	0.0	0.0
3.5	1.3	1.6	4.8	1.8
9.5	2.8	1.3	9.9	1.2
15	3.8	1.3	14.4	0.9
20.5	4.5	1.6	17.4	1.4
26.5	4.1	1.1	17.1	0.7
30	2.2	1.4	10.0	1.4

stupre.f routine which is called when secondary electrons, positrons and photons are to be produced. In the comscw.f routine energy deposition scoring is tailored to calculate dose only from these particles. The latter must be activated through the USERWEIG card (with WHAT(6) > 0) in the FLUKA input file. The dose from particles that are selected in the stupre.f routine is scored as a USRBIN output. Both routines must be linked with the input file to generate a FLUKA executable. A scoring volume with the resolution of 0.075 cm in y and z, and 0.3 cm i x direction is used to simulate the 2D dose distribution in the water phantom.

Figure 4.16 shows 2D distribution of the total and bremsstrahlung dose integrated over a 0.3 cm thin slice along the central beam axis in water for 200 MeV and 2 GeV with $f/1.2$. The cross-section for bremsstrahlung production decreases with increasing electron energy. At shallow depths, where the electron energy is close to the nominal energy, the dose from bremsstrahlung is almost negligible. The depth threshold for dose deposition by bremsstrahlung increases with initial electron energy. Most of the bremsstrahlung photons produced directly by VHEEs follow the initial electron trajectory [57] and consequently accumulate a maximum dose at the depth of the *volumetric element.* However, a large number of photons are produced at an angle slightly larger than the electron angle, and they undergo scattering. This explains why the *volumetric element* including only photon dose is larger than that of the total dose. Photons contribute to the total dose more at the exit than the entrance of the phantom. The

ratios of total and photon dose are similar for both electron energies. Approximately 27% of the total dose arises from particles produced by photon interactions.
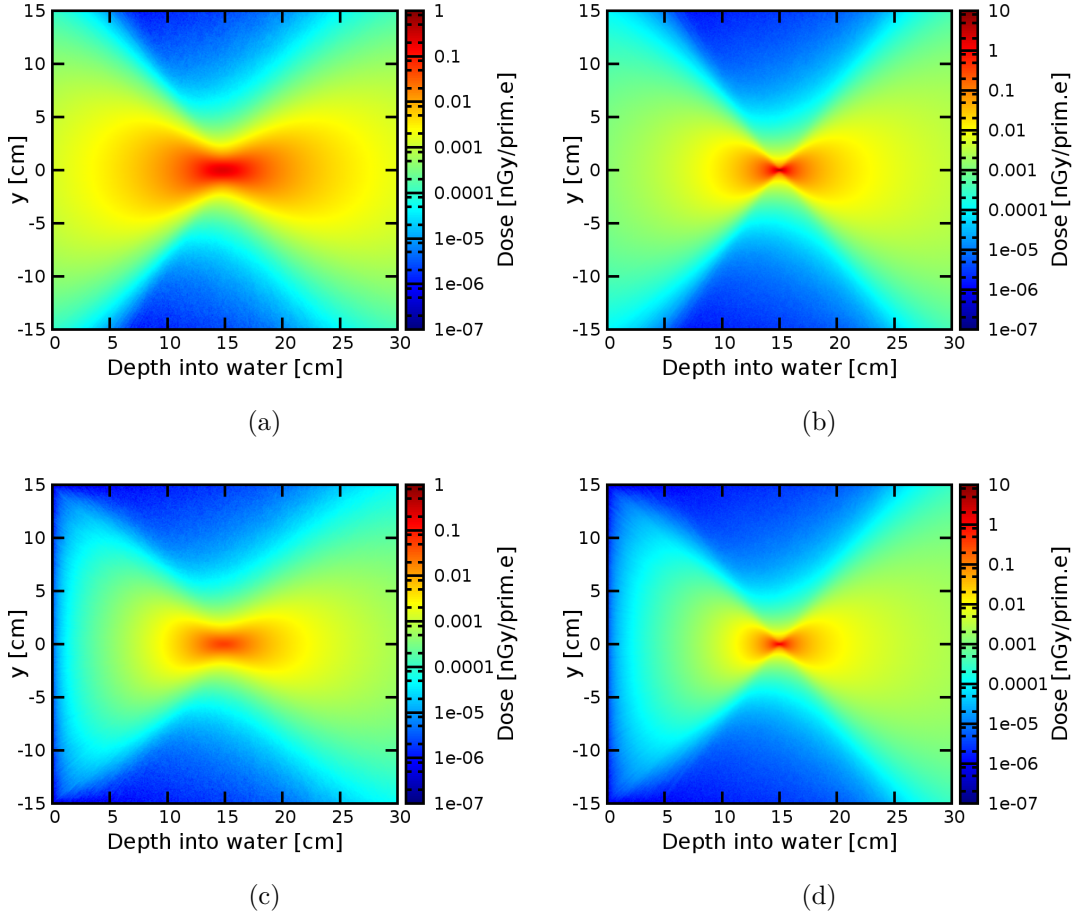
Figure 4.16: 2D distribution of total (a, b) and bremsstrahlung (c, d) dose in water for 200 MeV (a, c) and 2 GeV (b, d) electron beams focused with $f/1.2$.

Positrons

Figures 4.17a and 4.17b show the total dose (including contribution of all secondary radiation) deposited on the central beam axis (on-axis dose) across the phantom and in the surrounding phantom volume (off-axis dose) for 200 MeV and 2 GeV beams normalised to a 2 Gy peak dose, respectively. The FLUKA physics settings for positrons is described in subsection 4.2.2. Figures 4.17c and 4.17d show the corresponding plots of dose deposited by positrons. The on-axis dose is calculated in a longitudinal $0.3 \times$

0.3×30 cm^3 slice at the centre of the phantom. The off-axis dose corresponds to the dose integrated over the phantom volume outside of this central slice. A small drop in the off-axis depth-dose profiles for 2 GeV and both *f-numbers* results from the small beam size at the focus, which leads to dose deposition mostly on-axis. The total and positron dose profiles are similar, except for a slower build-up at the phantom surface. The total and positron doses are slightly higher off the central axis than on the central axis in the regions near the surface and exit of the phantom for $f/1.2$ and both electron energies. Table 4.7 summarises the contribution of positron dose to the total dose on-axis and off-axis for 200 MeV and 2 GeV focused with $f/1.2$. For 200 MeV and $f/1.2$ the contribution of both off-axis and on-axis positron doses is 3.8%, however for $f/11.5$, positrons contribute more to the dose off the central axis. Significant difference between contribution of positron dose off-axis and on-axis for the selected beam geometries is obtained for a GeV beam. The contribution to the dose off-axis is 1.3 times higher than on-axis for $f/1.2$ whereas it is 78 times lower for $f/11.2$. The contribution of positron dose is generally higher for $f/1.2$ than $f/11.5$ for both electron energies.

Table 4.7: Percentage contribution of positron doses to the total dose for 200 MeV and 2 GeV focused with $f/1.2$ and $f/11.5$.

f-no.	200 MeV		2 GeV	
	off-axis (%)	on-axis (%)	off-axis (%)	on-axis (%)
1.2	3.8	3.8	10.8	8.6
11.5	3.0	2.7	0.1	7.8

Neutrons and muons

The FLUKA physics settings for muons and neutrons is described in subsection 4.2.2. Muons were only produced for GeV beams and their contributions to the total dose was about 10^{-8} Gy for a 2 Gy target dose while neutrons deposited about 10^{-12} Gy for both energies and the same target dose.
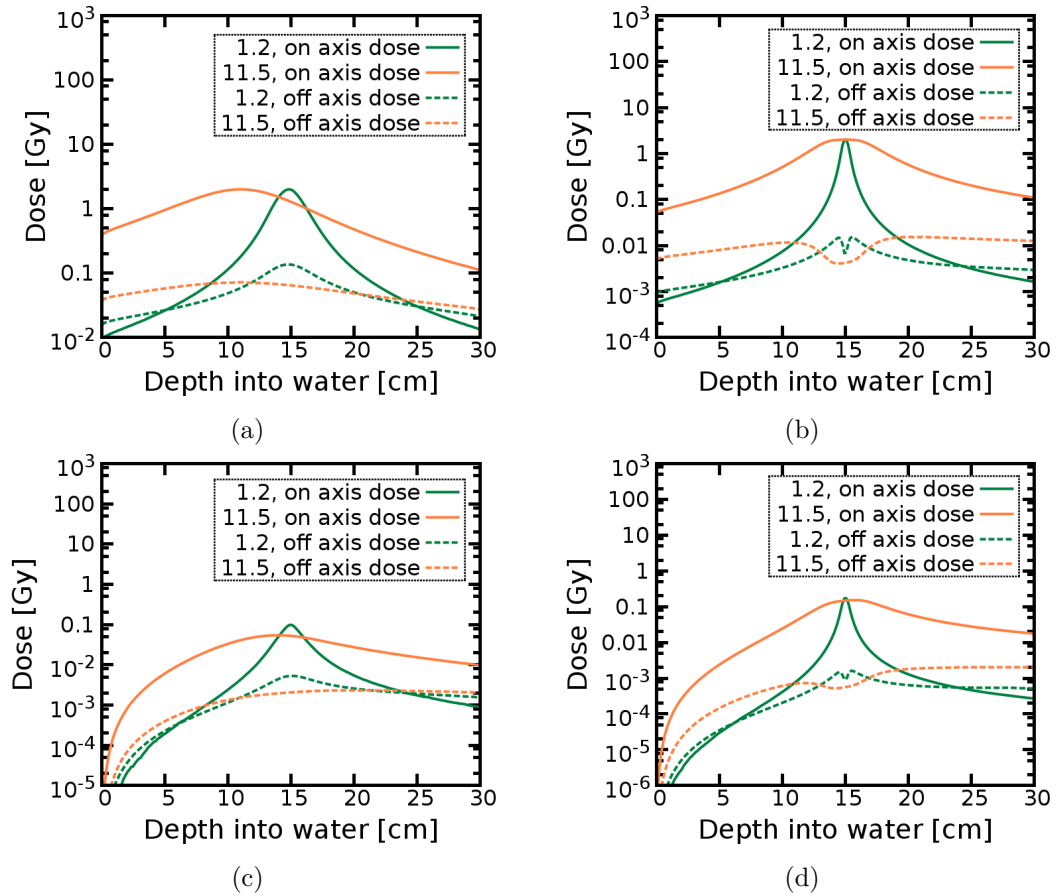
Figure 4.17: On-axis and off-axis dose as a function of depth for 200 MeV and 2 GeV electron beams focused at 15 cm from the entrance of the water phantom (in vacuum) for $f/1.2$ and $f/11.5$. Plots show the total (a, b) and positron (c, d) dose normalised to a 2 Gy peak dose for 200 MeV and 2 GeV electron energies, respectively.

Induced radioactivity

The fraction of total dose within the patient is not deposited directly during irradiation. This is because radiation travels through materials with complex composition and density higher than that of water. For example, bones and muscles primarily consist of hydrogen, oxygen and salts of calcium, phosphate, magnesium and fluorine, which become activated during irradiation. The FLUKA setup, shown in Figure 4.18, is used to simulate the activity induced by focused VHEEs and UHEEs, and proton beams for comparison. Simulations have been performed with layers of bone structure and skeletal muscle embedded in water. The phantom is a $30 \times 30 \times 30$ cm^2 cube made

89

of alternately inserted two layers of skeletal muscle and two layers of compact bone separate by water. The tissue layers are 3 cm thick each and are placed at 5, 8, 16 and 19 cm depth from the entrance. The muscle and bone compounds, specified in ICRU Report 37 [143], have a density of 1.04 g/cm^3 and 1.85 g/cm^3, respectively. The IR-RPROFI card is used to define dose rate of 2 Gy/s. The beam intensity was set to 9.9×10^8/cm^2 for 200 MeV, 0.6×10^8/cm^2 for a 2 GeV electron beam and 0.5×10^8/cm^2 for a 147 MeV proton beam. The transport of heavy ions is included with the IONTRANS card (WHAT(1) = HEAVYION). The PEANUT model is activated at all energies to perform hadronic interactions at high-precision. The activity from the produced radioactive nuclides is calculated using RESNUCLEi cards with the DCYSCORE cards set to 1, 5, 10, 20, 45, 60 minutes and 24 hours. The dose from the radioactivity was estimated with the USRBIN card linked to the DCYSCORE cards for corresponding post-irradiation time intervals.

Results obtained for 200 MeV and 2 GeV electron beam energy show that radioactive isotopes such as ^{10}C, ^{11}Be, ^{16}N and ^{23}Ne are formed in the phantom within 1 minute after irradiation. However, because of the short half-life of these isotopes (the longest is $\sim$ 37 s) other radioactive forms are produced soon after. Also, within one minute after irradiation traceable amounts of common positron emitters such as ^{11}C, ^{13}N, ^{15}O are produced. Assuming delivery of 2 Gy of dose in one second, the total activity 1 minute after irradiation is about 240 Bq for 200 MeV and 600 Bq for 2 GeV, an order of magnitude lower than the total activity of naturally present radioactive isotope ^{40}K in the human body. After 1 hour the activity decreases to 5 Bq for 200 MeV and 9 Bq for 2 GeV. In 24 hours after irradiation with 2 GeV beam the activity level is lower than the background radiation under standard conditions. For 200 MeV, isotopes such as ^{24}Na, ^{42}K, ^{32}P can still be detected, but the total activity is reduced by more than three orders of magnitude. Higher energy beams produce more isotopes and a higher total activity in the first few minutes, but the activity decreases quickly and becomes negligible for both cases after 24 hours.
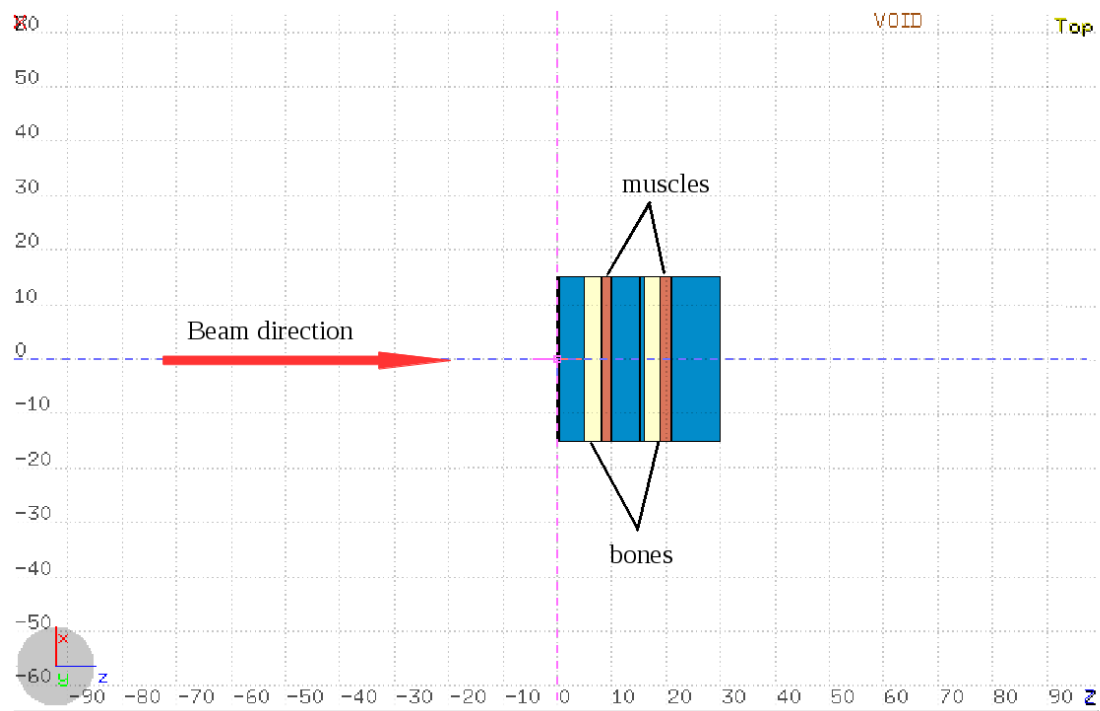
Figure 4.18: FLUKA setup for simulating induced activity in the water tank with samples of bone and muscles compounds.

The maximum dose deposited in the water phantom from the induced radioactive products is accumulated very precisely in the focal spot, however it is $5-6$ orders of magnitude lower than the target dose (2 Gy) after 1 min. Induced activity is a significant issue in proton therapy. Protons can directly trigger the nuclear reactions such as ^{16}O(p, pn)^{15}O, ^{14}N(p, 2p2n)^{11}C, ^{16}O(p, 3p3n)^{11}C within the body. The dose from induced activity after 1 minute estimated at depth of 15 cm for a 147 MeV proton beam is 5 and 2.5 times lower than for 200 MeV and 2 GeV, respectively while after 60 minutes it becomes approximately the same level as for 2 GeV beam. The dose from induced radioactivity is cumulated mainly in the bones and muscles and decreased by a factor of 20 and 4 from 1 minute to 1 hour after irradiation for 200 MeV and 2 GeV beams, respectively. Most of the post-irradiation activity is directly induced by bremsstrahlung and is confined within a limited region of space, because the nuclear cross-section is only a very small fraction of the total photon cross-section and photon penetration in matter is governed mainly by electromagnetic interactions.

Table 4.8: Maximum dose within 0.1 cm slice at 15 cm per 2 Gy at the target from the activity induced within $1 - 60$ min. after irradiation.

Time	Dose (μGy)		
(min.)	200 MeV electrons	2 GeV electrons	147 MeV protons
1	12.22	5.87	2.61
5	3.35	1.63	0.68
10	0.95	0.43	0.12
20	0.33	0.12	0.04
45	0.12	0.04	0.02
60	0.07	0.02	0.01

4.2.3   Distribution of linear energy transfer

Electron interactions with a matter result in modifications to their trajectories (direction straggling). For high energy particles, which penetrate a long distance into the material and undergo multiple interactions, the complete particle track cannot be easily predicted by Monte Carlo simulations. To a first approximation the energy deposition per particle, so called linear energy transfer (LET) [187, 188], is estimated as a sum of energy losses (dE) over a tiny portion of the particle track, which is considered a nearly straight line. Such localised energy transfer can be calculated by means of Monte Carlo simulations by limiting the energy transfer to secondary charged particles which are known as δ-rays. If an energy cut-off of δ-rays is imposed, the calculations will give a restricted LET [189] (L_Δ):

$$L_\Delta = \frac{dE_\Delta}{dl} \tag{4.4}$$

where dE_Δ is the energy lost by a charged particle due to electronic collisions, with the energy transfer below the threshold Δ, while traversing the distance dl. For monoenergetic beams, LET values are easily obtained from tables [190], but in the case of clinical beams analytical calculations have to be performed to obtain realistic predictions.

Determination algorithm to calculate the averaged LET

Two general methods for calculating the spatial distribution of LET in Monte Carlo simulations, the track-averaged (LET_t) and dose-averaged LET (LET_d), were proposed by Wilkens and Oelfke [191]. The formulas are based on the electronic stopping power (nuclear stopping power is neglected) and give unrestricted LET (the production of δ-rays is neglected):

$$LET_t(z) = \frac{\int_0^\infty S_{el}(E)\Phi(E,z)dE}{\int_0^\infty \Phi(E,z)dE} \tag{4.5}$$

$$LET_d(z) = \frac{\int_0^\infty S_{el}(E)D(E,z)dE}{\int_0^\infty D(E,z)dE} \tag{4.6}$$

where $S_{el}(E)$ is the electronic stopping power of primary charged particles with kinetic energy E, $D(E,z)$ is the dose from primary charged particles with kinetic energy E at location z, and $\Phi(E,z)$ is the particle fluence. High LET particles have a stronger biological effect than low LET particles as long as LET does not result in dose deposited in excess of that required to achieve a cell kill, which is often referred to as the overkill effect ($\sim 100 - 150$ keV/μ) [186].

Methods

The dose-averaged LET algorithm was used to simulate the 3D LET distribution in a water phantom for focused and collimated VHEEs. The dose term in equation 4.7 (D(E, z)) is estimated using the electronic stopping power (S_{el}) and fluence spectrum ($\Phi(E,z)$) based on the slowing down approximation, which is discussed in chapter 3:

$$D(E,z) = \frac{S_{el}(E)\Phi(E,z)}{\rho(z)}. \tag{4.7}$$

The dose-averaged LET is then calculated as:

$$LET_d(z) = \frac{\int_0^\infty S_{el}(E)D(E,z)dE}{\int_0^\infty D(E,z)dE} = \frac{\int_0^\infty S_{el}^2(E)\Phi(E,z)dE}{\int_0^\infty S_{el}(E)\Phi(E,z)dE}. \tag{4.8}$$

In FLUKA, the function GETLET and the fluscw.f routine are used to obtain the

dose-averaged LET (LET_d) values. The GETLET function calculates S_{el} based on tabulated LET values for unrestricted LET for the defined particle type, energy and material. Two USRBIN fluence cards are used to score the electron fluence (WHAT(2) = ELECTRONS) in a $30 \times 30 \times 30$ cm^3 water phantom. The stopping power values (S_{el} and S_{el}^2) obtained with the GETLET function are multiplied by the 3D fluence distributions from the USRBIN scoring volumes using the fluscw.f routine, which is activated by the USERWEIG card in the FLUKA input file. In order to obtain the LET_d in the unit of keV/μm the division of the results from both operations is performed offline using ad-hoc python script. The transport and production thresholds for δ-particles are set to 100 keV. The FLUKA output fluence values are estimated in 3D by using USRBIN card which provide options for binning intervals hence the phantom does not need to be voxelized.

Results

The calculated LET values for VHEEs agree well with the literature values for an electron within the energy range typical for the clinical electron beams (0.22 keV/μm). Figures 4.19 and Figure 4.20 show the 2D distribution of LET for 200 MeV and 2 GeV focused beams with $f/1.2$ and $f/11.5$ and collimated beam (f/∞). The LET distribution depends on the beam geometry. For the selected beam geometries and electron energies high LET particles are distributed far from the central beam axis. For small beam angles the lowest LET values are found around the beam channel. However, the LET within the beam channel is only slightly higher, and uniformly distributed up to a depth of the *volumetric element*, after which it starts to decrease. The total LET is peaked at 2.09 and widely distributed between $0.2 - 0.27$ keV/μm. In contrast, for $f/1.2$ the total LET is peaked at 2.09 and 2.12, it is uniform within the beam channel across the phantom and is lower than for $f/11.5$ within the beam channel. For 2 GeV the mean LET value was found to be slightly higher than for 200 MeV for focused and collimated beams.

(a)

(b)

(c)
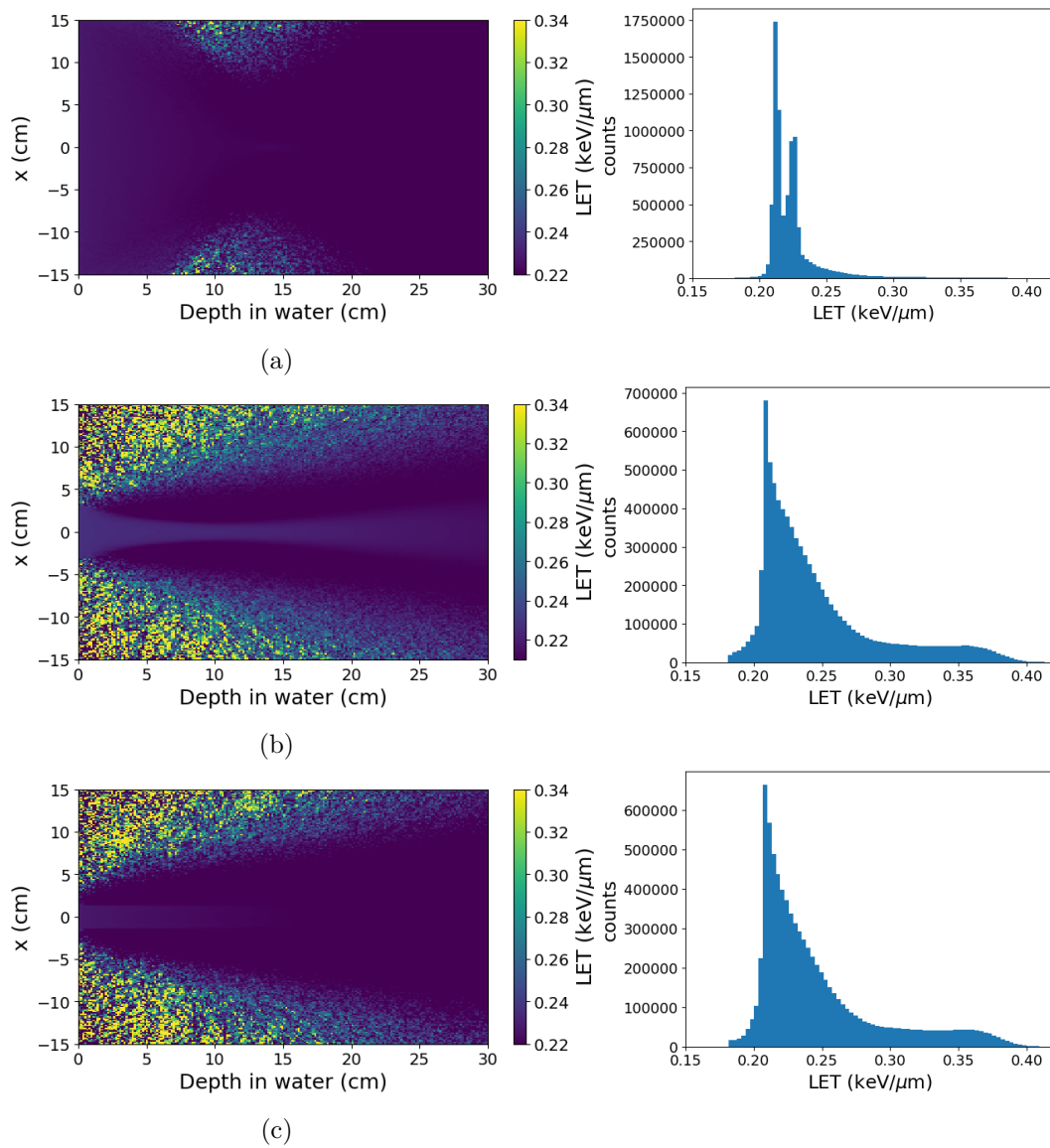
Figure 4.19: 2D LET distribution and 1D LET histograms simulated for 200 MeV beam focused with $f/1.2$ (a) and $f/11.5$ (b) and collimated (c).

(a)

(b)

(c)
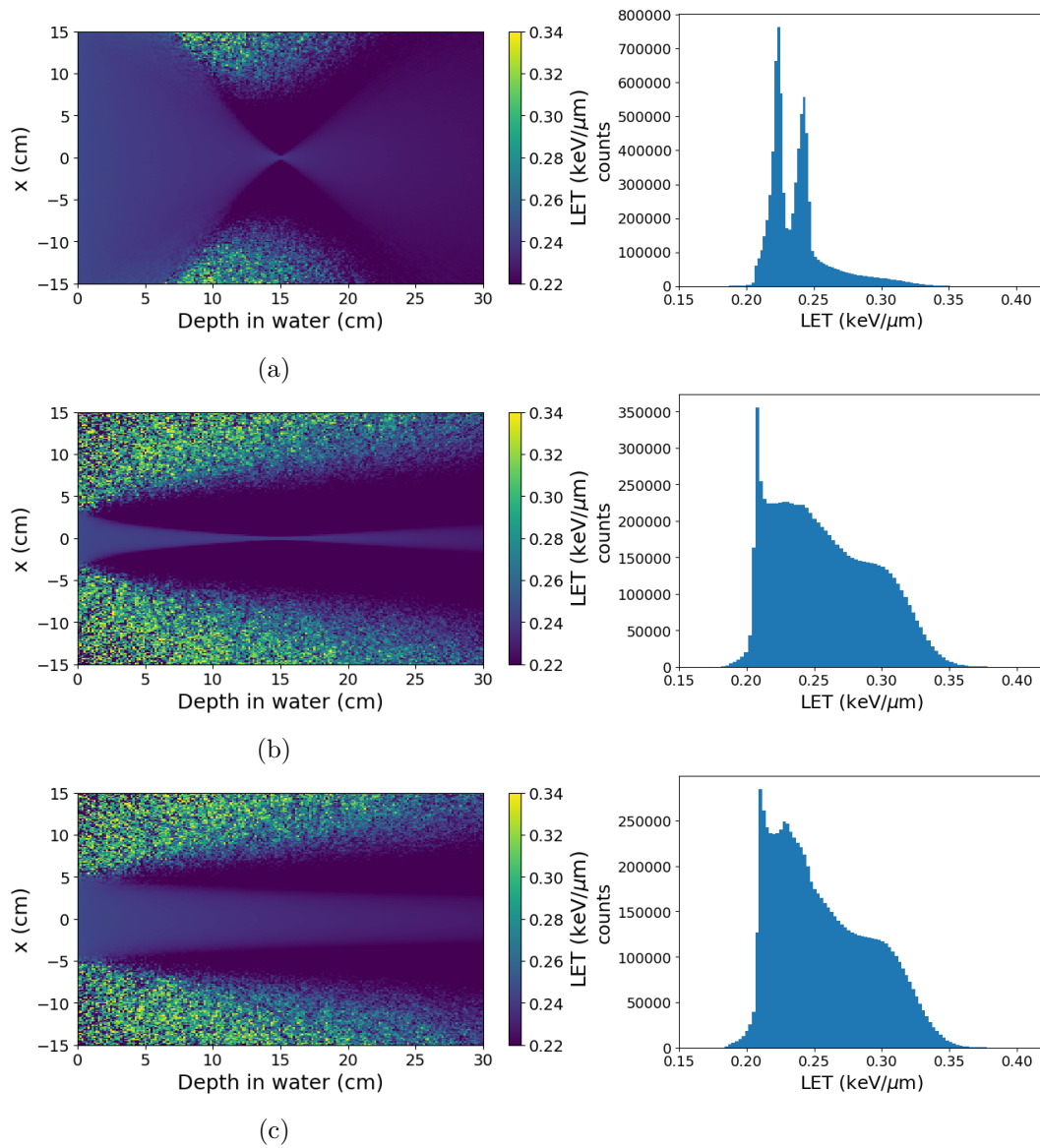
Figure 4.20: 2D LET distribution and 1D LET histograms in water simulated for 2 GeV beam focused with $f/1.2$ (a) and $f/11.5$ (b) and collimated (c).
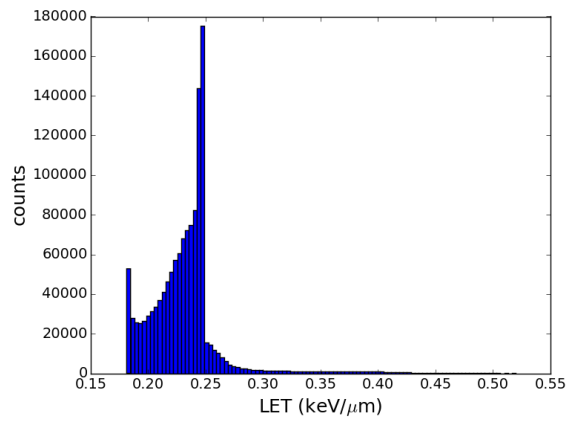
(a) 0.23 keV/μm
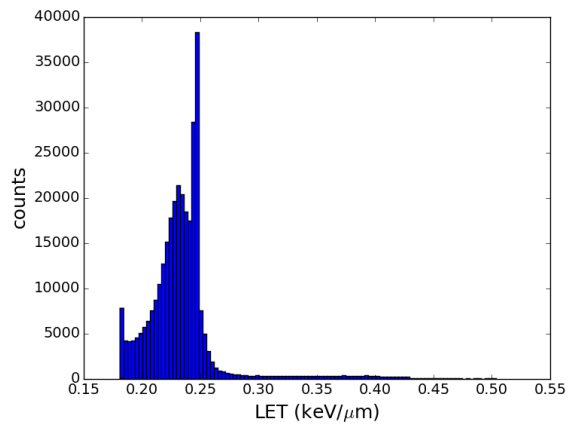
(b) 0.23 keV/μm
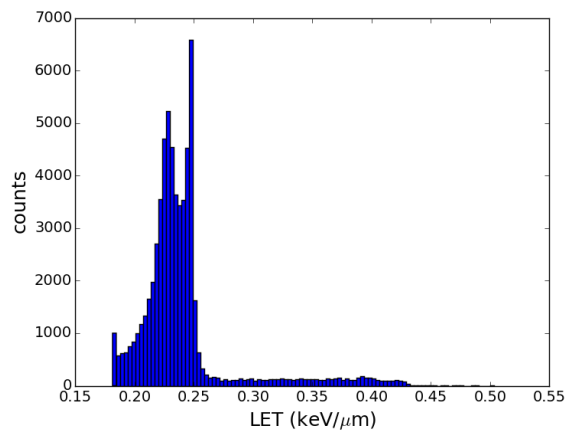
(c) 0.24 keV/μm

Figure 4.21: LET histograms obtained for 50 (a), 100 (b) and 200 (c) bins defined in each dimension of USRBIN mesh, defined in the phantom volume, for 200 MeV electron beam focused with $f/1.2$ for 200 MeV using 100 keV threshold for electron and photon production in water and electron and photon transport cut-offs.

97

(a) 0.22 keV/μm

(b) 0.41 keV/μm

(c) 0.24 keV/μm

(d) 0.46 keV/μm
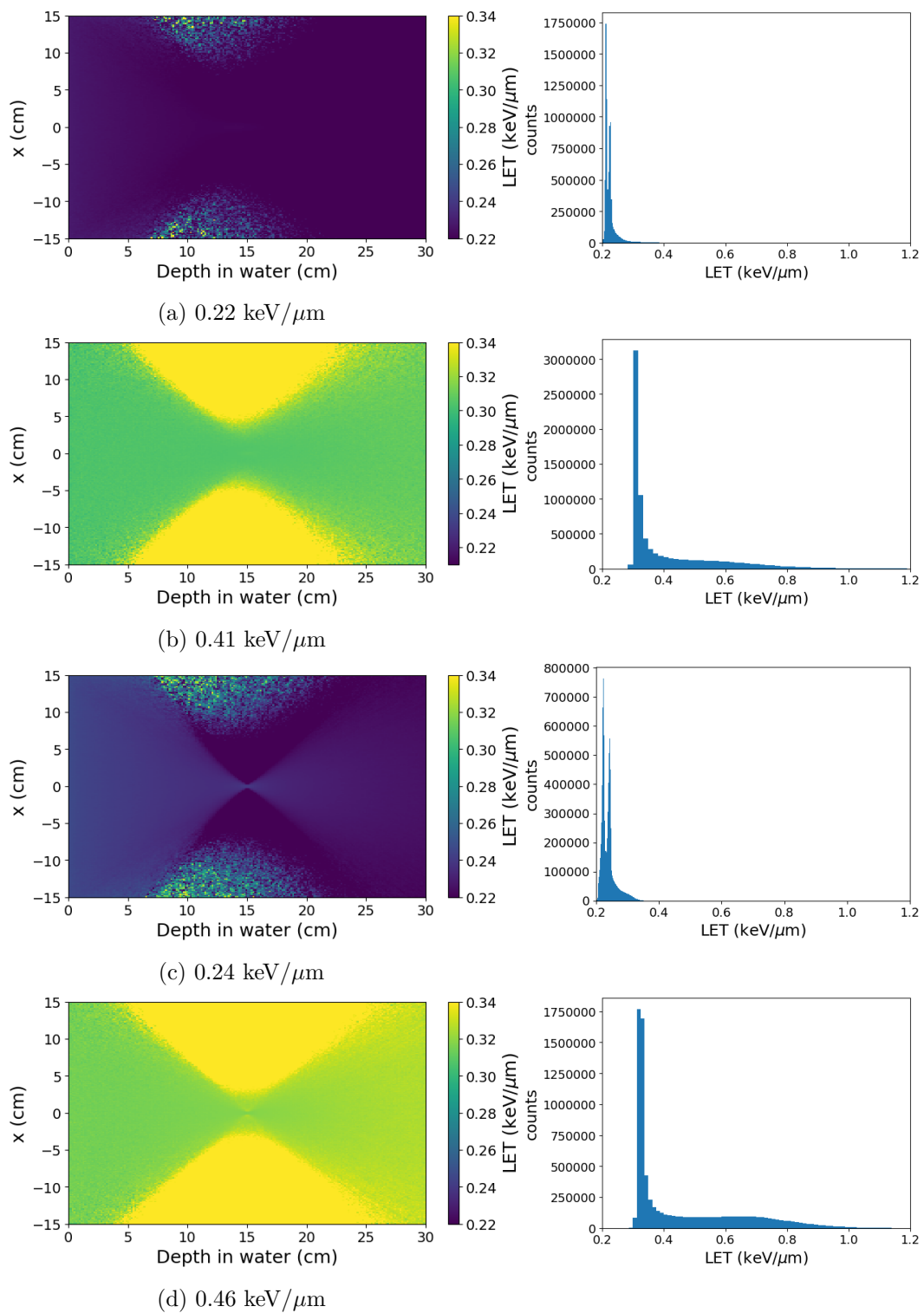
Figure 4.22: 2D LET distribution and 1D LET histograms in water simulated for *f-number f/1.2* for 200 MeV (a, b) and 2 GeV (c, d) using 100 keV (a, c) and 10 keV (b, d) thresholds for electron and photon production in water and electron and photon transport cutoffs.

Potential source of uncertainties

The robustness of the discussed method to calculate 2D LET using FLUKA MC code is validated with different FLUKA input parameters. The simulated 2D LET distributions are not strictly continuous but rather have a discrete character due to the spatial structure of the USRBIN detector. The resolution of the USRBIN scoring mesh dictates the number, range and distribution of the calculated LET values, as shown in Figure 4.21. Simulations are performed using three different bin widths, 0.15, 0.3 and 0.6 cm. The mean LET values obtained are 0.23, 0.23 and 0.24 keV/μm, respectively. The results indicate no major difference in the mean LET value while varying the bin size.

It should also be noted that the energy thresholds for electron and photon production (cut-off thresholds) should be carefully defined to avoid over- or under-estimating the LET value. The LET is calculated based on the fluence distribution of primary and secondary electrons. If the EMCUT threshold for δ-particles is low, more secondary low energy electrons cause a shift of the mean LET towards higher values. Figure 4.22 shows simulations of LET distribution for 200 MeV and 2 GeV with 100 keV, default cut-offs for the PRECISIO setting, and 10 keV threshold set in the EMCUT card. Lower cut-off thresholds result in twice as high mean LET.

4.3 Summary

In this chapter preliminary study on focused VHEEs as a radiotherapy modality are presented. FLUKA Monte Carlo simulations show that a high dose *volumetric element* as small as 0.1-1 cm^3, assuming a perfectly spherical shape, can be created at a typical depth of deep-seated tumour (15 cm) using strongly focused beams. This local spatial dose enhancement is an effect of increased electron density at the tumour depth, achievable by combining a high-energy electron beam with a focusing geometry. However, the position of the *volumetric element* is not always at the chosen depth defined in vacuum due to electron scattering. For 200 MeV and f/11.5 the focus is shifted towards the entrance of the water phantom by almost one third of the tumour size. The

effect can be completely eliminated by using lower *f-number* or higher incident energy. Furthermore, the transverse and longitudinal shape of the *volumetric element* can be altered by these two parameters. The peak surface and exit doses for a single beam are reduced by more than one order of magnitude compared to collimated beams.

VHEEs interacting with tissue act as a source of mixed radiation, comprising mostly secondary electrons, photons, positrons and neutrons. The mechanism of dose deposition were studied in detail. Low-energy electrons and positrons deposit the largest fraction of total dose (27%) arising from particles produced by photon interactions (Table 4.9). The remaining dose is deposited by primary electrons. The contribution from neutrons and induced radioactivity to the total dose in the phantom was found negligible for both 200 MeV ans 2 GeV beams.

Table 4.9: Contribution of primary and secondary radiation to the total dose.

Radiation	Fraction of total dose
primary electrons	$\sim 73\%$
positrons and secondary electrons	$\sim 27\%$
neutrons	$< 1\%$
muons	$< 1\%$
induced activity	$< 1\%$

The calculated LET values for VHEEs agree well with the literature values, however the distribution of LET in tissue depends on the beam geometry. For the selected beam geometries and electron energies high LET particles are distributed far from the central beam axis whereas around beam channel the LET is the lowest. It was also found that from VHEE to UHEE regimes LET increases slightly with incident electron energy.

Chapter 5

Calibration of GafChromic EBT3® films

The experimental results discussed in this chapter are the outcome of the collaborative effort between the University of Strathclyde, PTB and NPL. Radiochromic films dosimeters were used to measure the absorbed dose in water for electron beams with energies between 16 and 49 MeV and doses up to 60 Gy. The principles of how these dosimeters work are discussed in detail in the following sections. The response of EBT3 films is used to determine calibration curves for dose measurements that were performed at CERN with focused VHEEs. The results are compared with measurements performed using the clinical linear accelerator at NPL for an electron energy of 12 MeV. The energy dependence of the EBT3 films was studied for the development of suitable detectors that could serve as accurate and reliable dosimeters for VHEEs in the future.

5.1   Radiation dosimeters

Dosimetry plays a fundamental role in assuring the delivery of a particular dose with a desired spatial distribution. Exposure to ionising radiation is detected and measured by radiation dosimeters. Each dosimeter has its own features, which make it more suitable for one specific application rather than another. The essential feature of future

dosimeters for VHEEs is its energy independence, which is the subject of this Chapter.

Two types of dosimetry exist: absolute and relative [192]. In absolute dosimetry, the dose absorbed in water is established by determining other dose related quantities from that directly measured by a dosimeter. Absolute dosimeters fall into three main categories: calorimetric, chemical, and ionometric. Calorimeters, which measure absolute dose from a temperature rise, represent the first group. Common chemical dosimeters, such as Fricke and alanine, measure chemical change in the absorbing medium. Dosimeters from the third group, such as ionisation chambers, measure charge, which is proportional to the number of ions induced by radiation in a sensitive volume. The response of relative dosimeters, such as radiochromic films, can not be directly related to the absorbed dose, and, therefore, must be verified against readings from absolute dosimeters in a well-defined radiation field prior to the actual measurements. This procedure is referred to as calibration. Dosimetry protocols that include details of the dosimeters to be used, measurement conditions and calculation procedures have been introduced by organisations such as the International Atomic Energy Agency, the Bureau International Des Poids et Mesures (BIPM) and International Commission on Radiation Units and Measurements (ICRU).

5.1.1 Ionisation chambers

The ionisation chamber is the gold standard dosimeters for particle therapy relative measurements [193], because it has a wide dose-rate range, exhibits insignificant change in response with beam energy, and does not degrade with accumulated radiation dose. They are also commonly used to determine absorbed dose in conventional radiotherapy [194]. The principles of operation of all ionisation chambers are similar. Examples of commercial designs are thimble, plane-parallel, spherical, well-type and silicon/diamond diodes. A typical geometry comprises two electrodes (central and outer) connected to a high voltage supply of typically $100 - 1000$ V and separated by an insulator, a gas-field sensitive volume (0.005 - 50,000 cm^3). Radiation propagating through the chamber ionises the gas and produces ion pairs. A potential is applied between the electrodes to create an electric field that causes electrons and positive ions to move

towards the electrodes. The charge accumulated on the electrode surfaces is measured by an electrometer that provides a signal proportional to the number of pairs of ions created in the sensitive volume, which gives the radiation dose. Two types of ionisation chambers, the parallel plate Advanced Markus Chamber and the Cylindrical Free-air Ionisation Chamber, have been used to perform measurements of the transverse beam profile and absolute dose. The parallel-plate Advanced Markus® Electron Chamber (PTW 34045 # 1279) was developed at PTW-Freiburg Physikalisch-Technische Werk-stätten for absolute dose measurements in water and solid state phantoms. The small sensitive volume (0.02 cm^3) provides high spatial resolution for distribution measurements in small field sizes. A flat energy response is obtained for electron energies between 2 and 45 MeV.

5.1.2   EBT3 films

Radiochromic films (RCF) are commonly used either for the monitoring and characterisation of radiation fields (beam shape verification) or two-dimensional relative dosimetry for doses up to 30 Gy for a wide range of radiation sources (electrons, protons and photons) [195, 196, 197, 198]. They are also common dosimetry tools in IMRT [199] and stereotactic radiosurgery [200]. Measurements reported here have been performed using GafChromic EBT3® (External Beam Therapy) films [201], which do not require darkroom or chemicals for response development. The EBT3 film response can be read with a film scanner or digitiser and analysed using commercial software or custom scripts.

EBT3 films comprise a single active layer, about 30 μm thick (the thickness can vary slightly between different production lots), laminated between two transparent polyester films with a thickness of 125 μm each. This symmetric design eliminates any dependence of its orientation on the scanner. Moreover, these peripheral layers contain microscopic silica spheres that prevent the film surface adhering to the scanner bed, and therefore Newton's Ring artefacts are not present in digital images of scanned films. The middle layer incorporates the active component, stabilisers and other additives to provide a nearly energy independent response with a wide dynamic range and strong

absorbance in the red spectrum (575-675 nm). The detailed chemical composition of EBT3 films used in the experiments is listed in Table 5.1.

Upon irradiation, the active monomer polymerises to form a dark polymer dye. This process takes around 24 hours after irradiation. The response can vary by up to 4.3% between 1 and 24 hours after irradiation for doses between 0.3 and 4 Gy. For doses less than 2 Gy the response stabilises after nearly 30 minutes [199]. The yellow marker dye added to each layer decreases its UV/light sensitivity. The film response is energy independent in the MeV range and changes by up to 10% for lower energies. For electron energies between 6 and 16 MeV at reference measurement conditions in water, the energy dependence of EBT3 film was found to be uniform within 0.5%, with uncertainties close to 1.6% [202]. Moreover, EBT3 offer a sub-millimeter spatial resolution, which is particularly suitable for small field sizes, and therefore for dosimetry of focused VHEE beams. In the experiments performed here all films were handled and used according to manufacturer's specifications [201] and AAPM TG-55 [203].

Table 5.1: Composition and structure of Gafchromic EBT3® films (personal communication with Vertec Scientific Ltd, UK.).

Layer	d	ρ	Composition (atom%)								
	(μm)	(g/cm^3)	H	Li	C	N	O	Na	S	Al	Cl
P	125	1.35	36.4	0.0	45.5	0.0	18.2	0.0	0.0	0.0	0.0
A	30	1.2	56.3	0.7	28.5	0.3	12.4	0.1	0.1	1.4	0.2
P	125	1.35	36.4	0.0	45.5	0.0	18.2	0.0	0.0	0.0	0.0
O			43.0	0.2	39.8	0.1	16.2	0.0	0.0	0.5	0.1

P - polyester, A - active, O - overall

5.2   Calibration of EBT3 films at PTB

5.2.1   Experimental setup

EBT3 films have been irradiated using electron beams with energies between 16 and 49 MeV at the PTB research electron accelerator, described in chapter 2. The experimental setup is shown in Figure 5.1. A $30 \times 30 \times 30$ cm^3 water phantom made of 2 cm thick poly-methyl methacrylate (PMMA) walls was placed 2 m from the 0.1 mm thick copper accelerator exit window. EBT3 films were fixed inside the water phantom using custom-

made PMMA holders for two configurations: a single film placed at the reference depth for dose measurements (Figure 5.2, left), and a stack of films for depth-dose measurements (Figure 5.2, right). The holder was attached to a motorised positioning system using a PMMA rod and aligned with the 0.3 cm thick PMMA window at the front of the phantom (Figure 5.1). Concrete bricks were placed behind the phantom to dump electrons and X-rays.
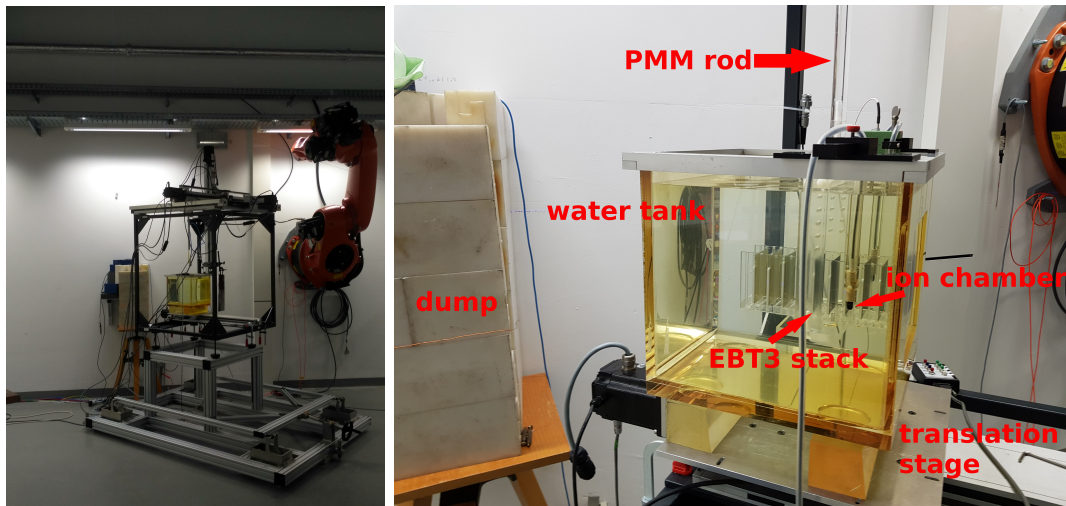
Figure 5.1: EBT3 irradiation setup at the PTB research accelerator.

5.2.2 Beam characteristics

The calibration was performed for 8 electron beam energies between 16 MeV and 49 MeV. Figure 5.3 shows the energy spectra measured by the magnetic spectrometer in the high energy section of the PTB accelerator (Figure 2.2 "F") and a magnified energy spectrum of the beam with central energy of 31.1 MeV. For all configurations, the energy spread was less than 0.3%. The transverse profile in horizontal and vertical planes measured in vacuum before the exit window were Gaussian with FWHM between 2.1 and 3.2 mm, and divergence $< 0.1°$. The beam size (FWHM) generally decreases with incident energy as shown in Table 5.2. The electron beam charge was measured before the exit window of the accelerator using an ICT. The absorbed dose in water is proportional to the delivered total charge, as shown in Figure 5.4.
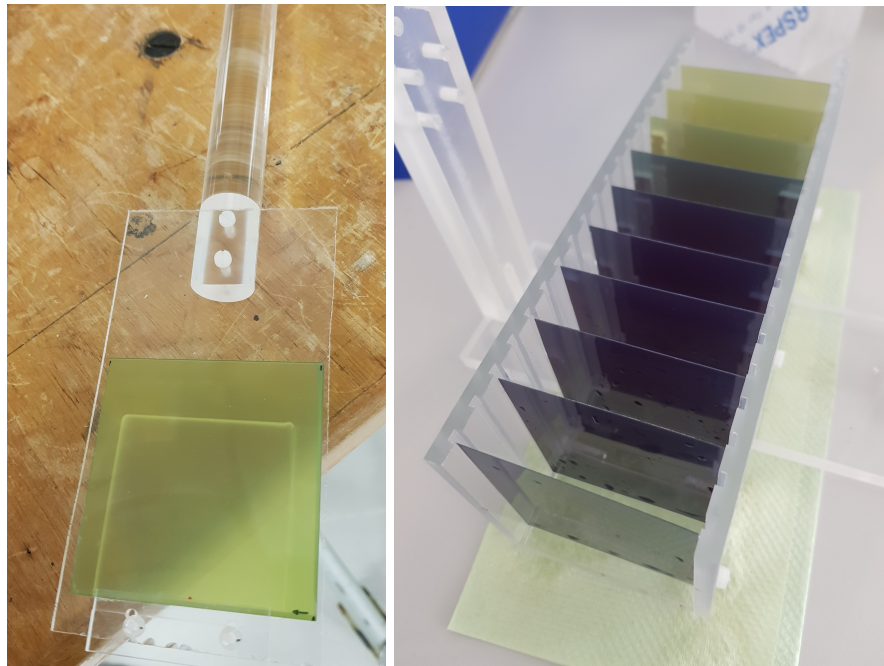
Figure 5.2: PMMA holders designed for irradiation of a single EBT3 film (left) and a stack of EBT3 films (right).

5.2.3 Measurement conditions

The dose measured inside the water phantom depends on experimental conditions such as source-to-surface distance (SSD), field size, phantom material and dimensions. Therefore, dosimetry calibrations are performed in conditions that reproduce, as closely as possible, established protocols. The recommendations of IAEA TRS-398 [176] and ICRU [124] Report 35 were followed in determining the initial conditions, as discussed in the following sections.

Phantom

Water is the recommended reference medium for dose measurements with electron beams [176, 124]. The water phantom is $30 \times 30 \times 30$ cm^3, as described in subsection 5.2.1. The walls extend to at least 5 cm beyond the largest beam size employed at the depth of measurements, following the IAEA and ICRU recommendations. The walls are made of PMMA, with a density of 1.19 g/cm^3.
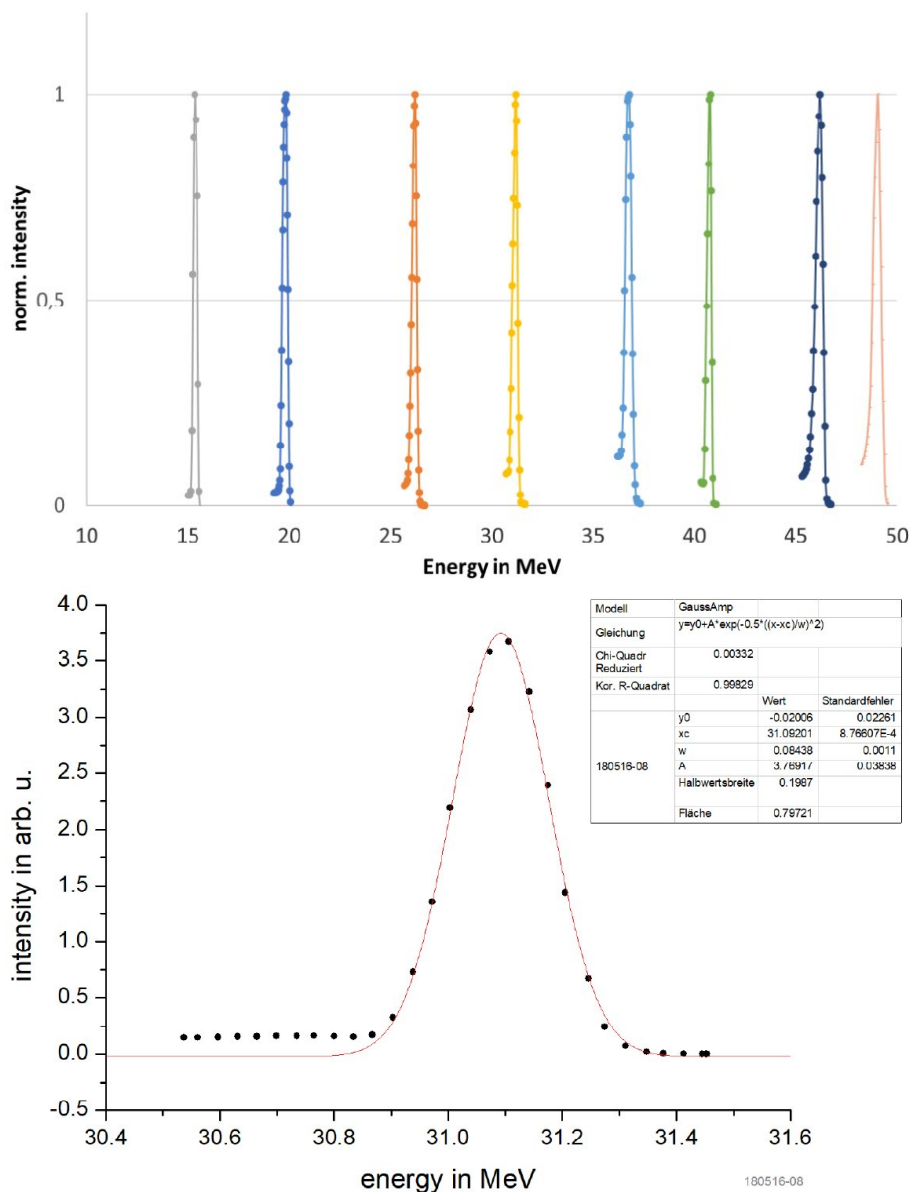
Figure 5.3: Electron beam spectra measured at the PTB research accelerator.

Source to surface distance

The recommended ICRU field size at the reference point of the ionisation chamber, centre of the entrance foil, or 1.3 mm below surface of the protection cap of the Advanced Markus chamber, is 10×10 cm^2 for SSD of 100 cm. In this experiment the SSD was defined as the distance between the accelerator exit window and the phantom entrance.

Table 5.2: Summary of the electron beams properties measured at the PTB research accelerator.

Energy [MeV]	Energy spread [%]	Beam size [mm]	
		$\mathbf{FWHM}_x$	$\mathbf{FWHM}_y$
15.78	0.25	2.6	2.6
19.63	0.25	3.1	3.1
25.51	0.17	3.1	3.1
31.01	0.10	3.1	3.1
35.92	0.19	2.1	2.4
41.20	0.08	3.1	2.7
46.42	0.17	3.2	2.6
48.88	0.25	2.1	2.6
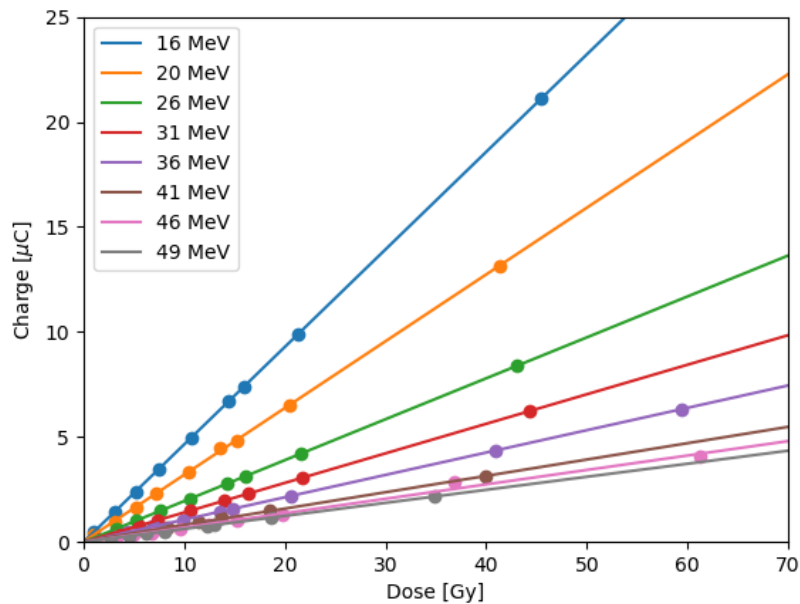
Figure 5.4: Dose as a function of charge measured at the PTB research accelerator for electron energies between 16 and 49 MeV.

The beam diverges along this path because of scattering in the exit window and in air. FLUKA simulations show that for a SSD of 200 cm, the beam size (FWHM) is greater than 10 cm at the entrance of the phantom for all beam energies. Figure 5.5 shows the depth-dose profile produced by the PTB research accelerator for a 20 MeV electron beam with SSD = 200 cm (FWHM ≈ 10 cm) and by the PTB medical Linac Elekta

Precise Treatment System$^{\text{TM}}$ using the recommended SSD = 100 cm and field size of 10×10 cm^2 and the same electron energy. When the distance between the central axis and field edge is more than the lateral range of scattered electrons, lateral scatter equilibrium occurs and the depth-dose for a specific electron energy is independent of the field dimensions, as shown in Figure 5.6. This condition is fulfilled for 20 MeV electron beams when the field size is larger than 10×10 cm^2. However, the depth-dose profile produced by the research accelerator for SSD = 200 cm is flatter at the top and the peak is shifted by approximately 2 cm away from the phantom entrance in comparison to the profile produced by the PTB medical linac with SSD = 100 cm. This difference is due to the built-in primary collimator and scattering foils used in the PTB medical linac to produce rectangular field shapes in the treatment head, which also increases the contribution of bremsstrahlung in the tail of the depth-dose curve. At half the peak height both profiles become close to each other. The depth in water at which the dose is equal to 50% of the maximum dose is defined as beam quality (R_{50}) [176].
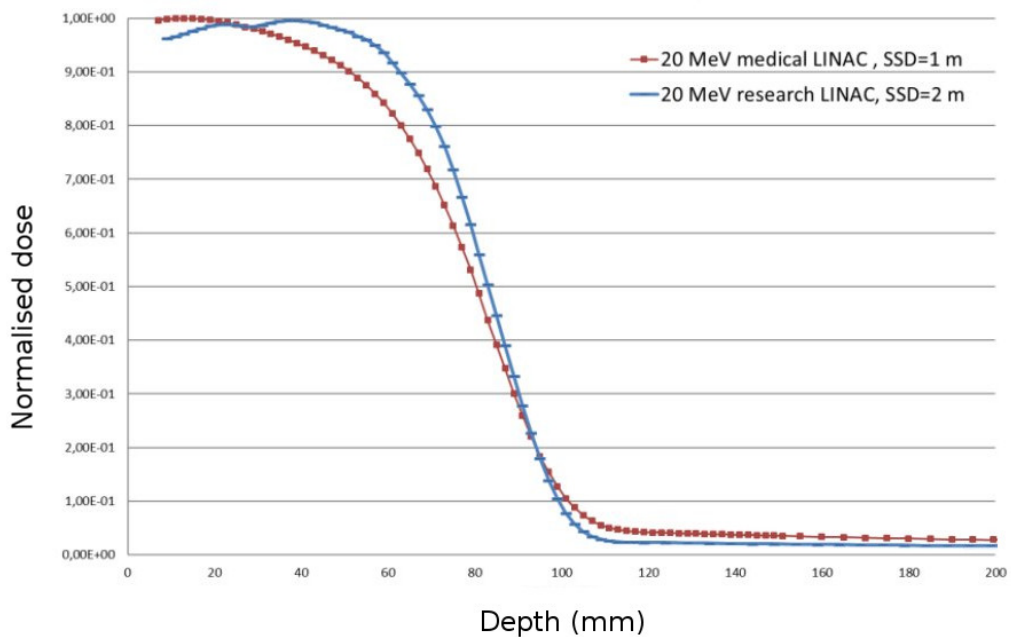
Figure 5.5: Normalised depth-dose profiles for 20 MeV electron beam energy measured at PTB using the medical linac Elekta Precise Treatment System$^{\text{TM}}$ with SSD = 100 cm and the research accelerator with SSD = 200 cm.
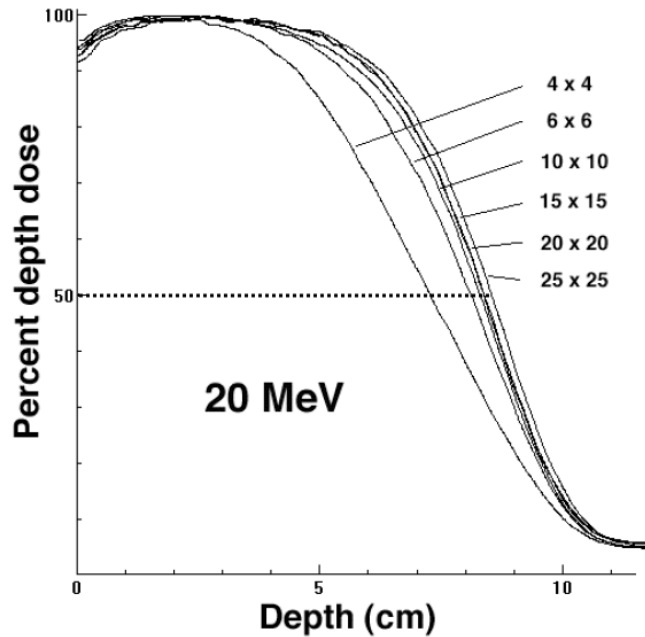
Figure 5.6: PDD curves for different field sizes for a 20 MeV electron beam from a medical linear accelerator [204].

The recommended beam quality is specified with respect to the field size at the phantom surface, which is measured with a constant SSD = 100 cm. For field size of 10×10 cm^2 R_{50}, this should be ≤ 7 g cm^{-2} for 16 MeV electron energy at the phantom surface, whereas for larger field sizes, at least 20×20 cm^2, R_{50} should be > 7 g cm^{-2} for the same electron energy at the phantom entrance [176]. When the electron energy increases, the field size decreases and more electrons are concentrated around the central axis, and therefore the depth-dose profile results in lower R_{50}, as shown in Figure 5.6. Figure 5.7 shows the relationship between R_{50} and incident electron beam energy for the Gaussian beam of the PTB research accelerator (SSD = 200 cm) and the tabulated values for different rectangular field sizes obtained using scattering foil measured at the phantom surface under reference conditions (SDD = 100 cm) [205]. The literature data shows that the beam quality under reference conditions remains constant for field sizes between 10×10 cm^2 and 20×20 cm^2, and is proportional to the incident electron energy. The precise choice of field size, shape and SSD is not critical as long as R_{50} is in the recommended range of any additional constrains set for the

output factors. However, it should not be less than 10×10 cm^2 at the phantom surface due to electron equilibrium effects. The larger SSD and the presence of Gaussian profile slightly influence the quality of the PTB beam. The value of R_{50}, for 20 MeV and 40 MeV, is 8 cm (or g cm^{-2}) and 16 cm (or g cm^{-2}), which is smaller than the beam quality index for a uniform 10×10 cm^2 field for the same incident energy, respectively.
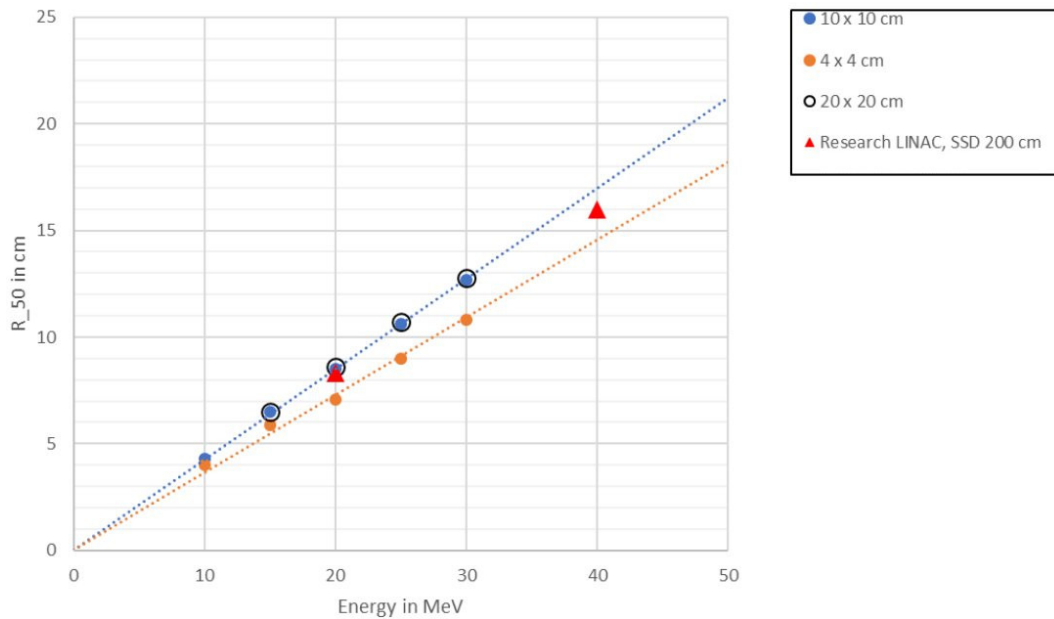
Figure 5.7: R$_{50}$ values as a function of electron beam energy under reference conditions and for different field sizes [205] and linear fits (dashed line). The red triangles show the beam quality factors for 20 and 40 MeV electron beams produced by the PTB research accelerator.

Temperature and pressure

In addition to the previously discussed measurement conditions, the response of the detectors can be affected by the environment. The mass of air in the cavity volume of the ionisation chambers is subject to atmospheric variation, such as fluctuations of temperature, humidity and pressure. The values of these quantities under reference conditions and during calibration are listed in Table 5.3.

Table 5.3: Reference conditions recommended for the calibration of ionisation chambers using Co-60 γ radiation in standard laboratories and during the calibration measurements performed at PTB.

Influence quantity	Reference	Calibration at PTB
Water temperature (°C)	20	18-19
Air temperature (°C)	20	18-19
Air pressure (kPa)	101.3	100.4-101.3
Humidity (%)	50	50-55

Reference depth

The reference depth (z_{ref}) is a common parameter used in in-phantom dosimetry. The absorbed dose is measured at the intersection of the beam central axis with the plane defined by z_{ref}. The reference depth for electron beams is [206]:

$$z_{ref} = 0.6R_{50} \; [\text{g/cm}^2] - 0.1 \; [\text{g/cm}^2]. \tag{5.1}$$

A device designed by PTB (*U-BOOT*), shown in Figure 5.8, is used for the precise measurement of the distance between the dosimeter (ionisation chamber/EBT3 film) and the phantom window. The value of z_{ref} is the distance in water (z_w) that includes water equivalent thickness of the phantom window and protection cap of the ionisation chamber. The water equivalent thickness of the phantom window is calculated as the product $t_{win} \cdot \rho_{pl}$, where t_{win} is the thickness of the window (0.3 cm) and ρ_{pl} is the mass density of plexiglass (1.19 g/cm^3). The Advanced Markus chamber is supplied with a waterproof PMMA cap with thickness of 0.87 mm (t_c). The value of z_{ref} is equal to:

$$z_{ref} = z_w + t_{win}\rho_{pl} + t_c\rho_{pl}. \tag{5.2}$$

The calculated reference depths for all beam energies used in the PTB experiment are given in Table 5.4. The phantom window is included in the calculation of z_{ref} for electron energies of 26 MeV and 49 MeV, respectively, and the film is placed at the exact reference depths. The remaining energy measurements were performed at depths that did not include the window contribution and correction factors were applied to
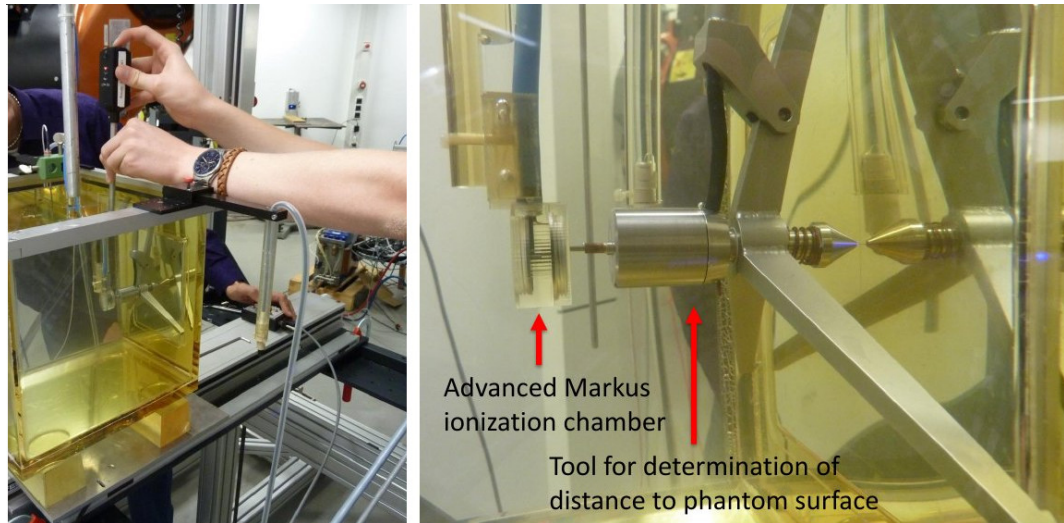
Figure 5.8: *U-BOOT* device for measuring z_{ref}.

the measurements with the Advanced Markus chamber to obtain the dose at the actual depth of the film.

Table 5.4: Reference depths determined for electron beams with energy between 16 and 49 MeV at the PTB research accelerator.

Energy [MeV]	z_{ref} [g/cm^2]
16	3.72
20	4.67
26	5.98*
31	7.18
36	7.98
41	8.76
46	9.20*
49	9.63

including the PMM phantom window

5.2.4 Determination of the Advanced Markus chamber response

Reference dosimetry for the beam quality Q is typically undertaken using ionisation chambers calibrated in terms of absorbed dose to water at a reference beam quality Q_0. The Advanced Markus Chamber at PTB was calibrated at the reference quality

Co-60 (S-Co, photon energy of 1,250 keV), which is an international standard in radiation dosimetry. Two dosimetry protocols, the International Code of Practice for the Dosimetry of External Radiotherapy Beams IAEA TRS-398 (Andreo et al., 2000) [176] and the German DIN protocol DIN 68002 (DIN 2016) [207] were followed.

Absorbed dose in water

The absorbed dose to water at the reference depth z_{ref} is [207]:

$$D_{w,Q} = (M - M_0)Nk_\rho k_h k_s k_p k_E, \tag{5.3}$$

where M is the reading of the ionisation chamber, M_0 is a reading when the beam is off, N is the absorbed dose to water calibration coefficient for the ^{60}Co reference beam quality. The influence of the air density, humidity, ion recombination, polarity and radiation quality are considered by including the correction factors k_ρ, k_h, k_s, k_p, k_E, respectively. The first two are calculated as explained in the IAEA TRS-398 Code of Practice (Andreo et al., 2000) [176]. The third parameter corrects for the effect of recombination of positive ions with free electrons or negative ions. The fourth correction factor takes into account a phenomenon known as the polarity effect, where the polarity of the collecting volume is reversed under saturation conditions due to a Compton current induced by the collision of high-energy photons with the central electrode, and the extra cameral (chamber) current collected outside the sensitive volume. The energy dependent beam quality conversion factor k_E corrects for differences between the reference beam quality Q_0 and the actual beam quality Q during measurements, as well as difference in the characteristics of the ionisation chambers.

Ionisation chamber k_s factor

Under ideal conditions, the charge released in an ionisation chamber is proportional to the absorbed dose. However, due to recombination less charge is collected on electrodes than produced in the sensitive volume. Ion recombination causes the ion collection efficiency to be less than unity. The factor k_s is calculated as the ratio of the current

$I(V)$ measured for an operating voltage V, and the saturation current I_{sat}. It can also be derived from a linear fit to the data of the Jaffé diagram [208, 209]. The k_s factor was determined at depths 30 and 150 mm as shown in Figure 5.9.
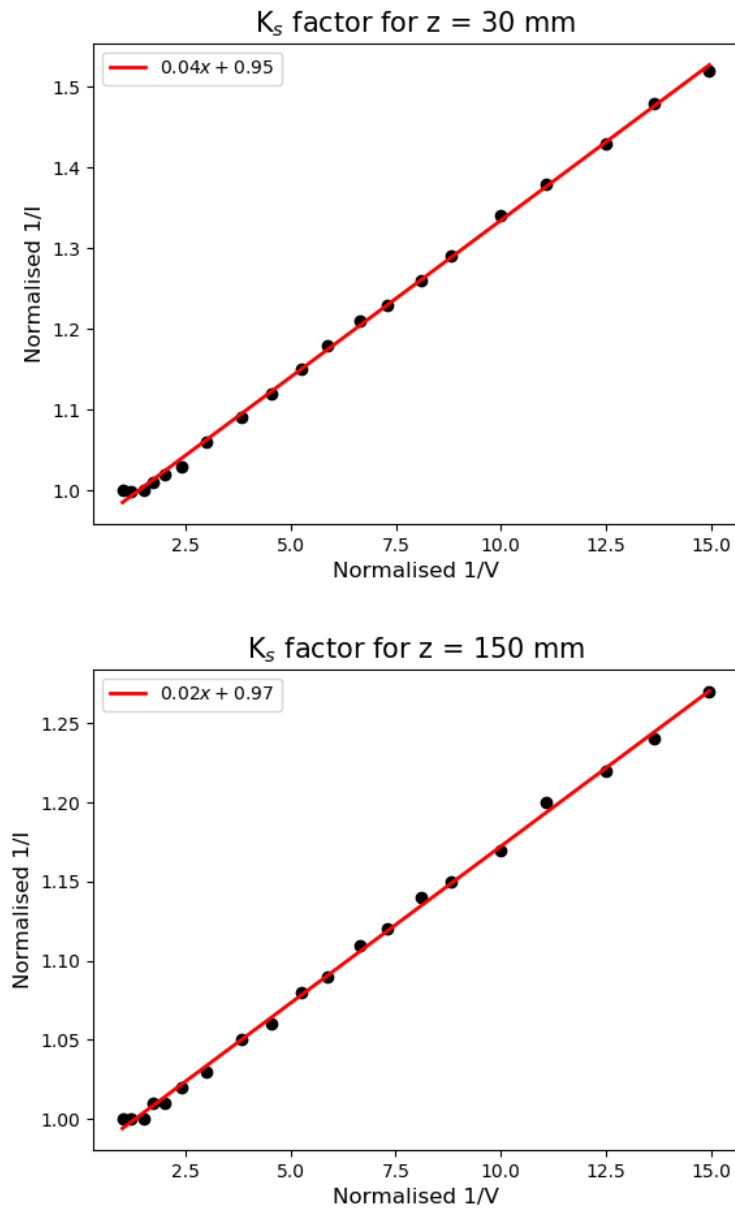
Figure 5.9: Jaffé diagrams for 41 MeV beam energy at depths of 30 and 150 mm, respectively.

5.2.5 Determination of the EBT3 film response

The protocol for preparing and reading the films described in this section is based on Devic *et al.,* [197]. This method is followed for the measurements performed both at PTB and at CERN.

Film preparation

Absolute dose calibration of GAFCHROMIC® EBT3 films (Advanced Materials Group, Ashland Inc.) was performed using films from the same batch from lot number 06141702. Each box contained 25 rectangular 8" × 10" sheets. The films were kept in shaded bags or aluminium foil and stored in a secure room maintained at room temperature (not exceeding 25°), excluding the days when the films were transported. The accumulated time-temperature history was recorded with a temperature indicator provided by the manufacturer. The films were marked and numbered prior to cutting to ensure that the film pieces could be easily identified when scanning and placed back together to form the original sheet. Each film was cut with scissors into 12 rectangular pieces of 6.75 cm × 6.35 cm for the PTB experiment and with a guillotine paper cutter machine into 4 strips per sheet with the dimensions of 6.75 × 21.5 cm for the CERN experiment. The remaining EBT3 sheets were cut into squares of 3 cm × 3 cm for the NPL calibration.

EBT3 response reading

All films were scanned one week after irradiation using a multichannel Flat Bed EPSON 10000XL Pro Scanner. The scanner was warmed up by performing 10 scans of the empty scanner bed. A preview scan was taken to select the area of interest (film) from the image of the whole scanner bed and perform scans of each film within this area. This procedure reduces scanner errors, such as light noise, and scanning time. The positioning of a film on the scanner bed is shown in Figure 5.10. Each film was precisely aligned with the centre of the scanner bed using a black frame fixed to the surface of the scanner bed to eliminate light non-uniformity effects. The short side of the film was placed perpendicular to the motion of the light source (landscape orientation). This increases the amount of light captured by the light detection system. A digital image

of each film was acquired in transmission and using RGB-positive mode with depth of 16 bits per colour channel, which gives 2^{16} - 1 = 65,535 maximum pixel value. The spatial resolution was 127 dpi, corresponding to a pixel size of 0.2 mm × 0.2 mm. The images were saved in TIFF format (Tagged Image File Format) and analysed with an *ad-hoc* python script.
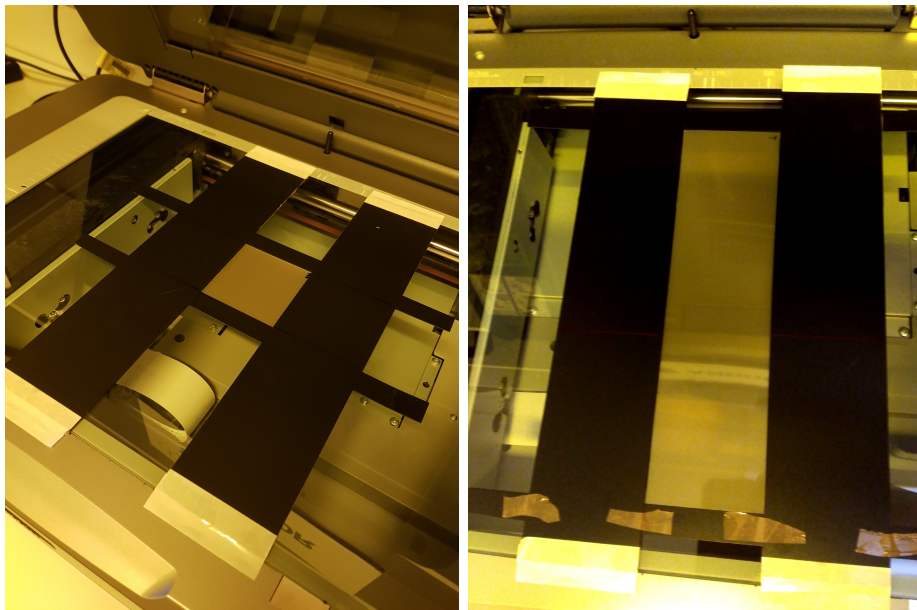
Figure 5.10: Positioning of the EBT3 film on the scanner bed for the film samples used at PTB (left) and CERN (right). The plastic black frame was designed to enable proper alignment of the film with the central area of the scanner bed and to reproduce this position for each film.

Image processing

The EBT3 films were analysed according to the protocol described in the review by Devic *et al.,* [197]. The image processing algorithm consists of several steps. The pixel values (PV) for each colour channel are extracted from the digital image of the scanned film as a double precision matrix for each colour channel. A Wiener filter is applied to remove the noise caused by the scanner and non-uniformity of the film sensitive layer. A region of interest (ROI) of 13 × 13 pixels is selected from the central area of the film. This ROI size corresponds to the dimensions of the sensitive volume of the Advanced Markus Chamber used in the experiment. The film response is determined from the

average pixel value over the selected ROI.

Dose calculation

Exposure of EBT3 films to ionising radiation produces blue-coloured dye-polymer that causes darkening of the film. The degree of film darkening is related to the radiation intensity and is quantified using the concept of net optical density ($netOD$). The $netOD$ is calculated using the Beer-Lambert law [37]:

$$netOD = \log_{10}\left(\frac{I}{I_0}\right) = \log_{10}\left(\frac{PV_{before}}{PV_{after}}\right), \tag{5.4}$$

where I_0 and I are the readings for the unexposed and exposed film pieces, respectively. These values correspond to pixel values before (PV_{before}) and after (PV_{after}) exposure, which are the average pixel values over the predefined ROI in a digitalised image of the film. The associated standard deviation, assuming uncorrelated errors, is [210]:

$$\sigma_{netOD} = \frac{1}{\ln(10)}\sqrt{\left(\frac{\sigma_{PV_{before}}}{PV_{before}}\right)^2 + \left(\frac{\sigma_{PV_{after}}}{PV_{after}}\right)^2}, \tag{5.5}$$

where $\sigma_{PV_{before}}$ and $\sigma_{PV_{after}}$ are the standard deviations of the pixel values within the ROI for the film before and after exposure, respectively. The relationship between $netOD$ and dose D is based on a measured change in optical density obtained for the predefined doses. The calibration curve is a fit to the measured optical density values using EBT3 film and dose using reference dosimeter (e.g. ionisation chamber). The fitting function should increase monotonically, have a zero moment equal to 0, and give minimum relative uncertainties. Devic *et al.,* [211] proposed the following analytical function that fulfils the aforementioned criteria:

$$D = a \cdot netOD + b \cdot netOD^n, \tag{5.6}$$

where a, b and n are best-fit values of each parameter in the model. The corresponding uncertainties for the dose is calculated using the formula:

$$\sigma_D = \frac{\sqrt{netOD^2 \cdot \sigma_a^2 + netOD^{2n} \cdot \sigma_b^2 + (a + n \cdot b \cdot netOD^{n-1})^2 \cdot \sigma_{netOD}^2}}{D}, \qquad (5.7)$$

where σ_a, σ_b are uncertainties of the fitting parameters in Equation 5.6.

5.2.6 Results

The experiments were carried out at the German national metrology institute PTB. The response of EBT3 films is investigated in the energy range of 16 - 49 MeV. The dose measurements for reference dosimetry were carried out using the Advanced Markus chamber, which has a response that is traceable to the PTB primary standard water calorimeter. In the experiment films were irradiated to produce doses between 1 and 40 Gy for all electron energies. An additional irradiation at 60 Gy was performed for 36 MeV and 46 MeV energies. The EBT3 calibration curves are presented in the following section together with the measurements performed using the clinical linear accelerator at NPL, for an electron energy of 12 MeV.

Depth-dose distribution

Monte Carlo simulations were undertaken to model irradiation of a water phantom on the beamline at the PTB facility. Figure 5.11 shows the central axis depth-dose distribution obtained using EBT3 stacks embedded in water and the simulations data obtained with FLUKA. The simulations agree well with the experiment.
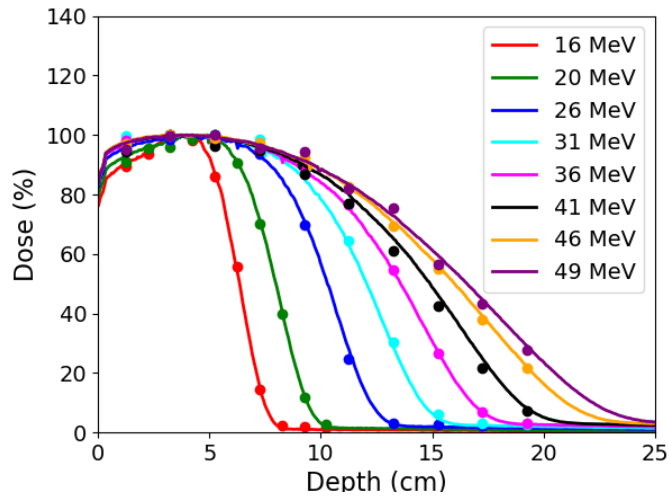
Figure 5.11: Central axis depth-dose distributions for electron energies 16-49 MeV. Experimental data (points) and simulations (line).

Dose response curves

Figure 5.12 shows the dose as a function of the *netOD* for all energies and channels. The standard deviation of the optical density is calculated according to the formula 5.5. For doses up to 8 Gy, the red channel provides the most sensitive response for EBT3 films. The fitting parameters for all electron energies are listed in Table 5.5.

The factor n accounts for the non-linear saturation of the film at doses higher than 1 Gy and strongly depends on the dose range under investigation. Below 1 Gy the dose grows linearly with the optical density and the contribution from the n term is negligible. Figure 5.13 shows the n factor as a function of energy. The mean values of n are 3.40, 2.51 and 2.66, with standard deviation of 7%, 7% and 22% for the red, green and blue channels, respectively. As a comparison, values reported in the literature are 3.1 [212] for the same film type and scanner as here, and 2.5 [211] for EBT films (previous generation).

Table 5.5: Fit parameters of the calibration curves presented in Figure 5.12.

Energy [MeV]	a		b		n	
	Value	Error	Value	Error	Value	Error
red channel						
16	9.83	0.99	60.89	0.81	3.32	0.11
20	8.50	0.92	51.21	0.75	3.23	0.11
26	8.41	0.71	60.64	0.55	3.09	0.07
31	8.79	1.20	55.24	0.99	3.36	0.14
36	11.72	1.05	69.95	0.89	3.70	0.13
41	9.96	0.83	63.43	0.96	3.62	0.13
46	12.12	1.19	64.13	1.02	3.67	0.15
49	8.92	0.39	59.65	0.39	3.19	0.05
green channel						
16	12.84	1.59	74.40	1.05	2.54	0.09
20	10.07	1.53	65.90	1.03	2.24	0.07
26	10.10	1.15	73.63	0.73	2.34	0.05
31	12.80	3.49	69.88	2.28	2.50	0.20
36	10.84	3.79	89.23	2.56	2.54	0.17
41	13.97	1.38	84.84	1.45	2.68	0.10
46	16.13	1.22	77.12	0.87	2.79	0.08
49	10.83	1.70	74.71	1.25	2.44	0.10
blue channel						
16	39.76	4.08	322.16	43.22	2.79	0.21
20	-6.23	24.59	284.88	21.25	1.82	0.24
26	35.03	4.03	273.39	27.28	2.56	0.17
31	18.52	13.33	414.11	81.82	2.35	0.30
36	33.64	23.27	2399.06	2440.13	3.85	1.12
41	16.48	18.25	512.69	170.43	2.38	0.42
46	38.19	1.96	326.96	15.03	2.76	0.08
49	37.06	1.76	314.94	25.01	2.75	0.11

The results obtained using the PTB research accelerator for two extremes of the energy range under investigation have been compared with a calibration performed using the 12 MeV NPL clinical accelerator and EBT3 films from the same lot. Figure 5.14 shows that the results are in excellent agreement within the dynamic range.
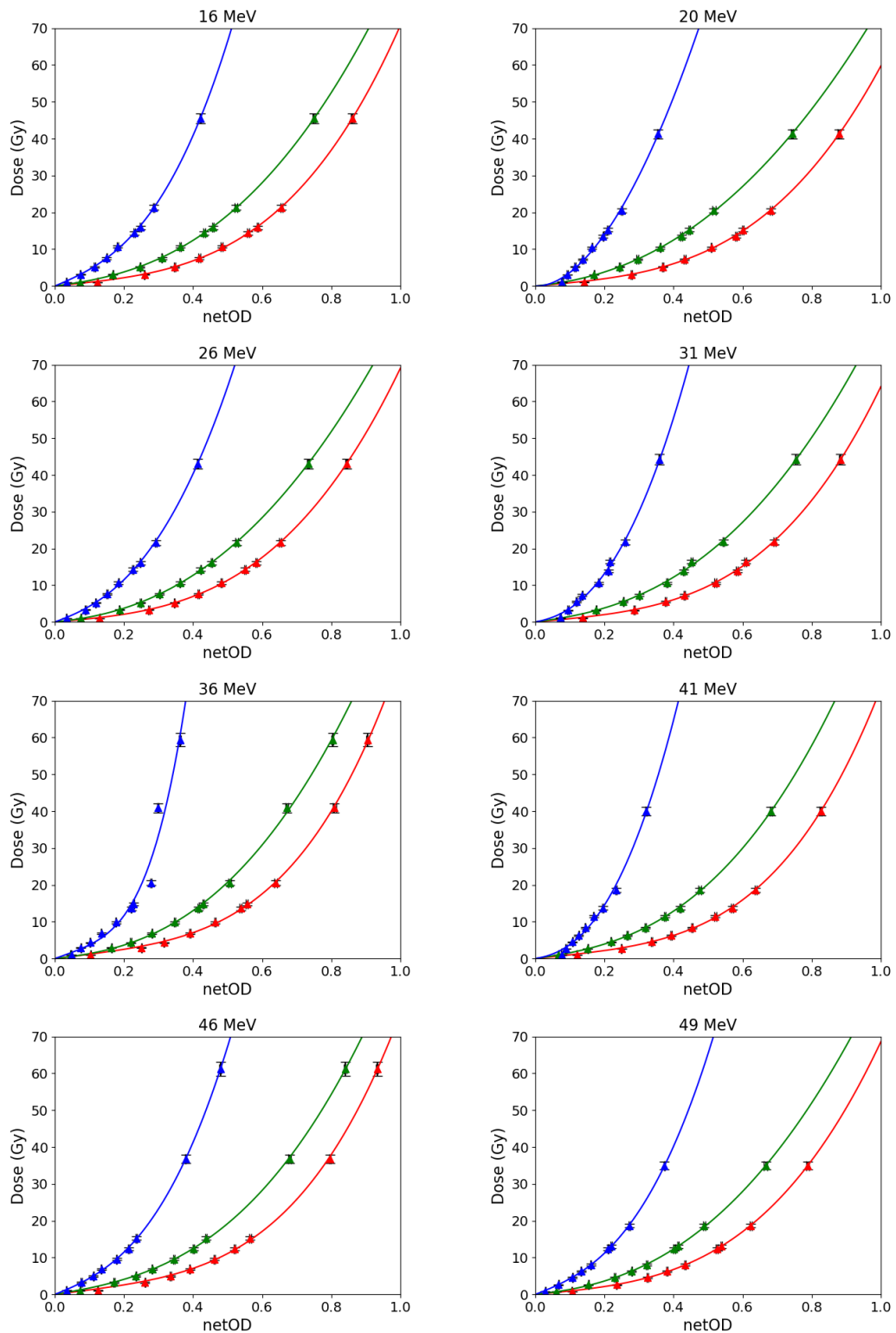
Figure 5.12: EBT3 dose response curves obtained using the PTB research accelerator for electron beam energies between 16 and 49 MeV. The lines are fits with function 5.6 of the experimental data (triangles). The colours correspond to the channel.
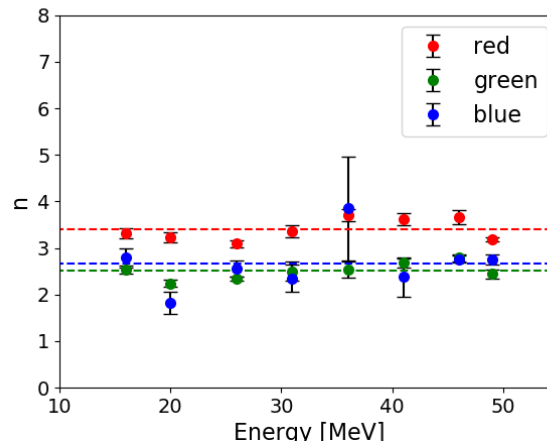
Figure 5.13: Fit n parameter (equation 5.6) for red, green and blue channels obtained using the PTB research accelerator for electron energies between 16 and 49 MeV. Dashed curves indicate mean values for all energies and channels.

A blind test has been performed to verify these results. Table 5.6 shows doses calculated for 6 optical densities between 0.1 and 1.1 using the calibration parameters given in Table 5.5. The largest standard deviations of dose are found for the lowest and the highest optical density. These correspond to doses below 1 Gy and above 40 Gy, which are subject to large uncertainties.

Table 5.6: Doses calculated for chosen optical densities using the red channel from the calibration curves obtained at PTB for electron energies between 16 and 49 MeV.

Energy [MeV]	Optical density					
	0.1	0.3	0.5	0.7	0.9	1.1
	Dose (Gy)					
16	1.01	4.07	11.01	25.51	51.76	94.37
20	0.88	3.60	9.72	22.15	44.10	79.01
26	0.89	4.00	11.34	26.04	51.37	90.64
31	0.90	3.60	9.77	22.81	46.67	85.77
36	1.19	4.32	11.22	26.86	57.89	112.46
41	1.01	3.80	10.13	24.39	52.26	100.54
46	1.23	4.41	11.10	25.80	54.47	104.33
49	0.93	3.96	10.99	25.35	50.65	90.67
SD [%]	13.36	7.56	6.31	6.59	8.36	11.29
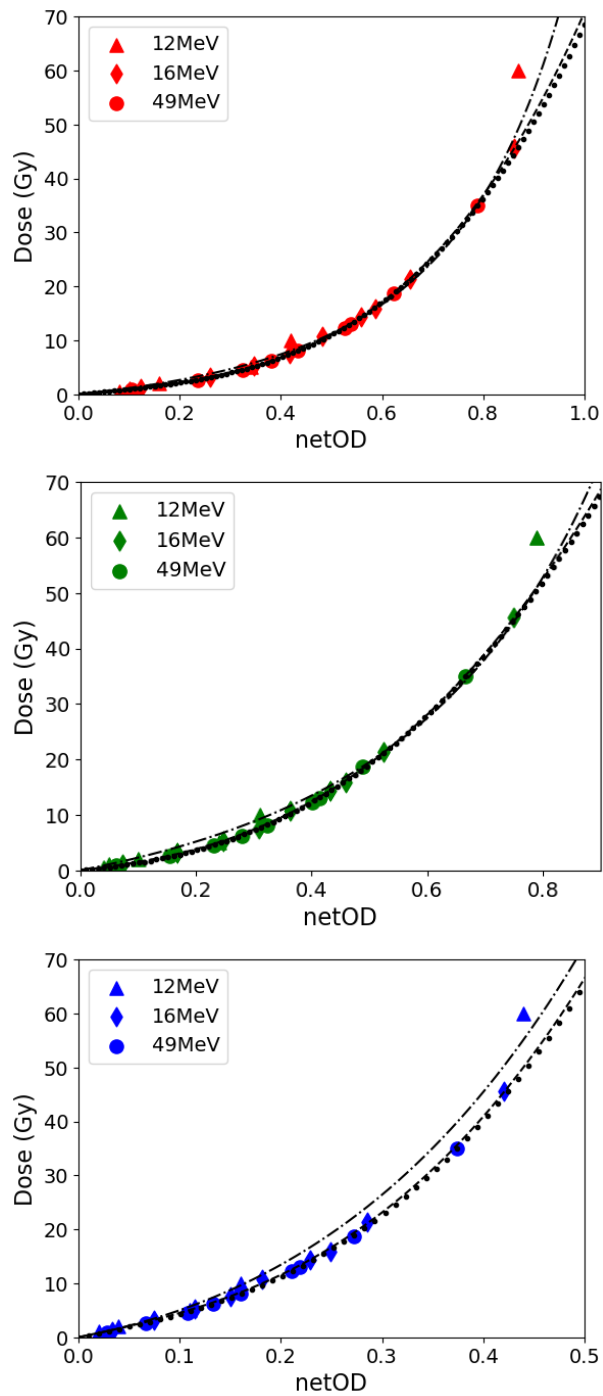
Figure 5.14: EBT3 dose response curves (red channel) obtained using the PTB (16 and 49 MeV) and NPL (12 MeV) accelerators for red (top), green (middle) and blue (bottom) channels. Dashed and dotted lines are fits for 16 and 49 MeV respectively, whereas dashed-dotted line is fit for 12 MeV.

EBT3 response at high doses

The response of EBT3 films to doses between 0.5 and 899.5 Gy was investigated using the Elekta Synergy® clinical accelerator at NPL for a nominal electron energy of 12 MeV under the reference conditions described in IAEA TRS-398 (Andreo et al., 2000) [176]. At high doses the response of EBT3 films is strongly non-linear and Formula 5.6 no longer produces a satisfying fit of the data. Therefore, a new formula, proposed by Feng *et al.,* [213], is investigated. The *n*-order polynomial function of optical density is replaced by the second order rational function given by:

$$D = \frac{a_2 \cdot netOD^2 + a_1 \cdot netOD}{netOD^2 + b_1 \cdot netOD + b_0},$$

(5.8)

where a_1, a_2, b_0, b_1 are fitting parameters. Calibration curves obtained using this formula are shown in Figure 5.15 for all channels. At doses greater than 150 Gy the red channel becomes less sensitive than the green channel. The fit parameters are given in Table 5.7. In Figure 5.16 the fits using formulas 5.6 and 5.8 are compared for all channels.

The second order rational formula 5.8 (dotted lines in the figure) provides a satisfactory fit over the whole dose range, but it is less accurate at low doses for the red and green channels. In this range the accuracy can be improved for the green channel by only fitting dose points up to 60 Gy (dashed line). The additional improvement would require extra dose points in the range 10-60 Gy to fulfil fitting conditions.
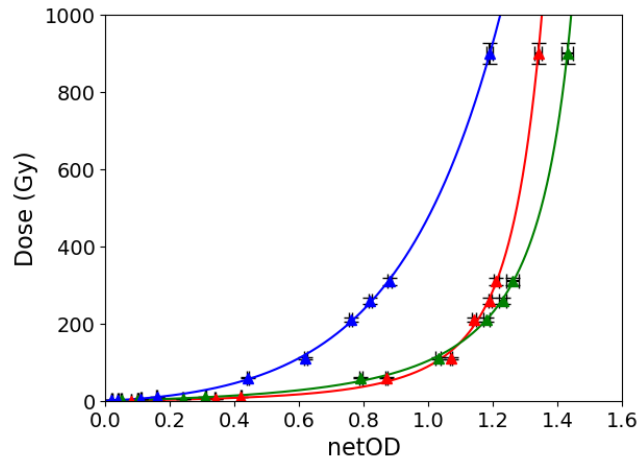
Figure 5.15: EBT3 dose response curves obtained using the NPL 12 MeV clinical electron accelerator. The fits use the formula 5.8. Each colour corresponds to the respective colour channel.

Table 5.7: Resultant coefficients for the best fit calibration curves using formula 5.8.

Parameter	Value
red channel	
a_1	21.87
a_2	$3.78 \cdot 10^{-11}$
b_0	2.21
b_1	-2.96
green channel	
a_1	69.61
a_2	$1.65 \cdot 10^{-14}$
b_0	3.40
b_1	-3.73
blue channel	
a_1	129.12
a_2	332.08
b_0	3.60
b_1	-3.63
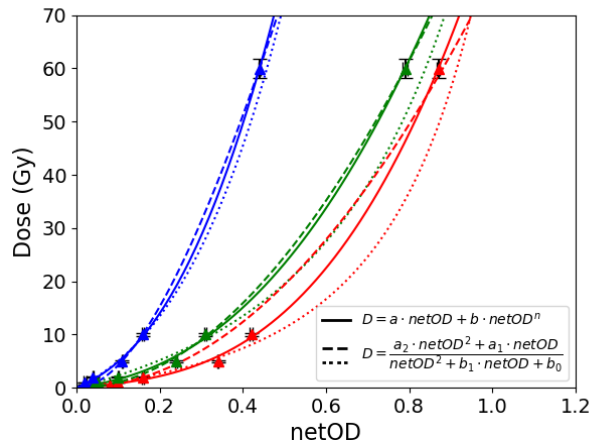
Figure 5.16: EBT3 dose response curves up to 60 Gy obtained using the NPL 12 MeV clinical electron accelerator. Solid lines represent fits for the formula 5.6. Dotted and dashed lines represent fits for the formula 5.8 using the whole dose range (up to 900 Gy) and up to 60 Gy, respectively. Each colour corresponds to the respective colour channel.

5.2.7 Uncertainty budget

The uncertainty of the dose measurements with the Advanced Markus Chamber performed at PTB was about 3%. The uncertainty of the optical density, related to the precision of film reading, includes the uncertainty resulted from the position on the scanner bed, which contributes about 2% for the red, 3% for the green, and 4.5% for the blue channel, if the position was aligned with the centre of the scanner bed. Furthermore, it also includes the uncertainty of the electron field uniformity, reproducibility of the radiochromic film and scan quality, all of which contribute less than 1% to the overall uncertainty [214].

5.2.8 Summary

The response of EBT3 films to doses between 1 and 60 Gy was measured for electron energies between 16 and 49 MeV at the PTB research accelerator. The standard deviation of the n factor is within 7% for the red and green channels. These results indicate that EBT3 films are nearly energy independent for electron energies beyond

clinical energy ranges and up to 49 MeV. Furthermore, the experimental results were cross-checked with MC simulations. The results show no significant deviations for all energies. An additional calibration for doses between 0.5 and 899.5 Gy was performed using the 12 MeV clinical accelerator at NPL. The calibration curves obtained for all energies and both accelerators are in excellent agreement for doses up to 30 Gy. For some energies and doses above 10 Gy variations are observed, possibly due to different accelerator settings. Formula 5.6 is less accurate for doses above 40 Gy and can be replaced by the rational function 5.8 at high doses.

Chapter 6

Dosimetry of Very High Energy Electrons

The measurements described in this chapter were performed at CERN using the electron accelerator at the CLEAR user facility, described in chapter 2. The response of EBT3 films and alanine dosimeters were characterised for electron energies of 58 MeV and 151 MeV for low (< 40 Gy) and high doses (> 40 Gy). Both dosimeters are energy independent within the therapeutic energy range (6 – 25 MeV) [202, 215, 216]. The response of these dosimeters to electron energies above 25 MeV is studied here.

6.1   Alanine dosimeters

Alanine is used as a secondary standard dosimeter by many national metrology institutes around the world [217, 218]. The structural form of alanine (CH_3-CH-(NH_2)-COOH, Ala) belongs to the group of organic α-amino acids, which build protein structures in the human body. In the form of polycrystalline powder, alanine is mixed with high melting point binding materials, such as paraffin wax, to enable manufacture of pellets, films or any other custom geometries. Purified alanine, L-α and DL-α alanine, or combination of both, exposed to radiation, produce very stable free radicals, where the most common is CH_3-C·H-COOH [219]. The mechanism of energy absorption in the molecular structure of alanine is similar to absorption in tissue. Free radicals pro-

duced in alanine exposed to radiation have unpaired electrons that can be measured with electron paramagnetic resonance spectroscopy (EPS). Alanine dosimeters have an energy independent response above 100 keV [220] and are more suitable for measurements in high-dose ranges due to the very low signal-to-noise ratio observed for low doses [221]. Alanine demonstrates exceptional post-irradiation response stability. The change in response over time does not exceed the measurement uncertainty. However, the response of alanine depends strongly on the temperature of the dosimeters during irradiation and can change by up $0.1\%/^\circ$C [222, 223, 224]. Alanine has been shown to produce accurate measurements from 1 Gy up to 10^5 Gy [225], although the response becomes non-linear above a few hundred Gy. The standard practice for alanine dosimetry has been established in ISO/ASTM 51607:2004(E) [226]. Alanine is a water equivalent material, has weak dependence on the irradiation beam quality, small energy dependence (negligible from 6 to 25 MV beam qualities [227]) and high radiation yield factor (number of radicals generated per unit of absorbed energy). The essential features of these dosimeters from the radiotherapy point of view are the non-destructive read-out and the small size, which makes them suitable for dosimetry in small field sizes.

6.2   Experimental setup

The setup was installed after the spectrometer on the CALIFES beamline described in chapter 2. A $30 \times 30 \times 30$ cm^3 phantom with 6 mm thick PMMA walls is filled with water and mounted on a movable stage, as shown in Figure 6.1. A step motor moves with precision of 2.5 μm per step in the direction perpendicular to the beamline axis to change the position of the beam on the EBT3 film strip. The electron beam exits the vacuum system through a 0.1 mm thick aluminium window and passes through a lead collimator consisting of a $100 \times 100 \times 50$ mm^3 rectangular cuboid with a 10 mm diameter hole to produce a flat electron distribution. The distance between the collimator and the phantom entrance is 100 mm. An Integrating Current Transformer (ICT) measures the beam charge in front of the phantom. An alignment laser and a

movable mirror are mounted between the exit window and the collimator to define the beamline axis and help positioning the phantom and films. A dump made of 15×20 graphite blocks surrounded by 10×10 cm^2 cubic iron bricks was constructed to stop electrons and X-rays after the phantom. Two temperature probes were installed, one in air next to the concrete dump and one in water at the rear of the tank, as shown in Figure 6.2.
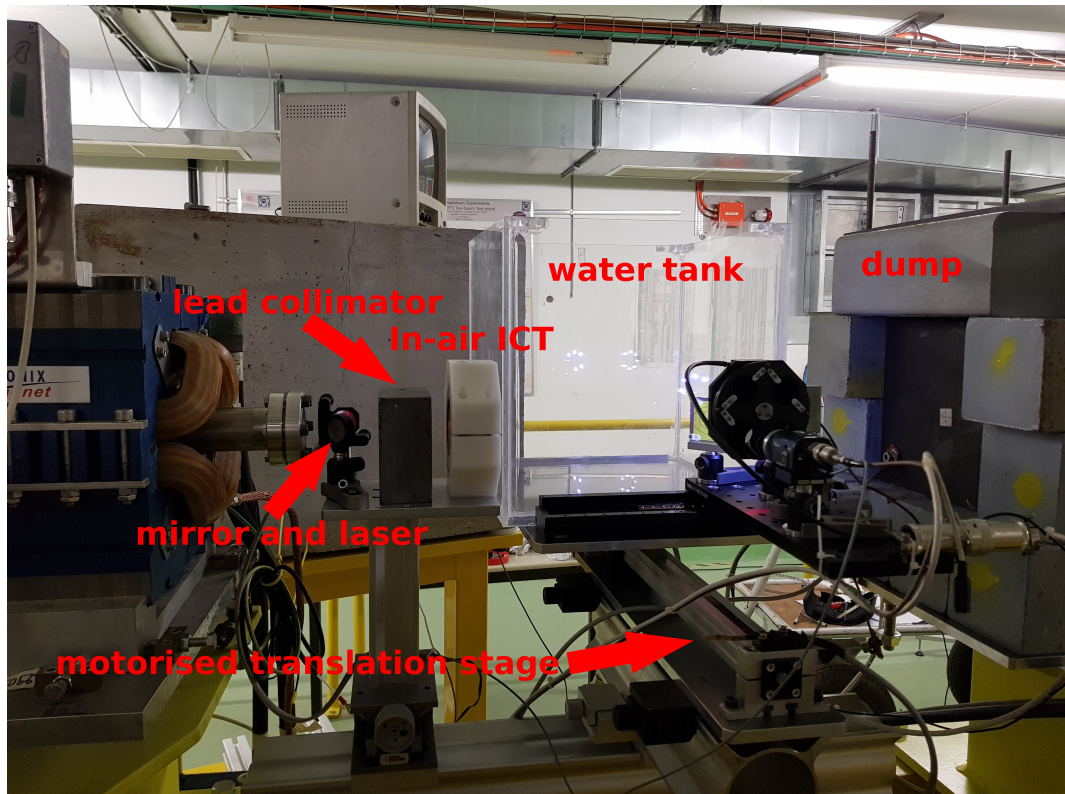
Figure 6.1: Experimental setup at the CLEAR facility.
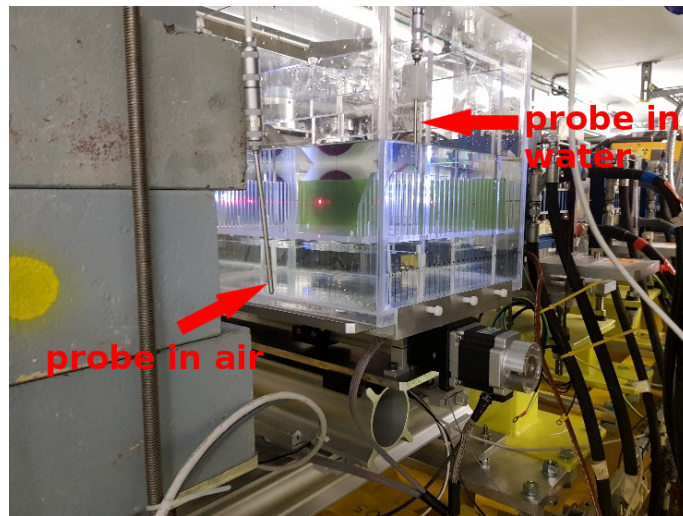
Figure 6.2: Location of the temperature probes and phantom alignment using a laser.

6.3   Beam parameters

The accelerator parameters are listed in Table 2.3. The beam profile measured before the collimator was Gaussian in both horizontal and vertical planes. The total charge at the entrance of the phantom was 4.4 – 80 nC for 58 MeV and 4.5 – 60 nC for 151 MeV.

6.4   Preparation of samples

The EBT3 films were cut into 6.75×21.5 cm strips (4 strips per sheet) and fixed inside the water phantom using custom-made holders, as shown in Figure 6.3. The alanine dosimeters were provided by the PTB institute in Germany and produced by the company Harwell Dosimeters. They consist of about 91% of L_α-alanine (microcrystalline) and 9% of paraffin used as binder. A mix of these two materials has density of about 1.2 g/cm^3 and effective atomic number $Z_{eff} = 7.2$. A single pellet has diameter of 4.9 mm, height of 3 mm and weight of 60 mg. The alanine samples were arranged in stacks of four pellets to improve the statistics. Four stacks were attached to each EBT3 film strip using a Scotch tape with properties close to water, and films were marked to identify the pellet position during scanning.
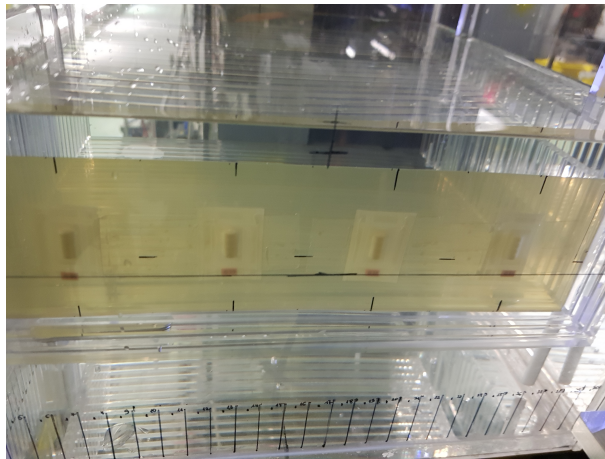
(a)

(b)
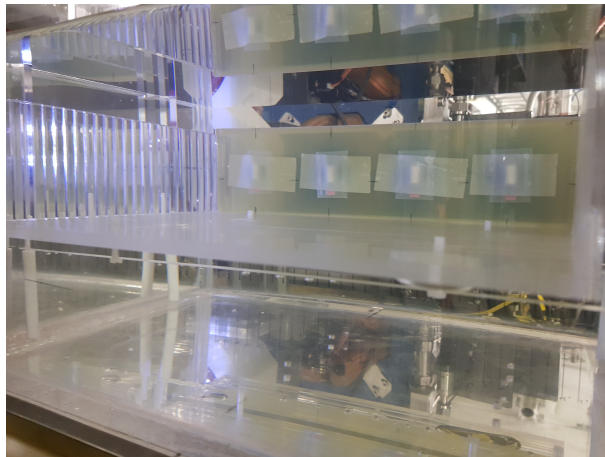
(c)

Figure 6.3: An EBT3 film with glued alanine stacks. Photograph from (a) the front before and (b) after irradiation, and (c) the back.

6.5 Dose reading

The dose deposited in the alanine pellets was read-out at PTB using a system based on electron paramagnetic spin resonance. Each pellet was individually placed in the spectrometer shown in Figure 6.4, which counts the number of unpaired electrons from radiation-induced radicals. The concentration of free radicals (the number of radicals per unit mass of irradiated alanine) is proportional to the absorbed dose. After irradiation the alanine pellets were stored in plastic pockets, isolated from a dry environment. This protected the radicals from recombining and therefore loss of signal (fading), which is about a few parts in 10^3 per year [228].

Figure 6.4: Electron paramagnetic resonance spectroscopy system at PTB.

In the spectrometer alanine pellets are exposed to microwaves at a fixed frequency and a varying magnetic field. In order for resonance to occur the frequency between two

electron states should match the frequency of the microwaves. Electrons gain energy through photon absorption, which is monitored and converted into a spectrum. The dose is determined relative to a reference substance, but also relative to the signal produced by pellets that have been irradiated with a known dose (usually 25 Gy) in the ^{60}Co reference field at PTB. Five spectra were recorded by rotating each alanine pellet by 72° and the average of the amplitudes was calculated to reduce positioning uncertainties. The estimated time of handling and signal measurement for a single pellet sample is around 10 minutes.

There are two methods to perform alanine dose read-out. In the first method (standard) two functions representing a pure alanine spectrum (alanine base function) and un-irradiated pellet combined with the spectrum of the reference substance (reference base function), called based functions, are fitted to the measured spectrum (experimental spectrum) by the least-squares method (Figure 6.5). The base functions are determined on each day of measurement in a daily calibration of the spectrometer. In the second method (non-standard) an experimental signal is represented as a linear combination of the pure alanine signal (S_0), baseline and noise. The three components are shown in Figure 6.6. The alanine ESR signal under investigation (experimental signal) is fitted using the extrapolated data for the reference dose of 25 Gy using a least-squares method. The dose is determined from a manual peak to peak measurement performed for the negative and positive maxima of the fit function [229, 218]. This method is less accurate but can be used to estimate doses > 25 Gy. The signal from four pellets irradiated simultaneously is averaged to yield the dose-normalised amplitude [230]

$$A_D = \frac{A_m}{\bar{m}} \cdot \bar{m}^b \cdot D^b \cdot K_{pos} \cdot K_T. \tag{6.1}$$

The index b refers to the base function. The meanings of the terms in equation 6.1 are as follows:

$A_m = \bar{m} \cdot \frac{1}{n} \sum_{i=1}^{n} \frac{A_i}{m_i}$ average mass-normalised EPR amplitude, n is the number of pellets irradiated simultaneously,

$\bar{m} = \sum_{i=1}^{n} m_i$ average mass of the simultaneously irradiated pellets,

$\bar{m}^b$ average mass of the pellets used to construct the base function,

D^b dose delivered to the pellets used to construct the base function,

$K_{pos} = \dfrac{k_{pos}}{k_{pos}^b}$ correction factor for the positioning,

$K_T = \dfrac{k_T}{k_T^b}$ correction factor for the irradiation temperature $k_T = 1 - c_T \cdot (T - T_0)$, where c_T is a temperature coefficient equal to 1.82 ± 0.08 [231].

Further details can be found in the technical report PTB-Dos-55 [230].
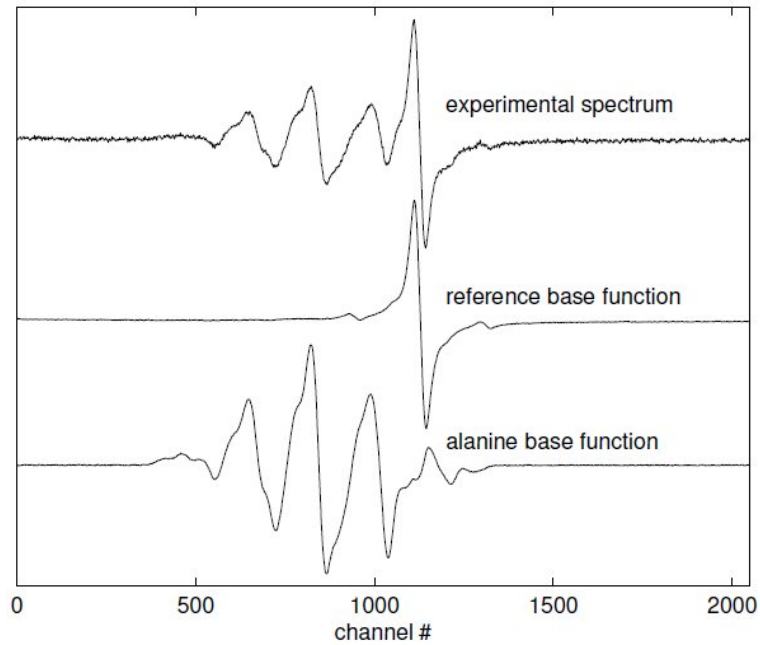
Figure 6.5: Alanine signal reading using base functions (standard method) [232].
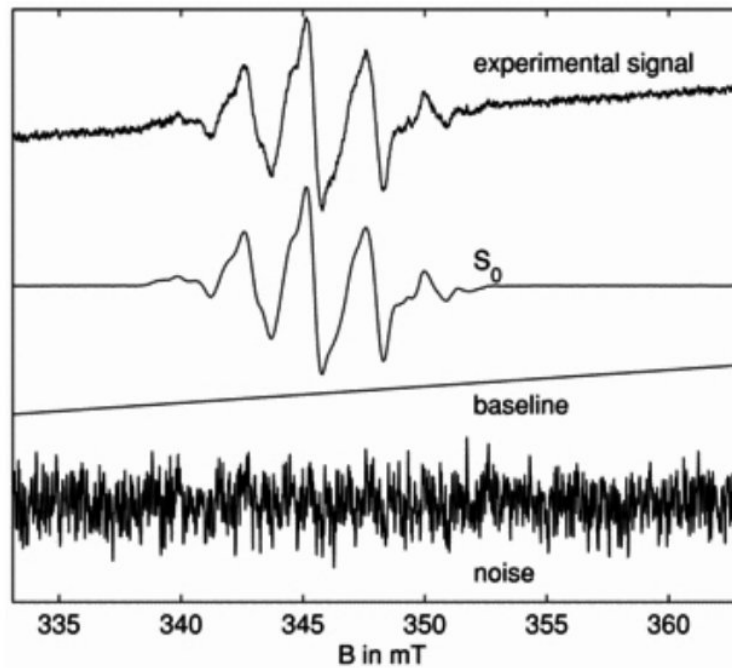
Figure 6.6: Alanine signal reading using peak to peak method (non-standard method) [233].

Dose reading from the EBT3 films was performed following the methods described in section 5.2.5. The dose was calculated at the position where the 4 alanine pellets were located, based on an average pixel value over the diameter of the pellets. Figure 6.7 shows scans of the irradiated EBT3 film strips for the red channel. The alanine pockets were cut with scissors and had irregular shapes, therefore additional marks were made on the edges of the strips to indicate the position of the middle of each stack in transverse and vertical directions. The markers around each spot are the positions of the corners of the plastic pocket. Doses up to 40 Gy were calculated using the calibration curve obtained for 49 MeV electron energy at the PTB research accelerator (Table 5.5). For higher doses the calibration curve obtained at the NPL clinical accelerator for 12 MeV (Table 5.7) was used.
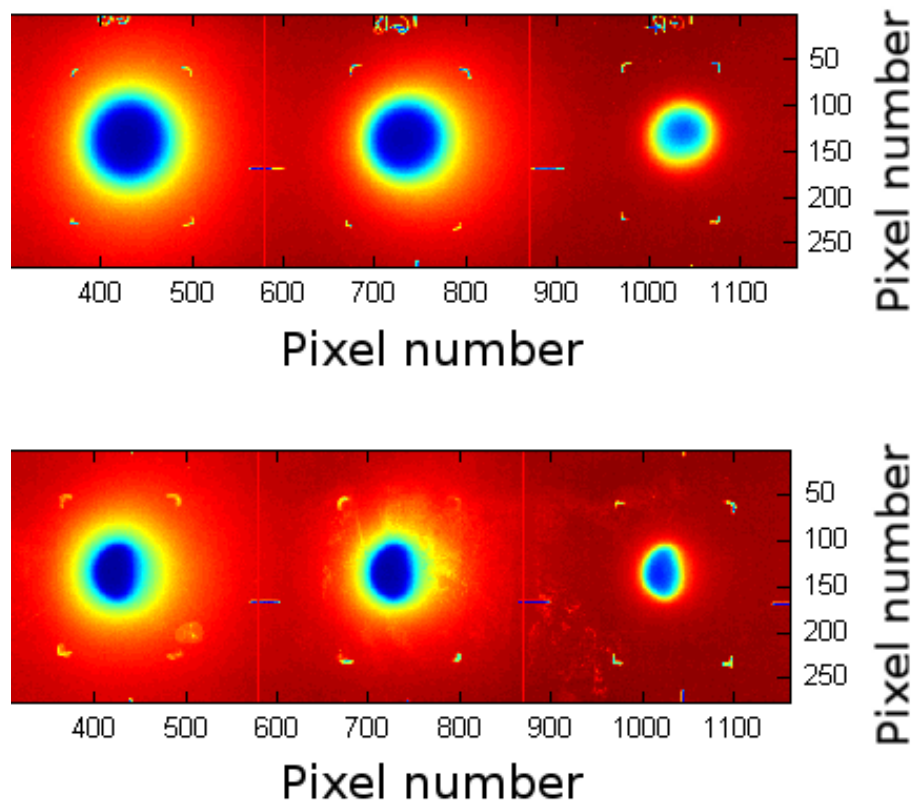
Figure 6.7: Scans of EBT3 strips (red channel) irradiated with 58 MeV (upper) and 151 MeV (lower) electron beams at the CLEAR facility.

6.6   Measurement conditions

The alanine signal depends on the sample temperature during irradiation. It changes by about 0.1%/°C [222, 223, 224]. The temperature of water and air was measured by the probes shown in Figure 6.2, with precision up to 0.01°C, before irradiation of each EBT3 strip and is listed in Table 6.1 for each electron energy. The reference temperature used to calculate the correction factor is 20°C. The reference depth was fixed at 4.2 cm for all electron energies. This value was determined with FLUKA simulations prior to the experiment at a depth just after the peak dose, in the region of electron equilibrium and water equivalent thickness of the 0.6 cm thick plexiglass wall, for 151 MeV, the highest energy that was used during irradiation.

Table 6.1: Measurement conditions during calibration of EBT3 films and alanine at the CLEAR user facility.

Parameter	58 MeV	151 MeV
Water temperature (°C)	21.43	20.50
Air temperature (°C)	23.06	21.02

6.7   Results

Figures 6.8 – 6.10 show the 2D dose profiles generated by 58 and 151 MeV electron beams for nominal doses from 20 to 368 Gy. The doses measured by EBT3 films were lower than the nominal doses by a factor of 7.7. This is due to an incorrect calibration of the ICT unit, which was discovered during the analysis of the results. For doses below 40 Gy the calibration coefficients from the formula 5.6 obtained from the calibration performed for electron energy of 50 MeV at the PTB research accelerator, were used to calculate the absorbed dose. For doses above 40 Gy the calibration coefficients from the formula 5.8 obtained from the calibration performed at NPL with 12 MeV electron beam were used to estimate the absorbed dose.

The dose measured by the EBT3 films at the positions of the alanine pellets is calculated as an integral dose within the regions indicated by the coloured bars. The dose distribution within the pellets is inhomogeneous across the stack due to the small beam size. Figure 6.11 shows the dose measured by each individual alanine pellet and corresponding EBT3 film pieces. The response of EBT3 films below 20 Gy is in agreement with the dose measured by alanine within their associated uncertainties for all channels. The response of the three channels is consistent for doses below 100 Gy and agrees well, within associated uncertainties, with the results obtained for alanine except for the second top pellet (orange bar in Figures 6.8 - 6.10), for which the dose gradient was found to be the largest.
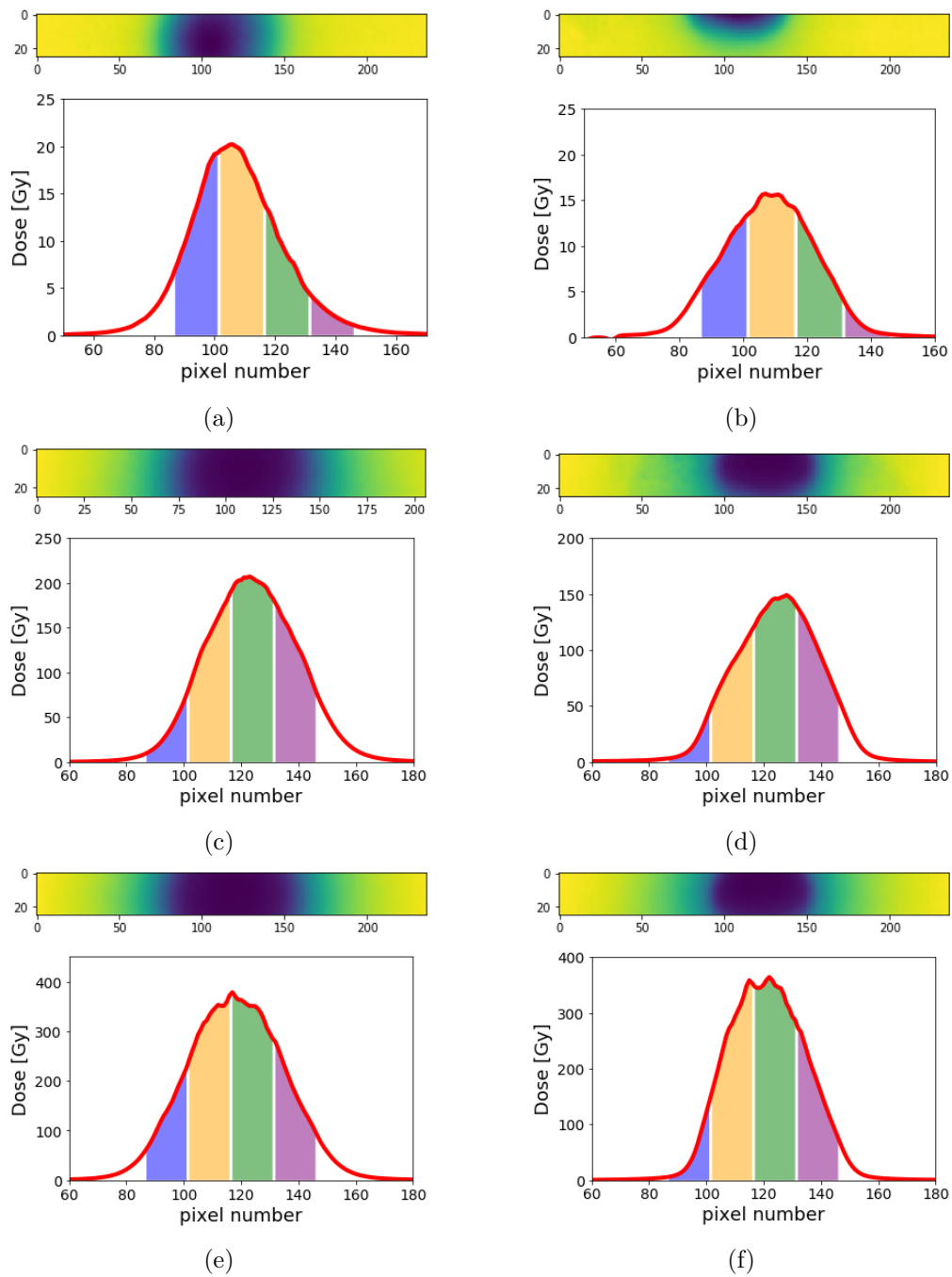
Figure 6.8: 2D and integrated dose profiles in the portions of EBT3 films covered by alanine stacks calculated using the red channel. The positions of the four individual pellets within the stacks are marked with the colour bars, where the violet colour indicates the position of the first pellet starting from the bottom of the stack. Samples were irradiated with electron energies of 58 (a, c, e) and 151 MeV (b, d, f), giving nominal doses of 20 Gy (a), 27 Gy (b), 217 Gy (c), 240 Gy (d), 368 Gy (e) and 360 Gy (f), respectively at the CLEAR user facility.
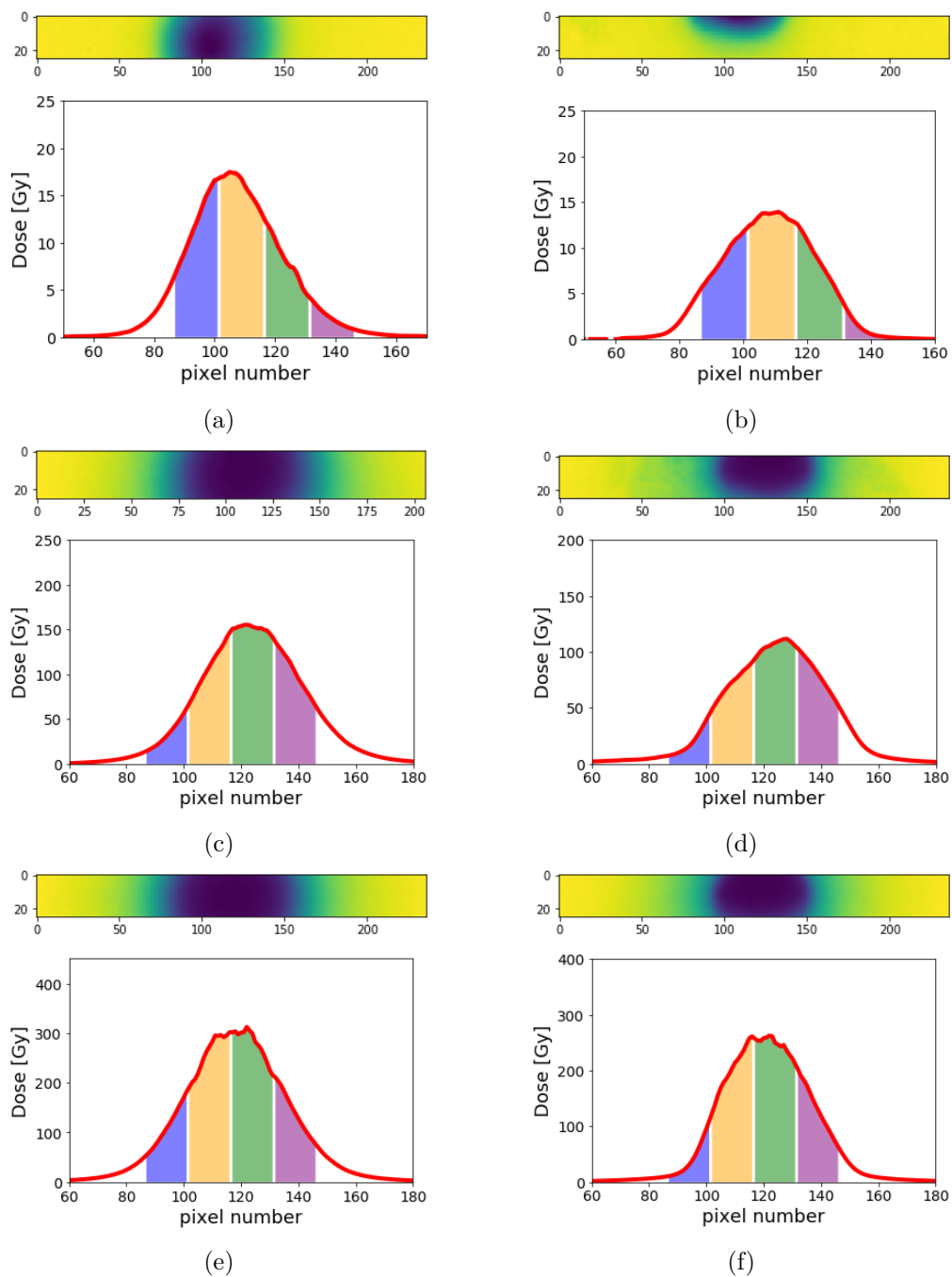
Figure 6.9: 2D and integrated dose profiles in the portions of EBT3 films covered by alanine stacks calculated using the green channel. The positions of individual pellets are marked with the colour bars where the violet colour indicates the position of the first pellet starting from the bottom of the stack. Samples were irradiated with electron energies of 58 (a, c, e) and 151 MeV (b, d, f), giving nominal doses of 20 Gy (a), 27 Gy (b), 217 Gy (c), 240 Gy (d), 368 Gy (e) and 360 Gy (f), respectively at the CLEAR user facility.

141
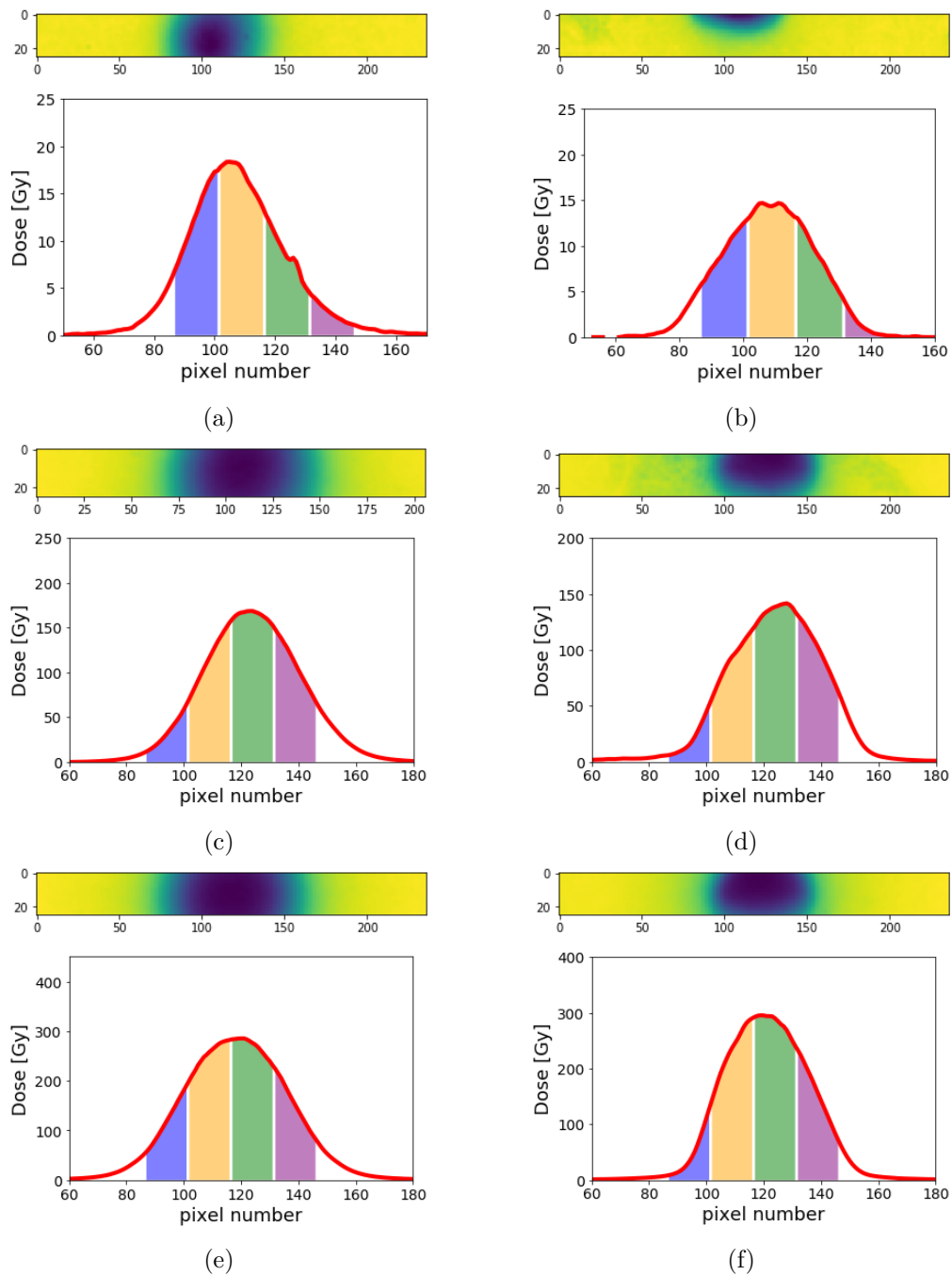
Figure 6.10: 2D and integrated dose profiles in the portions of EBT3 films covered by alanine stacks calculated using the blue channel. The positions of individual pellets are marked with the colour bars where the violet colour indicates the position of the first pellet starting from the bottom of the stack. Samples were irradiated with electron energies of 58 (a, c, e) and 151 MeV (b, d, f), giving nominal doses of 20 Gy (a), 27 Gy (b), 217 Gy (c), 240 Gy (d), 368 Gy (e) and 360 Gy (f), respectively at the CLEAR user facility.

142
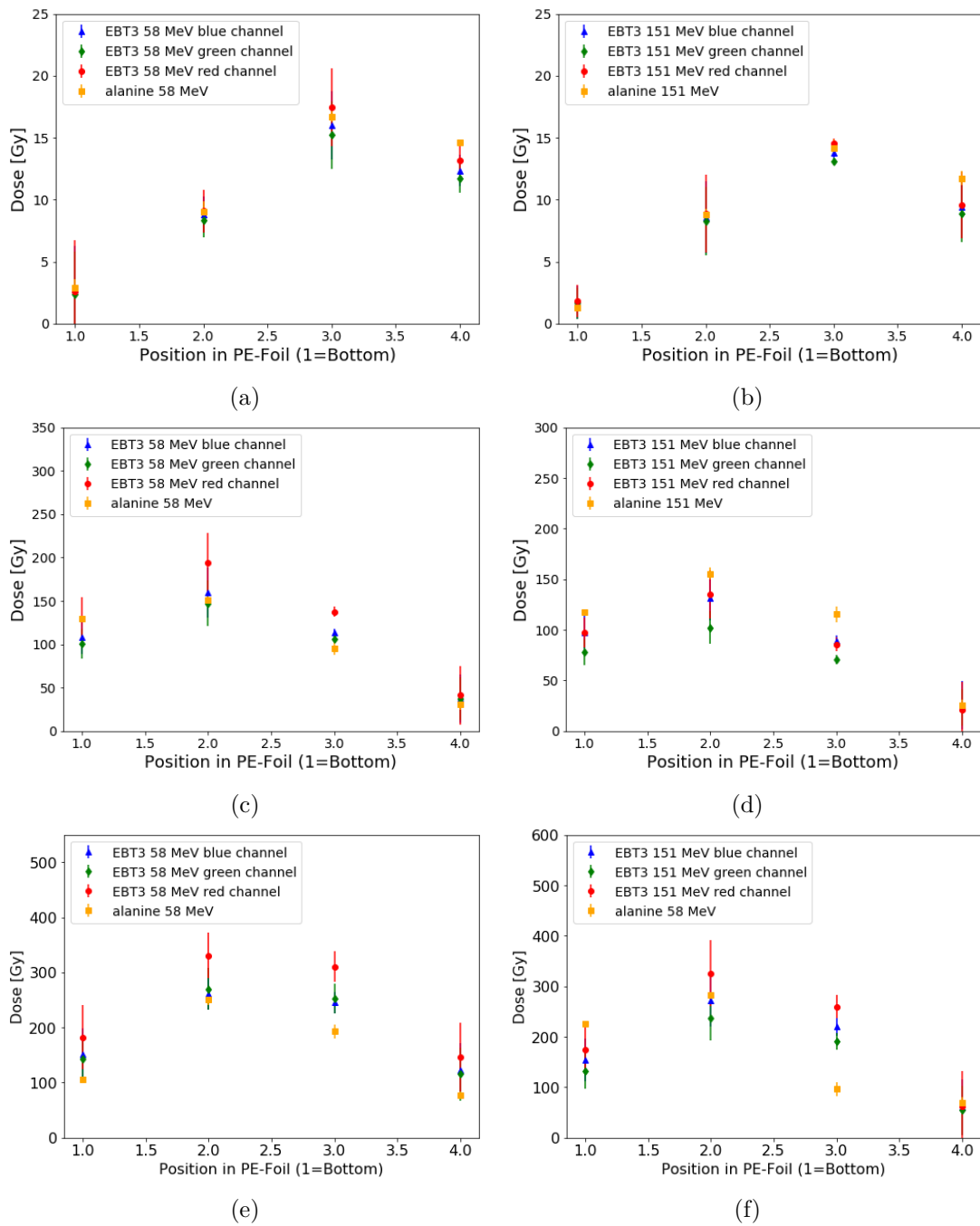
Figure 6.11: EBT3 and alanine doses measured at the positions 1-4 (corresponding to 4 alanine pellets) after irradiation with electron energies of 58 MeV (a, c, e) and 151 MeV (b, d, f), giving nominal doses of 20 Gy (a), 27 Gy (b), 217 Gy (c), 240 Gy (d), 368 Gy (e) and 360 Gy (f), respectively at the CLEAR user facility.

143

6.8 Uncertainty budget

The main contribution to the measurement uncertainties is the position of alanine with respect to the beam and EBT3 film sample. The pellets were kept in a plastic pocket to ensure that the relative position of the pellets in the stack is unchanged during irradiation. The positioning tolerance within a pocket is around 2 pixels (0.4 mm). The alanine was attached to the EBT3 films with a precision of ± 5 pixels (± 0.5 mm), which is the thickness of the black markers serving as position indicators. The pockets remained for a long time in vertical position in water. The force of gravity and water pressure resulted in the stacks being displaced from their initial positions in the vertical and horizontal planes. These positions were corrected using photographs of the prepared stacks, which were taken before and after irradiation, giving a maximum shift of 10 pixels (2 mm) in vertical plane and 13 pixels (2.6 mm) in horizontal plane. The variation of the reference depth is assumed to be equal to the thickness of the holder slot (2 mm) in which the EBT3 film was hold during the irradiation.
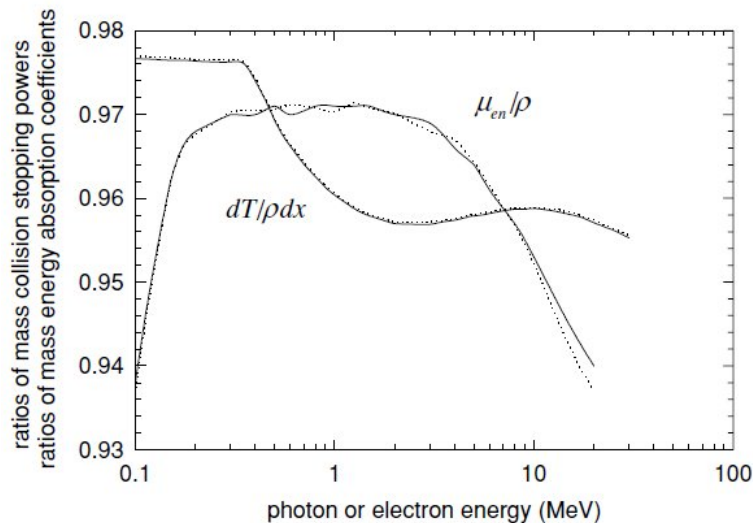
Figure 6.12: Ratios of mass energy absorption coefficients (μ_{en}/ρ) of alanine to water and of dosimeter material to water obtained from Mass En program (http://dax.northgate.utah.edu/MassEn.html)[215] based on NIST cross-sections [234] and ratios of restricted mass collision stopping powers ($dT/\rho dx$). Solid lines are for the ratios of pure alanine to water while the dotted lines are for pellet material (4% polyvinyl pyrrolidone) to water.

Additional uncertainties result from the large dose gradients within the pellets (5 %) and inhomogeneous field due to the small beam size with respect to the dimension of the stack. For VHEE energies the ratio of mass energy absorption coefficients of alanine to water is no longer constant, as shown in Figure 6.12, which can result in significant underestimation of the dose if not included in the dose evaluation.

6.9 Summary

This work demonstrates that alanine and EBT3 films can be reliably used for dosimetry of electron beams with energies up to 150 MeV and doses up to 368 Gy using all three channels. For high doses the blue channel might be preferable as the film response is closer to the dose given by alanine which has a dynamic range of up to 150 kGy. The differences between the doses measured by EBT3 and alanine result from the large dose inhomogeneity within the pellets arising from the small beam size used in the experiment. More precise methods would be required to further investigate the reliability of the relative response of alanine and EBT3 films to VHEE beams. However, this study provides a baseline for dosimetry assessment of electron beams that exceed clinical energy ranges, which supports future studies of FLASH radiotherapy using deeper penetrating electron beams, such as VHEEs.

Chapter 7

Experimental investigation of focused Very High Energy Electrons at the CLEAR user facility

This chapter describes the first experimental measurements of the depth-dose distribution of focused VHEE beams in a water phantom and compares these results with the predictions of the Monte Carlo simulations discussed in chapter 4. The experiment has been performed at the CERN user facility CLEAR using an S-band RF accelerator capable of producing electron beams with energies up to 220 MeV. Detailed description and the specifications of the accelerator are included in chapter 2.

7.1   Methods

This section describes the experimental setup, including the electron beam focusing optics and diagnostics. Data analysis, interpretation of the results and Monte Carlo simulations are also discussed.

7.1.1   Experimental setup

The CALIFES beamline was reconfigured as follows. Two triplets of electromagnetic quadrupoles (EMQs), with nominal gradient up to 11.2 T/m (Table 2.6), were used to focus the electron beam into a $30 \times 30 \times 30$ cm^3 PMMA tank placed 21.5 cm downstream from the last quadrupole. The first triplet, installed after the last RF deflecting cavity (MKS31 in Figure 7.1), is used to expand the beam over a length of about 3 m to produce the desired beam size in the second quadrupole triplet, which focuses the beam into the phantom. The electron beam exits the vacuum system through a 0.1 mm aluminium window and propagates in air for about 20.2 cm to the phantom. An integrating current transformer (ICT - Bergoz, ICT-055-070-5.0, SN 3350) is placed between the window and the phantom to measure the beam charge. The PMMA tank was filled with water during irradiation and mounted on a movable stage for precise translation in the direction perpendicular to the beam propagation axis. Irradiation was performed for up to 4-5 different stage positions using a stack of 21.5×6.75 cm^2 EBT3 strips mounted on a custom-designed holder and spaced by 1 cm, as shown in Figure 7.2. The films were replaced after irradiation and the procedure was repeated for different electron energies. The beam size in air was measured with an optical transition radiation (OTR) screen mounted on a translation stage that could move up to 20 cm along the beamline axis. In one case the measurement was repeated with a stack of EBT3 films in an empty PMMA tank (I am currently running simulations to include this data).
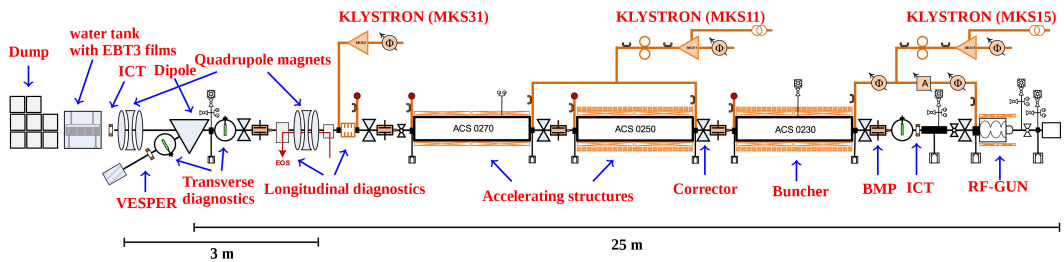
Figure 7.1: CLEAR beamline prepared for the experiment.
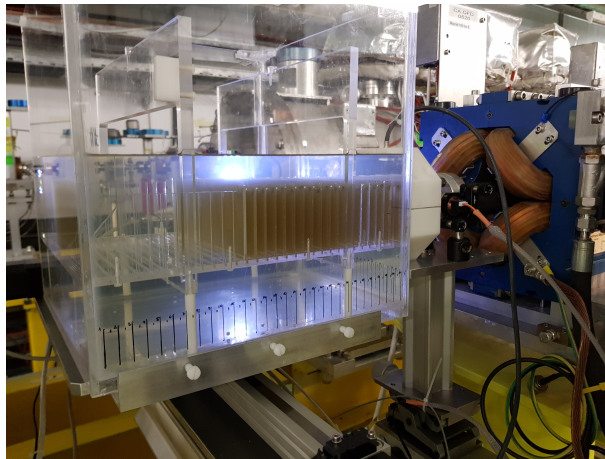
Figure 7.2: Water phantom with the EBT3 stack immersed in water.

7.1.2   Focusing configuration

Two electron beam energies are investigated (158 and 201 MeV) for different focusing strengths (between $f/11.2$ and $f/18.2$), obtained by adjusting the magnetic fields in the two quadrupole triplets. Three configurations are reported here. For 158 MeV the beam was focused at 14 cm from the phantom entrance with $f/11.2$ and at 10 cm with $f/12.3$, as measured using the OTR screen in air. For 201 MeV the beam was focused at 10 cm from the phantom entrance with $f/18.2$. FLUKA MC simulations show that the position of the focal spot is unchanged in vacuum and in air. It was originally intended to produce strong and symmetrical focusing, but this would have required installing larger quadrupoles in the CLEAR beamline, which was not possible in the allocated experimental time. Therefore, the beam was focused only in the horizontal plane. In the vertical plane, the beam is collimated or slightly diverging. In some cases the beam was clipping in the vacuum pipes and in the rectangular chamber of the electron spectrometer, resulting in a square beam profile in the vertical plane, with "shadows" produced by scattered electrons. In the horizontal plane the beam profile was approximately Gaussian for $f/12.3$ and $f/18.2$, but rectangular for $f/11.2$.

The Twiss parameters were measured with a quadrupole scan, as shown in Table 7.1. The beam transport was optimised using the software package MAD-X [235]. The magnetic gradients applied to individual quadrupole magnets for all focused beam

geometries are listed in Table 7.2. A plot of the beam envelope using the obtained Twiss parameters and optimised quadrupole settings is shown in Figure 7.3. The focal length, defined from the middle of the last quadrupole, are 46.8 cm for 158 MeV and $f/11.2$, 42.8 cm for 158 MeV and $f/12.3$, and 42.8 cm for 201 MeV and $f/18.2$, respectively. Films were irradiated with a charge of 0.92 nC (8 shots) for $f/11.2$, 0.58 nC (10 shots) for $f/12.3$ and 0.62 nC (10 shots) for $f/18.2$, based on the ICT measurements.

Table 7.1: Optimised beam parameters.

Parameter	158 MeV		201 MeV	
	Horizontal	Vertical	Horizontal	Vertical
beta (m)	9.03	5.88	11.40	5.30
alpha	-1.73	0.25	-1.90	-0.18
normalised emittance (mm · mrad)	6.80	6.90	5.80	11.40

Table 7.2: Optimised gradients applied to the quadrupole magnets.

Quadrupole	Gradient (T/m)		
	158 MeV ($f/10.9$)	158 MeV ($f/10.4$)	201 MeV ($f/18.2$)
Q350	8.55	8.55	0.00
Q355	10.26	10.26	11.40
Q360	0.00	0.00	0.00
Q510	11.40	11.40	2.31
Q515	8.04	8.21	7.17
Q520	10.49	11.06	10.98

7.1.3 Dose measurements

After exposure, the films are read using an Epson Expression 10000XL flatbed scanner and processed according to the procedure described in chapter 5. The pixel value before irradiation (PV_{before}) in equation 5.4 is defined as the average pixel value of four regions with dimensions of 5×5 pixels at the corners of the square area of 100×100 pixels which includes a beam spot in the centre. The dose is calculated as the peak value using the red colour channel and the formula 5.6. The calibration coefficients $a = 9$, $b = 60$, and $n = 3.2$, used to calculate the absorbed dose, were obtained from the calibration performed for electron energy of 50 MeV at the PTB research accelerator.
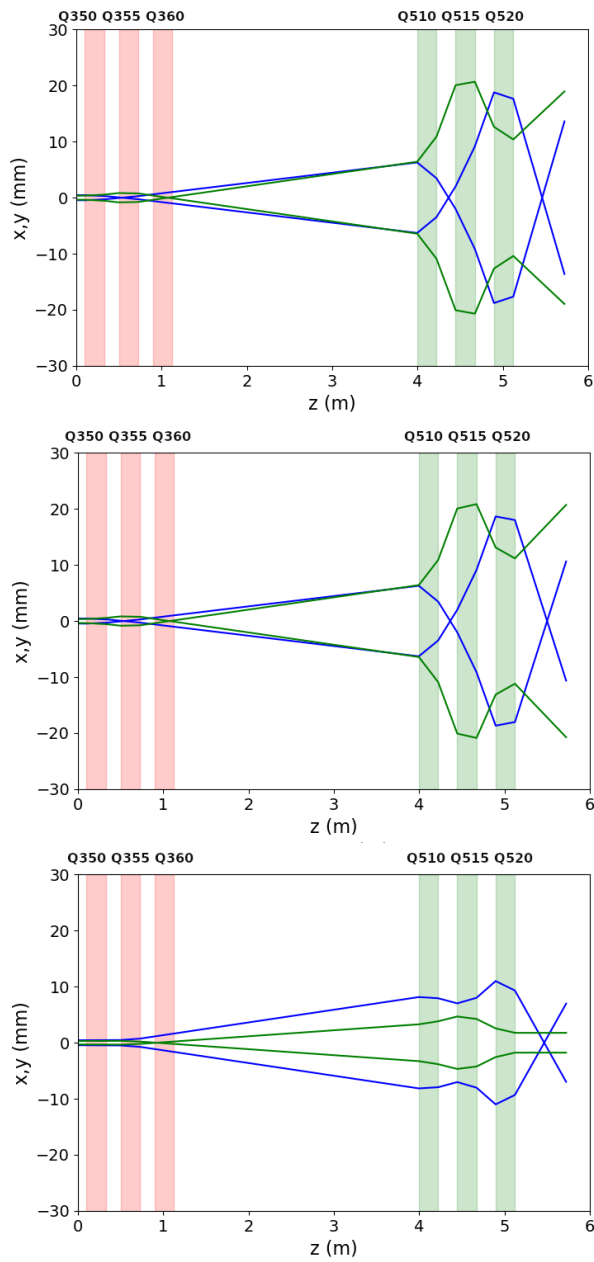
Figure 7.3: Optimised beam envelope (from top to bottom) for 158 MeV and $f/11.2$, 158 MeV and $f/12.3$, and 201 MeV and $f/18.2$. The blue line is a beam envelope in the horizontal plane and the green line in the vertical plane. Red and green bars indicate positions of the quadrupole magnets presented in Figure 2.17 of the experimental beamline.

7.2 FLUKA simulations

Monte Carlo FLUKA simulations were performed to model the beam envelope and depth-dose distribution in a water phantom for the same beam configurations used in the experiment. The electron beam initial size and divergence at the entrance of the tank was calculated from the focal length measured with the OTR screen and from the beam size in the first EBT3 film. The profile in the vertical plane was rectangular for all *f-numbers*. The profile in the horizontal plane was Gaussian for $f/12.3$ and $f/18.2$ and rectangular for $f/11.2$, as discussed in subsection 7.1.2. The OTR diagnostic could not be used to determine the transverse beam size, because it was not configured to save the full 2D images, but only the coefficients of Gaussian fits in the horizontal and vertical planes. These results were not reliable because of the non-Gaussian beam profiles.

The energy deposition is scored using a `USRBIN` card with resolution of 0.025 cm in directions perpendicular to the beam propagation axis, and 0.079 cm along the beam axis. The depth-dose curves were obtained by averaging the dose in a volume of $0.025 \times 0.025 \times 30$ cm^3 with the longer dimension parallel to the central beam axis. Simulations are performed with 10^7 particles and 5 cycles, which resulted in statistical uncertainties of less than 3.2% for all beam geometries. The physics settings, energy threshold for production and transport of delta particles and survival probabilities of secondary particles are described in detail in chapter 4.

7.3 Results

Figure 7.4 shows the measured transverse dose profiles at 5 depths for 158 MeV (both *f-numbers*), and 201 MeV. A 3D reconstruction of the dose distribution was based on fitted functions: third order polynomial and square root of third order polynomial, for the envelopes in vertical and horizontal planes across the whole film stack, respectively. The line focus results in the formation of elliptical spots. As the beam propagates deeper into the phantom, however, the transverse beam shape becomes symmetrical due to scattering.

Figure 7.5 shows the full-width-at-half-maximum (FWHM) obtained from the EBT3 films (data points) and from FLUKA Monte Carlo simulations (solid curves) for different beam geometries. Figure 7.6 shows the corresponding depth-dose profiles, including also simulations results obtained for symmetrical focus (green curves) and collimated beam (purple curves) using the FWHM at the phantom entrance obtained experimentally in the focusing plane ($FWHM_x$). The FLUKA results, normally expressed in Gray per primary, have been rescaled to match the charge recorded with the ICT unit. The curves for collimated and symmetric beams have been normalised to the same peak dose obtained experimentally. The beam charge is higher by a factor 6.3, 7.1 and 5.3, respectively.

Table 7.3: FWHM obtained from the horizontal and vertical projections of the transverse beam profile acquired by EBT3 film at the focus, and peak dose depth in water (measured by EBT3 films) and in air (measured by the OTR screen) from the phantom entrance.

	158 MeV, $f/11.2$	**158 MeV, $f/12.3$**	**201 MeV, $f/18.2$**
fwhm$_x$ (mm)	3.8	5.6	3.0
fwhm$_y$ (mm)	3.7	4.9	2.0
Depth in air (cm)	14	10	10
Depth in water (cm)	6.4	7.7	5.7

Measurements and simulations show that the peak dose is located at a depth of about 5-6 cm inside the phantom for all beam geometries. Scattering in water shifts the focus position, with respect to the reference position in air (Table 7.3), as observed also in the simulations discussed in chapter 4. The displacement depends on the *f-number* and on the electron energy. For the configurations used in the experiment, the focus was shifted towards the phantom entrance by 7.6, 2.3 and 4.0 for $f/11.2$, $f/12.3$ and $f/18.2$, respectively. The smallest spot size at the focus is about 3 mm (FWHM), obtained for 201 MeV energy.
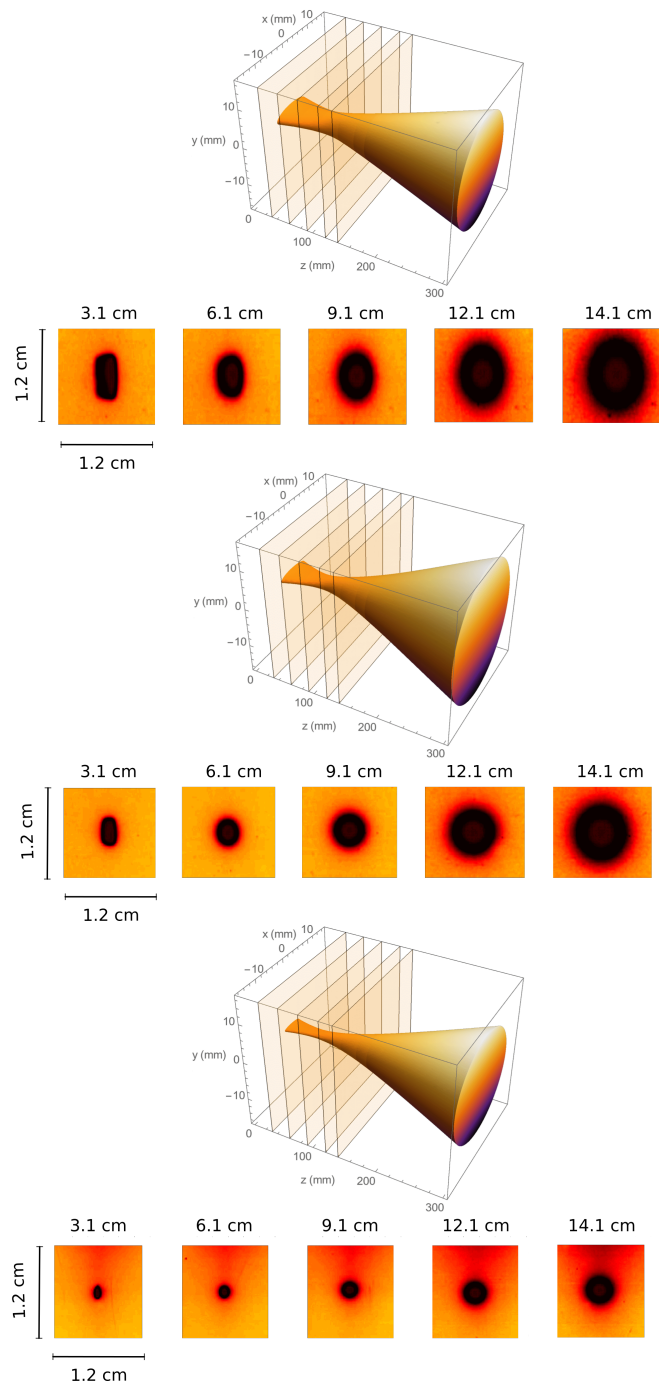
Figure 7.4: 3D reconstruction of the dose distribution generated by focused electron beams in water based on transverse beam profiles measured using a stack of EBT3 films for 158 MeV $f/11.2$ (top), 158 MeV $f/12.3$ (middle), and 201 MeV $f/18.2$ (bottom). Dose profiles in the films at selected depths are also included. Figure provided by Dr. Enrico Brunetti.
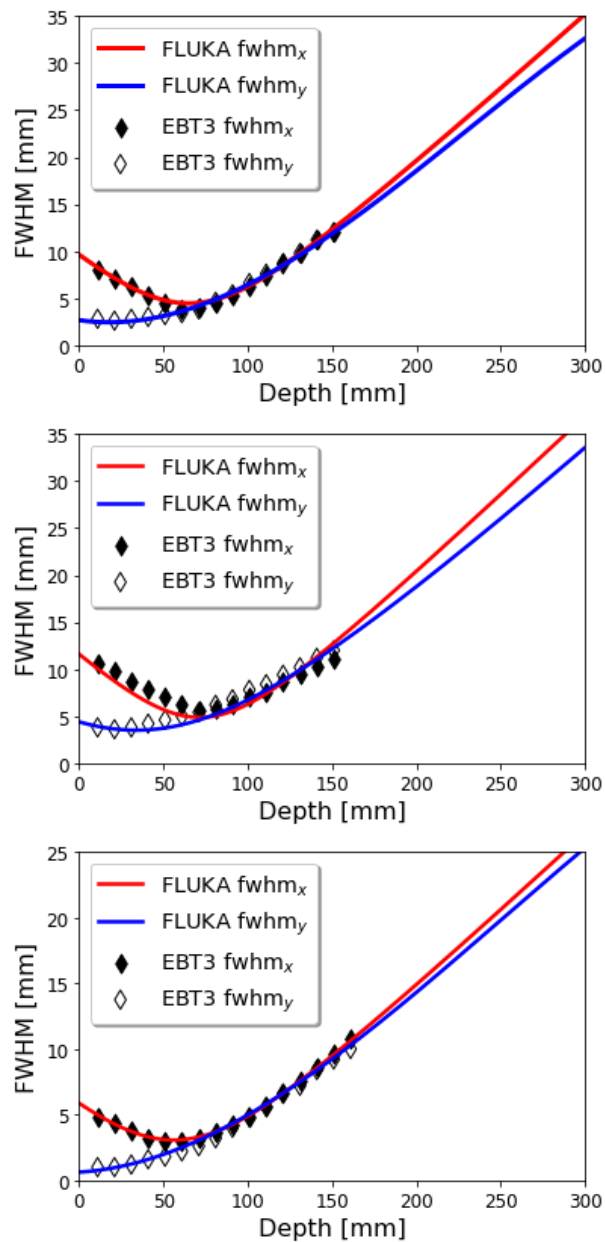
Figure 7.5: Size (FWHM) of the dose distribution in the horizontal (full diamonds) and vertical (empty diamonds) planes measured using a stack of EBT3 films in a water phantom for focused electron beams with parameters 158 MeV and $f/11.2$ (top), 158 MeV and $f/12.3$ (middle), and 201 MeV and $f/18.2$ (bottom). Solid lines are FLUKA simulation results in the horizontal (red) and vertical (blue) planes.
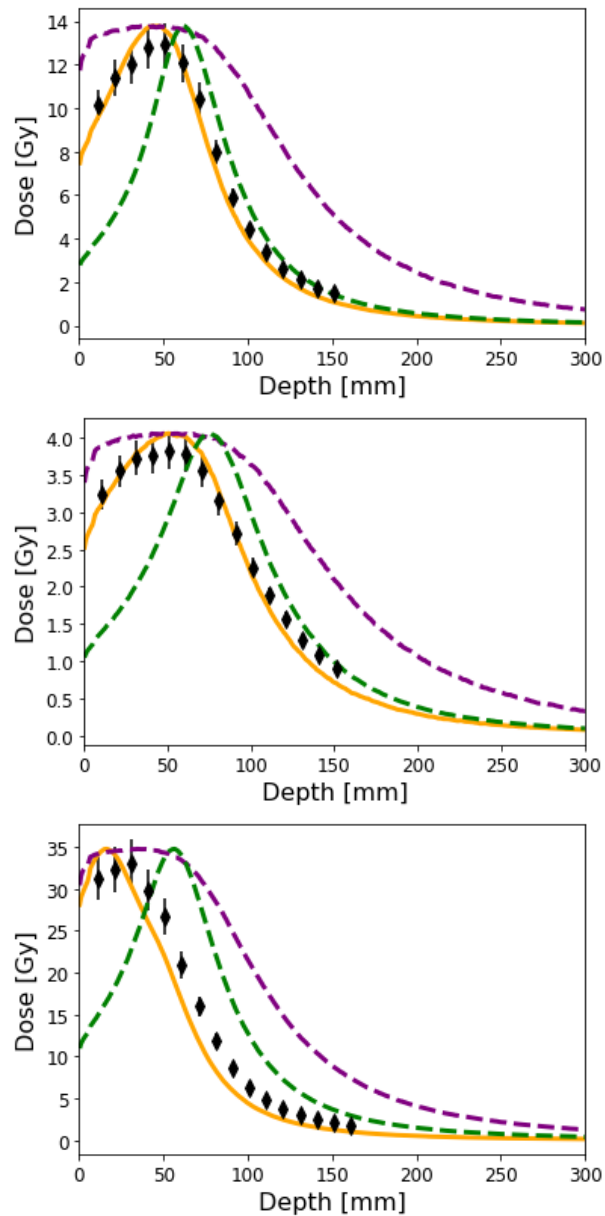
Figure 7.6: On-axis dose profile measured using a stack of EBT3 films in a water phantom for focused electron beams with parameters 158 MeV and $f/11.2$ (top), 158 MeV and $f/12.3$ (middle), and 201 MeV and $f/18.2$ (bottom). The orange curves are the results of FLUKA simulations for the same configuration used in the experiment. Green dashed lines are FLUKA simulation results obtained for symmetrical focus and purple ashed lines for a collimated beam.

Table 7.4 includes peak dose values for all *f-numbers*. The line focus results in an enhanced peak dose by a factor of 4.4, 6 and 1.7 times for $f/11.2$, $f/12.3$ (158 MeV) and $f/18.2$ (201 MeV), respectively, compared with a collimated beam. These numbers for the symmetrically focused beams are 1.4, 1.3 and 0.6 in order of increasing *f-number*. Symmetrical focus reduces the surface peak dose by 4, 3.2, 2.5 times, respectively, compared with collimated beams and around two times less than this, compared with a line focus.

Table 7.4: Peak dose for different beam geometries obtained with FLUKA MC code estimated for charged delivered experimentally.

	Peak dose (Gy)		
	158 MeV, $f/11.2$	**158 MeV, $f/12.3$**	**201 MeV, $f/18.2$**
Line focus	13.82	4.07	34.65
Symmetrical focus	10.03	3.03	11.98
Collimated beam	2.32	0.92	4.21

7.4   Summary

Experiments using focused VHEE beams confirm the depth-dose enhancement predicted by the simulations described in chapter 4. The dose was concentrated into a well defined *volumetric element* at a depth of about 5-6 cm. For fixed electron energy, the peak dose decreases with *f-number*. For smaller *f-numbers* the *volumetric element* is more symmetrical. Monte Carlo simulations were performed to model the irradiation of a water phantom on the CLEAR user facility beamline. For the experimental configuration of line focus the dose was enhanced by up to 8 times. Simulations predict an enhancement up to 16 for symmetrical focusing, but this configuration could not be investigated experimentally because there was not enough time to upgrade the power supplies of the first quadrupole triplet and install larger aperture quadrupoles in the second triplet. Control of the peak dose and its depth using focusing geometry with beam scanning could be utilised to target hypoxic regions.

Chapter 8

Discussion and future work

8.1 Discussion and conclusions

Current electron radiotherapy utilises low-energy electrons with an energy less than 25 MeV, which have shallow penetration depths and thus are only useful for the treatment of superficial tumours or for intra-operative radiotherapy [236]. VHEEs (50 – 250 MeV) have the potential to deliver precisely high doses deep into tissue, owing to the high inertia which results from their relativistic mass. As reported for the first time by DesRosiers [58, 57], advantages of VHEEs are deep penetration, low penumbra, and the absence of electronic disequilibrium and particle range straggling at tissue interfaces. However, the approximately uniform depth-dose profile produced by a single collimated VHEE beam presents an obstacle to the translation of VHEET to future clinical trials due to the potentially high risk of secondary tumours or radiation damage of the skin. Over the past 70 years many studies have been carried out to reduce the off-axis dose resulting from scattering. These mainly focused on treatment planning using multiple beams and the use of external magnetic fields to control the dose distribution of electrons up to 70 MeV.

As a first step towards clinical implementation this thesis presents and discusses a proof-of-principle study of focused VHEE beams. The dose distributions in tissue-equivalent material were investigated experimentally and numerically using FLUKA Monte Carlo simulations. FLUKA provides an accurate implementation of the physics

relevant to the transport of charged particles in magnetic and electric fields up to TeV energies [237]. The physics settings for VHEEs have been chosen based on work by A. Subiel [177, 72], where FLUKA predictions for VHEEs are found to be consistent with experimental predictions for diverging beams with energies close to 165 MeV. The present thesis considers different beam focusing configurations, defined by the *f-numbers* and where a strongly focused beam is consistent with *f-numbers* less than $f/3.8$. The simulations presented here show that a single focused VHEE beam can produce a high dose small *volumetric element* at the typical depths of deep seated tumours (15 cm). High energy eliminates dose depth effects, while beam focusing concentrates the desired dose into the target, deep in tissue, while simultaneously spreading the electrons over a large volume of normal tissue, which protects against receiving high doses. Furthermore, ultra-high energies (2 GeV) have been shown to further reduce scattering and also the size of the *volumetric element*, compared with 200 MeV beams. Tumours with irregular shapes and larger sizes can be treated by scanning the focused beam over the desired volume, or by delivering the beam from multiple directions.

The application of collimated VHEEs in radiotherapy has been shown to be limited by the skin cumulative dose, which becomes prohibitively large (more than 70% of the peak dose) when sufficient doses are delivered deep into the patient's body by one beam. Strongly focused beams result in a significant reduction in the total and peak dose at the entrance and exit, compared with collimated and weakly focused beams. Moreover, beam characteristics such as energy and *f-number* can introduce additional degrees of optimisation in treatment planning for focused VHEEs to produce highly conformal dose distributions at the target depth. Other beam parameters, not considered here, such as energy distribution and beam profile will be investigated in the future to assess their impact on dose distribution in tissue.

FLUKA MC simulations have been used to determine the distribution of both primary and secondary particles and the induced activity. The radiation produced by VHEE beams is spatially dependent and multi-component in tissue-equivalent media, which also has an impact on the individual component dose distributions. It is observed that the largest fraction of the central-axis dose is deposited by low-energy electrons

and positrons arising from photon and electron interactions. Particles produced by secondary photons contribute to approximately 27% of the total dose across the whole phantom. The dose deposited in the phantom from the induced radioactive products accumulates in the focal spot where it has a maximum. Assuming delivery of the standard clinical fraction of dose (2 Gy), dose deposited by induced radioactivity is 5-6 orders of magnitude lower than the prescribed dose and 5 times higher than for 147 MeV protons at the same depth after 1 min. However, induced radioactivity decreases faster for electrons than for protons due to different types of radioactive decay products. The dose deposited by secondary particles and induced radioactivity can be of concern because of the relatively high biological response of tissue to activated elements. This is quantified by the relative biological effectiveness (RBE), which is defined as the ratio of absorbed dose of a reference radiation type (e.g. X-ray) to absorbed dose of the radiation of interest. The RBE is related to the linear energy transfer (LET), a concept introduced in chapter 4. The majority of secondary particles in VHEE therapy, i.e. electrons, photons and positrons, are low LET particles. The LET of electrons is found to vary between 0.2-0.27 keV/μm, which is 4-5 times lower than for photons. Neutrons, on the other hand, have high LET and can induce significant radiation damage even if present in small numbers. However the contribution of neutrons dose to the total dose is negligible for the standard target dose (2 Gy) for both 200 MeV and 2 GeV beams. Furthermore, simulations for 200 MeV focused beams show that about 10^{-4} neutrons/cm^2/prim.e are produced in the energy range of 0.1 MeV-10 MeV, where the RBE is up to 20 times higher than for photons [238]. Assuming a radiotherapy fraction that delivers 2 Gy in the volumetric element, we estimate that 10^7 neutrons/cm^2 would be produced in the whole phantom. For focused VHEEs, these are concentrated in the volumetric element, making the radiobiological effectiveness of the irradiation dependent on the depth, which is desirable for RBE geometry-directed treatment planning for hypoxic cancers [239]. Knowledge of the radiobiology of VHEEs is essential for achieving a uniform cell kill throughout volumes with heterogeneous radiosensitivity. For instance, selective placement of concentration regions of high LET secondary particles in hypoxic regions of the tumour, so-called LET-painting [240, 241], would be

highly desirable and might improve tumour control. The study of secondary radiation for beams produced by clinical accelerators is also important from the radioprotection point of view. The study of yield of neutrons and bremsstrahlung from the patient and beam modifiers in photon and proton therapy is necessary to assess the amount of shielding required. Intensity modulation and field shaping using standard MLC would not be feasible for VHEEs in a standard clinical setting due to the potentially large amounts of induced secondary radiation. Therefore, a scanning system would preferable in future implementations of focused VHEEs.

Another area requiring more progress is in VHEE dosimetry. Currently, no dosimetry protocols exist for electron beam energies exceeding 20 MeV, and additional measurements had to be performed prior to the focused VHEE experiment to characterise the response of detectors, alanine and EBT3 radiochromic films, to energies up to 150 MeV. These two standard dosimeters are energy independent within therapeutic energy ranges (6 – 16 MeV) [202], but the energy dependence and robustness beyond electron energies of 20 MeV has not been studied. The response of EBT3 films to nominal doses ranging from 1 to 60 Gy was investigated with the research accelerator at PTB for electron energies between 16 and 49 MeV. Results were validated against the reading of an Advanced Markus Chamber and FLUKA simulations in the dose range of interest. The response of EBT3 films for electron energy of 49 MeV was found to agree well with the responses obtained for 20 MeV, which was traceable to the primary standard established by PTB. Therefore, the calibration curve obtained for 49 MeV energy was used to determine doses measured at CERN. The EBT3 films were found to be energy independent for electron energies up to 49 MeV and could be reliably used for dosimetry following the proposed protocol. Additional measurements were performed at NPL using EBT3 films and doses reaching 900 Gy. The results were used to calculate doses measured by EBT3 films irradiated at CERN using high beam charge. The calibration curve for NPL measurements was obtained using a second order rational function, which provided a satisfactory fit over a whole dose range. This study provided a baseline for dosimetry assessment of electron beams exceeding the nominal clinical energy ranges, which could also support future studies of FLASH radiotherapy using deeper

penetrating beams and extremely high doses.

In chapter 7 the first experimental measurements of the depth-dose distribution of focused VHEE beams in a water phantom were presented and discussed. Both experiments and simulations show an enhancement of the doses deposited at depth of the focus, as predicted by previous theoretical studies in chapter 4. The dose was concentrated into a well-defined volumetric element at depth of about 5-6 cm. The smallest spot size at the focus was about 3 mm (FWHM) for 201 MeV energy. Focusing results in peak dose enhancement of up to 8 times, compared with a collimated beam and sparing of the surface dose up to 29%. This value could be reduced substantially using symmetrically focused beams, which would also deliver the peak dose deeper into the body. However, the VHEE beams produced by the accelerator at CERN could be sharply focused in one plane with the available quadrupole magnets to create a line focus. Symmetric focusing could be achieved in the future by upgrading the power supplies of the first quadrupole triplet and employing larger aperture quadrupoles in the second triplet. Further design of large aperture focussing systems would be required to future clinical translation. Large-aperture, high-gradient quadrupole magnets are already widely used and may overcome these limitations. Already available superconducting magnets have a 33 T/m central gradient with inner aperture diameter of 240 mm and magnetic length of 2 m, [242], which would be capable of producing beams with $f/1.2$.

VHEEs are an excellent choice for scanning radiation delivery because they are light, cost effective to accelerate and sufficiently energetic to deliver dose to any region of the human body. A scanning system for VHEEs would be simpler and less expensive than for heavy particles, such as protons or carbon ions. In the light of a novel superconducting gantry designed at CERN, GaToroid [243], which bends a treatment beam without the need for a rotating structure, the scanning of VHEEs seem to be even more promising. The superconducting coils that are organised in toroidal shape magnets substantially reduce the weight and overall size of the gantry, compared with conventional technology. The size of accelerators for VHEET could be reduced using new accelerator technologies such as compact high-gradient X-band structures

designed at CERN. Currently available high energy accelerators producing 200 MeV electron beams with an average current of 1000 nA would deliver a single radiotherapy fraction (2 Gy) in 20 ms, assuming strong focusing, with a further reduction in irradiation time to 0.6 ms for 2 GeV beam energy with similar current. In conventional radiotherapy a prescribed dose (70 Gy), which is usually divided into smaller fractions and administered in 35 days, can be delivered in 700 ms.

Current advances in laser-plasma wakefield accelerators are compact, cost-effective and an efficient method of delivering VHEE therapy because the laser beam can be divided into several beams using mirrors and Pockels cells, polarisers and diffractive optics. This creates the possibility of a large number of beams, each driving mm long accelerators, to produce VHEE beams in a treatment delivery room [244]. Laser-driven beams deliver VHEE beams with femtosecond bunch length. The unique characteristic of light is that laser beams can be multiplexed and transported to treatment rooms without requiring shielding, which reduces the costs of building large infrastructures. Additional advantages of these types of accelerators is that they are multimodal. Laser-driven electron bunches can be used to produce protons and ions, high brightness X-ray and gamma ray pulses, all in one laboratory using the same laser beam. The recently established Scottish Centre for the Application of Plasma-based Accelerators (SCAPA), located at the University of Strathclyde, UK, aims to exploit multidisciplinary applications.

8.2 Outlook and future work

There are still many issues that needed to be addressed before VHEE radiotherapy can be used for treatment of cancer patients. The radiobiological effect of VHEEs is still not fully understood. In 2012 the University of Strathclyde started the first experimental investigations of cell survival after irradiation with VHEEs. Beyond that there is no record of any ongoing studies in this area. The distribution of secondary radiation and induced activity produced by VHEEs in tissue-equivalent materials was investigated together with LET distribution for electrons. The results provide an insight into mech-

anisms of dose depositions. The quantitative predictions of biological effect (RBE) from LET values are not possible. LET does not provide an accurate indication of the actual energy deposited in small target volumes of interest at level of individual cells, where single and double DNA strand breaks take place. This is partly because the amount of energy that can be deposited in the target volume (cells) is currently unmeasurable. Therefore, development of suitable micro- and nano-dosimetry is necessary to explain the dose response relationship in cells or smaller than that environments.

On the other hand, there are many treatment planning studies with VHEEs, but only a few performed using real 3D scans of cancer patients. Statistics on treatment outcomes using patient data are necessary to find optimal constraints for VHEEs. Nevertheless, current in-house treatment planning system for VHEEs must be further developed. An accurate physics and real beam parameters from clinical accelerator for VHEE therapy should be implemented and for the latest the design of a treatment machine is necessary. In the final step the NTCP and TCP models should be validated for VHEEs based on radiobiological studies. Further treatment planning studies should also be carried out to establish beam geometries for single or scanned focused VHEEs that offers the best balance between satisfactory tumour control and treatment latency for different clinical cases.

Most of the FLASH radiotherapy studies have been conducted using electron beams from linear accelerators with energies of about 6 MeV or 20 MeV [53]. However, low energy is not practical because of limited penetration depth. The application of clinical photons in FLASH radiotherapy, on the other hand, is problematic due to technical problems such as melting of linac tungsten targets struck by high dose rate electrons. VHEEs have significantly increased practical range and do not require a metal converter. Moreover, focused VHEEs could deliver sufficient dose rates especially using sub-picosecond bunches that can be produced by high-current laser-plasma accelerators. The Strathclyde Intense Laser Interaction (SILIS) Studies Group has recently shown, experimentally and theoretically, that an unprecedented high charge (10 − 500 nC), stable but relatively broad energy spread and divergent beam with an energy up to several MeV can be generated. These beams will be used to conduct a study of

methods for dose rate independent dosimetry.

The *in-situ* dose verification for VHEEs is also required to verify treatment plans and reduced uncertainties. Assuming delivery of 2 Gy of dose with 200 MeV beam energy, 10^{10} positrons are produced in the volumetric element, which is two orders of magnitude higher than the number of positrons delivered by the most commonly used radioactive tracer ^{11}C during positron emission tomography. Some of these positrons will interact with atomic electrons in tissue. The result of the collision is the annihilation of the electron and positron, and the creation of gamma ray photons. These two gammas, with energy of 511 keV each, travel in opposite directions and can be detected in PET. In contrast to diagnostic PET, where radioactive tracer introduce additional dose into the patient, VHEEs can work as 'tracer', therefore no dose will be delivered beyond what is deposited during the treatment.

List of Figures

List of Tables

Bibliography

[1] MacMillan Cancer Support. Cancer in numbers. `https://www.macmillan.org.uk/about-us/media-centre/facts-and-figures/cancer-in-numbers.html`, 2018. (accessed August 11, 2018).

[2] International Agency for Research on Cancer. Global Cancer Observatory. `http://gco.iarc.fr/today/`, 2018. (accessed January 27, 2020).

[3] W C Röntgen. Ueber eine neue art von strahlen. *Annalen der Physik*, 300(1): 1–11, 1898.

[4] E H Grubbé. *X-ray treatment; its origin, birth and early history.* Bruce Publishing, 1949.

[5] N Foray. Victor despeignes (1866–1937): comment un hygiéniste devint le premier radiothérapeute de l'histoire. *Cancer Radiothérapie*, 17(3):244–254, 2013.

[6] L Freund. Ein mit röntgen-strahlen behandelter fall von naevus pigmentosus piliferus. *Wiener Medizinische Wochenschrift*, 47:428–434, 1897.

[7] L S Taylor. History of the international commission on radiological protection (ICRP). *Health Physics*, 1(2):97–104, 1958.

[8] A H Becquerel. Sur les radiations invisibles émises par les corps phosphorescents. *Comptes rendus de l'Académie des Sciences*, 122:501–503, 1896.

[9] P Curie. Sur une substance nouvelle radio-active, continue dans la pechblende. *Comptes rendus de l'Académie des Sciences*, 127:175–178, 1898.

[10] R F Mould. The discovery of radium in 1898 by Maria Sklodowska-Curie (1867-1934) and Pierre Curie (1859-1906) with commentary on their life and times. *The British Journal of Radiology*, 71(852):1229–1254, 1998.

[11] H Becquerel and P Curie. Action physiologique des rayons du radium. *Comptes rendus de l'Académie des Sciences*, 132:1289–1291, 1901.

[12] H Danlos and P Bloch. Note sur le traitement du lupus érythémateux par des applications du radium. *Annales de Dermatologie et de Syphilogie*, 2:986–988, 1901.

[13] E Lysholm. Apparatus for the production of a narrow beam of γ-rays in treatment by radium at a distance. *Acta Radiologica*, 2(6):516–519, 1923.

[14] G Failla. Design of a well-protected radium 'Pack'. *American Journal of Roentgenology*, 20(2):128–141, 1928.

[15] W Stentström. Methods of improving the external application of radium for deep therapy. *American Journal of Roentgenology*, 11:176–186, 1924.

[16] D W Fry, R B R S Harvie, L B Mullett, and W Walkinshaw. A travelling-wave linear accelerator for 4 MeV electrons. *Nature*, 162(4126):859–861, 1948.

[17] R R Wilson. Radiological use of fast protons. *Radiology*, 47(5):487–491, 1946.

[18] C A Tobias, J H Lawrence, J L Born, R K McCombs, J E Roberts, H O Anger, B V A Low-Beer, and C B Huggins. Pituitary irradiation with high-energy proton beams a preliminary report. *Cancer Research*, 18(2):121–134, 1958.

[19] J R Castro. Results of heavy ion radiotherapy. *Radiation and Environmental Biophysics*, 34(1):45–48, 1995.

[20] P H Fowler and D H Perkins. The possibility of therapeutic applications of beams of negative π-mesons. *Nature*, 189(4764):524–528, 1961.

[21] C F Von Essen, H Blattmann, J F Crawford, P Fessenden, E Pedroni, C Perret, M Salzmann, K Shortt, and E Walder. The piotron: initial performance,

preparation and experience with pion therapy. *International Journal of Radiation Oncology •Biology •Physics*, 8(9):1499–1509, 1982.

[22] Particle Therapy Co-Operative Group. Particle therapy facilities in operation. `https://www.ptcog.ch/index.php/facilities-in-operation/`. (accessed August 18, 2018).

[23] V L Martinez Marignac, L Mondragon, and J L Favant. Sources of ionizing radiation and their biological effects: An interdisciplinary view, from the physics to cell and molecular biology. *Clinical Cancer Investigation Journal*, 8(4):129, 2019.

[24] D T Goodhead. The initial physical damage produced by ionizing radiations. *International Journal of Radiation Biology*, 56(5):623–634, 1989.

[25] W Friedland, H G Paretzke, F Ballarini, A Ottolenghi, G Kreth, and C Cremer. First steps towards systems radiation biology studies concerned with DNA and chromosome structure within living cells. *Radiation and Environmental Biophysics*, 47(1):49–61, 2008.

[26] R Téoule. Radiation-induced DNA damage and its repair. *International Journal of Radiation Biology and Related Studies in Physics, Chemistry and Medicine*, 51(4):573–589, 1987.

[27] D T Goodhead. Initial events in the cellular effects of ionizing radiations: clustered damage in DNA. *International journal of radiation biology*, 65(1):7–17, 1994.

[28] Z Nikitaki, V Nikolov, I V Mavragani, E Mladenov, A Mangelis, D A Laskaratou, G I Fragkoulis, C E Hellweg, O A Martin, D Emfietzoglou, V I Hatzi, G I Terzoudi, G Iliakis, and A G Georgakilas. Measurement of complex DNA damage induction and repair in human cellular systems after exposure to ionizing radiations of varying linear energy transfer (LET). *Free Radical Research*, 50(sup1): S64–S78, 2016.

[29] A Schipler, V Mladenova, A Soni, V Nikolov, J Saha, E Mladenov, and G Iliakis. Chromosome thripsis by DNA double strand break clusters causes enhanced cell lethality, chromosomal translocations and 53BP1-recruitment. *Nucleic Acids Research*, 44(16):7673–7690, 2016.

[30] Canadian Nuclear Association teachnuclear. Effects of ionizing radiation on DNA. `https://teachnuclear.ca/all-things-nuclear/radiation/biological-effects-of-radiation/effects-of-ionizing-radiation-on-dna/`, 2020. (accessed January 27, 2020).

[31] G W Barendsen. Dose fractionation, dose rate and iso-effect relationships for normal tissue responses. *International Journal of Radiation Oncology ·Biology ·Physics*, 8(11):1981–1997, 1982.

[32] T T Puck and P I Marcus. Action of X-rays on mammalian cells. *Journal of Experimental Medicine*, 103(5):653–666, 1956.

[33] M Bellamy, J Puskin, N Hertel, and K Eckerman. An empirical method for deriving RBE values associated with electrons, photons and radionuclides. *Radiation Protection Dosimetry*, 167(4):664–670, 2015.

[34] B Emami. Tolerance of normal tissue to therapeutic radiation. *Reports of radiotherapy and Oncology*, 1(1), 2013.

[35] E B Podgoršak. *Radiation oncology physics: a handbook for teachers and students.* International Atomic Energy Agency, 2005.

[36] Deutsches Krebsforschungszentrum. Biological models. `http://www.dkfz.de/en/medphys/appl_med_rad_physics/Biological_models.html`. (accessed January 16, 2019).

[37] J H Lambert. *Photometria sive de mensura et gradibus luminis, colorum et umbrae (1760)*. Wilhelm Engelmann, 1892.

[38] W H Bragg and R Kleeman. XXXIX. on the α-particles of radium, and their loss of range in passing through various atoms and molecules. *The London, Edinburgh, and Dublin Philosophical Magazine and Journal of Science*, 10(57):318–340, 1905.

[39] J Van Dyk and J J Battista. Cobalt-60: an old modality, a renewed challenge. *Current Oncology*, 3(10), 1996.

[40] J Van Dyk. *The modern technology of radiation oncology*. Medical Physics Publishing, 1999.

[41] A Ammar. Opening lecture: Lars Leksell's vision-radiosurgery. *Acta Neurochirurgica Supplementum*, 62:1–4, 1994.

[42] C A Perez, J A Purdy, W Harms, R Gerber, M V Graham, J W Matthews, W Bosch, R Drzymala, B Emami, S Fox, E Klein, H K Lee, J M Michalski, and Simpson J R. Three-dimensional treatment planning and conformal radiation therapy: preliminary evaluation. *Radiotherapy and Oncology*, 36(1):32–43, 1995.

[43] J M Galvin, A R Smith, R D Moeller, R L Goodman, W D Powlis, J Rubenstein, L J Solin, B Michael, M Needham, C J Huntzinger, and Kligerman M M. Evaluation of multileaf collimator design for a photon beam. *International Journal of Radiation Oncology •Biology •Physics*, 23(4):789–801, 1992.

[44] E S Sternick. *The theory and practice of intensity modulated radiation therapy.* Advanced Medical Publishing, 1997.

[45] T Bortfeld. IMRT: a review and preview. *Physics in Medicine & Biology*, 51(13): R363–R379, 2006.

[46] K Otto. Volumetric modulated arc therapy: IMRT in a single gantry arc. *Medical Physics*, 35(1):310–317, 2008.

[47] G Kurup. Cyberknife: a new paradigm in radiotherapy. *Journal of Medical Physics*, 35(2):63, 2010.

[48] M Hadziahmetovic, B W Loo, R D Timmerman, N A Mayr, J Z Wang, Z Huang, J C Grecula, and S S Lo. Stereotactic body radiation therapy (stereotactic ablative radiotherapy) for stage i non-small cell lung cancer-updates of radiobiology, techniques, and clinical outcomes. *Discovery Medicine*, 9(48):411–417, 2010.

[49] T Depuydt. Proton therapy technology evolution in the clinic: impact on radiation protection. *Annals of The International Commission on Radiological Protection*, 47(3-4):177–186, 2018.

[50] A Schätti. *Towards the treatment of moving targets with scanned proton beams: experimental verification of motion mitigation techniques with Gantry 2 at PSI.* PhD thesis, Swiss Federal Institute of Technology, 2013.

[51] D A Jaroszynski, R Bingham, E Brunetti, B Ersfeld, J Gallacher, B van Der Geer, R Issac, SP Jamison, D Jones, M De Loos, A Lyachev, V Pavlov, A Reitsma, Y Saveliev, G Vieux, and S M Wiggins. Radiation sources based on laser-plasma interactions. *Philosophical Transactions of the Royal Society A: Mathematical, Physical and Engineering Sciences*, 364(1840):689–710, 2006.

[52] L H Gray, A D Conger, M Ebert, S Hornsey, and O C A Scott. The concentration of oxygen dissolved in tissues at the time of irradiation as a factor in radiotherapy. *The British Journal of Radiology*, 26(312):638–648, 1953.

[53] M Durante, E Bräuer-Krisch, and M Hill. Faster and safer? FLASH ultra-high dose rate in radiotherapy. *The British Journal of Radiology*, 91(1082):20170628, 2018.

[54] P J Hoskin. Hypoxia dose painting in prostate and cervix cancer. *Acta Oncologica*, 54(9):1259–1262, 2015.

[55] S Delanian and J-L Lefaix. Current management for late normal tissue injury: radiation-induced fibrosis and necrosis. *Seminars in Radiation Oncology*, 17(2): 99–107, 2007.

[56] V Favaudon, L Caplier, V Monceau, F Pouzoulet, M Sayarath, C Fouillade, M-F Poupon, I Brito, P Hupé, J Bourhis, J Hall, J-J Fontaine, and M-C Vozenin. Ultrahigh dose-rate FLASH irradiation increases the differential response between normal and tumor tissue in mice. *Science Translational Medicine*, 6(245):245ra93, 2014.

[57] C DesRosiers, V Moskvin, A F Bielajew, and L Papiez. 150–250 MeV electron beams in radiation therapy. *Physics in Medicine & Biology*, 45(7):1781, 2000.

[58] C M DesRosiers. *An evaluation of very high energy electron beams (up to 250 MeV) in radiation therapy.* PhD thesis, University of Purdue, 2004.

[59] V Moskvin, F Salvat, D K Stewart, and C M DesRosiers. Penelope Monte Carlo engine for treatment planning in radiation therapy with Very High Energy Electrons (VHEE) of 150–250 MeV. In *Nuclear Science Symposium Conference Record*, pages 1961–1966. Institute of Electrical and Electronics Engineers, 2010.

[60] L Papiez, C DesRosiers, and V Moskvin. Very high energy electrons (50–250 MeV) and radiation therapy. *Technology in Cancer Research & Treatment*, 1(2):105–110, 2002.

[61] C DesRosiers, V Moskvin, M Cao, C Joshi, and M Langer. Lung tumor treatment with very high energy electron beams of 150–250 Mev as compared to conventional megavoltage photon beams. *International Journal of Radiation Oncology •Biology •Physics*, 72(1):S612, 2008.

[62] C DesRosiers, V Moskvin, M Cao, C J Joshi, and M Langer. Laser-plasma generated very high energy electrons in radiation therapy of the prostate. In *Commercial and Biomedical Applications of Ultrafast Lasers VIII*, volume 6881, page 688109. International Society for Optics and Photonics, 2008.

[63] C Yeboah, G A Sandison, and V Moskvin. Optimization of intensity-modulated very high energy (50–250 MeV) electron therapy. *Physics in Medicine & Biology*, 47(8):1285, 2002.

[64] C Yeboah and G A Sandison. Optimized treatment planning for prostate cancer comparing IMPT, VHEET and 15 MV IMXT. *Physics in Medicine & Biology*, 47(13):2247, 2002.

[65] T Fuchs, H Szymanowski, U Oelfke, Y Glinec, C Rechatin, J Faure, and V Malka. Treatment planning for laser-accelerated very-high energy electrons. *Physics in Medicine & Biology*, 54(11):3315, 2009.

[66] I Martínez-Rovira, G Fois, and Y Prezado. Dosimetric evaluation of new approaches in grid therapy using nonconventional radiation sources. *Medical Physics*, 42(2):685–693, 2015.

[67] M Bazalova-Carter, B Qu, B Palma, B Hårdemark, E Hynning, C Jensen, P G Maxim, and B W Loo. Treatment planning for radiotherapy with very High-Energy Electron beams and comparison of VHEE and VMAT plans. *Medical Physics*, 42(5):2615–2625, 2015.

[68] B Palma, M Bazalova, B Hardemark, E Hynning, B Qu, B W Loo, and P G Maxim. Evaluation of the performance of Very High-Energy Electron (VHEE) beams in radiotherapy: Five clinical cases. *Medical Physics*, 42(6):3568, 2015.

[69] Bianey Palma, Magdalena Bazalova-Carter, Björn Hårdemark, Elin Hynning, Bradley Qu, B W Loo, and P G Maxim. Assessment of the quality of very high-energy electron radiotherapy planning. *Radiotherapy and Oncology*, 119(1): 154–158, 2016.

[70] E Schüler, K Eriksson, E Hynning, S L Hancock, S M Hiniker, M Bazalova-Carter, T Wong, Q-T Le, B W Loo, and P G Maxim. Very High-Energy Electron (VHEE) beams in radiation therapy; treatment plan comparison between VHEE, VMAT, and PPBS. *Medical Physics*, 44(6):2544–2555, 2017.

[71] O Lundh, C Rechatin, J Faure, A Ben-Ismaïl, J Lim, C De Wagter, W De Neve, and V Malka. Comparison of measured with calculated dose distribution from a 120 MeV electron beam from a laser-plasma accelerator. *Medical Physics*, 39(6): 3501–3508, 2012.

[72] A Subiel, V Moskvin, G H Welsh, S Cipiccia, D Reboredo, P Evans, M Partridge, C DesRosiers, M P Anania, A Cianchi, A Mostacci, E Chiadroni, D Di Giovenale, F Villa, R Pompili, M Ferrario, M Belleveglia, G Di Pirro, G Gatti, C Vaccarezza, B Seitz, R C Isaac, E Brunetti, S M Wiggins, B Ersfeld, M R Islam, M S Mendonca, A Sorensen, M Boyd, and D A Jaroszynski. Dosimetry of Very High Energy Electrons (VHEE) for radiotherapy applications: using radiochromic film measurements and Monte Carlo simulations. *Physics in Medicine & Biology*, 59 (19):5811, 2014.

[73] M Bazalova-Carter, M Liu, B Palma, M Dunning, D McCormick, E Hemsing, J Nelson, K Jobe, E Colby, A C Koong, S Tantawi, V Dolgashev, P G Maximb, and B W Loo. Comparison of film measurements and Monte Carlo simulations of dose delivered with very high-energy electron beams in a polystyrene phantom. *Medical Physics*, 42(4):1606–1613, 2015.

[74] A Subiel, V Moskvin, G H Welsh, S Cipiccia, D Reboredo, C DesRosiers, and D A Jaroszynski. Challenges of dosimetry of ultra–short pulsed very high energy electron beams. *Physica Medica*, 42:327–331, 2017.

[75] A Lagzda, R Jones, J Jones, K Kirkby, W Farabolini, and D Angal-Kalinin. Relative insensitivity to inhomogeneities on very high energy electron dose distributions. In *Proceedings of the 8th International Particle Accelerator Conference*, pages 4791–4794. International Particle Accelerator Conference, 2017.

[76] K Stewart, V Moskvin, and C DesRosiers. Design aspects for very high energy electron (150 to 250 MeV) acceleration for use in radiation therapy: beam shaping, electromagnetic scanning. In *IEEE Nuclear Science Symposium & Medical Imaging Conference*, pages 1622–1627. International Society for Optics and Photonics, 2010.

[77] L Papiez, T Bortfeld, and W R Hendee. Very high energy electromagnetically-scanned electron beams are an attractive alternative to photon IMRT. *Medical Physics*, 31(7):1945–1948, 2004.

[78] P G Maxim and B W Loo. Pluridirectional high-energy agile scanning electron radiotherapy (PHASER): extremely rapid treatment for early lung cancer. Technical report, Stanford University, 2015.

[79] P G Maxim, S G Tantawi, and B W Loo. PHASER: a platform for clinical translation of FLASH cancer radiotherapy. *Radiotherapy and Oncology*, 139:28–33, 2019.

[80] K Nakajima, J Yuan, L Chen, and Z Sheng. Laser-driven very high energy electron/photon beam radiation therapy in conjunction with a robotic system. *Applied Sciences*, 5(1):1–20, 2015.

[81] SLAC National Accelerator Laboratory. Phaser design. `https://www.youtube.com/watch?v=jgd2et9b5ag`, 2018. (accessed July 22, 2019).

[82] W H Bostick. Possible techniques in direct-electron-beam tumor therapy. *Physical Review*, 77(4):564, 1949.

[83] C C Shih. High energy electron radiotherapy in a magnetic field. *Medical Physics*, 2(1):9–13, 1975.

[84] M S Weinhous, R Nath, and R J Schulz. Enhancement of electron beam dose distributions by longitudinal magnetic fields: Monte Carlo simulations and magnet system optimization. *Medical Physics*, 12(5):598–603, 1985.

[85] D P Whitmire, D L Bernard, M D Peterson, and J A Purdy. Magnetic enhancement of electron dose distribution in a phantom. *Medical Physics*, 4(2):127–131, 1977.

[86] R Nath and R J Schulz. Modification of electron-beam dose distributions by transverse magnetic fields. *Medical Physics*, 5(3):226–230, 1978.

[87] B R Paliwal and A L Wiley. Magnetic field modification of electron beam dose distributions in inhomogeneous media. In *High Energy Electrons in Radiation Therapy*, pages 28–28. Springer, 1980.

[88] D P Whitmire, D L Bernard, and M D Peterson. Magnetic modification of the electron-dose distribution in tissue and lung phantoms. *Medical Physics*, 5(5): 409–417, 1978.

[89] D W Litzenberg, B A Fraass, D L McShan, T W O'Donnell, D A Roberts, F D Becchetti, A F Bielajew, and J M Moran. An apparatus for applying strong longitudinal magnetic fields to clinical photon and electron beams. *Physics in Medicine & Biology*, 46(5):N105, 2001.

[90] A F Bielajew. The effect of strong longitudinal magnetic fields on dose deposition from electron and photon beams. *Medical Physics*, 20(4):1171–1179, 1993.

[91] E Nardi and G Barnea. Electron beam therapy with transverse magnetic fields. *Medical Physics*, 26(6):967–973, 1999.

[92] Y Chen, A F Bielajew, D W Litzenberg, J M Moran, and F D Becchetti. Magnetic confinement of electron and photon radiotherapy dose: a Monte Carlo simulation with a nonuniform longitudinal magnetic field. *Medical Physics*, 32(12):3810–3818, 2005.

[93] Y Chen. *The magnetic confinement of electron and photon dose profiles and the possible effect of the magnetic field on relative biological effectiveness*. University of Michigan, 2005.

[94] M Sempert. New developments in high energy electron beam therapy with the 35 MeV brown boveri betatron. *Radiology*, 74(1):105–106, 1960.

[95] M A Earl and L Ma. Depth dose enhancement of electron beams subject to external uniform longitudinal magnetic fields: a Monte Carlo study. *Medical Physics*, 29(4):484–491, 2002.

[96] Y Glinec, J Faure, V Malka, T Fuchs, H Szymanowski, and U Oelfke. Radiotherapy with laser-plasma accelerators: Monte Carlo simulation of dose deposited by an experimental quasimonoenergetic electron beam. *Medical Physics*, 33(1): 155–162, 2006.

[97] D Jette. Magnetic fields with photon beams: dose calculation using electron multiple-scattering theory. *Medical Physics*, 27(8):1705–1716, 2000.

[98] X A Li, L Reiffel, J C Chu, and S Naqvi. Conformal photon-beam therapy with transverse magnetic fields: a Monte Carlo study. *Medical Physics*, 28(2):127–133, 2001.

[99] S J Wadi-Ramahi, S A Naqvi, and J C Chu. Evaluating the effectiveness of a longitudinal magnetic field in reducing underdosing of the regions around upper respiratory cavities irradiated with photon beams- a Monte Carlo study. *Medical Physics*, 28(8):1711–1717, 2001.

[100] Shahid A Naqvi, X Allen Li, Shada W Ramahi, James C Chu, and Sung-Joon Ye. Reducing loss in lateral charged-particle equilibrium due to air cavities present in X-ray irradiated media by using longitudinal magnetic fields. *Medical physics*, 28(4):603–611, 2001.

[101] G A McAuley, S L Heczko, T T Nguyen, J M Slater, J D Slater, and A J Wroe. Monte Carlo evaluation of magnetically focused proton beams for radiosurgery. *Physics in Medicine & Biology*, 63(5):055010, 2018.

[102] A Schüller, M Meier, C Makowski, S Pojtinger, and R-P Kapsch. e-Poster ResearchGate: Capabilities of the metrological electron accelerator facility (MELAF) for research in radiation effects. `https://www.researchgate.net/publication/319764393_Capabilities_of_the_metrological_electron_accelerator_facility_MELAF_for_research_in_radiation_effects`, 2008–2020. (accessed February 11, 2020).

[103] A Mosnier, M Authier, D Bogard, A Curtoni, O Delferriere, G Dispau, R Duperrier, W Farabolini, P Girardot, M Jablonka, J-L Jannin, A Luong, F Peauger, R Roux, and N Rouviére. The probe beam linac in CTF3. In *Tenth European Particle Accelerator Conference*, pages 679–681, 2006.

[104] Elekta Limited. *Elekta medical linear accelerator. Site planning construction information*. Elekta Limited, 2014.

[105] T P Wangler. RF linear accelerators. *Wiley, Weinheim*, 2008.

[106] W Wuensch. High-gradient breakdown in normal-conducting RF cavities. In *Proceedings of 8th European Particle Accelerator Conference*, page 134, 2002.

[107] S M Hanna. Applications of X-band technology in medical accelerators. In *Proceedings of the 1999 Particle Accelerator Conference*, volume 4, pages 2516–2518. Institute of Electrical and Electronics Engineers, 1999.

[108] K Derikum. A dedicated irradiation facility for radiotherapy dosimetry. In *World Congress on Medical Physics and Biomedical Engineering*, pages 53–55. Springer, 2009.

[109] A Schüller, J Illemann, F Renner, C Makowski, and R-P Kapsch. Traceable charge measurement of the pulses of a 27 MeV electron beam from a linear accelerator. *Journal of Instrumentation*, 12(03):03003, 2017.

[110] CERN. CLEAR official website. `https://clear.web.cern.ch/`, 2019. (accessed July 22, 2019).

[111] CERN. VESPER official website. `http://vesper.web.cern.ch`, 2017. (accessed July 04, 2019).

[112] T Tajima and J M Dawson. Laser electron accelerator. *Physical Review Letters*, 43(4):267, 1979.

[113] S P D Mangles, C D Murphy, Z Najmudin, A G R Thomas, J L Collier, A E Dangor, E J Divall, P S Foster, J G Gallacher, C J Hooker, D A Jaroszynski, A J Langley, W B Mori, P A Norreys, F S Tsung, R Viskup, Walton B R, and K Krushelnick. Monoenergetic beams of relativistic electrons from intense laser-plasma interactions. *Nature*, 431(7008):535–538, 2004.

[114] C G R Geddes, C Toth, J Van Tilborg, E Esarey, C B Schroeder, D Bruhwiler, C Nieter, J Cary, and W P Leemans. High-quality electron beams from a laser wakefield accelerator using plasma-channel guiding. *Nature*, 431(7008):538–541, 2004.

[115] J Faure, Y Glinec, A Pukhov, S Kiselev, S Gordienko, E Lefebvre, J-P Rousseau, F Burgy, and V Malka. A laser-plasma accelerator producing monoenergetic electron beams. *Nature*, 431(7008):541–544, 2004.

[116] W P Leemans, B Nagler, A J Gonsalves, C Toth, K Nakamura, C G R Geddes, E S C B Esarey, C B Schroeder, and S M Hooker. GeV electron beams from a centimetre-scale accelerator. *Nature Physics*, 2(10):696, 2006.

[117] W P Leemans, A J Gonsalves, H S Mao, K Nakamura, C Benedetti, C B Schroeder, C Tóth, J Daniels, D E Mittelberger, S S Bulanov, J L. Vay, C G R Geddes, and E Esarey. Multi-GeV electron beams from capillary-discharge-guided subpetawatt laser pulses in the self-trapping regime. *Physical Review Letters*, 113: 245002, 2014.

[118] A J Gonsalves, K Nakamura, J Daniels, C Benedetti, C Pieronek, T C H De Raadt, S Steinke, J H Bin, S S Bulanov, J Van Tilborg, C G R Geddes, C B Schroeder, C Tóth, E Esarey, K Swanson, L Fan-Chiang, G Bagdasarov, N Bobrova, V Gasilov, G Korn, P Sasorov, and W P Leemans. Petawatt laser guiding and electron beam acceleration to 8 GeV in a laser-heated capillary discharge waveguide. *Physical Review Letters*, 122(8):084801, 2019.

[119] I Blumenfeld, C E Clayton, F-J Decker, M J Hogan, C Huang, R Ischebeck, R Iverson, C Joshi, T Katsouleas, N Kirby, W Lu, K A Marsh, W B Mori, P. Muggli, E Oz, R H Siemann, D Walz, and M Zhou. Energy doubling of 42 GeV electrons in a metre-scale plasma wakefield accelerator. *Nature*, 445(7129): 741, 2007.

[120] R A Fonseca, L O Silva, F S Tsung, V K Decyk, W Lu, C Ren, W B Mori, S Deng, S Lee, T Katsouleas, and J C Adam. Osiris: A three-dimensional, fully relativistic particle in cell code for modeling plasma based accelerators. In *International Conference on Computational Science*, pages 342–351. Springer, 2002.

[121] THALES. Thales official website. https://www.thalesgroup.com/en, 2019. (accessed July 04, 2019).

[122] M P Anania, E Brunetti, S Cipiccia, D Clark, R Issac, G G Manahan, T McCanny, A W Reitsma, R P Shanks, G H Welsh, S M Wiggins, J A Clarke, M Poole, B J A Shepherd, M De Loos, and B Van der Geer. The ALPHA-X beam line: toward a compact FEL. In *Proceedings of the 31st International Free Electron Laser Conference*, 2009.

[123] G H Welsh, M P Anania, C Aniculaesei, E Brunetti, R T Liam Burgess, S Cipiccia, D Clark, B Ersfeld, M R Islam, R C Issac, G G Manahan, T McCanny, G Raj, A J W Reitsma, R P Shanks, G Vieux, S M Wiggins, D A Jaroszynski, W A Gillespie, A M MacLeod, B Van der Geer, and M De Loos. Electron beam quality measurements on the ALPHA-X laser-plasma wakefield accelerator. *Proceedings of the First International Particle Accelerator Conference*, 2010.

[124] G S Ibbott. Radiation dosimetry: electron beams with energies between 1 and 50 MeV. *Medical Physics*, 12(6):813–813, 1985.

[125] F Renner, A Schwab, R-P Kapsch, C Makowski, and D Jannek. An approach to an accurate determination of the energy spectrum of high-energy electron beams using magnetic spectrometry. *Journal of Instrumentation*, 9(3):03004, 2014.

[126] Physikalisch-Technische Bundesanstalt. PTB official website. https://www.ptb.de. (accessed July 22, 2019).

[127] K B Unser. Design and preliminary tests of a beam intensity monitor for LEP. In *Proceedings of the 1989 IEEE Particle Accelerator Conference. Accelerator Science and Technology*, pages 71–73. Institute of Electrical and Electronics Engineers, 1989.

[128] J Bergoz. Current monitors for particle beams. *Nuclear Physics*, 525:595–600, 1991.

[129] Bergoz Instrumentation. Bergoz instrumentation official website. `www.bergoz.com`, 2018. (accessed October 7, 2018).

[130] A Schüller, C Makowski, R-P Kapsch, R Nolte, and P Beck. Melaf-a 50 MeV electron accelerator facility for research in radiation effects. In *17th European Conference on Radiation and Its Effects on Components and Systems*, pages 1–4. Institute of Electrical and Electronics Engineers, 2017.

[131] U Iriso, G Benedetti, and F Pérez. Experience with YAG and OTR screens at ALBA. *9th European Workshop on Beam Diagnostics and Instrumentation for Particle Accelerators*, 5(2008.10):15, 2009.

[132] Y Yamazaki, T Kurihara, H Kobayashi, I Sato, and A Asami. High-precision pepper-pot technique for a low-emittance electron beam. *Nuclear Instruments and Methods in Physics Research, Accelerators, Spectrometers, Detectors and Associated Equipment*, 322(2):139–145, 1992.

[133] W Schottky. Über spontane stromschwankungen in verschiedenen elektrizität-sleitern. *Annalen der Physik*, 362(23):541–567, 1918.

[134] M Betz, O R Jones, T Lefevre, and M Wendt. Bunched-beam schottky monitoring in the LHC. *Nuclear Instruments and Methods in Physics Research, Accelerators, Spectrometers, Detectors and Associated Equipment*, 874:113–126, 2017.

[135] B X Yang and A H Lumpkin. Simultaneous measurement of electron beam size and divergence with an undulator. In *Proceedings of the 1999 Particle Accelerator Conference*, volume 3, pages 2161–2163. Institute of Electrical and Electronics Engineers, 1999.

[136] Northern Illinois Center for Accelerator and Detector Development. Fundamentals of accelerator physics and technology. `http://nicadd.niu.edu/~syphers/uspas/2018w/some-notes-on-ellipses.html`, 2019. (accessed August 23, 2019).

[137] E D Courant and H S Snyder. Theory of the alternating-gradient synchrotron. *Annals of Physics*, 3(1):1–48, 1958.

[138] B J Holzer. Beam optics and lattice design in high energy particle accelerators. In *Accelerators and Colliders*, pages 119–123. Springer, 2013.

[139] C Leroy and P-G Rancoita. *Principles of radiation interaction in matter and detection.* World Scientific, 2011.

[140] International Commission on Radiation Units and Measurements. Stopping powers and ranges for protons and α-particles. Report 49. *Journal of the International Commission on Radiation Units and Measurements*, 25(2), 1993.

[141] National Institute of Standards and Technology. Physical measurement laboratory. `https://www.nist.gov`. (accessed July 22, 2019).

[142] R R Wilson. The range and straggling of high energy electrons. *Physical Review*, 84(1):100, 1951.

[143] International Commission on Radiation Units and Measurements. Stopping powers for electrons and positrons. Report 37. *Journal of the International Commission on Radiation Units and Measurements*, 19(2), 1984.

[144] H Bethe. Zur theorie des durchgangs schneller korpuskularstrahlen durch materie. *Annalen der Physik*, 397(3):325–400, 1930.

[145] F Bloch. Zur bremsung rasch bewegter teilchen beim durchgang durch materie. *Annalen der Physik*, 408(3):285–320, 1933.

[146] W Bragg and M Kleeman. On the α-particles of radium. *Philosophical Magazine*, 10:600–602, 1905.

[147] J A Sorenson and M E Phelps. *Physics in nuclear medicine.* Grune & Stratton, 1987.

[148] S M Seltzer, J H Hubbell, and M J Berger. Some theoretical aspects of electron and photon dosimetry. In *National and international standardization of radiation dosimetry*. International Atomic Energy Agency, 1978.

[149] R D Evans and R D Evans. *The atomic nucleus*. McGraw-Hill, 1955.

[150] R D Evans. X-ray and γ-ray interactions. In *Fundamentals*, pages 93–155. Elsevier, 1968.

[151] I M Frank. Vavilov-Cherenkov radiation for electric and magnetic multipoles. *Soviet Physics Uspekhi*, 27(10):772, 1984.

[152] Glenn F Knoll. *Radiation detection and measurement*. John Wiley & Sons, 2010.

[153] J Yanch. Introduction to ionizing radiation, lecture notes. `https://dspace.mit.edu/bitstream/handle/1721.1/39132/22-01Fall-2003/OcwWeb/Nuclear-Engineering/22-01Introduction-to-Ionizing-RadiationFall2003/CourseHome/index.htm?sequence=1&isAllowed=y`, 2002-2007. (accessed February 11, 2020).

[154] A Einstein. On a heuristic point of view concerning the production and transformation of light. *Annalen der Physik*, pages 1–18, 1905.

[155] T Åberg. Unified theory of Auger electron emission. *Physica Scripta*, 1992(41):71, 1992.

[156] A H Compton. A quantum theory of the scattering of X-rays by light elements. *Physical Review*, 21(5):483, 1923.

[157] Y-S Tsai. Pair production and bremsstrahlung of charged leptons. *Reviews of Modern Physics*, 46(4):815, 1974.

[158] T Tagami. Quasi-deuteron model of atomic nuclei. *Progress of Theoretical Physics*, 21(4):533–561, 1959.

[159] A W Chao, K H Mess, M Tigner, and F Zimmermann. *Handbook of accelerator physics and engineering*. World scientific, 2013.

[160] I Plante and F A Cucinotta. Monte-carlo simulation of ionizing radiation tracks. *Application of Monte Carlo methods in biology, medicine and other fields of science*, pages 315–356, 2011.

[161] FLUKA Team. FLUKA official website. `http://www.fluka.org/fluka.php`, 2000–2019. (accessed July 22, 2019).

[162] G Battistoni, T Boehlen, F Cerutti, P W Chin, L S Esposito, A Fassò, A Ferrari, A Lechner, A Empl, A Mairani, Mereghetti, P Garcia Ortega, J Ranft, S Roesler, P R Sala, V Vlachoudis, and G Smirnov. Overview of the FLUKA code. *Annals of Nuclear Energy*, 82:10–18, 2015.

[163] G Battistoni, J Bauer, T T Boehlen, F Cerutti, M P W Chin, R Dos Santos Augusto, A Ferrari, P G Ortega, W Kozłowska, G Magro, A Mairani, K Parodi, P R Sala, P Schoofs, T Tessonnier, and V Vlachoudis. The FLUKA code: an accurate simulation tool for particle therapy. *Frontiers in Oncology*, 6:116, 2016.

[164] V Andersen, F Ballarini, G Battistoni, M Campanella, M Carboni, F Cerutti, A Empl, A Fasso, A Ferrari, E Gadioli, M V Garzelli, K T Lee, A Ottolenghi, M Pelliccioni, L S Pinsky, J Ranft, S Roesler, P Sala, and T Wilson. The FLUKA code for space applications: recent developments. *Advances in Space Research*, 34(6):1302–1310, 2004.

[165] F Ballarini, M Biaggi, L De Biaggi, A Ferrari, A Ottolenghi, A Panzarasa, H G Paretzke, M Pelliccioni, P Sala, D Scannicchio, M Zankl, and L W Townsend. Role of shielding in modulating the effects of solar particle events: Monte Carlo calculation of absorbed dose and DNA complex lesions in different organs. *Advances in Space Research*, 34(6):1338–1346, 2004.

[166] D E Cullen, S T Perkins, and S M Seltzer. Tables and graphs of electron interaction cross 10 eV to 100 GeV derived from the LLNL evaluated electron data library (EEDL), Z = 1–100. *Lawrence Livermore National Laboratory*, 31, 1991.

[167] D E Cullen, J H Hubbell, and L Kissel. EPDL97: the evaluated photo data

library '97 version. Technical report, Lawrence Livermore National Labolatory, 1997.

[168] G Marsaglia and W W Tsang. The 64-bit universal RNG. *Statistics & Probability Letters*, 66(2):183–187, 2004.

[169] L D Landau. On the energy loss of fast particles by ionization. *Journal of Physics*, 8:201–205, 1944.

[170] P V Vavilov. Ionization losses of high-energy heavy particles. *Journal of Experimental and Theoretical Physics*, 5, 1957.

[171] A Fasso, A Ferrari, J Ranft, and P R Sala. New developments in FLUKA modelling of hadronic and em interactions. In *Proceedings of The 3rd workshop on simulating Accelerator Radiation Environments*, volume 97, pages 32–43. National Laboratory for High Energy Physics, 1997.

[172] G Moliére. Theorie der streuung schneller geladener teilchen II mehrfach und vielfachstreuung. *Zeitschrift für Naturforschung A*, 3(2):78–97, 1948.

[173] H A Bethe. Moliére's theory of multiple scattering. *Physical Review*, 89(6):1256, 1953.

[174] M J Berger, J S Coursey, M A Zucker, and J Chang. *Stopping-power and range tables for electrons, protons, and helium ions.* National Institute of Standards and Technology, 1998.

[175] P R Almond, P J Biggs, B M Coursey, W F Hanson, M S Huq, R Nath, and D W O Rogers. AAPM's TG-51 protocol for clinical reference dosimetry of high-energy photon and electron beams. *Medical Physics*, 26(9):1847–1870, 1999.

[176] P Andreo, D T Burns, K Hohlfeld, M S Huq, T Kanai, F Laitano, V Smyth, and S Vynckier. *Absorbed dose determination in external beam radiotherapy.* International Atomic Agency, 2001.

[177] A Subiel. *Feasibility studies on the application of relativistic electron beams from a laser plasma wakefield accelerator in radiotherapy.* PhD thesis, University of Strathclyde, 2014.

[178] A Ferrari, P R Sala, A Fasso, and J Ranft. *FLUKA manual.* Italian National Institute for Nuclear Physics, 2005.

[179] S S Dietrich and B L Berman. Atlas of photoneutron cross sections obtained with monoenergetic photons. *Atomic Data and Nuclear Data Tables*, 38(2):199–338, 1988.

[180] H J Bhabha. The scattering of positrons by electrons with exchange on Dirac's theory of the positron. *Proceedings of the Royal Society*, 154(881):195–206, 1936.

[181] A Wambersie, T Landberg, and R Gahbauer. Prescribing, recording and reporting photon beam therapy: the problem of margins. *Patras Medical Physics*, 99:25–31, 1999.

[182] NIRST Physical Measurement Laboratory. Xcom: Photon cross sections database. `https://www.nist.gov/pml/xcom-photon-cross-sections-database`, 2019. (accessed February 10, 2020).

[183] W Friedland, M Dingfelder, P Kundrát, and P Jacob. Track structures, DNA targets and radiation effects in the biophysical Monte Carlo simulation code PAR-TRAC. *Mutation Research/Fundamental and Molecular Mechanisms of Mutagenesis*, 711(1-2):28–40, 2011.

[184] J Valentin. The 2007 recommendations of the International Commission on Radiological Protection. *Annals of International Commission on Radiological Protection*, 37(2):1–332, 2007.

[185] United States Nuclear Regulatory Commission. NRC regulations (10 CFR) part 35: Medical use of byproduct material. `https://www.nrc.gov/reading-rm/doc-collections/cfr/part035/`, 2019. (accessed February 10, 2020).

[186] E J Hall and A J Giaccia. *Radiobiology for the Radiologist.* Lippincott Williams & Wilkins, 2006.

[187] International Commission on Radiation Units and Measurements. Conversion coefficients for use in radiological protection against external radiation. Report 57. *Journal of the International Commission on Radiation Units and Measurements*, 29(2), 1998.

[188] International Commission on Radiation Units and Measurements. Quantification and reporting of low-dose and other heterogeneous exposures. Report 86. *Journal of the International Commission on Radiation Units and Measurements*, 11(2), 2011.

[189] International Commission on Radiation Units and Measurements. Fundamental quantities and units for ionizing radiation. Report 60. *Journal of the International Commission on Radiation Units and Measurements*, 31(1), 1998.

[190] International Commission on Radiation Units and Measurements. Reference data for the validation of doses from cosmic-radiation exposure of aircraft crew. Report 84. *Journal of the International Commission on Radiation Units and Measurements*, 10(2), 2010.

[191] J J Wilkens and U Oelfke. Analytical linear energy transfer calculations for proton therapy. *Medical Physics*, 30(5):806–815, 2003.

[192] P Andreo, J P Seuntjens, and E B Podgorsak. *Calibration of photon and electron beams.* International Atomic Energy Agency, 2005.

[193] P R Symonds, J A Mills, and A Duxbury. *Walter and Miller's Textbook of Radiotherapy: Radiation Physics, Therapy and Oncology.* Elsevier Health Sciences, 2019.

[194] P Andreo, D Burns, K Hohlfeld, M Huq, T Kanai, F Laitano, V Smyth, and S Vynckier. Absorbed dose determination in external beam radiotherapy: an international code of practice for dosimetry based standards of absorbed dose to

water. Technical Reports Series No. 398. *International Atomic Energy Agency*, 11(b):13–181, 2004.

[195] S Devic. Radiochromic film dosimetry: past, present, and future. *Physica Medica*, 27(3):122–134, 2011.

[196] S A Park, J W Kwak, M G Yoon, D H Shin, S B Lee, K H Cho, S K Kang, K J Kim, H S Bae, and S Y Park. Dose verification of proton beam therapy using the Gafchromic EBT film. *Radiation Measurements*, 46(8):717–721, 2011.

[197] S Devic, N Tomic, and D Lewis. Reference radiochromic film dosimetry: review of technical aspects. *Physica Medica*, 32(4):541–556, 2016.

[198] L Campajola, P Casolaro, and F Di Capua. Absolute dose calibration of EBT3 Gafchromic films. *Journal of Instrumentation*, 12(08):P08015, 2017.

[199] V C Borca, M Pasquino, G Russo, P Grosso, D Cante, P Sciacero, G Girelli, M R L Porta, and S Tofani. Dosimetric characterization and use of Gafchromic EBT3 film for IMRT dose verification. *Journal of Applied Clinical Medical Physics*, 14(2):158–171, 2013.

[200] C Huet, C Moignier, J Fontaine, and I Clairand. Characterization of the Gafchromic EBT3 films for dose distribution measurements in stereotactic radiotherapy. *Radiation Measurements*, 71:364–368, 2014.

[201] Ashland. Film QA^{TM}Pro calibration. `http://www.gafchromic.com/filmqa-software/filmqapro/calibration.asp`, 2019. (accessed August 14, 2019).

[202] P Sipilä, J Ojala, S Kaijaluoto, I Jokelainen, and A Kosunen. Gafchromic EBT3 film dosimetry in electron beams-energy dependence and improved film read-out. *Journal of Applied Clinical Medical Physics*, 17(1):360–373, 2016.

[203] A Niroomand-Rad, C R Blackwell, B M Coursey, K P Gall, J M Galvin, W L McLaughlin, A S Meigooni, R Nath, J E Rodgers, and C G Soares. Radiochromic

film dosimetry: recommendations of AAPM radiation therapy committee task group 55. *Medical Physics*, 25(11):2093–2115, 1998.

[204] E B Podgorsak. *Review of radiation oncology physics: a handbook for teachers and students.* International Atomic Energy Agency, 2003.

[205] E G Aird. *Central axis depth dose data for use in radiotherapy: 1996: a survey of depth doses and related data measured in water or equivalent media.* British Institute of Radiology, 1996.

[206] D T Burns, G X Ding, and D W O Rogers. R50 as a beam quality specifier for selecting stopping-power ratios and reference depths for electron dosimetry. *Medical Physics*, 23(3):383–388, 1996.

[207] Deutsches Institut für Normung. *Dosismessverfahren nach der Sondenmethode für Photonen-und Elektronenstrahlung-Teil 2: Dosimetrie hochenergetischer Photonen-und Elektronenstrahlung mit Ionisationskammern. DIN 6800–2:2008–03.* Beuth Verlag, 2008.

[208] G Jaffé. Zur theorie der ionisation in kolonnen. *Annalen der Physik*, 347(12): 303–344, 1913.

[209] G Jaffé. Zur theorie der ionisation in kolonnen. II. *Annalen der Physik*, 393(7): 977–1008, 1929.

[210] P R Bevington, D K Robinson, J M Blair, A J Mallinckrodt, and S McKay. Data reduction and error analysis for the physical sciences. *Computers in Physics*, 7 (4):415–416, 1993.

[211] S Devic, J Seuntjens, E Sham, E B Podgorsak, C R Schmidtlein, A S Kirov, and C G Soares. Precise radiochromic film dosimetry using a flat-bed document scanner. *Medical Physics*, 32(7):2245–2253, 2005.

[212] J Sorriaux, A Kacperek, S Rossomme, J A Lee, D Bertrand, S Vynckier, and E Sterpin. Evaluation of Gafchromic® EBT3 films characteristics in therapy photon, electron and proton beams. *Physica Medica*, 29(6):599–606, 2013.

[213] Y Feng, H F Tiedje, K Gagnon, and R Fedosejevs. Spectral calibration of EBT3 and HD-V2 radiochromic film response at high dose using 20 MeV proton beams. *Review of Scientific Instruments*, 89(4):043511, 2018.

[214] E Y L Marroquin, J A Herrera Gonzalez, M A Camacho Lopez, J E V Barajas, and O A García-Garduño. Evaluation of the uncertainty in an EBT3 film dosimetry system utilizing net optical density. *Journal of Applied Clinical Medical Physics*, 17(5):466–481, 2016.

[215] G G Zeng, M R McEwen, D W O Rogers, and N V Klassen. An experimental and Monte Carlo investigation of the energy dependence of alanine/EPR dosimetry: Ii. clinical electron beams. *Physics in Medicine & Biology*, 50(6):1119–1129, 2005.

[216] E S Bergstrand, H Bjerke, and E O Hole. An experimental investigation of the electron energy dependence of the EPR alanine dosimetry system. *Radiation Measurements*, 39(1):21–28, 2005.

[217] M F Desrosiers. Alanine-EPR high-dose radiation metrology. In *Applications of EPR in Radiation Research*, pages 489–507. Springer, 2014.

[218] M Anton. Development of a secondary standard for the absorbed dose to water based on the alanine EPR dosimetry system. *Applied Radiation and Isotopes*, 62 (5):779–795, 2005.

[219] S Nakagawa. ESR spectral change of radicals produced in L-alanine-3, 3, 3-d3 and L-alanine-d4.-a new pathway to produce the de-hydrogen radical and the hydrogen exchange reactions of the de-amino radical. *Radiation Physics and Chemistry*, 165:108406, 2019.

[220] E Waldeland, E O Hole, E Sagstuen, and E Malinen. The energy dependence of lithium formate and alanine EPR dosimeters for medium energy X-rays. *Medical Physics*, 37(7):3569–3575, 2010.

[221] M F Desrosiers, J M Puhl, and S L Cooper. An absorbed-dose/dose-rate dependence for the alanine-EPR dosimetry system and its implications in high-dose

ionizing radiation metrology. *Journal of Research of the National Institute of Standards and Technology*, 113(2):79, 2008.

[222] V Nagy, J M Puhl, and M F Desrosiers. Advancements in accuracy of the alanine dosimetry system. the influence of the irradiation temperature. *Radiation Physics and Chemistry*, 57(1):1–9, 2000.

[223] M F Desrosiers, S L Cooper, J M Puhl, A L McBain, and G W Calvert. A study of the alanine dosimeter irradiation temperature coefficient in the -77°C to +50°C range. *Radiation Physics and Chemistry*, 71(1–2):365–370, 2004.

[224] M F Desrosiers, M Peters, and J M Puhl. A study of the alanine dosimeter irradiation temperature coefficient from 25 to 80°C. *Radiation Physics and Chemistry*, 78(7–8):465–467, 2009.

[225] W L McLaughlin. ESR dosimetry. *Radiation Protection Dosimetry*, 47:255, 1993.

[226] American Society for Testing and Materials. Standard practice for use of an alanine-EPR dosimetry system. ISO/ASTM 51607: 2004 [ASTM E61]. *ISO/ASTM International*, 2004.

[227] E Waldeland and E Malinen. Review of the dose-to-water energy dependence of alanine and lithium formate EPR dosimeters and LiF TL-dosimeters- comparison with Monte Carlo simulations. *Radiation Measurements*, 46(9):945–951, 2011.

[228] J M Arber and P H G Sharpe. Fading characteristics of irradiated alanine pellets: The importance of pre-irradiation conditioning. *Applied Radiation and Isotopes*, 44(1–2):19–22, 1993.

[229] P H G Sharpe, K Rajendran, and J P Sephton. Progress towards an alanine/ESR therapy level reference dosimetry service at NPL. *Applied Radiation and Isotopes*, 47(11/12):1171–1175, 1996.

[230] M Anton and S Lelie. *Alanine dosimetry: uncertainty components*. Physikalisch-Technische Bundesanstalt Braunschweig und Berlin, 2009.

[231] M Krystek and M Anton. A least-squares algorithm for fitting data points with mutually correlated coordinates to a straight line. *Measurement science and Technology*, 22(3):035101, 2011.

[232] M Anton, P J Allisy-Roberts, C Kessler, and D T Burns. A blind test of the alanine dosimetry secondary standard of the PTB conducted by the BIPM. *Metrologia*, 51:06001, 2014.

[233] M Anton. Uncertainties in alanine/ESR dosimetry at the physikalisch-technische bundesanstalt. *Physics in Medicine & Biology*, 51(21):5419–5440, 2006.

[234] J H Hubbell and S M Seltzer. *Tables of X-ray mass attenuation coefficients and mass energy-absorption coefficients 1 keV to 20 MeV for elements Z = 1 to 92 and 48 additional substances of dosimetric interest*. National Institute of Standards and Technology, 1995.

[235] L Deniau, H Grote, G Roy, and F Schmidt. *The MADX program (Methodical Accelerator Design) version 5.03. 07 user's reference manual*. CERN Internal Document, 2017.

[236] F A Calvo. Intraoperative irradiation: precision medicine for quality cancer control promotion. *Radiation Oncology*, 12(1):36, 2017.

[237] L Quintieri, Maria G Pia, M Augelli, P Saracco, M Capogni, and G Guarnieri. Quantification of the validity of simulations based on Geant4 and FLUKA for photo-nuclear interactions in the high energy range. In *The European Physical Journal Web of Conferences*, volume 153, page 06023. Édition Diffusion Presse Sciences, 2017.

[238] C Streffer. The ICRP 2007 recommendations. *Radiation protection dosimetry*, 127(1-4):2–7, 2007.

[239] K L Eales, K E R Hollinshead, and D A Tennant. Hypoxia and metabolic adaptation of cancer cells. *Oncogenesis*, 5(1):e190–e190, 2016.

205

[240] E Malinen and Å Søvik. Dose or let painting-what is optimal in particle therapy of hypoxic tumors? *Acta Oncologica*, 54(9):1614–1622, 2015.

[241] N Bassler, J Toftegaard, A Lühr, B S Sørensen, E Scifoni, M Krämer, O Jäkel, L S Mortensen, J Overgaard, and J B Petersen. LET-painting increases tumour control probability in hypoxic tumours. *Acta Oncologica*, 53(1):25–32, 2014.

[242] L Tkachenko, I Bogdanov, S Kozub, V Sytnik, D Varentsov, S Zinchenko, and V Zubko. Development of wide-aperture quadrupole magnets for plasma experiments in the FAIR project. *Transactions on Applied Superconductivity*, 23(3): 4000204, 2012.

[243] Enrico Felcini, Luca Bottura, Jeroen van Nugteren, Gijs de Rijk, Glyn Kirby, and Bertrand Dutoit. Magnetic design of a superconducting toroidal gantry for hadron therapy. *Transactions on Applied Superconductivity*, PP(99), 2020.

[244] K Kokurewicz, G H Welsh, E Brunetti, S M Wiggins, M Boyd, A Sorensen, A Chalmers, G Schettino, A Subiel, C DesRosiers, and D. A. Jaroszynski. Laser-plasma generated Very High Energy Electrons (VHEEs) in radiotherapy. In *Medical Applications of Laser-Generated Beams of Particles IV: Review of Progress and Strategies for the Future*, volume 10239, page 102390C. International Society for Optics and Photonics, 2017.